AFRL-AFOSR-VA-TR-2024-0097

3D Thermo-Mechanical Modeling of Multilayered TBC's for Gas Turbine Engines

Valarezo, Alfredo
UNIVERSIDAD SAN FRANCISCO DE QUITO USFQ
DIEGO DE ROBLES S/N Y PAMPITE
QUITO, , 170157
ECU

01/12/2024
Final Technical Report

Air Force Research Laboratory
Air Force Office of Scientific Research
Arlington, Virginia 22203
Air Force Materiel Command

REPORT DOCUMENTATION PAGE

PLEASE DO NOT RETURN YOUR FORM TO THE ABOVE ORGANIZATION.

1. REPORT DATE	2. REPORT TYPE	3. DATES COVERED	
20240112	Final	START DATE 20200930	END DATE 20230929

4. TITLE AND SUBTITLE
3D Thermo-Mechanical Modeling of Multilayered TBC's for Gas Turbine Engines

5a. CONTRACT NUMBER	5b. GRANT NUMBER	5c. PROGRAM ELEMENT NUMBER
	FA9550-20-1-0075	
5d. PROJECT NUMBER	**5e. TASK NUMBER**	**5f. WORK UNIT NUMBER**

6. AUTHOR(S)
Alfredo Valarezo

7. PERFORMING ORGANIZATION NAME(S) AND ADDRESS(ES)
UNIVERSIDAD SAN FRANCISCO DE QUITO USFQ
DIEGO DE ROBLES S/N Y PAMPITE
QUITO 170157
ECU

8. PERFORMING ORGANIZATION REPORT NUMBER

9. SPONSORING/MONITORING AGENCY NAME(S) AND ADDRESS(ES)	10. SPONSOR/MONITOR'S ACRONYM(S)	11. SPONSOR/MONITOR'S REPORT NUMBER(S)
Air Force Office of Scientific Research 875 N. Randolph St. Room 3112 Arlington, VA 22203	AFRL/AFOSR IOS	AFRL-AFOSR-VA-TR-2024-0097

12. DISTRIBUTION/AVAILABILITY STATEMENT
A Distribution Unlimited: PB Public Release

13. SUPPLEMENTARY NOTES

14. ABSTRACT
The research conducted in this project primarily focused on the modeling and simulation of thermal barrier coatings (TBCs) in both 2D and 3D dimensions, employing the Finite Element Method (FEM). The study integrated diverse coating materials, encompassing their characteristic microstructures, incorporating defects such as interlamellar cracks, pores, and vertical cracks for strain compliance. This investigation comprehensively incorporated various strategies for material selection and process design from existing literature to enhance TBC performance.

15. SUBJECT TERMS

16. SECURITY CLASSIFICATION OF:			17. LIMITATION OF ABSTRACT	18. NUMBER OF PAGES
a. REPORT	b. ABSTRACT	c. THIS PAGE		
U	U	U	SAR	172

19a. NAME OF RESPONSIBLE PERSON	19b. PHONE NUMBER *(Include area code)*
JAMES LYKE	000-0000

Standard Form 298 (Rev.5/2020)
Prescribed by ANSI Std. Z39.18

FINAL REPORT

Principal Investigator: Prof. Alfredo Valarezo Ph.D.
Email: alfredo.valarezo@gmail.com
Phone: 593998674454
Project Title:

"3D THERMO-MECHANICAL MODELING OF MULTILAYERED TBCs FOR GAS TURBINE ENGINES"

Recipient Organization: Universidad San Francisco de Quito
Business Office Email: avalarezo@usfq.edu.ec
Report Due Date: 12-28-2023
Report Period Start Date; September 30th, 2020
Report Period End Date: until September 29th , 2023
Current Program Officer: LYKE, JAMES

GRANT NUMBER:

FA9550-20-1-0075

TEAM:

Prof. Lorena Bejarano
Prof. Marco León
Westly Castro
Emilio Bonilla
Samantha Criollo
Pedro Reina
Diego Morales
Krutskaya Yépez
Yupanki de la Cruz
Lois Cano

CÍRCULO DE CUMBAYÁ. P.O.BOX: 17-12-841 QUITO-ECUADOR
T.: (593 2)297-1700 AL 708. FAX.: (593 2)289 0070.
WWW.USFQ.EDU.EC

Table of Contents

Círculo de Cumbayá. P.O.Box: 17-12-841 Quito-Ecuador
T.: (593 2)297-1700 al 708. Fax.: (593 2)289 0070.
www.usfq.edu.ec

List of Figures

CÍRCULO DE CUMBAYÁ. P.O.BOX: 17-12-841 QUITO-ECUADOR
T.: (593 2)297-1700 AL 708. FAX.: (593 2)289 0070.
WWW.USFQ.EDU.EC

List of Tables

CÍRCULO DE CUMBAYÁ. P.O.BOX: 17-12-841 QUITO-ECUADOR
T.: (593 2)297-1700 AL 708. FAX.: (593 2)289 0070.
WWW.USFQ.EDU.EC

FA9550-19-S-0003 Grant from Air Force Office of Scientific Research Department of Defense
Report Document

Project title: "3D Thermo-Mechanical Modeling of Multilayered TBC´s for Gas Turbine Engines"

Principal Investigator: Alfredo Valarezo Ph.D. Institution: Universidad San Francisco de Quito Address: Diego de Robles y Vía Interoceánica Phone: 593 (2) 2971700 ext. 1048 Email: avalarezo@usfq.edu.ec	Co PI: Lorena Bejarano Ph.D. Business Contact: Alfredo Valarezo Ph.D. Address: Domingo Rengifo S/N y Av. Universitaria Phone: 593 (9) 98674454 Email: alfredo.valarezo@gmail.com

Report Abstract

The research conducted in this project primarily focused on the modeling and simulation of thermal barrier coatings (TBCs) in both 2D and 3D dimensions, employing the Finite Element Method (FEM). The study integrated diverse coating materials, encompassing their characteristic microstructures, incorporating defects such as interlamellar cracks, pores, and vertical cracks for strain compliance. This investigation comprehensively incorporated various strategies for material selection and process design from existing literature to enhance TBC performance.

Defects including mud-cracks, pores, interlamellar cracks, and material interfaces were systematically included in the models to achieve a theoretically grounded understanding of stresses, strain energies, and their interactions with the actual material microstructure, enabling the assessment of coating failure. The primary objective was to develop a robust modeling approach predicting interactions between layers of multiple materials, specifically Y2O3-7%ZrO2 (YSZ) and Gd2Zr2O7 (GDZ) in a TBC, overcoming computational limitations associated with microstructural details. The adopted approach involved a 2D analysis and the utilization of the OOF-2 tool for microstructure recognition. The 2D models, coupled with crack and porosity identification through image analysis, facilitated effective thermal conductivity simulations, in the first level of approach. Limitations arose from the identification of submicron defects, such as intersplat interfaces, leading to deviations in mechanical and thermal properties. However, the 2D approach provided important insights into the modeling approach for pre-selecting material configurations to be tested in 3D.

A Multiscale approach in 3D models was employed to replicate the traditional structure of gas turbine blades, progressing from millimeter to micron scales to assess the use of thin layers with varying density and/or compliance. Computational demands limited the use of the smallest features in mesoscale or global models. Instead, the strategy involved a combination of traditionally modeled geometrical features for interfaces, such as sinusoidal waves and mud-crack patterns, using honeycomb-like structures with virtual models and carefully reconstructed defects.

Results emphasized the high relevance of material interfaces in concentrating stresses due to thermal mismatch expansion and highlighted the impact of small cracks on stress concentration. The optimal structure emerged as a multilayered TBC with a YSZ layer in contact with the TGO, followed by a section of GDZ and a dense vertically cracked GDZ. This structure exhibited the lowest strain energies under thermal loading and reduced points of high stress concentration.

The findings also underscored the challenge of accurately predicting coating behavior due to the myriad of possible microstructural details. However, the integration of image analysis and FEM across multiple scenarios facilitated meaningful comparisons between different designs, aligning predictions with experimental results.

1. Accomplishments

This report aims to provide a comprehensive overview of the activities conducted during the project's development, outlining its objectives, achievements, challenges, and significant findings. Special emphasis will be placed on disseminating valuable insights to the scientific community within the Air Force and the broader public. The intent is to facilitate knowledge transfer, sharing both successful methodologies and encountered obstacles to contribute to collective learning.
The discussion will focus prominently on the outcomes of the modeling work, presenting key findings, advantages of modeling tools, relevant data, and visual representations supporting the results. Additionally, the report acknowledges the ongoing submission of two publications for peer-review evaluation as journal articles. Noteworthy is the dissemination of research through presentations at the Consortium of Thermal Spray Technology at Stony Brook University in July 2022, and at the International Materials Research Conference (IMRC) in Cancun in both August 2022 and August 2023;
The evaluation of the project's progress will include an assessment of the outlined schedule, considering deviations resulting from planned and unplanned milestones and actions. A meticulous breakdown of the budget allocation will be provided, showing minor deviations and justifications. Notably, the budget primarily supported personnel, including research assistants who, over the project's duration, enhanced their knowledge, earning graduate scholarships for master's or Ph.D. programs abroad.
In conclusion, this report will succinctly summarize key achievements and contributions, expressing gratitude to the Air Force Office of Scientific Research for advancing the realm of knowledge in this field.

The research team expresses deep gratitude to the Air Force Office of Scientific Research (AFOSR) for its vital financial support, playing a fundamental role in realizing this research's success. The funding has been instrumental in achieving key metallography milestones and advancing cutting-edge modeling techniques within our group. Our commitment is evident in the optimal allocation of funds, primarily directed towards engaging highly skilled personnel, reflecting our dedication to advancing knowledge in modeling and specifically, in TBCs. Collaborative initiatives with esteemed teams from the USA and Mexico, fostered through the support and networking opportunities provided by the AFOSR, have proven instrumental in elevating our research endeavors. Events like the International Materials Research Conference (IMRC), also supported by AFOSR have served as catalysts for forging enduring collaborations that extend beyond immediate projects. We recognize the enduring significance of TBCs, and the funder's support in the new era of advanced simulations provides insights into the real-world operation of future turbines and combustion engines, shaping the trajectory of technological advancements in these critical areas.

In this TBC modeling project, we strategically considered the selection of materials and the intentional introduction of defects during the composition of multilayered TBCs. Yttria-stabilized zirconia (YSZ), renowned for its low thermal conductivity and high fracture toughness, has been a prevalent choice. Additionally, newer zirconates, such as gadolinium zirconate (GDZ), gained prominence due to their high chemical resistance to the CMAS attack, preventing the fusion of silicates on TBC surfaces. Through plasma spray processing, versatile coatings with varying structures can be deposited—ranging from dense to porous and even mud-crack-like configurations. Employing SEM, micrographs were obtained from three different structures (dense, porous, dense vertically cracked) of two materials, deposited in combinations into five actual coatings. Subsequently, image analysis was conducted to mesh and capture the microstructure into a 2D FE model. The segmentation, meshing, and simulation were tailored based on thermal conductivity, and the results were compared with experimental data.

Once the 2D modeling proved effective in capturing microstructural effects on properties, thermomechanical modeling was implemented on prepared images. The detailed microstructure, including pores, interfaces, and open cracks, posed a challenge, making thermomechanical analysis intensive. However, the results, compared with burner-Rig tests, highlighted the superior performance of a multilayer coating—specifically, the lowest strain energy observed at the interface GDZ with YSZ and lower strain energy at the TGO-YSZ interface.

CÍRCULO DE CUMBAYÁ. P.O.BOX: 17-12-841 QUITO-ECUADOR
T.: (593 2)297-1700 AL 708. FAX.: (593 2)289 0070.
WWW.USFQ.EDU.EC

Transitioning to 3D modeling, the investigation spanned various scales—from a global perspective in millimeters, to mesoscale (selecting islands of the mud-crack structure), and ultimately, a microscale model analyzing a few microns of material from within a mud-crack pillar. Hand polishing and imaging at known depths were crucial for reconstructing the 3D microstructure, despite the challenges posed by the intricate details. Representative defects extracted from 3D models provided insights into their effects on preconceived ideal structures.
In all cases, a dedicated analysis delved into stresses in the in-plane and out-of-plane directions, strain energy, thermal conductivity, deformation and stress dynamics. These analyses aimed to provide comprehensive insights into potential delamination failures across a broad spectrum of fabricated coatings, contributing to a nuanced understanding of TBC behavior under various conditions.

2. Research Objectives and Aims:

The three main objectives outlined in the approved proposal were:

Aim 1. Assess coating performance of multilayered TBC´s using FEM on 2D SEM images of coating cross sections. OOF-2 (Object Oriented Finite Element Analysis of Microstructures, developed by NIST) software will be used to produce a meshed microstructure that will be loaded to ABAQUS FEA software, and subject it to heating in a cyclic manner. Solutions will be linked to the results of accelerated performance tests (i.e. burner rig test) to explain failure modes and distinguish microstructural key characteristics that can make a coating stand out among various proposed designs.

> Sub-Aim 1a: Define appropriate and quantifiable procedures for image processing and acquisition by developing polishing and imaging procedures (microscopy and OOF-2 analysis).
> Sub-Aim 2a: Use appropriate loading conditions by including as-sprayed residual stress conditions to the simulation model, and cyclic and graded thermal loading to observe mechanical stresses, strain energy, and their evolution.
> Sub-Aim 3a: Predict the effective thermal conductivity of the system and use this property as indicator of the suitability of the model (appropriate capture of microstructural features, and calculations).
> Sub-Aim 4a: Study the CMAS effect by the virtual generation of silicate molten particles on top of the 2D microstructures.

Aim 2. Address coating performance by modeling similar structures in a 3D approach. 2D SEM images will be processed in OOF3. Spatially ordered images obtained by controlled metallographic polishing will give birth to 3D meshed structures. At least three multimaterial/multilayer configurations will be tested. Sub-aims 1a to 4a will be applied to aim 2, but in 3D-configuration.

Aim 3. Propose artificially generated virtual microstructures in 2D. Simulated results will be presented and proposed to the Center for Thermal Spray Research (NY, USA), or the CENAPROT-Centro Nacional de Proyección Térmica or CIATEQ-CIDESI, National institutes (México) to produce actual samples, and conduct accelerated performance test that could suggest the applicability of the proposed designed coating.
A correct description of the kinetics of the materials for TGO (thermally grown oxide) growth, sintering, and presence and infiltration of CMAS will be carefully included in determining the stress states, and possible failure mechanisms by intrinsic and extrinsic degradation factors.

About Objective 1

To achieve Objective 1, our approach involved revisiting a comprehensive experimental study, led by Viswanathan et al.[1] from Stony Brook University's CTSR (Center for Thermal Spray Research), focusing on modeling five distinct multilayers (CTSR provided plenty of images for the study) These multilayers

CÍRCULO DE CUMBAYÁ. P.O.BOX: 17-12-841 QUITO-ECUADOR
T.: (593 2)297-1700 AL 708. FAX.: (593 2)289 0070.
WWW.USFQ.EDU.EC

underwent careful processing and characterization to identify potential failure modes in burner rig tests. Our methodology encompassed a quantifiable image processing procedure using OOF-2 analysis (details later). This approach effectively captured intricate details of porous, highly porous, and dense vertically cracked YSZ and GDZ coatings, along with their combinations within the same system.
Our project concentrated on developing a meticulous procedure for processing SEM images and selecting appropriate sections for finite element analysis. This involved capturing pores, cracks, interfaces, and vertical cracks representative of the microstructure. Researchers executed a detailed process, defining crack opening, continuity, and interconnections through simulation, graphic design tools, and iterations. Predictions of effective thermal conductivity were compared to actual measurements from laser flash experiments.
The modeling approach involved fixing temperatures on top and bottom sections, establishing a large block of material (top and bottom) with fixed temperature to achieve a uniform thermal gradient. Following a close prediction of thermal conductivity for the five combinations, the study progressed to modeling thermo-mechanical stresses.
In the subsequent phase of this objective, a heat cycle was introduced, linking thermal stress fields to failure modes based on the burner-rig test results for the five systems. High stresses were concentrated at layer interfaces, such as TGO-YSZ and YSZ-GDZ, correlating with observed failure and postulated high strain energy. Microstructural defects, particularly pores and cracks, significantly influenced stress fields.

In investigating failure modes, a correlation emerged between these occurrences and regions experiencing high S22 stresses and strain energy, particularly at interfaces. This correlation led to the opening of horizontal cracks and subsequent delamination, observed in both the YSZ-TGO and YSZ-GDZ interfaces. Notably, the former exhibited higher stress and strain energy. While failure was observed in either interface, a nuanced finding revealed two distinct thresholds—one leading to GDZ failure and another causing YSZ failure. Importantly, as YSZ demonstrates higher fracture toughness than GDZ, two thresholds are observed. When the GDZ threshold was reached, a shorter lifespan was noted, while achieving the YSZ threshold resulted in a more extended lifetime. Consequently, a microstructure predicting relatively lower S22 stress and strain energy on dense YSZ at the YSZ-TGO interface (and lower than the GDZ threshold) emerged as the best performer.

In summary, Objective 1 was achieved through a meticulous multilayer study, carefully characterizing and predicting experimental outcomes. Our 2D approach instills confidence that detailed model predictions and procedures can be extrapolated for a more advanced 3D prediction.
Simulation excluded consideration of as-sprayed residual stress conditions due to literature indications of stress relief during the initial heating cycle. Also, previous considerations of including CMAS were not included due to the lack and uncertainty of experimental results of the CMAS attack (properties, diffusion, depth of attack) which despite several attempts to obtain results, we were not able to compare them to actual experimental results (more in the future-work section).

About Objective 2

To fulfill Objective 2, our initial strategy involved producing images through controlled metallographic polishing at varying depths, enabling the reconstruction of microstructures in three dimensions for subsequent 3D studies using Image Analysis and the OOF-3 tool. While considering multimaterial configurations for reconstruction and subjecting them to a heat cycle, challenges emerged. The foremost difficulty pertained to acquiring high-detail microstructures and maintaining this precision in three dimensions. Moreover, the OOF-3 tool, no longer supported by NIST, (and other tools, like Dream-3D software) posed challenges in the cumbersome reconstruction of 3D microstructures. Considering these issues and recognizing the computational demands of detailed TBC microstructures, we transitioned to a multiscale approach.
This multiscale approach, transitioning from referential ideal microstructures to predict strain fields across large-sized, mesoscale, and micro-scale models, allowed us to incorporate micrometric defects obtained from metallography. Configurations chosen for this approach included the typical YSZ TBC, compared to a model transforming TBC into a dense vertically cracked YSZ and a dense vertically cracked multilayer YSZ GDZ—

Círculo de Cumbayá. P.O.Box: 17-12-841 Quito-Ecuador
T.: (593 2)297-1700 al 708. Fax.: (593 2)289 0070.
www.usfq.edu.ec

the latter chosen for its resemblance to the best-performing microstructure from the 2D study. This revised approach addressed research questions with demanding computational models while remaining manageable within our computational power constraints.

Detailed polishing procedures were employed to obtain images at progressively controlled depths. Following procedures from Objective 1, images underwent processing, focusing on specific defects for reconstruction in 3D. While there was potential to introduce profiles or reconstruct vertical cracks resembling mud cracks into the models, this was deemed computationally intensive and excluded. Instead, commencing with ideally controlled 3D models linked to our initial multilayer approach, we incorporated 3D microstructure reconstruction into the smallest sub-model created through the multiscale approach.

The most significant findings pertained to the interpretation of S22 stresses, S11 stresses, and strain energy on the TBC reconfigurations in three dimensions, encompassing mud-crack isles units and exploring the interaction of roughness profiles with stress fields surrounding microstructural nuances. The remarkable results include the discovery of high stresses at interfaces, stress concentrations surrounding micro-scale defects, and stress concentrations at the conclusion of vertical cracks. The possible interactions among these defects were explored, offering insights into regions with a higher probability of failure. Given the prediction of an ideal/real 3D microstructure, theoretical predictions of properties were considered less relevant compared to the theoretical understanding of geometrically controlled defects. Further details of these findings will be elaborated in the results section.

About Objective 3

For Objective 3, our initial proposition involved the artificial regeneration of virtual microstructures through collaboration with specialized research centers in thermal spray, both in Mexico and the USA. However, the outcomes over three years of research and modeling have led to a crucial realization. The concept of ideal microstructures, initially considered for actual production of coatings, may be too idealized. Consequently, the more appropriate approach is to model and derive insights from meticulously characterized sets of samples.
Unfortunately, the production and characterization of such samples extend beyond the scope and budget of the Ecuadorian group responsible for the modeling. While our research yielded noteworthy findings that could inform the proposal of ideally high-performing microstructures (for instance, spanning from the interface to the top layer, entails dense YSZ layers followed by functionally graded structures and top high-compliance DVC-GDZ structures and a multitude of variables, including thicknesses, compliance, periodicity and roughness height, etc.), limitations in production and testing prevented us from achieving this proposed aim. It's important to note that the work and models developed through Objectives 1 and 2 represent a substantial amount of effort invested during the period of this proposal.

Concluding remarks on Objectives and Aims.

In conclusion, the modeling approach proposed and developed in this project has been instrumental in enhancing our understanding of the thermomechanical stresses acting on TBCs at high temperatures, where direct measurement of coating performance is severely limited. The meticulous fine-tuning of our finite element method, coupled with a thorough depiction of TBC microstructures, brings significant value to the scientific community. This approach sheds light on the effects of microstructural defects, providing insights into the advantages and limitations of predicting coating properties and performance.
The transition from 2D to 3D modeling, coupled with comparisons to actual properties, enhances the robustness of our simulation predictions. Notably, the resurgence of interest in 3D understanding and modeling, complemented by actual measurements using advanced techniques like X-ray synchrotron diffraction, X-ray tomography, or digital image correlation, provides a compelling and complementary perspective to traditional 2D models. Still, there is more to learn and understand provided that the actual structures are 3D and not 2D.

Círculo de Cumbayá. P.O.Box: 17-12-841 Quito-Ecuador
T.: (593 2)297-1700 al 708. Fax.: (593 2)289 0070.
www.usfq.edu.ec

Looking toward the broader goals of the Air Force, TBCs remain a focal point for applications in combustion engines, turbines, combustors, spaceships, and beyond. Our contribution, particularly in multilayer and 3D modeling, advances the possibilities for understanding more efficient and higher-temperature structures. This not only addresses current applications but also provides valuable insights for designers projecting and foreseeing newer applications in the future.

3. Disemination and Publications:

This research project on TBCs, sponsored by the U.S. AFOSR, has yielded significant contributions to the scientific community. Two peer-reviewed manuscripts have been crafted, each addressing distinct aspects of TBCs and modeling of novel multilayered structures (please, see appendices 1 and 2). The first manuscript focuses on the 2D thermomechanical analysis of multi-layer, multi-material TBCs, destined for submission to the esteemed Journal of Surface and Coatings Technology (appendix 1). The second manuscript delves into the multi-scale modeling in 3D of dense vertically cracked YSZ and GDZ coatings (appendix 2), and it will be submitted to the Journal of the European Society of Ceramics—both journals boasting high impact factors, ensuring widespread dissemination of our findings.

In addition to publications, our team actively engaged with the scientific community through conference presentations. Four presentations were delivered during the project's timeline. The first, at the International Research Materials Conference (IMRC) in Cancun in early August 2022, introduced the work-in-progress on 2D simulations of multi-material, multi-layer TBCs. Another presentation occurred at the Consortium of Thermal Spray Research at Stony Brook University in late August 2022, centering on residual stresses in thermal spray coatings and TBCs. The consortium presentation involved representatives from ONRL, Tinker Air Force Base, and members of the American industry keenly interested in TBCs. Two more presentations took place at IMRC in August 2022, in 2D and 3D modeling results, at the Emerging Materials for Defense session sponsored by the SOARD from AFOSR. Both presentations that compile the most relevant results of this project are shared in appendices 3 and 4, respectively. Also, to enhance accessibility for educational purposes, videos showcasing the 3D models have been meticulously produced and made available on the web in video format for reference (link here) – and for reconstruction of selected defects from 2D images into 3D virtual objects (link to a video here).

Our commitment to dissemination extends beyond the finalization of this period. Future plans include an additional presentation at the IMECE Congress in New Orleans, USA, in November 2024, along with targeted presentations and meetings with researchers from ONRL, DEVCOM Army Research Laboratory, and AFOSR contacts. Leveraging our membership and network at the Consortium of Thermal Spray Research in Stony Brook University (where ONRL, DEVCOM Army Research Laboratory, and AFOSR are members), we aim to continuously share and discuss our research results in the next meeting in the summer 2024, fostering collaboration and advancements in thermal barrier coatings.

4. Changes in Schedule Adherence

Throughout the course of this project, our schedule evolved in response to the obtained results, prompting strategic decisions to optimize our work continually. The main challenge confronted was the substantial computational power demand for 3D models. To address this, we embraced multiscale modeling, introducing new milestones to navigate this complex terrain. However, persistent time constraints for modeling became apparent, impacting the project's progression in 2021 and 2022. The experimental work to obtain microstructural defects in 3D was conducted in simpler materials systems like cast iron, until reaching expertise to step into TBCs

CÍRCULO DE CUMBAYÁ. P.O.BOX: 17-12-841 QUITO-ECUADOR
T.: (593 2)297-1700 AL 708. FAX.: (593 2)289 0070.
WWW.USFQ.EDU.EC

The global pandemic further compounded serious challenges in 2020-2022, first preventing direct access to laboratories, but also diverting our time and University resources (not the grant moneys) to address urgent community needs, exemplified by contributing to the design of low-cost mechanical ventilators. Financial constraints also surfaced, hindering the acquisition of necessary equipment like a gold coater for sputtering, vital for SEM imaging. Delays ensued as the university hesitated to invest in the purchase amid pandemic uncertainties, with installation finally taking place in October 2022. Additionally, pandemic-related restrictions halted travel, impacting crucial interactions with research groups at Stony Brook University and CENAPROT in Mexico. Visa renewal difficulties exacerbated these challenges. Despite these setbacks, we remain confident in achieving the proposal's objectives.
The accompanying chart illustrates the project's progress, underscoring our resilience and determination to overcome obstacles and deliver impactful research outcomes.

Table 1. Gantt Chart for the project execution.

		Sept 2020-Feb 2021	Mar 2021-Aug 2021	Sept 2021-Feb 2022	Mar 2022-Aug 2022	Sept 2022-Feb 2023	Mar 2023-Aug 2023
	Activity	**Semester 1**	**Semester 2**	**Semester 3**	**Semester 4**	**Semester 5**	**Semester 6**
1	Kick off- Hiring of first project assistant						
2	Literature review for 2D simulations						
3	Work on polishing procedures in cast irons, and some carbide materials						
4	Acquisition of polishing tools						
5	Collaboration with Stony Brook University - Images provision						
6	2D image analysis-using phyton, Image J, photoshop, etc						
7	Literature review for 3D simulations						
8	Acquisition and installation of sputtering equipment for TBCs gold coating-SEM						
9	Work on polishing procedures in TBCs						
10	OOF-3 and Dream 3D exploration for 3D modeling						
11	3D image analysis-Autocad + Inventor						
12	IMRC 2022 presentation of 2D Modeling: Preliminary results						
13	Stony Brook University visit - Consortium for Thermal Spray Technology						
14	3D multiscale modeling						
15	Modeling of microscale defects into the multiscale modeling						
16	Equipment renewal for faster computing						
17	IMRC 2023 presentation of 2D and 3D Modeling						
18	Report and Manuscrit 2D modeling preparation						
19	Report and Manuscrit 3D modeling preparation						

Activities related to human capital
Acquisitions, supplies and Equipment
Activities of traveling for discussions and conferences

5. Changes in Budget and Budget Overview:

The budget allocation for this project is detailed in the following overview, and Table 5. The allocated funds, totaling $67,392, were thoughtfully distributed across various project components.

- Total Funding:
  - Received: $67,392
  - Actual Expense (2-year period + 1-year no-cost extension): $58,563
  - Surplus: $8,828
- The comprehensive Human Resources aspect involved faculty members, eight recently graduated engineers, and two undergraduate students.
  - Allocated Funds: $49,432
  - Actual Expense: $48,996
- Materials and Facilities:
  - Allocated Funds: $5,448
  - Actual Expense: $4,175

CÍRCULO DE CUMBAYÁ. P.O.BOX: 17-12-841 QUITO-ECUADOR
T.: (593 2)297-1700 AL 708. FAX.: (593 2)289 0070.
WWW.USFQ.EDU.EC

- Travel expenses remained untouched.
- The USFQ University incurred an Indirect Cost of $5,392, as planned.

Despite incurring travel costs during the development of the project, expenses for events such as the Cancun IMRC Congress and the Consortium of Thermal Spray Research were covered by the USFQ's budget for faculty travel. Consequently, the travel budget was retained, and we now seek approval to utilize the $8,828 surplus. Our proposal includes extending the hiring of a research assistant to conclude publication reviews and allocating the remaining half for travel costs. Specifically, we aim to present our results at the IMECE Congress of the American Society of Mechanical Engineers ASME in November 2024 and participate in the Consortium of Thermal Spray Research during the Summer Meeting in New York, USA. We express gratitude for your consideration and approval of this request.

Table 2. Allocated funds for the project.

	Category	Unit Price	QTY	2020	Unit Price	QTY	2021	Subtotal	Actual Expenses	Description
1	PI Faculty	$10.000,00	1	$10.000,00	$10.000,00	1	$10.000,00			Principal Investigator Salary. A total of 2.5 man-months is requested
2	Student graduated	$10.716,00	1	$10.716,00	$10.716,00	1	$10.716,00			Project Staff member, he/she is a student recent graduate. Support for a calendar year is requested
3	Undergraduate students	$2.000,00	2	$4.000,00	$2.000,00	2	$4.000,00			Undergraduate student support for a school year (10 months) is requested
				$26.736,00			$26.737,00	$49.432,00	$48.996,26	Within the budget
4	Materials and facilities									
	Solid Stated Drive-2T	$575,00	1	$575,00	$575,00	1	$575,00			SSDrive for data storage and fast computing
	UPS-Battery Pack 815 watts	$135,00	1	$135,00	$135,00	0	$ -			UPS to protect data connection with server
	Tripod Polisher"" 590TEM precision sample thinning for TEM	$1.380,00	1	$1.380,00	$1.380,00	0	$ -			Polishing tool to control depth of penetration
	Server Memory 32 GB SDRam	$139,00	0	$ -	$139,00	2	$278,00			SDRam to improve speed of computation
	Sample prep, and shipping				$400,00	1	$400,00			For Aim3, new samples are proposed
	Polishing supplies	$634,00	1	$634,00	$1.200,00	1	$1.200,00			Supplies for samples metallography preparation for microscopy. Second year, with Aim3, the need for supplies will increase
	Miscelaneous (power supplies, office supplies, monitors, mouses)	$ -	1	$ -	$271,00	1	$271,00			Miscelaneous expenses
				$2724,00			$2724,00	$5448,00	$4175,61	Within the budget
5	Travel			$3.560,00			$3.560,00	$7120,00		Travel costs are budgeted for faculty/student travel to USA to participate in discussions and conferences
6	Indirect Costs			$2.696,00			$2.696,00	$5392,00	$5.391,36	University's indirect cost rate of 8% for campus usage of computational and office facilities is requested - within the budget
	Total			$33.696,00			$33.696,00	$67392,00	$58.563,23	Within the budget
									$ 8.828,77	Surplus

6. Impacts and Future Directions:

In this research, we conducted an extensive analysis of multi-layered and multi-material Thermal Barrier Coatings (TBCs), addressing the intricacies of microstructure, including the well-known presence of pores, cracks, and micro-cracks. The project ventured into the challenging task of 3D modeling, exploring configurations like the mud-crack patterns of dense vertically cracked TBCs and interfaces between different zirconates, signifying a potential paradigm shift in TBC modeling. Noteworthy contributions include:

1. A successful use of the OOF-2 tool for defect capture in diverse TBC architectures, enabling detailed property predictions such as thermal conductivity from 2D image analysis. Despite acknowledged limitations, particularly regarding splat contact, the predictive power of property assessment is highlighted, especially when dealing with intricate microstructures.
2. For three-dimensional modeling, we adopted a multiscaling approach at millimeter, 100 micrometer, and 1 micrometer scales, accommodating finer meshings for more accurate results. The analysis exposed nuanced microstructural variations, emphasizing the need to move beyond idealized microstructures for a comprehensive understanding, incorporating factors like micro-defects, stress profiles, rumpling, sintering effects, among others.
3. To overcome 2D assumptions, our three-dimensional modeling considered geometrical defect' effects, reshaping stress distributions in volumetric spaces, leading to critical design implications. The study advises against stress concentration interactions in TGO-TBC and between different TBCs interfaces, highlighting potential failure points at crack tips and branching cracks.

CÍRCULO DE CUMBAYÁ. P.O.BOX: 17-12-841 QUITO-ECUADOR
T.: (593 2)297-1700 AL 708. FAX.: (593 2)289 0070.
WWW.USFQ.EDU.EC

4. Notably, the correlation between high strain energy and S22 stresses at interfaces suggests strategies like roughness control, crack-tip distancing, and optimal material placement. The proposed 3D-optimized model, featuring dense YSZ with high fracture toughness near the TGO interface, a increasing compliance through incremental porosity, and top layers DVC-GDZ coatings, presents a promising avenue for coatings with higher efficacy, particularly beneficial for high-temperature combustion engines.

The outcomes of this project extend beyond this specific application, carrying broader implications for the benefit of the U.S. Air Force and the scientific community for several other material systems and applications. The modeling tools employed here hold potential for similar complex microstructures, such as: Environmental barrier coatings (EBCs) (characterized by multiple compositions and cracking); Ceramic Matrix Composites (CMCs), EB-PVD coatings, laser additive manufacturing, and others. All of them stand to benefit from microstructural analysis and multiscaling modeling. The scope of applications expands to high-temperature environments, including transportation combustion engines, spaceships, space hybrid transportation planes, solid oxide fuel cells, and beyond, where the evaluation of actual performance is often limited. This declared broader perspective highlights the versatility and applicability of the developed modeling tools.

A compelling avenue for future research may involve:

- Exploring the inverse of the multiscaling approach, transitioning from microscale to macroscale. This project could derive material properties from the original microstructure, providing insights into TBC behaviors related to compliance, anelasticity, elastic behavior, and a comparative study of sintered versus as-sprayed conditions. Such an investigation could unlock valuable predictions about the macroscopic properties originating from intricate microstructures.
- Operational enhancements to the models could be achieved by incorporating the physics of TGO growth, sintering, creep, thermal gradients, and crack propagation, integrating fracture mechanics. The groundwork laid by the current results sets the stage for running more complex 3D models, offering a comprehensive understanding of TBC behavior under these multifaceted conditions. In due course, an examination of the CMAS effect could be undertaken, contingent upon the acquisition of a comprehensive set of samples, images, and corresponding measured properties.
- To enhance the applicability of image analysis models, a critical step is to test and validate them for various microstructures such as SPS (Solution Precursor Plasma Spray), EB-PVD, EBCs, and others. This validation process aims to refine and adjust image analysis procedures, ensuring adaptability across diverse microstructural scenarios. The careful prescription of procedures through this testing will contribute to the robustness and versatility of the image analysis models in different material systems and coating processes.

7. Acknowledgments:

The success of this research has been made possible through the invaluable support and funding provided by the Southern Office of Aerospace Research and Development (SOARD) at the Air Force Office of Scientific Research AFOSR. Our sincere appreciation extends to the dedicated officers at SOARD, Geoffrey Andersen, Stacy Manny, Daniel Montes, and the visit to our labs of Roger Greenwood, James Lyke and Chris Carson, whose assistance and collaboration facilitated the realization of these studies.

Special gratitude is extended to Professor Sanjay Sampath at the Center for Thermal Spray Research (CTSR) in Stony Brook University, whose collaboration played a key role in the project. Additionally, interactions, particularly at the International Materials Research Congress (IMRC), with Dr. Juan Muñoz from CENAPROT at CINVESTAV enriched our research endeavors.

CÍRCULO DE CUMBAYÁ. P.O.BOX: 17-12-841 QUITO-ECUADOR
T.: (593 2)297-1700 AL 708. FAX.: (593 2)289 0070.
WWW.USFQ.EDU.EC

We express our thanks to the collaborative efforts at USFQ (Universidad San Francisco de Quito), including the Research Support Office, especially to Natalia Araujo, Katherine Freire and Miguel Hernandez; and the Dean of Research, whose support was instrumental in acquiring the sputtering equipment.

The Principal Investigators (PIs) extend their gratitude to the students, research assistants, and colleague Faculty, who actively contributed with their intelligence and time, fostering progress in this research. Their dedication has been crucial to the project's advancement.
Moreover, our appreciation extends to the funding sources that have allowed nurturing our students and research assistants, enabling their engagement in meaningful research activities. We are pleased to note that several team collaborators have progressed to graduate studies in prestigious universities worldwide, in the United States and Europe, securing 2 Fulbright scholarships and other notable achievements. This reflects the positive impact of the research funding in fostering the next generation of scientists and advancing knowledge across various fields.

CÍRCULO DE CUMBAYÁ. P.O.BOX: 17-12-841 QUITO-ECUADOR
T.: (593 2)297-1700 AL 708. FAX.: (593 2)289 0070.
WWW.USFQ.EDU.EC

8. Project Execution:

In this section, we will present the intricacies of the methodologies and approaches implemented in the modeling of TBCs of this project, for more in detail explanation of the activities of the research. This includes details on three principal segments of the study, namely, modeling and simulation conducted in two-dimensional (2D) and three-dimensional (3D) spaces, along with the intricate reconstruction of micro-scale defects into three dimensions. Our exposition will include key milestones achieved throughout the course of the study, emphasizing the challenges encountered and the strategic methodologies employed to both implement and surmount these obstacles

The stage of the study dedicated to *2D simulations* delved into the meticulous image analysis of two-dimensional Scanning Electron Microscopy (SEM) images. While these images adhered to fixed SEM parameters within standard polishing methods, the inherent subjectivity in the analysis process persisted. Analysts faced the challenge of distinguishing between features resulting from the polishing process and actual defects within TBCs. Given the diverse array of features in TBCs, such as inter-splat interfaces, small pores, and micro-cracks, evaluators exercised judgment in determining the extent to which the microstructure could be adequately captured for processing into finite element methods. Multiple iterations were undertaken to derive a judicious representation of defects, drawing on the amalgamation of metallographic analysis experience and the prediction of thermal conductivity properties. Also, image processing proved insufficient in capturing crack limits or borders in vertical cracks, requiring an iterative process of stress analysis. This iterative process informed subsequent refinements in image analysis through graphic design, allowing corrections to the initial analysis.
Other challenges included the incorporation of uniform boundary conditions at tortuous roughness profiles, necessitating the assignment of virtual material blocks at the top and bottom of 2D microstructures to homogenize through-thickness temperatures. Additionally, the analysis of through-thickness properties in a 2D space mandated an examination of property and temperature gradient drop along vertical trajectories representative of one-dimensional heat conduction. Further details of the final procedures, slated for publication in a peer-reviewed paper, are expounded upon in the forthcoming section titled "2D Modeling and Simulations."

The phase of the study dedicated to *3D simulations* encountered notable challenges, particularly concerning the substantial demand for high computing power. Adopting a multi-scale strategy necessitated global-scale models that accurately represented the actual turbine coating system, ranging in the millimeter scale. These intricate models, due to their extensive elements and nodes, subjected simulations to durations of up to three to four weeks, with some iterations required to address non-convergence issues.
The idealization of diverse scenarios within the 3D models, including considerations such as the size of mud-crack structure islands, length of vertical cracks, and the extent of porosity, introduced challenges in optimizing the number and type of FEM elements. Achieving model convergence was paramount, and once attained, the representation of 3D models into 2D reports required additional effort. To enhance accessibility, videos showcasing the 3D models have been meticulously produced and made available on the web in video format for reference (link here).
The optimization of models across global, meso, and micro scales, striking a balance between computing time and accuracy, coupled with discerning the multitude of variables influencing stresses and strain energies, constituted the most challenging aspects of this study's 3D simulation section. For a more in-depth exploration of the final procedures, comprehensive details are provided in the forthcoming "3D Modeling and Simulations" section.

The phase dedicated to *modeling microstructural defects* presented experimental challenges, particularly in the meticulous production of images of the coating at depths ranging between 5 microns to 10 microns. This endeavor posed challenges in the formulation of polishing procedures, requiring careful consideration of each polishing variable (rotating speed, pressure, polishing media, etc.) Ensuring the reproducibility of polishing procedures across different operators, observing the impacts of sample tilting, sample choice, etc.,

Círculo de Cumbayá. P.O.Box: 17-12-841 Quito-Ecuador
T.: (593 2)297-1700 al 708. Fax.: (593 2)289 0070.
www.usfq.edu.ec

contributed to optimizing the polishing procedure and subsequent reconstruction of selected defects from 2D images into 3D virtual objects (link to a video here).
Significant effort was invested in obtaining defects within referential sample systems, such as gray cast iron or nodular cast iron, initially focusing on defects in the range of hundreds of microns. This groundwork paved the way for the subsequent approach to defects in the TBC, specifically within the 1 to 10 micrometer range. The team successfully reproduced various defects and achieved the potential to reproduce areas and volumes of coatings within the range of tenths of microns, marking a notable success. While the insertion of such models into larger simulations is constrained by computational power demands, individual defects can be effectively integrated into micro models within the micro-multiscale strategy. Comprehensive details of this modeling process, encompassing polishing, imaging, image analysis, and Computer-Aided Design (CAD), will be expounded upon in the forthcoming section titled "Modeling of Microstructural Defects by Polishing, Imaging, Image Analysis, and CAD."

2D Modeling and Simulations

The 2D simulation process began by modeling multilayer and multi-material TBCs introduced by Viswanathan et al. [1] with an ample characterization of mechanical properties, microstructure, and thermal properties. Here, we study the microstructure images of four micrographs per each of those five configurations of multilayered coatings from Viswanathan et al. The common configuration of TBCs consisting of a topcoat, a bond-coat, and a thin oxide layer (TGO) developed from the oxidation process of the bond coat is followed as baseline.
Five types of GDZ and YSZ combinations [1] are modeled and simulated here. Coatings of reference were deposited on a Rene 80 substrate with a thin bond-coat layer of NiCoCrAlYHfSi composition. The five multilayers are constituted from top to bottom, as follows (Figure 1):

a. Top layer: dense GDZ (low porosity). Mid-layer: porous GDZ. Bottom layer: DVC-YSZ.
b. Top layer: DVC GDZ. Mid layer: porous GDZ. Bottom layer: dense YSZ.
c. Top layer: DVC GDZ. Mid layer: porous YSZ. Bottom layer: dense YSZ.
d. Top and Mid layer: DVC GDZ. Bottom layer: dense YSZ.
e. Top layer: DVC GDZ. Mid and bottom layer: DVC YSZ.

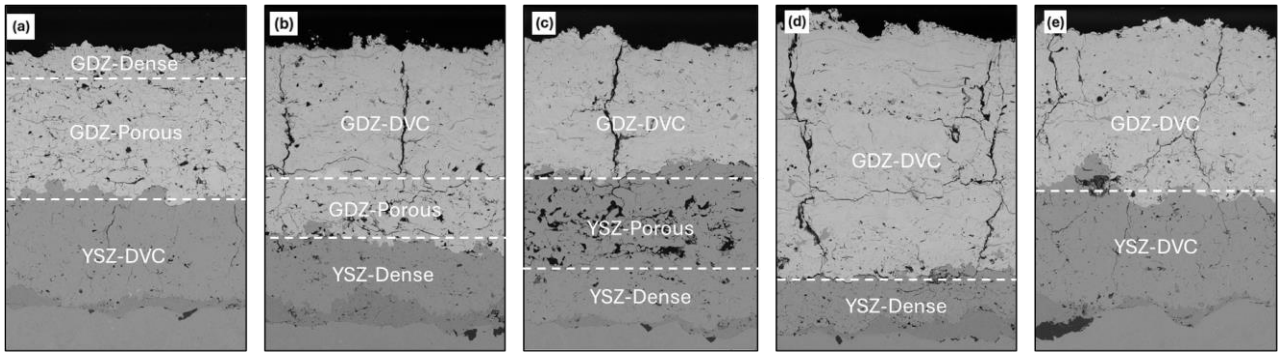

Figure 1. Microstructures of five multilayered/multi-material TBCs adopted from Viswanathan et. al [1]

Microstructure Image Processing
Four distinct SEM images with a magnification of 300x of each of the above-mentioned configurations were processed in a TIFF format. The images had a resolution of 1280x950 pixels. A python code was used to delimit each of the layers of the micrograph by applying contrast, stretching, equalization and denoising operations on the image. The code was also employed to transform the images from grayscale to binary with a threshold criterion based on the gray level difference of the YSZ, GDZ, bond coat, and substrate materials; and to separate the pores and cracks (vertical and horizontal) into another image, by applying a mask with a

CÍRCULO DE CUMBAYÁ. P.O.BOX: 17-12-841 QUITO-ECUADOR
T.: (593 2)297-1700 AL 708. FAX.: (593 2)289 0070.
WWW.USFQ.EDU.EC

threshold based on the gray level of each layer, to ease image processing. It is important to acknowledge that the threshold criterion is selected between a color range of grayscale of 35-45 for defects, 50-130 for the bond coat, and 140-200 for GDZ, depending on the clarity and quality of the image. Thus, it can be subjective to the analyst judgement to improve the discretization. The resin and the substrate materials are identified by discarding from the other regions.

Vertical cracks, horizontal cracks and globular pores were segmented on each image and layers, using ImageJ (v1.54f) Shape Filter Plugin. For this process, the angle of the defects and circularity was considered as a discretizing criterion. Angle ranges from 0° to 45° and from 135° to 180° were used for horizontal crack segmentation, whereas angle ranges from 45° to 135° were used for vertical crack segmentation. For globular pores segmentation, the circularity of the defects was considered, using a criterion from 0 to 1 which assures that only defects that resemble a circular geometry enter this category. After segmentation, images are processed on Sketchbook, a raster graphic software in which the layers margins are traced manually. Finally, the images with differentiated coating layers and defects are merged as graphical layers. Figure 2 shows an example of the analysis of multilayered coating C, where the segmentation of different layered materials can be observed together with the identification of defects (cracks, pores, etc.). In Figure 2, (*a*) shows the original SEM microstructure image; (*b*) is the same image after stretching, equalization, denoising, and tracing; (*c*) through (*f*), show the microstructure with the three types of defects in separated images, thus: (*c*) all defects, (*d*) globular pores only, (*e*) vertical cracks only, and (*f*) horizontal cracks only.

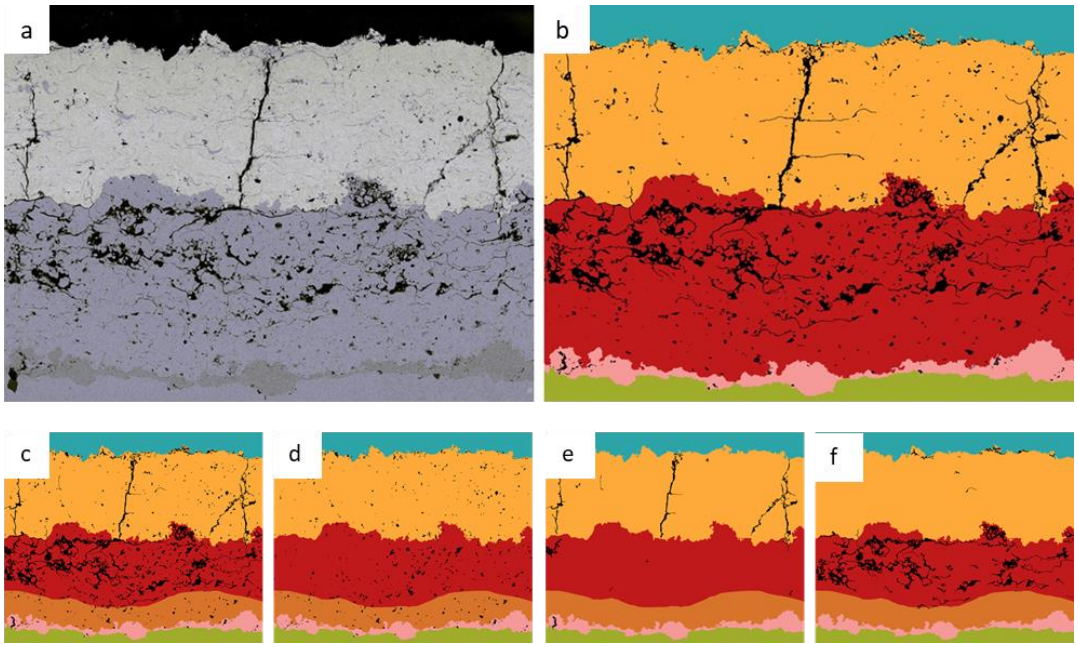

Figure 2. Image processing of coating type-C, TBC configuration. (a) Original gray scaled image followed by the processed image (b) after stretching, equalization, denoising, and tracing, (c) compounded image with each of its layers, (d) segmented image of globular pores, (e) segmented image of vertical cracks, (f) segmented image of horizontal cracks.

Finite element model and simulation for effective thermal conductivity

After the image-processing has been conducted, a finite element (FE) object-oriented package, OOF2 (version 2.1.19), was employed to create meshes for each layer and the corresponding defects. OOF2 is a C++ and Phyton package that recognizes in the image different areas that can be assigned with their respective material properties. Figure 3 shows the flowchart for the analysis of the microstructures and later, prediction of properties using FEA.

CÍRCULO DE CUMBAYÁ. P.O.BOX: 17-12-841 QUITO-ECUADOR
T.: (593 2)297-1700 AL 708. FAX.: (593 2)289 0070.
WWW.USFQ.EDU.EC

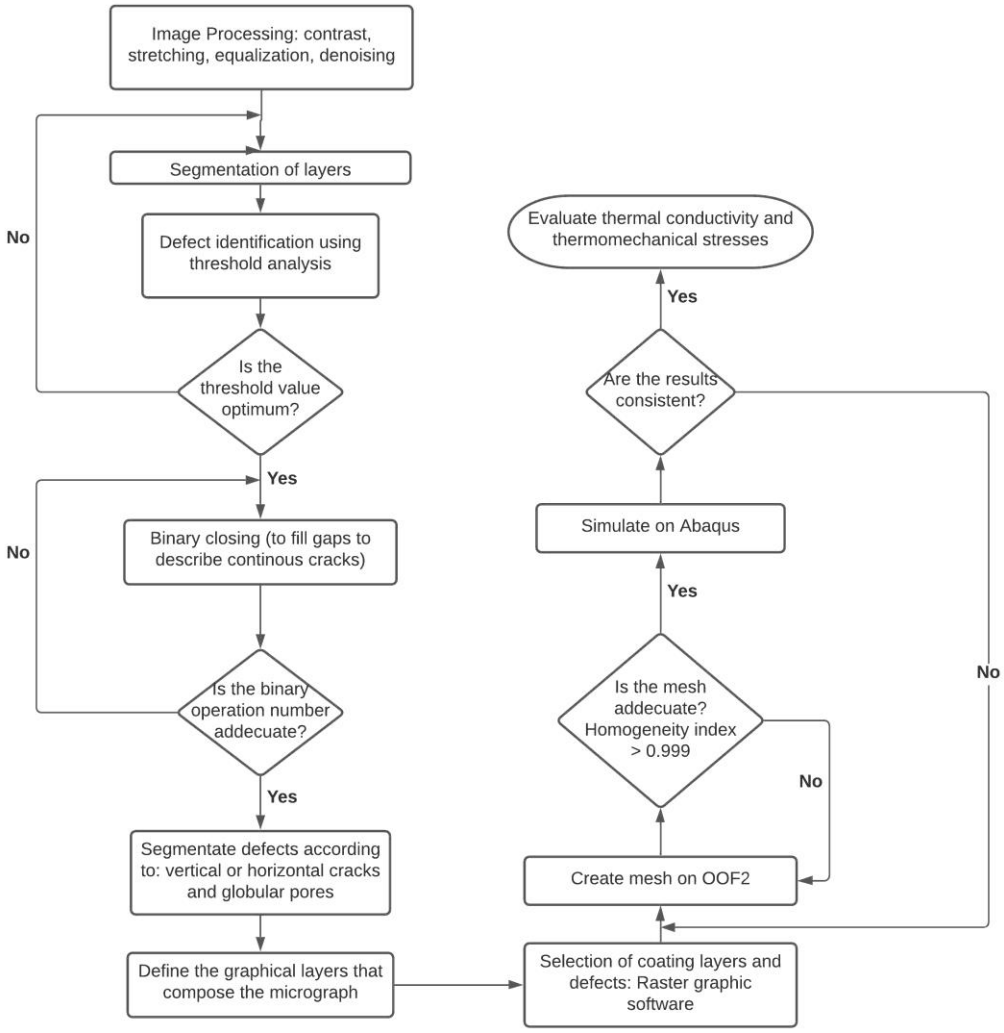

Figure 3. Flow chart for image analysis towards producing well-identified and meshed phases to simulate thermal conductivity and residual stresses of TBCs by means of finite element analysis FEA.

Abaqus (version 2022) was used for the FEA to predict the effective thermal conductivity of single and multilayered TBCs. For a single TBC layer, the mesh is created with three segments, one defined as a top block, followed by the TBC, and then a bottom block, all of them defined with the same material properties. In a multilayered case, the segments are similar, one as a top block, then the two layers (YSZ-GDZ), and the bottom block. In this case, the top and bottom segments adopt the material properties of the TBC that is sharing nodes with. This condition helps to distribute the heat transfer in a better way, avoiding issues with the profile (peaks and valleys) inherent of the micrograph's top and bottom boundary limits. The boundary nodes in the top and bottom are identified in the meshed micrograph as limits, assigning them the initial loads of 400°C and 25°C respectively. Also, a predefined field of 25°C is assigned to the entire model. Material properties for bulk materials are assigned according to Table 1.

The effective thermal conductivity, (k_{eff}) is calculated using the Fourier equation, as follows:

CÍRCULO DE CUMBAYÁ. P.O.BOX: 17-12-841 QUITO-ECUADOR
T.: (593 2)297-1700 AL 708. FAX.: (593 2)289 0070.
WWW.USFQ.EDU.EC

$$Q = k_{eff} * \left(\frac{\Delta T}{H}\right) \left[\frac{w}{m^2}\right] \quad \text{equation 1}$$

Where (Q) represents heat flux in the y-direction (through-the-thickness of the coatings), (k_{eff}) the effective thermal conductivity, (ΔT) the temperature gradient, and (H) thickness of the section in study. To calculate (k_{eff}), the image is divided into one hundred and fifty vertical paths, and the average heat flux in each path is considered in Fourier´s equation accounting for the precise temperature difference and distance between the top and bottom nodes. The top and bottom boundaries are considered isothermal, and the right and left boundaries are adiabatic. The high number of paths allow us to obtain a representative value of thermal conductivity. Heat flux is low on pores and cracks due to air low conductivity [2] and thus, cracks and pores have a high influence on thermal resistance by reducing the flux.

Finite element simulation for thermo-mechanical residual stresses

For the thermomechanical residual stress analysis, representative sections of each microstructure model were carefully selected. The model and methodology considered for the analysis is illustrated in Figure 4. To account for the oxidation effect of the bond-coat, a layer of thermally grown oxide (TGO) was incorporated between the YSZ layer and the bond-coat. This TGO layer of 4 µm in thickness was introduced during the segmentation of the images. In the model, temperature-dependent material properties were considered, according to Table 2. By incorporating temperature-dependent properties, the model can effectively capture the viscoelastic behavior of the bond coat which plays a significant role in absorbing and dissipating stresses during the thermal cycle.

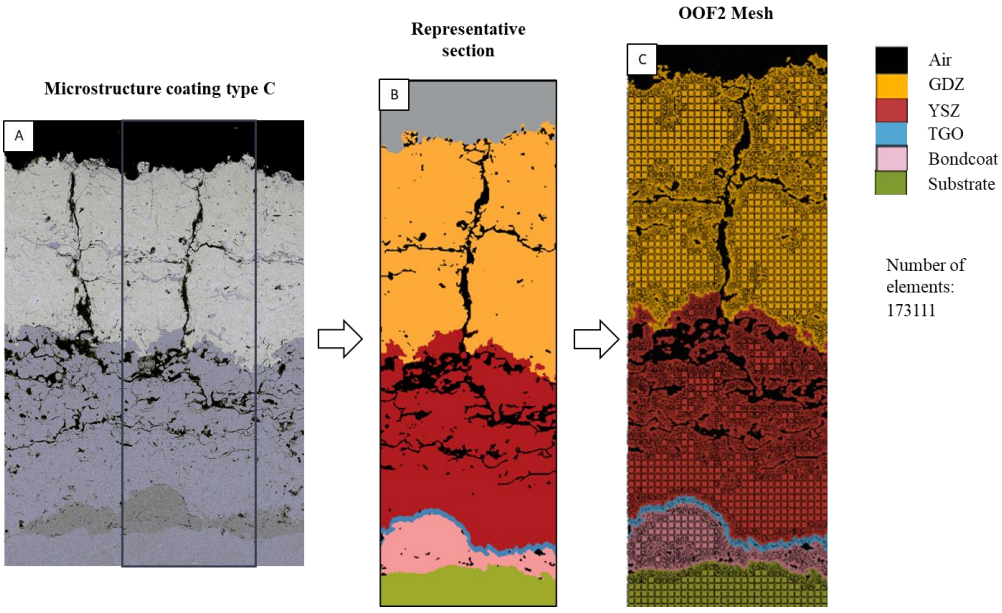

Figure 4. Image processing for thermal conductivity and thermomechanical analysis. (a) Original SEM Image in backscattering of the multilayered coating C, (b) Segmented image including substrate (in green), bond coat (in pink), TGO (in blue), and three layers of TBC –dense YSZ in the bottom (in red), porous YSZ in the middle (also in red), GDC-DVC in yellow. (c) Meshed image with identification of each layer, and finer mesh in the interfaces. The number of elements is 173,111 for this image. Air is identified in the top of the microstructure and in the pores and cracks as opened spaces. Homogeneity index: 0.999

The heat cycle analysis was carried out in three stages. The first one involved heating the model from an initial temperature of 25°C to 1000°C within 300 seconds. Subsequently, the temperature was maintained at 1000°C for 7200 seconds in the holding stage. Finally, the cooling phase was implemented, decreasing the model's temperature from 1000°C to 25°C, over 300 seconds. For the holding stage, a creep model was

CÍRCULO DE CUMBAYÁ. P.O.BOX: 17-12-841 QUITO-ECUADOR
T.: (593 2)297-1700 AL 708. FAX.: (593 2)289 0070.
WWW.USFQ.EDU.EC

integrated to account for the viscoelastic behavior, time dependent plastic strain of the bond coat at temperature. The creep follows the Norton model:

$$\dot{\varepsilon}_{eq}^{cr} = B * \left(\sigma_{eq}\right)^{n} \quad \text{equation 2}$$

Where $(\dot{\varepsilon}_{eq}^{cr})$ is the von Mises equivalent creep strain, $\left(\sigma_{eq}\right)$ is the von Mises equivalent stress, (B) and (n) are temperature-dependent properties of the materials that are listed in Table 1. The values of the property (B) at the temperatures in-between those given in Table 1 are interpolated logarithmically according to Aktaa et al. [3]

Table 3. Temperature dependent parameters of Norton creep considered for bond coat

T [°C]	$B\left[\frac{1}{s\ MPa^{n}}\right]$	n
≤600	6.54 x 10^{-19}	4.57
700	2.20 x 10^{-12}	2.99
800	1.84 x 10^{-7}	1.55
≥850	2.15 x 10^{-8}	2.45

The 2D models in this section are considered as in plane-strain. Regarding boundary conditions, the left side is designated as symmetrical, with movement restricted in the *x*-direction, and similarly, the bottom is symmetrical with movement restricted in the *y*-direction. In line with parameters from prior studies, a periodic boundary condition is established between the left and right edges to ensure seamless connectivity between corresponding nodes. This condition is mathematically expressed as:

$$u_r - u_l = u_b - u_a \quad \text{equation 3}$$

Here, *a* and *b* represent the corner bottom nodes, while *r* and *l* denote each subsequent on the right and left sides after *a* and *b*, respectively. The variable *u* signifies degrees of freedom, which, in this case, are two (x and y). To maintain an equal number of nodes on both sides, a mirror condition in the y-z plane was instituted in the assembly part and subsequently merged in the instance.
The simulation heat cycle is organized into four consecutive time steps: initial, heating, holding, and cooling. In the initial step, the stress is set to zero, and the temperature field to 298 K. As the simulation progresses to the heating step, the temperature linearly increases from 298 K to 1273 K over a five-minute interval. Subsequently, the holding step ensues, maintaining the temperature at 1273 K for 120 minutes. Finally, during the cooling step, the temperature decreases linearly from 1273 K to 298 K in five minutes. It is essential to note that the temperature is uniformly distributed throughout the entire geometry in each time increment of each step, ensuring an isothermal condition. The heating cycle is visually depicted in Figure 5, with the conclusion of the heating phase labeled as H1, the end of the holding phase as H2, and the conclusion of the cooling phase as C. This codification will be utilized to present the thermomechanical results.

CÍRCULO DE CUMBAYÁ. P.O.BOX: 17-12-841 QUITO-ECUADOR
T.: (593 2)297-1700 AL 708. FAX.: (593 2)289 0070.
WWW.USFQ.EDU.EC

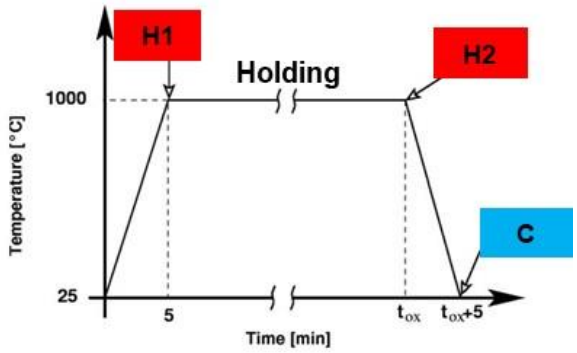

Figure 5. Visualization of the heat cycle. In the initial step, the stress is set to zero, and the temperature field to 298 K. In the heating step, the temperature linearly increases from 298 K up to 1273 K (H1-end of heating step) over a five-minute interval. Subsequently, the holding step ensues, maintaining the temperature at 1273 K for 120 minutes (H2-end of holding step). Finally, the temperature decreases linearly from 1273 K to 298 K in five minutes (C-end of cooling).

3D Modeling and Simulations

The 3D simulation process began by creating a large-scale model, referred to as the global model, which included three different TBCs: a dense YSZ coating and two honeycomb-like structures simulating DVC structures. The global models are in millimeter scale. Following this, the global model undergoes segmentation to create sub-models. The first sub-models, called mesoscale models, extract seven honeycomb units with refined mesh for improved accuracy. The last sub-models, microscale simulations, involve smaller pillars extracted from the honeycomb structures, scaled down to the micron level with finer mesh refinements to incorporate microstructural defects. Finite Element (FE) simulations using Abaqus 2020 analyze the response of assembled components (multiple layers) under specific conditions. The simulation process involves three primary stages: geometry definition (global, meso, and micro-scale models; and materials), components assembly, and modeling of defects, along with interaction specifications such as boundary conditions, meshing operations, and thermal loads.

Geometry description and materials

Figure 6 illustrates the geometry setup and material distribution for the simulated TBCs. In global models, three TBC-system arrangements are characterized, consisting of four layers—bulk substrate Ni-superalloy material, bond coat, Thermally Grown Oxide (TGO), and the TBC. The contact surface between layers is modeled with a sinusoidal profile. The models include 4 or 5 materials distributed in layers: Inconel 617 (10 mm) as substrate, a 100 µm bond coat, a 10 µm TGO layer, and a TBC layer in three configurations: YSZ dense (500 µm), YSZ dense (50 µm) followed by 450 µm of YSZ DVC, and YSZ dense (50 µm) followed by 50 µm of GDZ dense and 450 µm of GDZ DVC layers.

All materials are considered isotropic and linear elastic (except the bond coat). Gadolinium zirconate (GDZ) and Yttria-Stabilized Zirconia (YSZ) serve as oxide-based ceramics, acting as thermal barriers. GDZ is considered a chemical barrier, as well. The bond coat is elastic-plastic, facilitating adhesion and protecting against oxidation and corrosion. The yield strength of the bond coat varies with temperature, adopting properties from M-CrAlY. The TGO is an Al_2O_3 oxide layer acting as a chemical barrier, and in this study, it remains stable with no growth during thermal cycling. Thermomechanical properties of the materials are detailed in Table 2.

CÍRCULO DE CUMBAYÁ. P.O.BOX: 17-12-841 QUITO-ECUADOR
T.: (593 2)297-1700 AL 708. FAX.: (593 2)289 0070.
WWW.USFQ.EDU.EC

Table 4. Material properties used for the simulations.

Material	T, [°C]	ρ, [kg/m^3]	CTE 10^{-6}, [mm/mm]	E, [GPa]	*v*
GDZ	25	6320	8.65+0.00285T (80-1100°C)	91.6	0.323
	400				
	800				
	1000				
YSZ	25	5960	10.53+0.001T (100-1100°C)	50	0.2
	400	-			
	800	-			
	1000	-			
Bond Coat	25	7380	9.848 + 0.013T-0.000007T^2 (50-600°C)	250	0.3
	200			220	
	400			200	
	600	-		180	
	700	-		165	
	800	-		155	
	1000	7030		120	
TGO	25	3984	6.7596+0,0022T (300-900°C)	380	0.23
	300	-		-	-
	600	-		350	0.23
	800	-		340	0.25
	900	-		-	-
	1000	3868		315	0.25
Inconel 617	20	8360	-		
	25		11.6	211	0.3
	400		13.6	188	
	800		15.4	149	
	1000		16.3		

Global model

The TBC area under study in global models is a consistent square section with dimensions of 0.9 x 0.9 mm and heights of 10.61 mm for YSZ models and 10.66 mm for YSZ+GDZ models, employing a coarse mesh for computational efficiency while ensuring a large number of elements. Three TBC configurations—Dense YSZ, YSZ+DVC, and YSZ-GDZ +DVC models—were investigated. The DVC, represented by a hexagonal honeycomb pattern, had parameters like hexagon side length (*s*), pillar separations (*w*), and vertical crack length (*l*). For the YSZ-GDZ +DVC model, hexagon size (*s*) varied between 50, 100, and 150 µm with a constant 8 µm pillar separation, and the study of pillar separation (*w*) involved variations between 4, 8, and 12 µm with a fixed hexagon side length of 50 µm (Figure 6a-j). In this report, the study of hexagon size and crack width are not present for briefness.

Círculo de Cumbayá. P.O.Box: 17-12-841 Quito-Ecuador
T.: (593 2)297-1700 al 708. Fax.: (593 2)289 0070.
www.usfq.edu.ec

Mesoscale models

The mesoscale models are extracted from the DVC global models of YSZ and YSZ-GDZ, by keeping seven honeycombs with hexagon sides of (*s*) 100 µm and separation (*w*) of 8 µm (Figure 6e and 6f). The seven honeycombs are extracted from the center of the global model to avoid edge effects. These sub models get the parameters of strain and stress of the deleted parts of the global models by imposition of boundary conditions. The mesh is refined by reducing the size of elements allowing them to capture the complex geometry of the material layers. The reduction of computational efforts allows these models to explore the effect of a variable DVC depth (length of vertical crack -*l*) to be 0.45, 0.47, and 0.49 mm.

Microscale models

At the microscale, the TBC geometry undergoes further reduction until it achieves a surface square section of 60x60 µm (Figure 6 g,h,i), forming new sub-models for all configurations. As the interface between materials is shaped by a sinusoidal surface, the microscale model comprises of four valleys (four corners) and one peak after the reduction process. A significant advantage of these sub-models is their capability to incorporate microstructural defects, such as pores and cracks, with a moderate increase in computational demands. Numerous models were analyzed with varying levels of porosity: 0%, 10%, 20%, and 30% in the cross-sectional area, of the YSZ dense material and both DVC models near the TGO interface, Figures 6h and 6i, respectively.

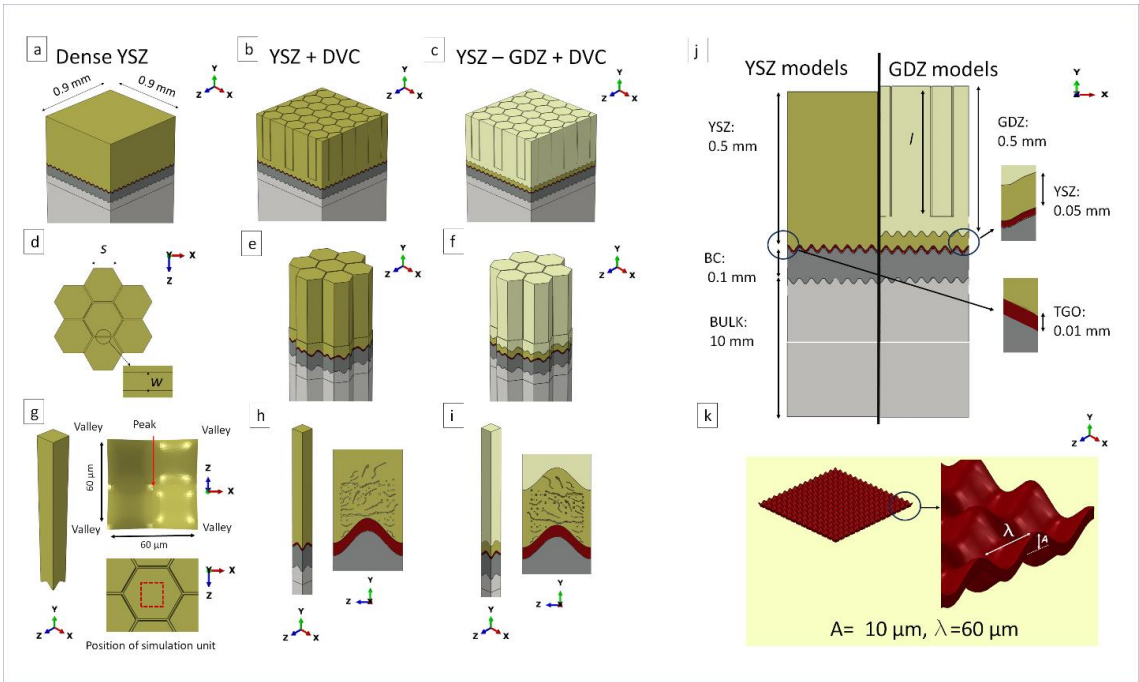

Figure 6. Comprehensive 3D Models employed in the study. a) Representation of the Dense Yttria-Stabilized Zirconia (YSZ) Model. b) Composite Model Integrating YSZ and Dense Vertically cracked (DVC) characteristics. c) Multilayered TBC including YSZ with GDZ in a DVC structure. d) Schematic detailing the honeycomb-like structure, with emphasis on the side parameter and interspace between honeycombs-top view. e) 3D model depicting the sub-model honeycomb structure for YSZ+DVC. f) 3D model exhibiting the sub-model honeycomb structure utilizing YSZ - GDZ +DVC. g) extracted DVC pillar from the central region of the honeycomb unit, presented in 3D, bottom view -one peak of the roughness at the center and four valleys at the corners. h) Three-dimensional pillar representation of YSZ +DVC, encompassing defects (pores, and cracks). i) Three-dimensional pillar representation of YSZ-GDZ +DVC displaying the multilayered encompassing defects (pores, and cracks). j) Cross-sectional view of the model presenting major dimensions of TBC model using YSZ and multilayer YSZ-GDZ. It includes the thickness of substrate, bond coat, TGO, and ceramic

CÍRCULO DE CUMBAYÁ. P.O.BOX: 17-12-841 QUITO-ECUADOR
T.: (593 2)297-1700 AL 708. FAX.: (593 2)289 0070.
WWW.USFQ.EDU.EC

TBC. k) Sinusoidal profile used at the interfaces. For exemplification, the TGO is presented to describe the wavelength (λ) and the amplitude (A)

Assembling process: boundary conditions, and meshing operations

The simulation employs tie constraints to define interaction between different layers, with the stiffer material designated as the master surface. In global models, the Inconel 617 bottom surface is set as ENCASTRE, ensuring zero displacement and rotations. Sub-models extend this condition to the entire geometry bottom surface, incorporating imposed strain on cut surfaces due to removed sections. Meshing operations are crucial for convergence and reliable results. Global models use a coarse mesh to conserve resources, employing quadratic tetrahedral (C3D10) and second-order quadratic brick (C3D20R) elements for YSZ sections, adjusting sizes based on proximity to interfaces. In mesoscale models, mesh refinement is applied, utilizing C3D10 and C3D20R elements for YSZ, GDZ, and DVC structures. Microscale models employ fine C3D10 elements for meshing. Boundary conditions and mesh configurations vary to ensure accurate representation of material layers and stress-strain behavior under thermal loads.

Thermal loading

Thermal loading in global models and sub-models is applied using predefined fields. The simulations are structured into four consecutive time steps: initial, heating, holding, and cooling. In the initial step, the temperature field is set at 298 K and remains constant throughout the entire geometry. During the heating step, the temperature starts at 298 K and increases linearly to 1273 K over a five-minute interval. Subsequently, the holding step begins, maintaining the temperature at 1273 K for 120 minutes. Finally, in the cooling step, the temperature decreases linearly from 1273 K to 298 K in five minutes. It is noteworthy that the temperature in each time increment of each step is uniform throughout the entire geometry as isothermal.

Modeling of microstructural defects by polishing, imaging, image analysis, and CAD

Before producing micrometer-scale TBC microstructures reconstructed in 3D, two reference materials were used to reconstruct, nodular and gray cast iron in the order of tenths to hundredths of micrometers. The advantage of this approach is that nodular cast iron has a spherical shape graphite that readily allows verification of alignment and depth between images, within the 3D model. Later, the reconstruction of gray cast iron flakes allowed the resemblance of amorphous shapes.

Details on the experimental procedure to obtain SEM microstructures of the cast iron samples is not described in this section for conciseness. The procedure for the YSZ-TBC only is presented, later. Some results from the reconstructed microstructure of the nodular cast iron in 3D is shown in Figure 7. Some results from the reconstructed microstructure of the nodular cast iron in 3D are shown in Figure 7. Figure 7a shows the initial reference image of the surface -image #1. Figure 7b shows the indentation made at image #45 and the 7c, the third mark at image #95. Figure 7d and 7e shows a 3D space with the three Vickers-pyramid indents reconstructed and surrounded by nodular graphite shown in white color.

CÍRCULO DE CUMBAYÁ. P.O.BOX: 17-12-841 QUITO-ECUADOR
T.: (593 2)297-1700 AL 708. FAX.: (593 2)289 0070.
WWW.USFQ.EDU.EC

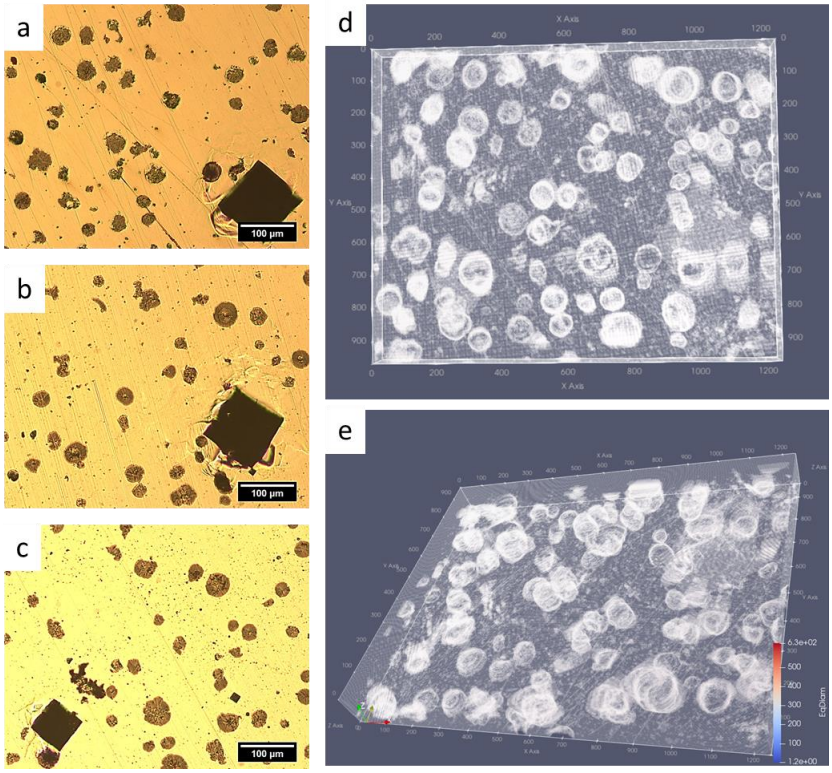

Figure 7. a) Optical microscope image #1 of nodular cast iron at 200x – First image- of the initial Vickers indentation; b) Image #45 – second Vickers indentation; c) Image #95 – third Vickers indentation, d & e) 3D-reconstruction of the microstructure.

The spatial detail of 3D gray cast iron microstructure is shown in Figure 8. Figure 8a shows the initial reference image of the surface and 8b the last image in a group of 50 images. Figure 8c shows a 3D space with the portion of the Vickers-pyramid indent reconstructed and surrounded by graphite flakes shown in white color.

CÍRCULO DE CUMBAYÁ. P.O.BOX: 17-12-841 QUITO-ECUADOR
T.: (593 2)297-1700 AL 708. FAX.: (593 2)289 0070.
WWW.USFQ.EDU.EC

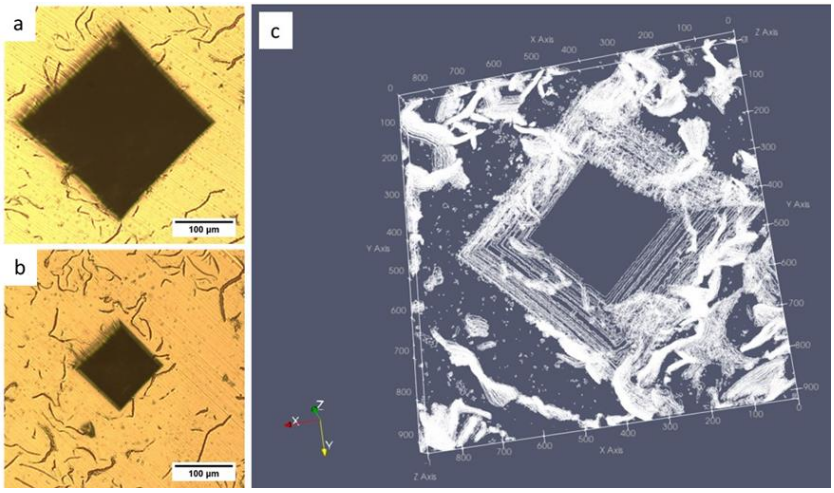

Figure 8. a) Optical microscope image of gray cast iron at 200x -reference image #1- of the initial Vickers indentation; b) last image of the Vickers indentation after 50 images- image #50, c) 3D-reconstruction of the microstructure.

The procedures developed in nodular cast iron and gray cast iron were used to reconstruct TBCs. The spatial resolution and the polishing steps were necessarily adjusted. However, the overall experimental procedure proposed guided successfully the reconstruction of TBCs in 3D.

To obtain the most representative microstructural defects and add them to the microscale models for TBCs, a YSZ sample was carefully polished to obtain micrographs at several subsequent depths with known distance. Following ASTM E 1920-03 Method-II, the metallographic guide for TS coatings, a polishing procedure was developed to achieve an optimum surface and eliminate imperfections. YSZ samples were mounted on epoxy resin and polished following best practices. The grinding process was performed with a semi-automatic polisher, using 120, 240, 320, 400, and 600 grit sandpaper. Once the grinding process was finished, the polishing process continued using cloths of 9, 3 and 1 µm diamond solutions. The parameters used in the grinding and polishing of the samples can be seen in Table 3.

Círculo de Cumbayá. P.O.Box: 17-12-841 Quito-Ecuador
T.: (593 2)297-1700 al 708. Fax.: (593 2)289 0070.
www.usfq.edu.ec

Table 5. Description of the procedure for sample preparation of YSZ coating for grinding and fine polishing. The depth-controlled polishing procedure allows to obtain images at known depths to reconstruct the defects in the microstructure in three dimensions.

Grinding and Polishing					
Surface	**Coolant/lubricant**	**Abrasive size/type**	**Time [min]**	**Force [N]**	**Surface speed [rpm]**
Abrasive paper	Water	120-240-320-400-600 grit	5	20	300
Soft cloth	Water-based suspension	9 µm-3 µm-1 µm diamond	5	20	300
Depth Controlled Polishing					
Surface	**Coolant/lubricant**	**Abrasive size/type**	**Time [min]**	**Force [N]**	**Surface speed [rpm]**
Soft cloth	Water-based suspension	3 µm-1 µm diamond	5	20	300

Samples were subjected to three indentations of a Vickers hardness tester using a Wilson Hardness Vickers 432 SVD instrument with a diamond indenter and HV0.5 kg load on the polished surface to establish reference positions and depths. Afterward, a 4 nm gold layer was sputtered onto the sample for SEM observation using a JEOL LT300 microscope. The Vickers indentation mark facilitated alignment of subsequent photos, measurement of polishing depth, and identification of defects. Following the initial photo, the polishing process was reiterated with 3 and 1 µm diamond water-based suspensions. Photos were taken at new depths estimated as one seventh of the average diagonal's length. The depth variation was registered between 5 µm and 10 µm. SEM photos were aligned using the Vickers mark in ImageJ software, applying thresholding adjustments to convert the images into 8-bit black-and-white format and eliminate background noise, as illustrated in Figure 9. A video illustration can be seen in this link.

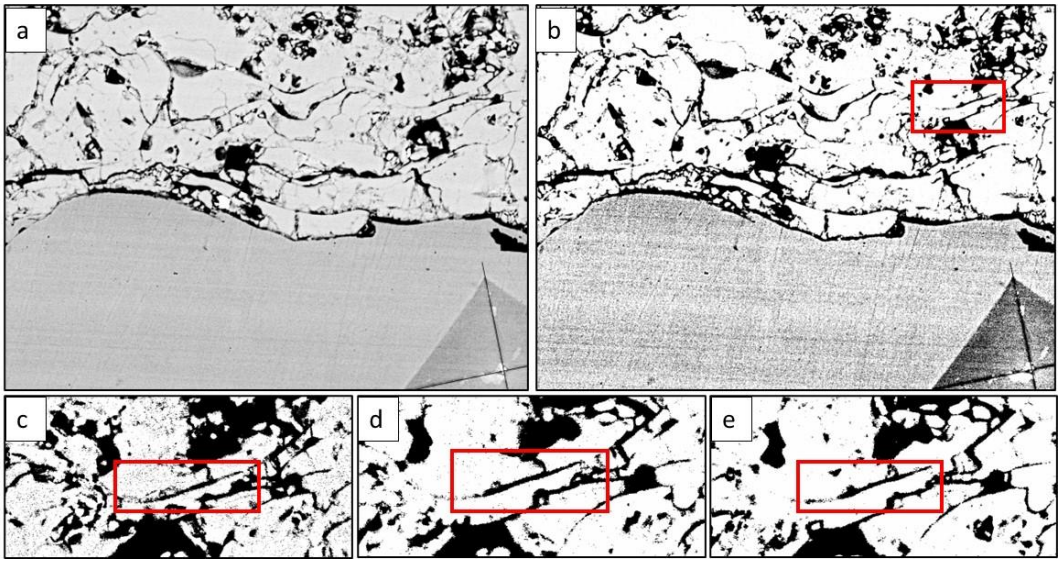

Figure 9. Microstructural defect analysis in TBC. a) Yttria-Stabilized Zirconia (YSZ) coating deposited via Air Plasma Spraying (APS), featuring a Vickers indentation in the bottom right corner. b) Image analysis of micrograph a) in black-and-white. c) Selection of a specific defect for detailed analysis and tracking. d) Image corresponding to the same defect as depicted in c), captured at a different depth. e) Image corresponding to the same defect as depicted in c) and d), captured at a different depth. Tracking of these defects (c, d, e) is facilitated by monitoring the positional changes and alterations in size of the Vickers indentation.

Círculo de Cumbayá. P.O.Box: 17-12-841 Quito-Ecuador
T.: (593 2)297-1700 al 708. Fax.: (593 2)289 0070.
www.usfq.edu.ec

Defects of interest are isolated in the black/white images and traced using Autodesk AutoCAD. Several images of various individual defects were aligned at different depths on planes to be joined, creating a transitional shape between all the sketches in Autodesk Inventor. A solid of the defect is obtained in a 3D model. The procedure is illustrated in Figure 10 presenting 3 images out of the 8 used to reconstruct the crack.

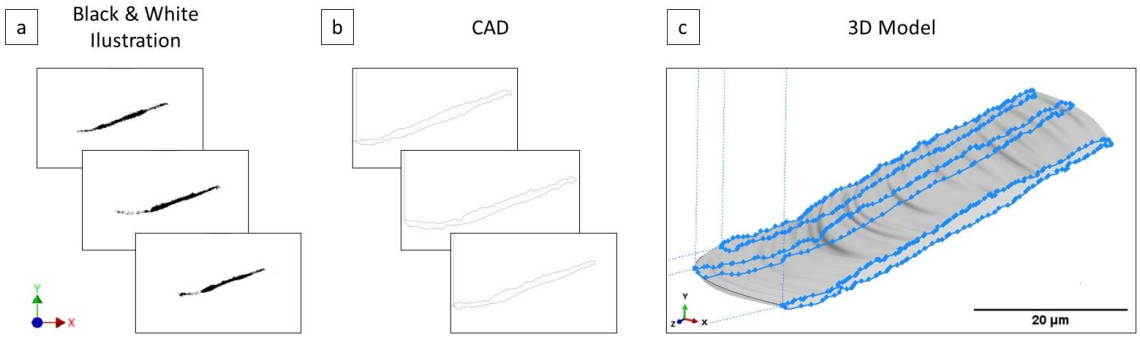

Figure 10. Horizontal crack reconstruction from eight images at varied depths. a) Illustration of three segmented images depicting the process of extracting the horizontal crack of interest. b) Computer-aided design (CAD) representation demonstrating the tracing of the defect on the tested images in a), and c) 3D model portraying the horizontal crack, offering a comprehensive visualization of its structural characteristics.

Círculo de Cumbayá. P.O.Box: 17-12-841 Quito-Ecuador
T.: (593 2)297-1700 al 708. Fax.: (593 2)289 0070.
www.usfq.edu.ec

9. Results and Findings:

2D Modeling - Key Results

Effective Thermal Conductivity Results – Analysis in Single- and Multi-layer TBCs

The thermal conductivity simulation results were compared with experimentally determined coating-property values obtained by Viswanathan et al.[1] using the laser flash technique on free-standing samples. Figure 11 presents a comprehensive comparison between the experimental and simulated thermal conductivities of the various combinations of YSZ and GDZ. It is noteworthy that certain intricacies, such as small cracks, pores, interlamellar interfaces, or partially bonded splats, might not be fully captured by image analysis. This characteristic was particularly evident in previous simulation results for YSZ coatings [2,4]. However, despite these challenges, the comparison across the five structures and the combination of materials and defects exhibits a consistent trend relative to the experimental values, as illustrated in Figure 11.

It is crucial to emphasize that, while the simulation may not capture all microscopic details, the trends observed align closely with the experimental outcomes. Notably, the simulated values consistently demonstrate a similar standard deviation, remaining below 5% for the largest standard deviation observed. This consistency underscores the precision and reliability of the image analysis procedure applied across various regions and structures, revealing a relatively low deviation.

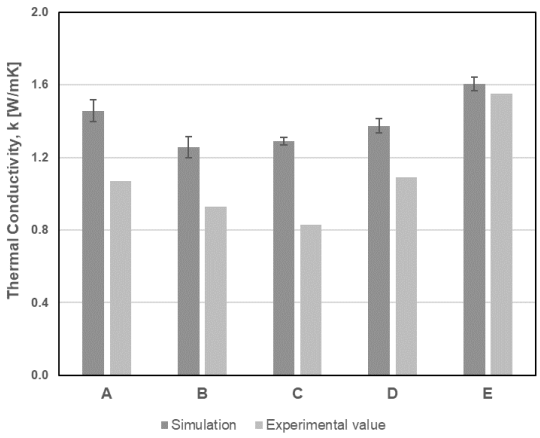

Figure 11. Simulation and experimental results of effective thermal conductivity of various multilayer TBCs.

The deviation between simulated results and reported experimental values can be attributed to several factors. These include: (a) the oversight of contact resistance among splats of both similar and dissimilar materials; (b) the utilization of user-defined threshold values for image processing, introducing subjectivity in separating pores and cracks; (c) a two-dimensional approximation of the model, which, given the three-dimensional nature of thermal conductivity, introduces limitations when adapting the model to a 2D microstructure; and (d) an insufficient number of elements in the mesh, leading to an inaccurate representation of cracks, pores, and material transitions that impact heat flow barriers.

In this study, a quantitative method has been rigorously employed to address the issue of image processing, identifying defects and phases with defined ranges for shapes and grayscale to minimize user bias in the analysis. Additionally, the OOF-2 tool has been instrumental in meshing interfaces between defects and bulk material, as well as between dissimilar materials, contributing to a more accurate representation of the complex thermal barrier coating system.

CÍRCULO DE CUMBAYÁ. P.O.BOX: 17-12-841 QUITO-ECUADOR
T.: (593 2)297-1700 AL 708. FAX.: (593 2)289 0070.
WWW.USFQ.EDU.EC

As depicted in Figure 11, coatings B and C exhibit the lowest thermal conductivity, primarily attributed to the high porosity of the porous GDZ and YSZ layers, respectively, serving as effective thermal barriers to heat flow. In contrast, configurations A and E display higher conductivity due to a reduced number of defects. Configuration E demonstrates the highest thermal conductivity, likely owing to its low porosity percentage and overall high density [1]. Supporting this observation, Table 3 provides the percentage of defects per configuration, while Figure 11 illustrates the temperature distribution. Supporting this observation, Table 4 provides the percentage of defects per configuration, while Figure 11 illustrates the temperature distribution. The average defect percentage has been categorized into horizontal cracks, vertical cracks, and globular pores, with horizontal cracks identified as the defects most influential in relation to heat flow in the through thickness direction.

Table 6. Average defects percentage measured by Image Analysis on multilayers A-E. Dark black regions are compared to the coating area to obtain the percentage of defects of each composite. Nominal values of the general percentage of defects are comparable to typical TBCs.

	Percentage of defects (%)			
Group	General	Horizontal cracks	Vertical Cracks	Globular Pores
A	4.46 ± 1.24	0.91 ± 0.13	1.11 ± 0.27	2.48 ± 0.25
B	6.15 ± 0.72	2.62 ± 0.27	1.91 ± 0.29	1.67 ± 0.13
C	6.70 ± 0.18	3.68 ± 0.21	1.52 ± 0.27	1.54 ± 0.10
D	3.30 ± 0.48	0.67 ± 0.16	1.56 ± 0.12	1.07 ± 0.14
E	2.58 ± 0.31	0.29 ± 0.08	1.20 ± 0.18	1.26 ± 0.04

Figure 12 illustrates the image analysis and simulation of thermal gradients in the various multi-layer coating systems. The figure comprises original SEM images, followed by image analysis, segmentation, and defect identification. Subsequently, segments are meshed using the OOF-2 tool, depicting thermal gradient results through the thickness. The top boundary of the TBC is fixed at 400°C, while the bottom boundary remains fixed at 25°C. The thermal gradient reveals an intensified effect of thermal resistance due to horizontal micro-cracks. Notably, in cases A, B, and C, elevated temperatures persist in regions preceding the appearance of numerous horizontal defects. This effect is most pronounced in B and C, whereas in cases D and F, temperatures distribute more uniformly or linearly from top to bottom in a steady state.

This analysis highlights the significant variation in thermal gradients among different coatings, potentially influencing thermal stresses. While this study does not address thermal gradients in thermomechanical stresses, it emphasizes that the presence of defects can markedly alter the thermal barrier effects of various coatings in preserving substrate materials.

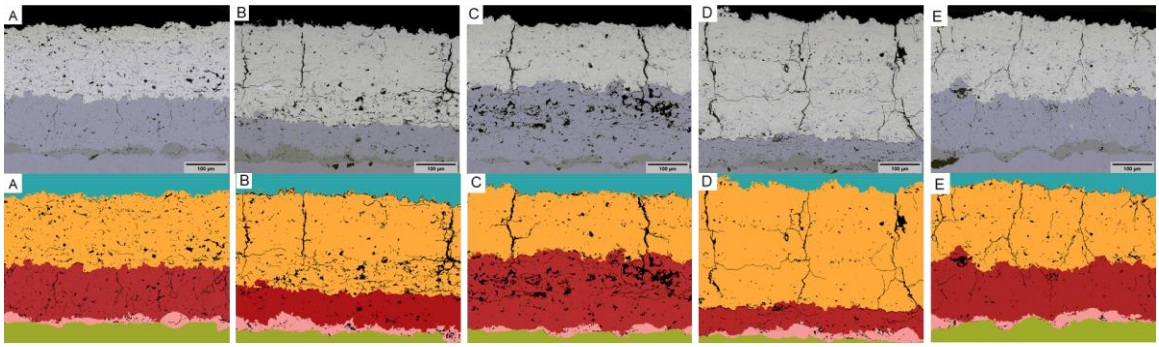

Círculo de Cumbayá. P.O.Box: 17-12-841 Quito-Ecuador
T.: (593 2)297-1700 al 708. Fax.: (593 2)289 0070.
www.usfq.edu.ec

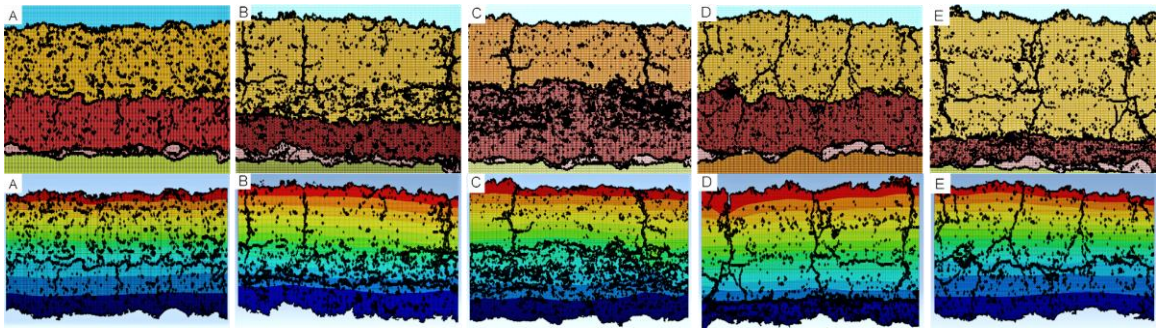

Figure 12. Image analysis and simulation of thermal gradients in multilayer/multimaterial coating system A-E, including their respective thermal conductivities and pore-crack architecture. The temperature is fixed in the top boundary layer at 400°C and at the bottom boundary layer at 25°C. The first row shows the original version of the images, second row presents the image analysis including segmentation and defect identification. The third row shows the images with their respective mesh using OOF-2 tool, and the fourth row shows the FEA results of the temperature gradient through the thickness considering the influence of thermal conductivity of the materials, and thermal resistance of cracks and pores.

Observations of thermal gradients indicate that distinct regions within the multilayered TBC serve as varying thermal barriers, with different defects playing specific roles as thermal resistors. Through modeling and image segmentation, a more in-depth analysis becomes possible, allowing each contributing factor to be quantified in terms of reduced thermal conductivity. More of this analysis per defect and per material layer is presented in appendix 2.

While the methodology has demonstrated high performance in predicting the reduction of thermal conductivity attributable to various specific structural elements (defects -pores, microcracks, vertical cracks, dissimilar materials, etc.), it acknowledges the inherent challenge of predicting perfect property values. Nevertheless, the research methods employed, coupled with comparisons to actual properties, instill confidence in progressing to the next analysis of thermomechanical stresses. In this context, where direct property comparisons may be unfeasible, the prediction of stresses will be correlated with performance tests (burner rig test), as presented in the subsequent section.

Thermomechanical FE Simulations

In Figure 13, the thermomechanical stress analysis unfolds throughout the heating cycle, considering the expansion of the substrate material, bond coat, TGO, and TBC, and accounting for their inherent expansion mismatches, resulting in thermal residual stresses. The model, symmetric with respect to the left-hand axis, undergoes a rightward displacement of nodes on the right-hand side during heating. Expansion is also considered along the *y*-positive axis, causing nodes to move upwards (not presented here for brevity).

The *x*-positive axis displacement is visually represented by the rightward movement of nodes until the conclusion of heating (H1), with subtle variations persisting by the end of the holding time (H2). During the cooling phase, the displacement diminishes (C). Notably, inelastic phenomena occur in the bond coat, contributing to a residual change in displacement and generating residual stresses.

The representation in Figure 13, corresponding to the multilayered sample “C”.

CÍRCULO DE CUMBAYÁ. P.O.BOX: 17-12-841 QUITO-ECUADOR
T.: (593 2)297-1700 AL 708. FAX.: (593 2)289 0070.
WWW.USFQ.EDU.EC

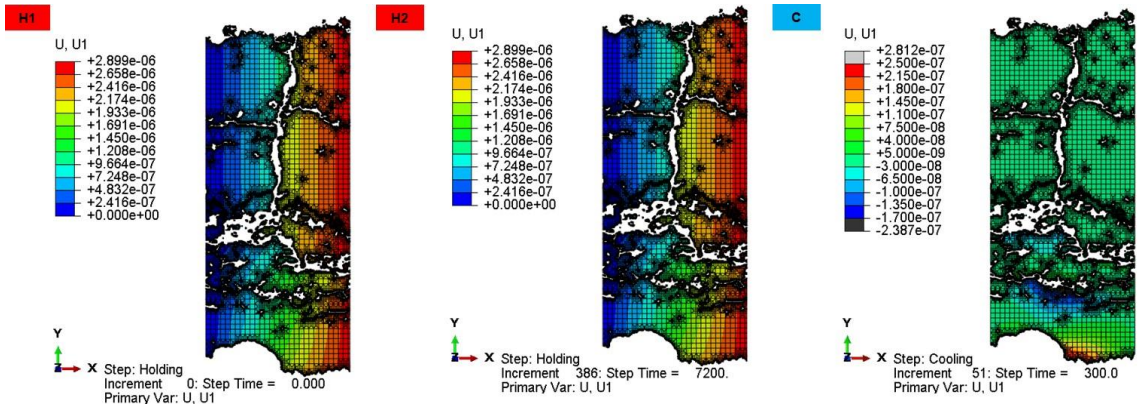

Figure 13. Simulation results of *x*-axis displacement for coating sample C. The illustration depicts rightward movement of nodes, progressing from the initiation of heating (H1) through the end of the holding time (H2) and concluding at the end of the cooling phase (C)

In Figure 14, the presentation of residual stresses and strain energy corresponding to the multilayered sample C is presented. S11 stresses, representing in-plane stresses, predominantly exhibit tension, attributed to the larger expansion of the substrate material compared to the TBCs. This tension is further influenced by the yielding and creep of the bond coat, resulting in high tensile stresses in the TBC near the TGO and marginal compressive stresses in the coating at the end of heating. Throughout the holding period, slight stress variations occur due to bond coat creep, and by the end of cooling, the stresses predominantly transition into compression, driven by the substrate material contracting more than the ceramic TBC. Stress concentrations are notable near the TGO interface, with tensile stresses at the TBC-TGO interface peak and compressive stresses in the valley zone.

Regarding S22 stresses in the through-thickness direction, values are nearly null or negligible at the end of heating and holding, except near the TBC-TGO interface. By the end of cooling, stresses grow significantly at the TBC-TGO interface peak in tension and in compression in the valley zone. The coating's structure, inclusive of porosity, microcracks, and vertical cracks, influences the distribution of S22 stresses, diminishing almost to negligible levels away from the TBC-TGO interface.

Examining strain energy, concentration occurs near the TBC-TGO interface, notably increasing by the end of cooling. Both S22 stresses and strain energy play a key role in causing delamination at the peak of the roughness profile, as the literature provides evidence.

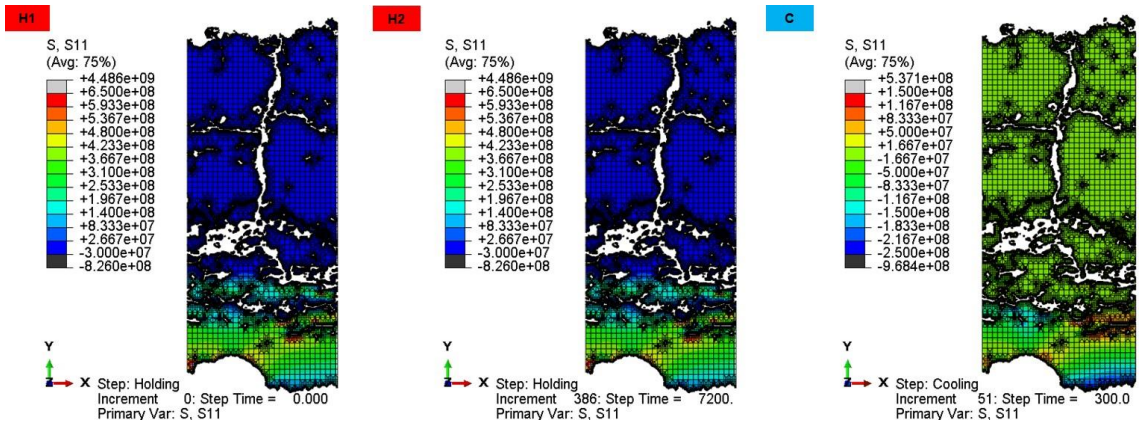

CÍRCULO DE CUMBAYÁ. P.O.BOX: 17-12-841 QUITO-ECUADOR
T.: (593 2)297-1700 AL 708. FAX.: (593 2)289 0070.
WWW.USFQ.EDU.EC

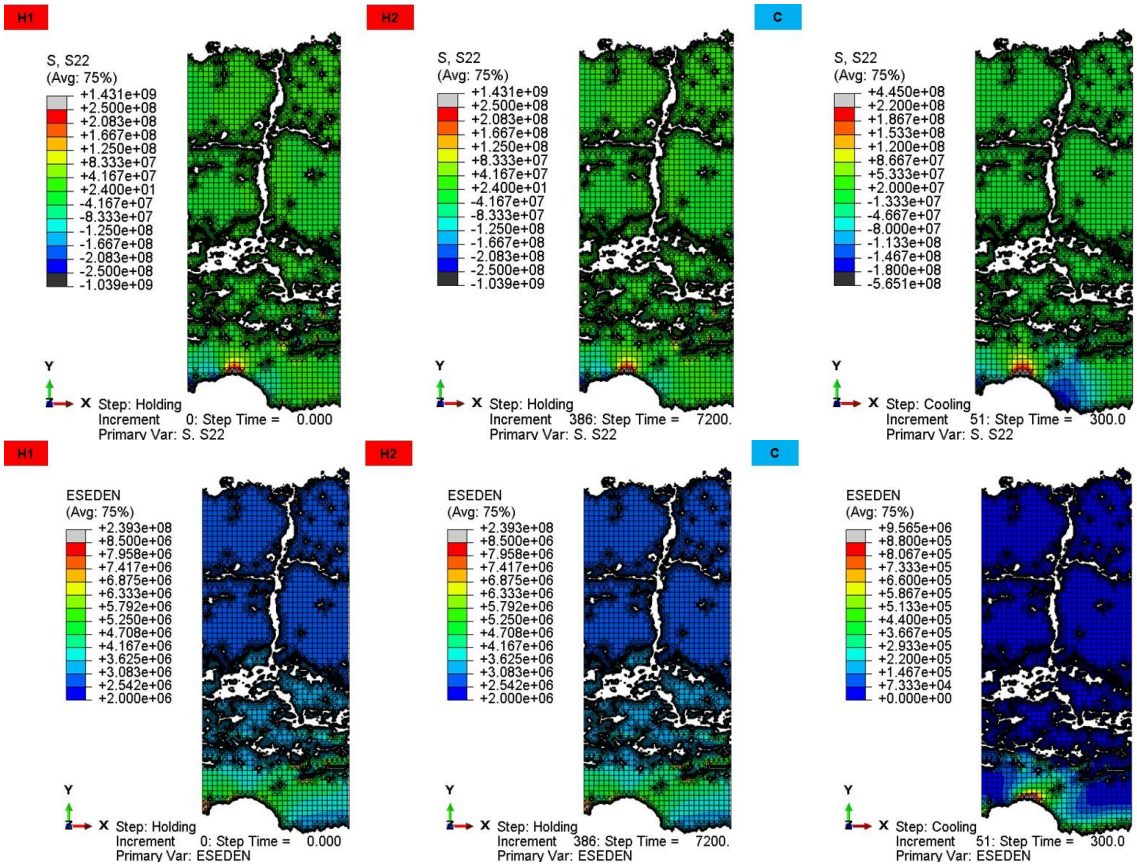

Figure 14. Simulation results illustrating S11 and S22 stresses, along with strain energy (ESEDEN by Abaqus), for multilayered coating C. The presented data corresponds to the end of the heating stage (H1), the end of the holding time (H2), and the conclusion of the cooling stage (C).

For the sake of brevity, the analysis for coatings A, B, D and E is not presented here. The reader is refered to appendix 2 for those details. In Figure 15, the discussion centers on the relationship of the failure locus of coatings A, B, and C in relation to the elastic strain energy computed as average values obtained from the strain energy maps. Coatings A and B experience failure at the GDZ-YSZ interface, with this interface registering strain energy values between 30 to 40 J/m^2. In contrast, coating C, failing at the YSZ-TGO interface, exhibits remarkably low strain energy in the GDZ at the same GDZ-YSZ interface.

According to the burner-rig tests, coating C demonstrates a significantly longer lifetime compared to B and A, as per Viswanathan et al.'s results [1]. Coating A, identified as the least performing before the tests, registers the highest strain energy at the GDZ-YSZ interface among the three coatings. Given GDZ's lower fracture toughness, it is hypothesized that once GDZ reaches a threshold of elastic strain energy, along with other potential factors such as large S22 tensile stresses during heating, the coating may undergo delamination.

In coatings B and C, both featuring GDZ-DVC top layers, the transition for C occurs from a porous YSZ to a DVC-GDZ, while for B, the transition is from dense YSZ to porous GDZ. It is hypothesized that the porous GDZ, with lower fracture toughness, may delaminate at this transition point, reaching the threshold of strain energy. Coating C endures longer as strain energy is concentrated in the denser YSZ coating, expected to possess higher fracture toughness. Transitions from one material to another, especially through a porous YSZ in this case, significantly reduce strain energy at the interface of two dissimilar materials (YSZ-GDZ). Those

CÍRCULO DE CUMBAYÁ. P.O.BOX: 17-12-841 QUITO-ECUADOR
T.: (593 2)297-1700 AL 708. FAX.: (593 2)289 0070.
WWW.USFQ.EDU.EC

being the reasons why coating C has an improved performance even compared to traditional single layer YSZ-TBCs.

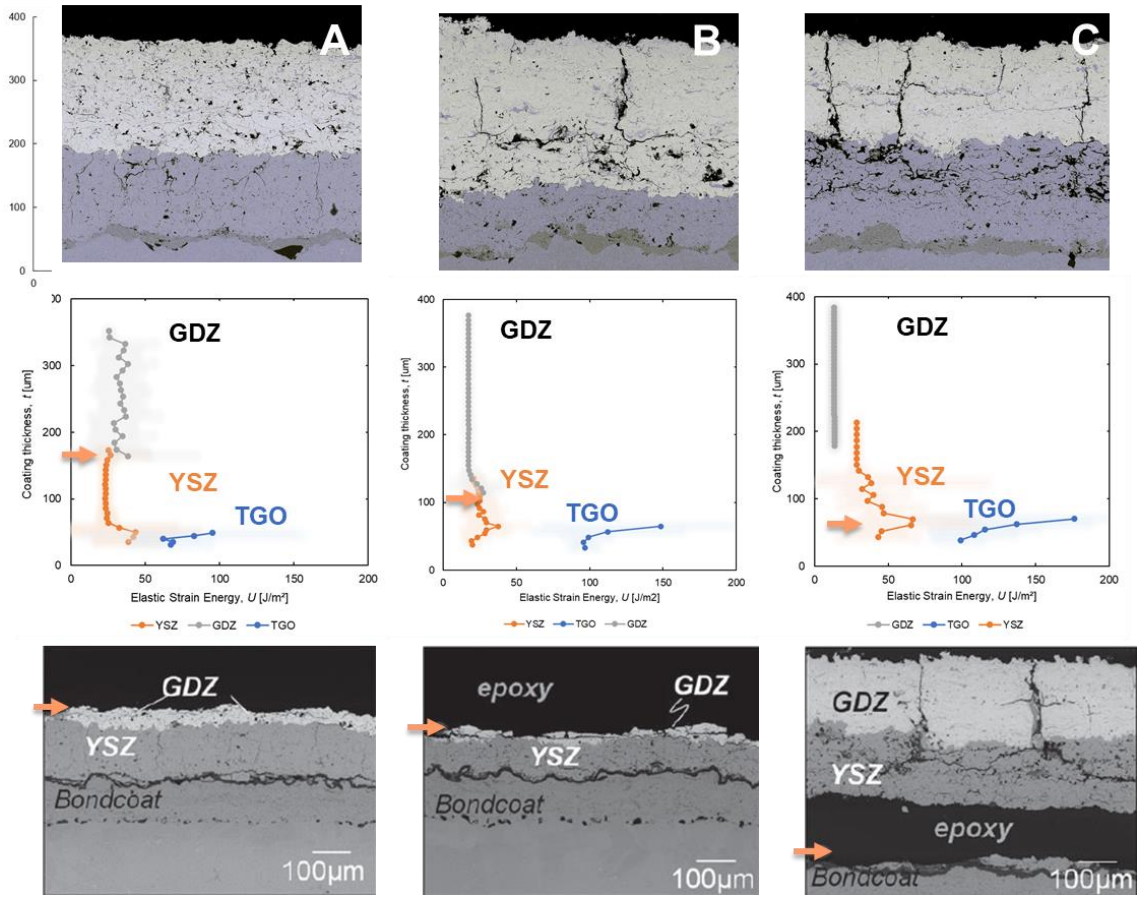

Figure 15. Comparative analysis of multilayered coatings A, B, and C. The figure includes original SEM images showing the distance through the thickness; the elastic strain energy changes through the thickness in the TGO, YSZ, and GDZ materials; and the locus of failure, as per Viswanathan et al.[1], to illustrate the region of failure.

The current FEA analysis, characterized by a detailed examination of the microstructure encompassing material segmentation, interface identification, and the discernment of features such as vertical cracks, microcracks, and pores, significantly enhances our comprehension of the underlying factors driving the failure of TBC coatings.
The thorough depiction of various microstructural elements contributes to a nuanced understanding of residual stress and strain energy distributions throughout the coating thickness. It is emphasized that each microstructural feature plays a role in redistributing stresses and strain energy, particularly important at the material interfaces where the mismatch of thermal expansion heightens the likelihood of failure.

The application of FEA is critical in revealing sharp transitions between areas with distinct characteristics, overcoming limitations inherent in previously employed analytical methods [1]. Although the current approach does not include certain concurrent phenomena, such as sintering, TGO growth, or thermal gradients, its demonstrated potential in unraveling the mechanics of the coating empowers designers to make informed judgments for the development of enhanced performance designs.
Further details of this study are detail in the manuscript “Thermo-Mechanical Modeling of Multilayered TBCs for Gas Turbine Engines” in appendix 2.

CÍRCULO DE CUMBAYÁ. P.O.BOX: 17-12-841 QUITO-ECUADOR
T.: (593 2)297-1700 AL 708. FAX.: (593 2)289 0070.
WWW.USFQ.EDU.EC

3D Modeling - Key Results

In the following section, we summarize a few key results from the modeling of TBCs in three dimensions:

Simulation results in Global Models

Figure 16reveals18 reveals cross-sectional views of halved TBC models: dense YSZ, DVC YSZ, and DVC YSZ-GDZ. Emphasis is on the crucial role of S22 stresses at the cooling phase end, impacting TGO-YSZ interface failure, especially. In-plane stresses (S11) are pivotal for understanding interactions with vertical cracks, especially in DVC configurations. The accompanying presentation in Figure 16 provides insights into the system's stored strain energy (ESEDEN by Abaqus).

In the TBC-YSZ dense structure, pronounced stress concentrations emerge near the TGO interface. Highly compressive S22 stresses are located in the valleys of the TGO-YSZ interface, with lower residual stresses in the upper TBC towards the surface. Notably, edge effects manifest due to computational constraints limiting the modeled section's size. Increased stresses are observed near edges and the center of the squared volume, particularly evident in the YSZ dense TBC. As depicted in Figure 1618, contrastingly, DVC structures show reduced edge effects, thanks to vertical cracks accommodating stresses.

Observations at the TGO interface of TBCs consistently show high compressive stresses in valleys and elevated tensile stresses at peaks across three models in S22 stresses. In S11 stresses, concentrations occur at vertical crack ends, influencing the stress profile at TGO-TBC and YSZ-GDZ interfaces in multilayer TBCs.

Regarding strain energy, dense YSZ concentrates energy near the TGO interface, while YSZ+DVC has similar values in a larger volume. The multilayer YSZ-GDZ structure exhibits optimal conditions with lower strain energy and evenly distributed high-magnitude stresses in larger volumes.

S22 in-plane stress ranges from +80 to -300 MPa, and S11 stress ranges from +100 to -280 MPa, aligning with literature-reported values. Strain energy falls within 2-7 MJ per cubic meter. Noteworthy details include the use of a honeycomb-like DVC structure with a lateral length (s) of 100 µm and a fixed vertical crack width (w) of 8 µm, ensuring a realistic representation of microstructures.

Círculo de Cumbayá. P.O.Box: 17-12-841 Quito-Ecuador
T.: (593 2)297-1700 al 708. Fax.: (593 2)289 0070.
www.usfq.edu.ec

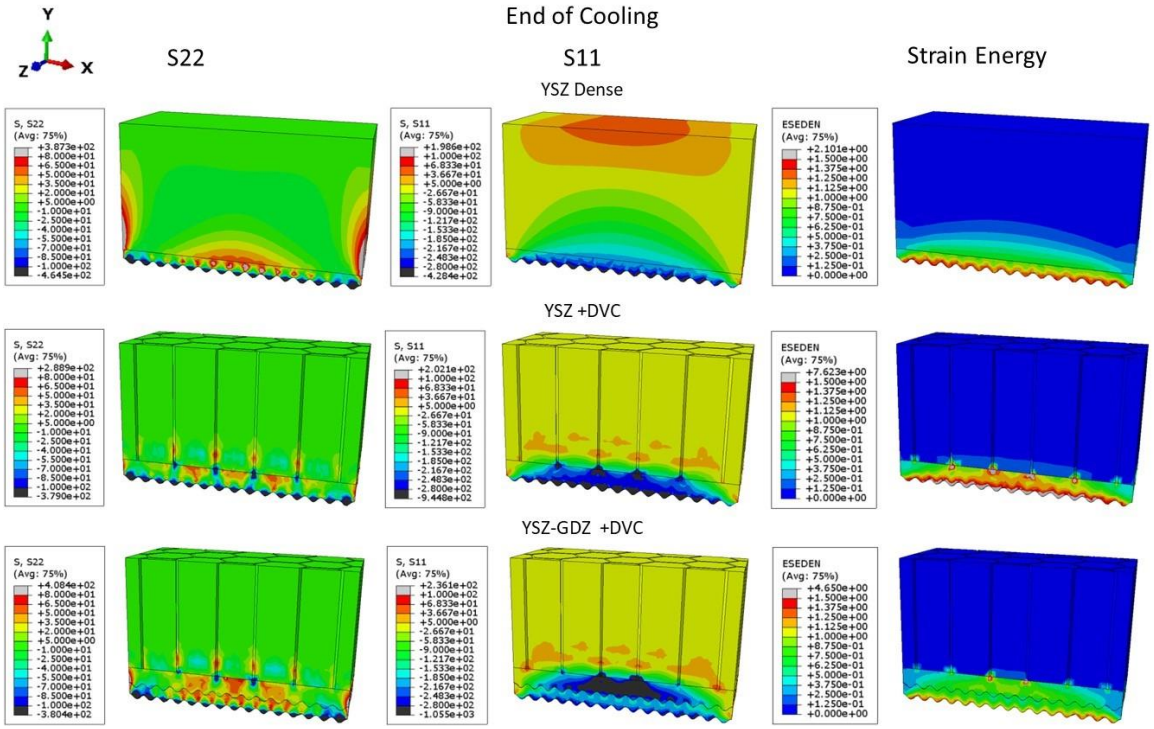

Figure 16. Stress analysis in global models post-cooling. Results showcase stress conditions at the end of the cooling phase. The original models are bisected to highlight stresses (S22, S11 – in MPa) and strain energy (ESEDEN by ABAQUS -in mJ/mm^3). The examined models encompass YSZ-Dense, YSZ+DVC, and YSZ-GDZ+DVC, the latest employ honeycombs with parameter s =100 µm, and spacing w = 8 µm in the DVC structures.

Figure 1719 offers a bottom view of the TBCs, providing insight into the area in direct contact with the TGO. This perspective reveals compressive residual stresses in the valleys and tensile residual stresses at the peaks in S22. In the DVC structures, the bottom view illustrates the projection of the honeycomb-like structure, emphasizing its arrangement.

The honeycomb-like structure does not notably reduce stresses in the TGO-TBC interface; however, a lower number of high tensile positions is recognized for the DVC coatings, especially for YSZ+DVC. Nonetheless, it's crucial to acknowledge that the honeycomb-like structure contributes to mitigating maximum tensile stresses.

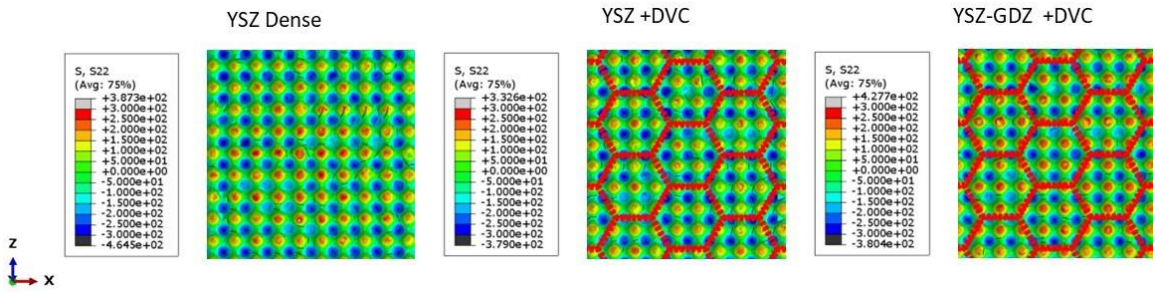

Figure 17. S22-Stresses in the YSZ -bottom view (in the YSZ-TGO interface) in post-cooling global models. The analyzed models include YSZ-Dense, YSZ+DVC, and YSZ-GDZ+DVC, with a specific focus on the latter to assess the impact of honeycombs on the stress distribution (honeycombs are projected on the interface).

CÍRCULO DE CUMBAYÁ. P.O.BOX: 17-12-841 QUITO-ECUADOR
T.: (593 2)297-1700 AL 708. FAX.: (593 2)289 0070.
WWW.USFQ.EDU.EC

In the TBC, heating induces tensile stress until the bond coat yields, entering a steady state. Cooling elevates stresses to their maximum near room temperature. S22 stress becomes highly tensile at the interface peak, shifting slightly during cooling. The valley experiences low tensile stresses during heating, transitioning to a compressive state at yielding, reaching maximum compressive stress during cooling. For S11 orientation, stresses shift slightly towards tensile until bond coat yielding, then transitioning to a compressive state. During cooling, both peak and valley residual stresses shift to a compressive condition.

Figures 18b and 18d illustrate the dynamics of S11 and S22 stress varying within the heat cycle at different positions. Figures 18a and 18c show S11 and S22 stress maps at the end of the cooling stage. These insights, derived from the YSZ-TBC dense model, align with 2D simulations, with positions 1-3 often having negligible stress values, and positions 4-5 representing points of possible failure due the high residual stress.

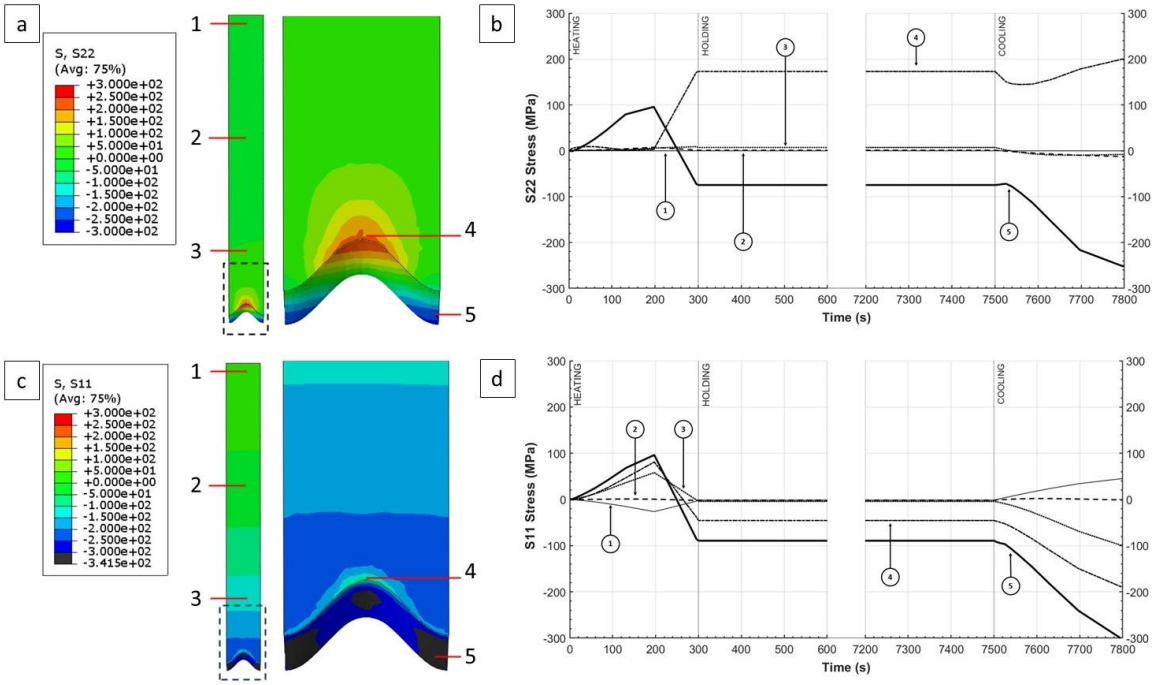

Figure 18. Stress analysis in various cross-sectional positions of dense YSZ global model TBC. a) Positions designated for S22 stress analysis, at the end of cooling. b) Temporal evolution of S22 stress across the stages of heating, holding, and cooling for designated positions 1 through 5. c) Positions designated for S11 stress analysis, at the end of cooling. d) Temporal evolution of S11 stresses across the stages of heating, holding, and cooling for designated positions 1 through 5.

Círculo de Cumbayá. P.O.Box: 17-12-841 Quito-Ecuador
T.: (593 2)297-1700 al 708. Fax.: (593 2)289 0070.
www.usfq.edu.ec

Simulation results in Mesoscale Models: Interaction between vertical crack and roughness – proximity of crack end to the interfaces

In Figure 19, the proximity of vertical crack ends to the interfaces is explored for YSZ and multilayer YSZ-GDZ configurations. Crack length varies from 0.45 mm to 0.47 mm up to 0.49 mm, being the longest one closer to the interfaces between different materials. Figure 19a and 19b show S22, and S11 stresses, respectively.

As crack tips approach interfaces, there's a dynamic interaction between stress distribution at the tip and profile-generated stresses, intensifying stresses around isles.

This nuanced analysis highlights the intricate relationship between crack positioning and stress distribution within the TBC volume, emphasizing the importance of understanding this interplay for optimizing structural performance.

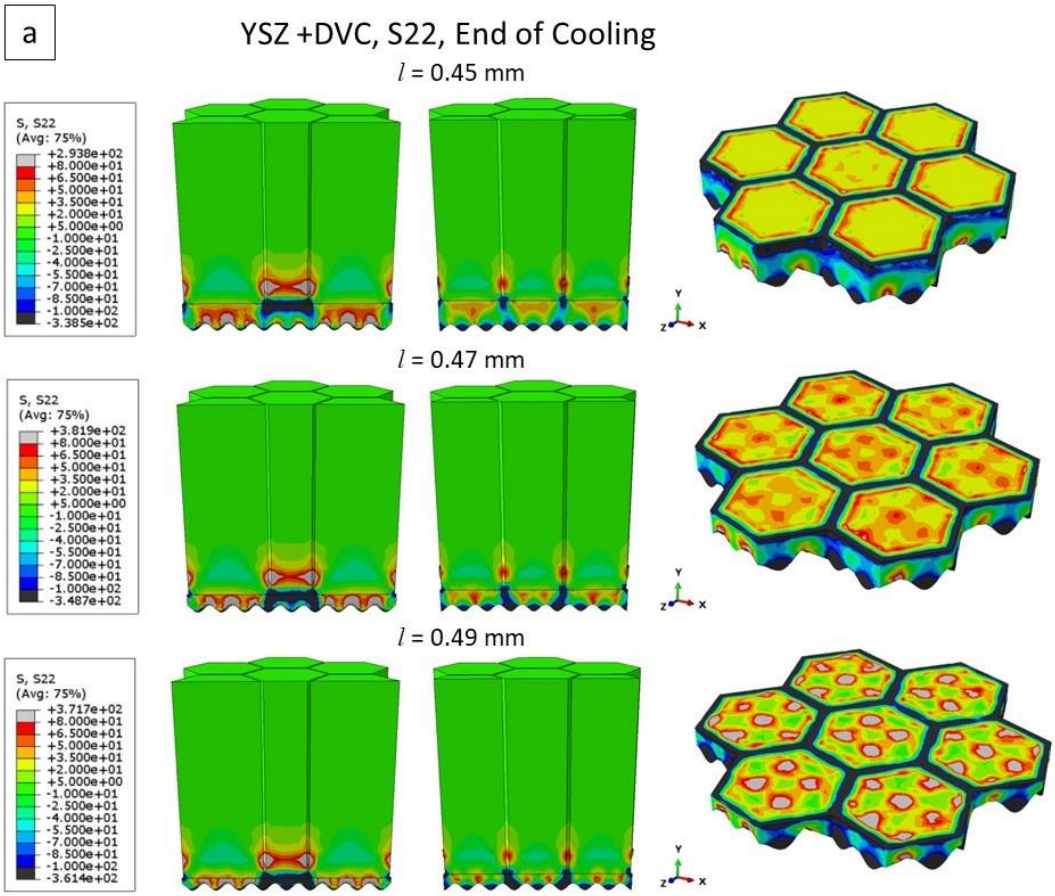

Círculo de Cumbayá. P.O.Box: 17-12-841 Quito-Ecuador
T.: (593 2)297-1700 al 708. Fax.: (593 2)289 0070.
www.usfq.edu.ec

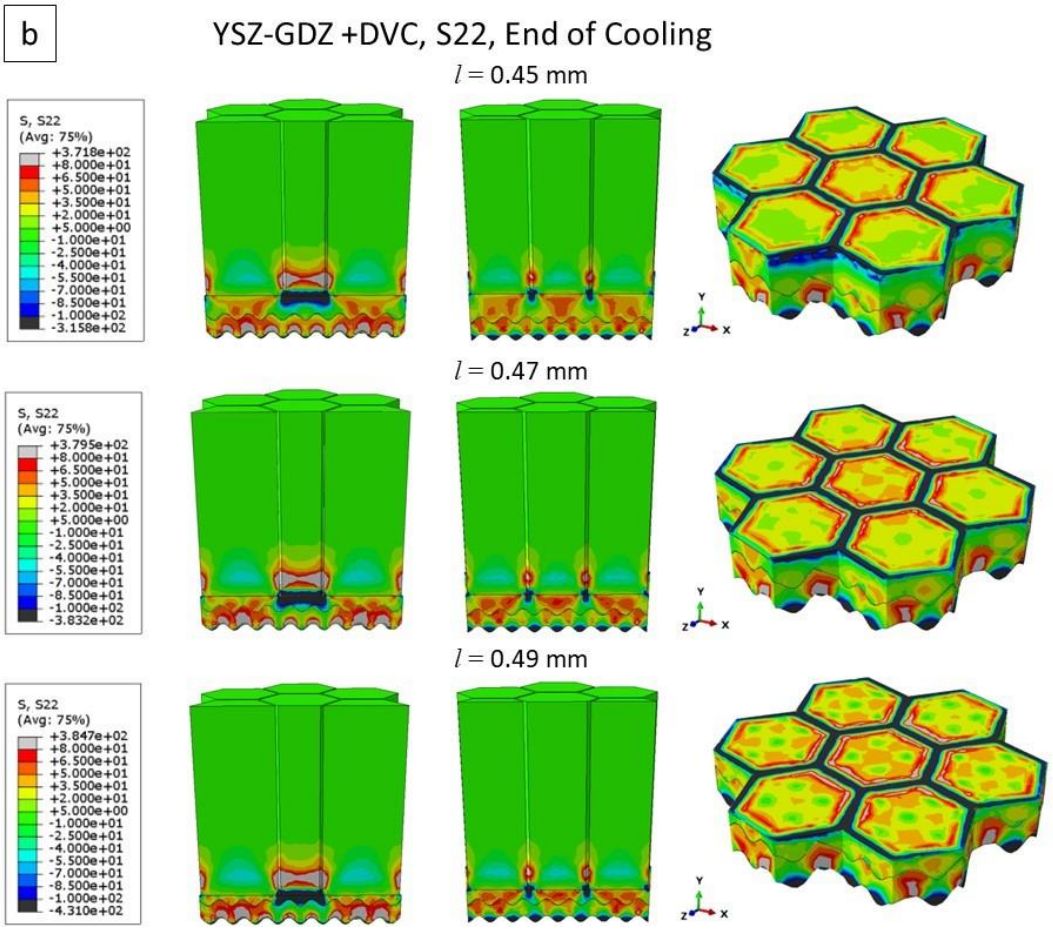

Figure 19. Analysis of stresses varying vertical crack length in mesoscale models of multilayer YSZ-GDC+ DVC with honeycomb-like structures. Results illustrate stress conditions at the end of the cooling phase for models incorporating honeycomb structures with varying vertical crack length. The original models are sectioned to emphasize a) S22- and b) S11-stresses at two distinct distances: firstly, at the edge of a side of the honeycomb, and secondly, across the entire honeycomb structure. Horizontal views are presented at a depth corresponding to the vertical crack's conclusion. The honeycomb length parameter (l) is systematically modified from 0.45 to 0.47 and 0.49 mm, while the parameter (s) is held constant at 100 µm, and (w) at 8 µm.

Examining the stresses on the interfaces with TGO and between YSZ and GDZ from a bottom view, a consistent pattern emerges, Figure 20.

As the crack approaches the interface, the S22 stresses at the peaks amplify for both YSZ and the multilayer YSZ-GDZ at both interfaces. This finding is crucial, highlighting that the interaction of crack tips with interfaces augments stresses at the peaks. In practical terms, this implies it is advantageous to design vertical cracks through processing, that commence farther away from multi-material interfaces.

This strategic approach can contribute to optimizing stress distributions within the TBC structure. This strategy has been adopted from the paper developed by Viswanathan et al.[1], and the results from the 2D simulations. In Figure 20, a comparative analysis from the bottom view is conducted on the proximity of crack tips to the TGO interfaces for both the YSZ-DVC coating and the multi-layer YSZ+GDZ-DVC coating. Although the magnitude of stresses appears similar in both coatings, a notable distinction arises in their effects.

CÍRCULO DE CUMBAYÁ. P.O.BOX: 17-12-841 QUITO-ECUADOR
T.: (593 2)297-1700 AL 708. FAX.: (593 2)289 0070.
WWW.USFQ.EDU.EC

Particularly, in the YSZ coating, the impact of crack end proximity is significantly more pronounced as the cracks approach the TGO interface. In contrast, for the multi-layer configuration, where crack tips approach the interface between the two zirconates, the effect over the TGO interface to increase stresses is comparatively smaller. This trend poses potential challenges for the longevity of the two interfaces, emphasizing the need for careful consideration in designing and managing stress concentrations in these critical regions.

In both YSZ-TGO interfaces, the stress range spans from -300 MPa up to +400 MPa, but for the interface between zirconates, stresses range between +180 to about -30 MPa. Regardless, a consistent trend is observed: as the tip of the vertical crack approaches the interface, S22 stresses escalate in magnitude.

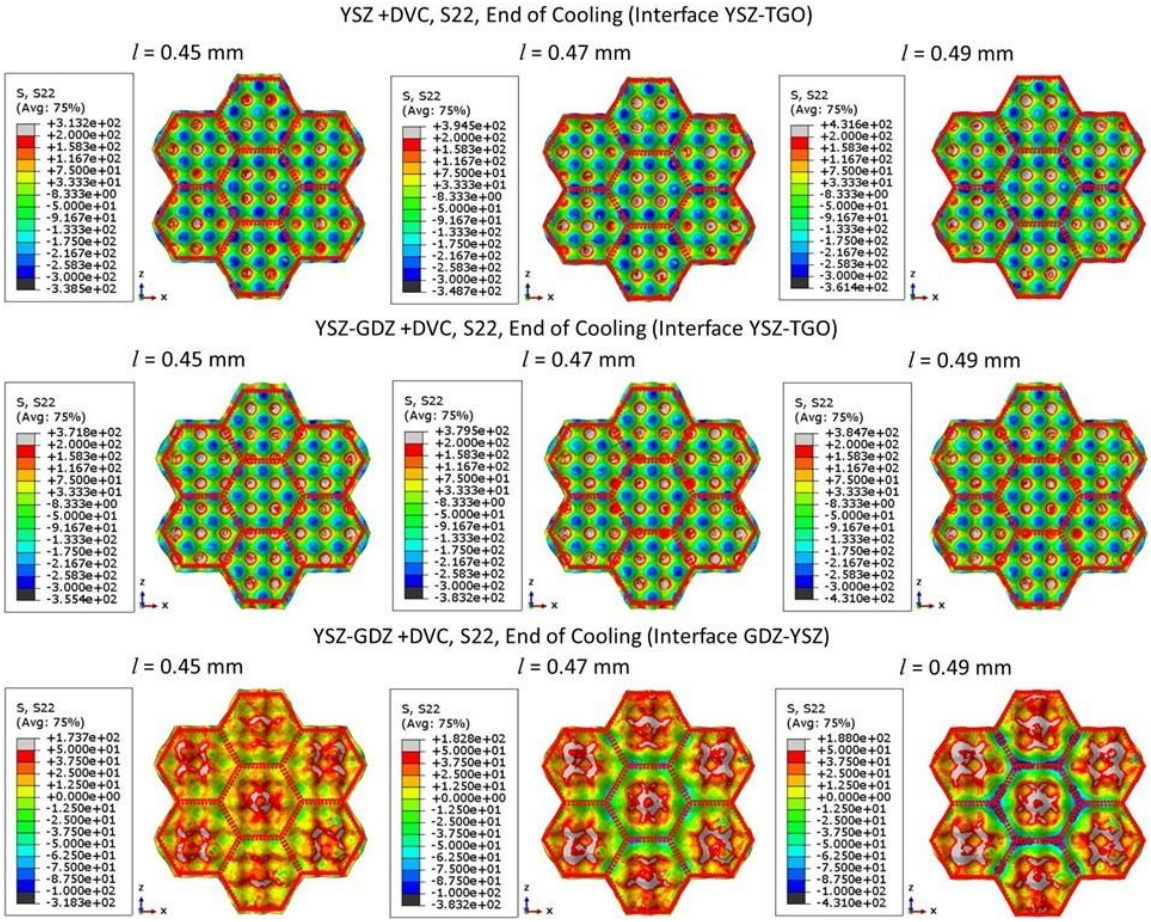

Figure 20. S22-Stresses in the YSZ -bottom view in post-cooling mesoscale models. The analyzed models include YSZ-DVC (in the TGO-YSZ interface), YSZ-GDC+DVC (in the TGO-YSZ interface), and YSZ-GDC+DVC (in the YSZ-GDZ interface), with a specific focus on vertical crack's length on the stress distribution (honeycombs are projected on the interface). The honeycomb length parameter (l) is systematically modified from 0.45 to 0.47 and 0.49 mm, while the parameter (s) is held constant at 100 μm, and (w) at 8 μm.

Simulation Results in Microscale Models: Effect of defect presence with the TBCs (increasing percentage of defects)

In addressing computational challenges related to simulating small defects in TBC microstructures, experiments were conducted on a sub-model of minimal dimensions in YSZ-GDZ. Figure 21 illustrates four

CÍRCULO DE CUMBAYÁ. P.O.BOX: 17-12-841 QUITO-ECUADOR
T.: (593 2)297-1700 AL 708. FAX.: (593 2)289 0070.
WWW.USFQ.EDU.EC

outcomes, ranging from a defect-free reference unit to models with escalating defect concentrations (10%, 20%, and 30%). Micro-models with refined meshing and accurately reconstructed defects provide a comprehensive overview of the impact of defect concentration on structural characteristics. Defects are consistently located across successive microstructures until reaching a 30% defect presence, measured in a 2D image section, aligning with common metallography practices.

In Figure 21a, S22 stresses range from approximately +300 MPa to -300 MPa, with high tensile stresses at the peak and high compressive stresses in the valleys of the interface profile. The introduction of cracks, especially those perpendicular to the out-of-plane direction of S22 stresses, alters stress distribution. Figure 21b demonstrates similar behavior in S33 stresses (S11 equivalent), with compressive stresses near the TGO interface transitioning to tensile stresses as TBC approaches the surface.

Horizontal cracks and their tips exhibit heightened interaction with S22 stress, by redistributing the stress field and amplifying their magnitude; while vertical running microcracks and defects induce stress redistribution, especially influenced by S33 stress (S11 equivalent).

For example, a large horizontal crack in the 20% and 30% cases significantly alters S22 stress distribution, reducing the highest tensile stress at the peak center and displacing it to the sides. The horizontal orientation of crack tips concentrates significant S22 stresses. (Figure 22 provides a bottom view of the four units.)

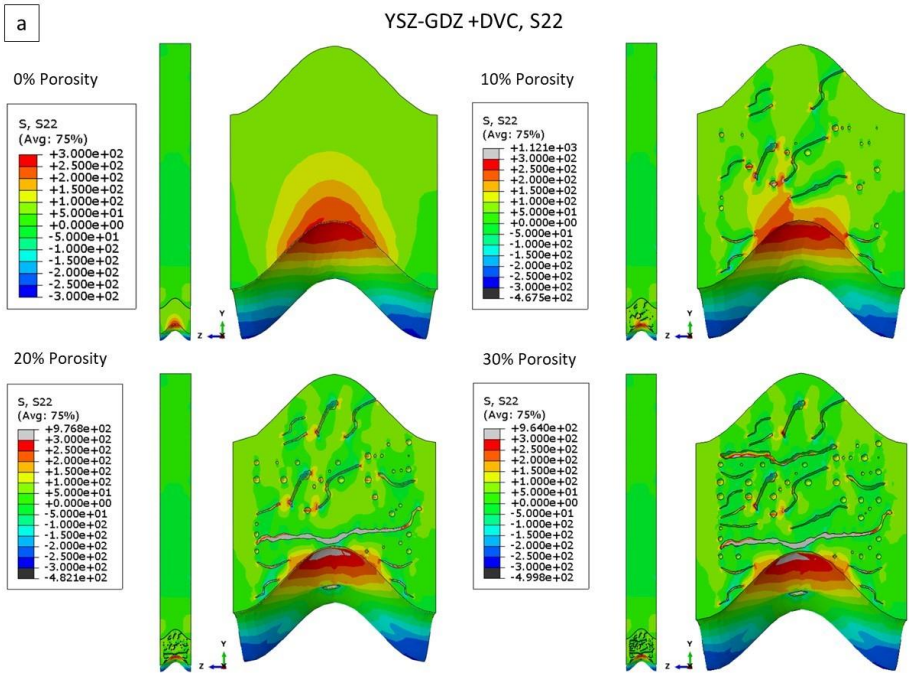

CÍRCULO DE CUMBAYÁ. P.O.BOX: 17-12-841 QUITO-ECUADOR
T.: (593 2)297-1700 AL 708. FAX.: (593 2)289 0070.
WWW.USFQ.EDU.EC

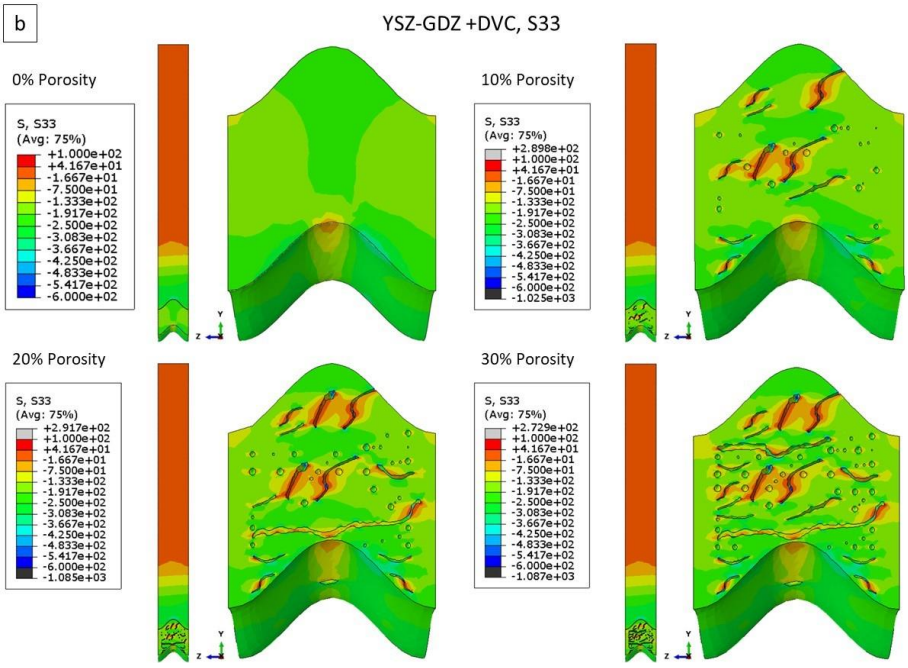

Figure 21. Stresses analysis in microscale models of multilayer YSZ-GDC+ DVC with varying defect percentage. Results illustrate stress conditions at the end of the cooling phase for models extracted from honeycomb structures with systematically varied percentages of defects (pores and cracks). Original models are partitioned to underscore a) S22- and b) S33-stresses at half the minimal unit, inclusive of a peak and four valleys. Post-cut, the image presents the peak at the top and the projection of two valleys in the bottom corners. The defect percentage is incrementally adjusted from 0 to 10, 20, and 30%. Defects, randomly distributed, are derived from actual microstructures and digitized for insertion into the model, progressively added to enhance model complexity.

Interestingly, when viewed from the bottom in Figure 22, the presence of defects, including a large horizontal crack affecting S22 stresses, does not significantly impact the region of the interface for S33 stresses.

The distinct behaviors of S22 and S33 stresses underscore the intricate influence of defects, their location, orientation, and percentage, on stress redistribution within the TBC microstructure.

CÍRCULO DE CUMBAYÁ. P.O.BOX: 17-12-841 QUITO-ECUADOR
T.: (593 2)297-1700 AL 708. FAX.: (593 2)289 0070.
WWW.USFQ.EDU.EC

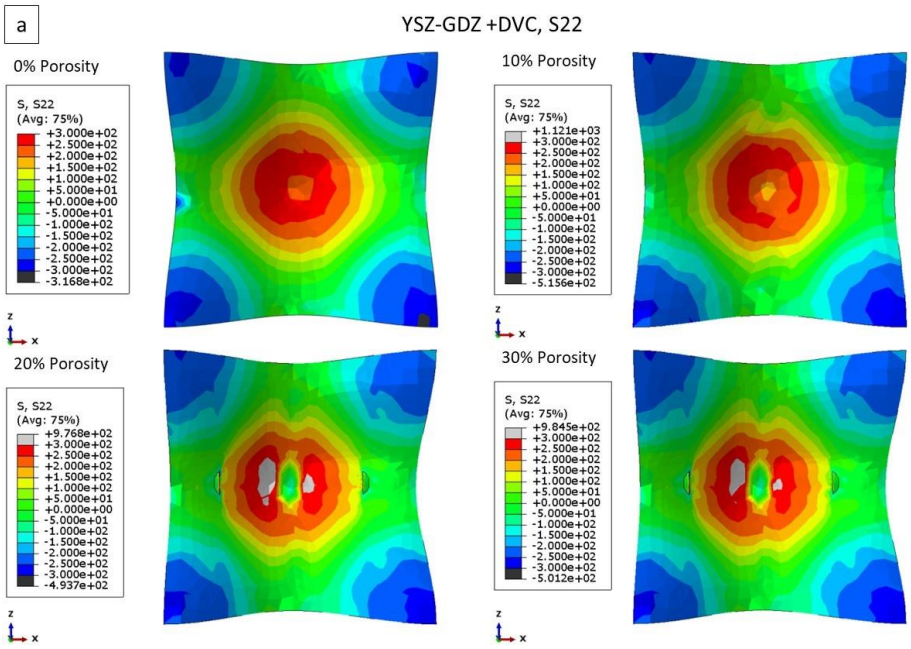

Figure 22. Stresses Analysis in YSZ at the TGO-YSZ interface within microscale models of multilayer YSZ-GDC+ DVC with varying defect percentage. Results show the stress field from the bottom view at the end of the cooling phase with systematically varied percentages of defects (pores and cracks). Models present a) S22- and b) S33-stresses, inclusive of a peak and four valleys. The defect percentage is incrementally adjusted from 0 to 10, 20, and 30%

Further details of this study are detail in the manuscript “Multiscale Finite Element 3D Modeling of Thermomechanical Stresses in Dense Vertically Cracked YSZ And Multilayered YSZ-GDZ TBCs” in appendix 1.

Círculo de Cumbayá. P.O.Box: 17-12-841 Quito-Ecuador
T.: (593 2)297-1700 al 708. Fax.: (593 2)289 0070.
www.usfq.edu.ec

10. Appendices:

Appendix 1: Manuscript of paper:
MULTISCALE FINITE ELEMENT 3D MODELING OF THERMOMECHANICAL STRESSES IN DENSE VERTICALLY CRACKED YSZ and MULTILAYERED YSZ-GDZ TBCs

Appendix 2: Manuscript of paper:
THERMO-MECHANICAL MODELING OF MULTILAYERED TBCs FOR GAS TURBINE ENGINES

Appendix 3: Presentation at International Materials Research Conference, August 15th 2023. Cancún Mexico. Entitled:
RESIDUAL STRESSES AND ELASTIC STRAIN ENERGY IN MULTILAYERED/MATERIAL TBCS: THEIR RELATIONSHIP TO FAILURE.

Appendix 4: Presentation at International Materials Research Conference, August 15th 2023. Cancún Mexico.
3D MODELING OF THERMAL STRESSES IN MULTI-LAYER/MATERIAL TBCS FOR GAS TURBINE ENGINES

CÍRCULO DE CUMBAYÁ. P.O.BOX: 17-12-841 QUITO-ECUADOR
T.: (593 2)297-1700 AL 708. FAX.: (593 2)289 0070.
WWW.USFQ.EDU.EC

11. List of Symbols, Abbreviations and Acronyms

TBCs	Thermal Barrier Coatings
YSZ	Yttria Stabilized Zirconia
GDZ	Gadolinium Zirconate
OOF	Object oriented finite element.
FEA	Finite element analysis
FEM	Finite element method
DVC	Dense Vertically Cracked
CMAS	Calcium-Magnesium-Aluminosilicates

12. References

1. Viswanathan, V., Dwivedi, G. & Sampath, S. Multilayer, multimaterial thermal barrier coating systems: Design, synthesis, and performance assessment. *J. Am. Ceram. Soc.* **98**, 1769–1777 (2015).
2. Tan, Y., Longtin, J. P. & Sampath, S. Modeling Thermal Conductivity of Thermal Spray Coatings: Comparing Predictions to Experiments. *J. Therm. Spray Technol.* **15**, 545–552 (2006).
3. Aktaa, J., Sfar, K. & Munz, D. Assessment of TBC systems failure mechanisms using a fracture mechanics approach. *Acta Mater.* **53**, 4399–4413 (2005).
4. Kulkarni, A. a. *et al.* Advanced Microstructural Characterization of Plasma-Sprayed Zirconia Coatings Over Extended Length Scales. *J. Therm. Spray Technol.* **14**, 239–250 (2005).

CÍRCULO DE CUMBAYÁ. P.O.BOX: 17-12-841 QUITO-ECUADOR
T.: (593 2)297-1700 AL 708. FAX.: (593 2)289 0070.
WWW.USFQ.EDU.EC

Appendix 1:

Manuscript of paper:
MULTISCALE FINITE ELEMENT 3D MODELING OF THERMOMECHANICAL STRESSES IN DENSE VERTICALLY CRACKED YSZ and MULTILAYERED YSZ-GDZ TBCs

CÍRCULO DE CUMBAYÁ. P.O.BOX: 17-12-841 QUITO-ECUADOR
T.: (593 2)297-1700 AL 708. FAX.: (593 2)289 0070.
WWW.USFQ.EDU.EC

MULTISCALE FINITE ELEMENT 3D MODELING OF THERMOMECHANICAL STRESSES IN DENSE VERTICALLY CRACKED YSZ and MULTILAYERED YSZ-GDZ TBCs

Alfredo Valarezo, Westly Castro, Carlos Bonilla, Krutskaya Yépez, Lorena Bejarano

Institute for Energy and Materials, Department of Mechanical Engineering, Universidad San Francisco de Quito, Quito, Ecuador

* Corresponding Author:

E-mail: alfredo.valarezo@gmail.com ; Tel: +593-2971700 ext. 1048

Abstract

Traditional models of Thermal Barrier Coatings (TBCs) in gas turbine engines are often oversimplified as 2D structures, neglecting crucial defects like vertical and horizontal cracks. This study focuses on the three-dimensional (3D) simulation of TBCs, specifically four-layer configurations: a dense vertically cracked (DVC) of Yttria-Stabilized Zirconia (YSZ) or Gadolinium Zirconate (GDZ) top layer, followed by a dense YSZ layer, a thermally grown oxide (TGO), and a bond coat layer. Emphasis is placed on the representation of layer interfaces, defects recreation from metallographic sectioning, and a mud-crack pattern for the top layer at different modeling scales. Utilizing the finite element method via Abaqus software, our models undergo isothermal thermal cycles with careful computational structuring. Results reveal the thermal response of TBCs, showcasing stresses and strain energy. Stress concentrations at the tip of horizontal interlamellar cracks and vertical cracks in the DVC structure significantly impact the multilayered system. Comparative analysis highlights lower residual stresses and strain energy in the multilayer GDZ structure compared to YSZ counterparts. Increased residual stresses at interfaces (TGO-YSZ and YSZ-GDZ) are noted. Comparative assessments with two-dimensional models validate our simulation procedure, revealing differences. The highest stress distributions (+200 MPa to -200 MPa -S22) are observed in the YSZ-dense layer near the TGO interface; and noteworthy are the S11 high compressive stresses (-350 to –200 MPa) in YSZ-GDZ interface, both at the end of cooling. However, these values may vary due to the presence of DVC coating cracks and interlamellar defects. The study explores the size effect of mud crack isles, length of vertical cracks, and defect density. Strategies for designing coatings to enhance engine efficiency are suggested, based on our comprehensive simulations.

Introduction

Thermal barrier coatings (TBCs) have played a key role in the protection of high-temperature components in gas turbine engines. Understanding the phenomenon of residual stresses in TBCs is essential for enhancing their efficiency. The successful application of TBCs in gas turbines demands careful material selection and a comprehensive understanding of their properties[1–3]. This process involves depositing specialized coatings, such as Yttria-Stabilized Zirconia (YSZ) and Gadolinium Zirconates (GDZ), or others, to act as thermal barriers, reducing heat transfer to the substrate and safeguarding it from extreme temperatures[4]. Managing thermal residual stresses is critical to ensure TBCs' long-term reliability under demanding operating conditions. Investigating stress fields and strain energy aids in devising strategies to enhance the resilience and longevity of TBCs[5–8].

Traditionally, these coatings have been modeled as two-dimensional structures with infinitely large in-plane dimensions. However, the presence of defects, such as pores, horizontal and vertical cracks, has generated an increasing interest in the three-dimensional (3D) evaluation of TBCs. As a result, advanced 3D modeling methodologies, including Finite Element Method (FEM), X-ray Microtomography, and 3D Digital Image Correlation (DIC), have gained prominence[9–11]. FEM enables in-depth analyses of stress, strain, and temperature distribution, allowing to vary loading and thermal conditions[11–16]. By synergistically employing various 3D modeling techniques, researchers gain unprecedented insights into TBC behavior, unlocking avenues for optimizing coating designs and enhancing overall performance in critical industrial applications. Extensive research has scrutinized the mechanical, microstructural, and thermal properties, coupled with detailed examinations of TBC compositions and processing methods. A critical review of pertinent literature is presented to elucidate the current 3D modeling landscape using FEM for TBC simulation.

Key considerations in TBC modeling, as outlined by Baker and Seiler[15], emphasize stress divergence in 3D simulations, the crucial role of interface shapes, and the necessity for accurate material behavior descriptions. These considerations guide this study, particularly in exploring stress fields in 3D, crack interactions, and defects while accounting for relevant material properties. Few 3D modeling studies have been published. Chun Li et al.'s work, employing analytical and FEM models, indicates high residual stress near the TGO-TBC interface, negligible pore impact on residual stress distribution, and a significant effect of microcrack densities within specific ranges[9]. Similar results are discussed in this study. Other works in 3D modeling, including Wei et al.'s [16] 3D TBC cracking model and Jinnestrand and Sjöström's [17]exploration of delamination crack initiation, offer insights, notwithstanding our model's omission of explicit crack propagation.

Studies by Yang Tan et al.[13] and Kulkarni et al.[12] in 2D modeling highlight the potential of FEM for predicting thermal conductivity, acknowledging limitations in capturing microstructural defects (i.e., intersplat interfaces). Discussions by Chen and Lee delve into properties, delamination, and failure mechanisms, with Bumgardner et al. [11]shedding light on vertical and horizontal crack interactions and their impact on strain energy. Explorations of TBC compositions, such as Schmitt and Doleker's focus on rare earth doped YSZ and GDZ, align with our study, emphasizing reduced thermal conductivity and the benefits of GDZ's phase stability. Performance assessments by Mahade et al.[18,19] and Zhou et al.[20] in multilayered YSZ-GDZ (SPS and APS) provide insights into TBC durability and superiority under isothermal or burner-rig test conditions versus YSZ coatings. Investigations by Viswanathan et al.[21] into multilayer, multimaterial TBC systems,

including DVC structures, enrich the understanding of failure locations and high strain energy in TBC interfaces (like the present results).

In this study, we simulate the behavior of three-dimensional TBCs composed of four layers: the upper one is a dense vertically cracked (DVC) YSZ layer or GDZ, followed by a dense YSZ layer, the thermally grown oxide (TGO) and a bond coat layer. We pay special attention to the geometry and properties of the interfaces between these constitutive layers, and the recreation of a mud-crack pattern for the top layer. The FEM using Abaqus software was used to solve the complex models and sub-models created of the multilayer systems. The multiscaling approach is used to first model the TBC in the millimeter range (global model) to subsequently extract a smaller region of analysis and refine systematically the mesh for simulation (mesoscale model). A third step, using a smaller region (micro-scale) is used to insert microcracks and porosity. The strain fields are exported as initial conditions for the smaller scale models. The 3D structures were subjected to thermal cycles composed of three steps: heating (from 298 K to 1273 K in 300 s), holding (for 7200 s -including yielding on the bond coat), and cooling (in 300 s). The models are carefully structured to reduce computational time.

The results of this study are expected to show the thermal response of the TBC (stress, strain, displacement, strain energy) and highlight the effect of stress concentrations caused by the DVC structure, which will help understanding how the TBC behaves under thermal loading and how the DVC layer influences the stress distribution and damage initiation. The results are compared with their 2D counterpart to validate the simulation procedure and highlight the differences, which will help assessing the accuracy and reliability of the 3D models and identify the advantages and limitations of using 2D or 3D approaches. Stresses are significantly high at the interfaces, near defects, and at the tip of vertical cracks. The TGO-YSZ interface manifests significant thermal mismatch effects showing tensile stresses during heating followed by an important relief to compressive stresses due to the yielding of the bond-coat. At the end of cooling, in the S22 direction, stresses range between +150 to +200 MPa in peaks, while valleys exhibit a similar order of magnitude in compression. Notably, S22 tensile stresses are identified as increasing the risk of coating failure. On the other hand, YSZ-GDZ interface for the multilayer system, shows high S11 compressive stresses, ranging from -300 to –350 MPa in peaks and -200 to -250 MPa at the end of cooling. However, these values and stress distribution over the TBCs may be altered by the presence of cracks from the DVC coating or from intersplat micro-craks, depending upon the geometry of the defects, which will be discussed in detail. Microstructural defects were recreated to study stress fields to simulate realistic scenarios of the TBC and investigate how defects affect the performance and durability of the TBC. The 3D approach and detailed analysis of interfaces and defects provide valuable information for optimizing the durability and performance of thermal barrier coatings used in gas turbine engines.

Experimental Methods

Simulation

The simulation process commences with the generation of a large-scale model (the so called here, global model), from which smaller ones are derived, each possessing initial simulated strain fields from the original. The global models include three different TBCs: a dense YSZ coating and two honeycomb like structures, emulating DVC structures, as depicted in Figure 1 a, b and c, respectively. The global models lie within the millimeter scale.

Subsequently, the global model undergoes a segmentation process, transforming it into a sub-model. In this context, the geometry of the global model is reduced to a volume of interest with a refined mesh. Stress and strain data from the global model are then transposed to the sub-model as specific boundary conditions, eliminating the need to simulate large global models repeatedly[22]. The first sub-models, so-called mesoscale models, are reduced portions of the geometry extracting seven honeycomb units (one centered and six-surrounding honeycombs) with mesh refinements to improve the accuracy of the results, Figure 1e and f. The last sub-models include microscale simulations constituted by smaller pillars extracted from the center of one honeycomb structure, as illustrated in Figure 1g, whose geometric dimensions are scaled down to the order of microns, incorporating finer refinements on the mesh to facilitate the inclusion of microstructural defects, Figures 1h and i.

The FE simulation is conducted using Abaqus 2020, enabling a thorough analysis of the response of assembled components (multiple layers) under specific conditions. The simulation process can be delineated into three primary stages: geometry definition (global, meso, and micro scale models; and materials), components assembly, modeling of defects, and interaction specifications (boundary conditions, meshing operations, and thermal loads), as follows.

Geometry description and materials

The geometry setup and material distribution of the simulated TBCs are presented in Figure 1j. In the foundation of global models, three arrangements of TBC-systems are characterized by four layers of fixed thickness—bulk substrate Ni-superalloy material, bond coat, TGO, and the TBC. Notably, the contact surface between layers is modeled with a sinusoidal profile with an amplitude A=10 μm and a wavelength λ=60 μm (Figure 1k).

The models consist of 4 or 5 materials distributed in layers according to the configuration being studied, Inconel 617 of 10 mm is used as substrate, a layer of bond coat of 100 μm, a layer of TGO of 10 μm and a layer of TBC in three different configurations: YSZ dense of 500 μm (Figure 1a, 1j), YSZ dense of 50 μm followed by 450 μm of YSZ DVC (Figure 1b), and YSZ dense of 50 μm followed by 50 μm of GDZ dense and 450 μm of GDZ DVC layers (Figure 1c, 1j).

All layers of materials are considered isotropic, and linear elastic (except the bond coat). The gadolinium zirconate (GDZ) is an oxide-based ceramic that acts as a thermal barrier and chemical barrier to resist aggressive environments. Yttria-Stabilized Zirconia (YSZ) is also an oxide-based ceramic and acts as thermal barrier and structurally stable coating. The bond coat is considered an elastic-plastic material, with plastic deformation occurring during the thermal cycles. Its function is to improve the adhesion between the substrate and the top layers giving some level of protection against oxidation and corrosion by allowing the TGO growth. The yield strength of bond coat depends on the temperature. Here, the properties of M-

CrAlY published by Aktaa et al. are adopted from [13,23–26]. The TGO is Al_2O_3 oxide layer that forms between the ceramic layers and the bond coat. This layer acts as a chemical barrier to protect the metallic substrate. In this study, a stable TGO layer with no growth during thermal cycling is considered. The thermomechanical properties of the materials used are presented in Table 1.

Table 1. Material properties used for the simulations.

Material	T, [°C]	ρ, [kg/m^3]	CTE 10^{-6}, [mm/mm]	E, [GPa]	*v*
GDZ	25	6320	8.65+0.00285T (80-1100°C)	91.6	0.323
	400				
	800				
	1000				
YSZ	25	5960	10.53+0.001T (100-1100°C)	50	0.2
	400	-			
	800	-			
	1000	-			
Bond Coat	25	7380	9.848 + 0.013T-0.000007T^2 (50-600°C)	250	0.3
	200			220	
	400			200	
	600	-		180	
	700	-		165	
	800	-		155	
	1000	7030		120	
TGO	25	3984	6.7596+0,0022T (300-900°C)	380	0.23
	300	-		-	-
	600	-		350	0.23
	800	-		340	0.25
	900	-		-	-
	1000	3868		315	0.25
Inconel 617	20	8360	-		
	25		11.6	211	0.3
	400		13.6	188	
	800		15.4	149	
	1000		16.3		

Global models

As depicted in Figure 1 a-c, the area of the TBC under study for the global models is a square section with dimensions of 0.9 x 0.9 mm with a total height of 10.61 mm for the YSZ models and 10.66 mm for the YSZ+GDZ models. These dimensions are kept constants for all models. To enhance computational efficiency, global models employ a coarse mesh to capture stress and strain deformation data for the entire TBC. Although the mesh is coarse, the number of elements is significantly large to assure the efficacy of the results.

As described before, in the global models, three types of TBC configurations were studied: Dense YSZ, YSZ+DVC, and YSZ-GDZ +DVC models. The DVC is represented by a hexagonal honeycomb (HC) pattern characterized by the length of the hexagon side *a* (Figure 1d), the separations between pillars b (Figure 1d), and the length of the vertical cracks (Figure 1j). The size of the honeycomb is studied for the YSZ-GDZ +DVC model varying the hexagon size (S*)* between 50, 100, and 150 µm with a consistent pillar separation of 8 µm. The study of the effect of the separation between pillars was conducted varying the separation (*w)* between 4, 8, and 12 µm, with a hexagon side of 50 µm.

Mesoscale models

The mesoscale models are extracted from the DVC global models of YSZ and YSZ-GDZ, by keeping seven honeycombs with hexagon sides of *(S)* 100 µm and separation *(w)* of 8 µm (Figure 1e and f). The seven honeycombs are extracted from the center of the global model to avoid edge effects. These sub models get the parameters of strain and stress of the deleted parts of the global models by imposition of boundary conditions. The mesh is refined by reducing the size of elements allowing them to capture the complex geometry of the material layers. The reduction of computational efforts allows these models to explore the effect of a variable DVC depth (length of vertical crack) to be 45, 47, and 49 µm.

Microscale models

At the microscale, the TBC geometry undergoes further reduction until it achieves a surface square section of 60x60 µm (Figure 1 g,h,i), forming new sub-models for all configurations. As the interface between materials is shaped by a sinusoidal surface, the microscale model comprises of four valleys (four corners) and one peak after the reduction process. A significant advantage of these sub-models is their capability to incorporate microstructural defects, such as pores and cracks, with a moderate increase in computational demands. Numerous models were analyzed with varying levels of porosity: 0%, 10%, 20%, and 30% in the cross-sectional area, of the YSZ material of YSZ dense and both DVC models near the TGO interface, Figures 1h and i, respectively.

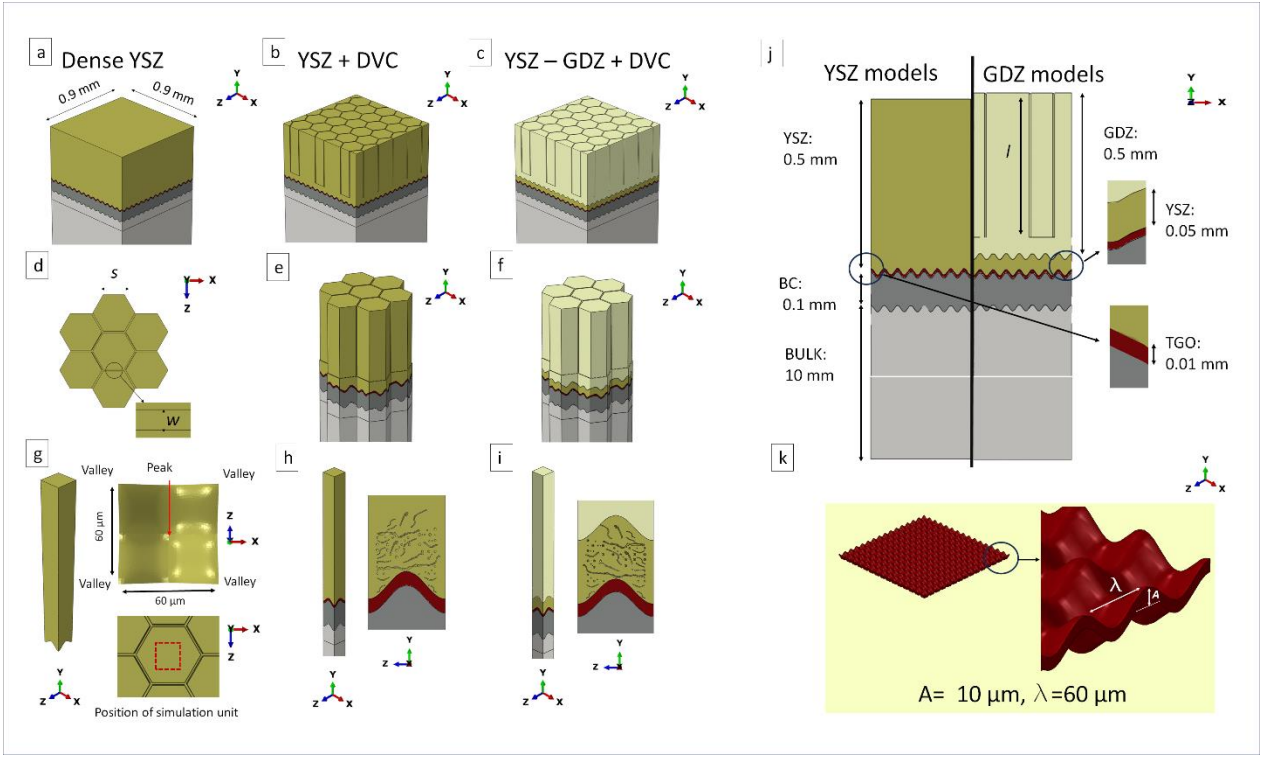

Figure 1. Comprehensive 3D Models employed in the Study. a) Representation of the Dense Yttria-Stabilized Zirconia (YSZ) Model. b) Composite Model Integrating YSZ and Dense Vertically cracked (DVC) characteristics. c) Multilayered TBC including YSZ with GDZ in a DVC structure. d) Schematic detailing the Honeycomb-like Structure, with emphasis on the side parameter and interspace between honeycombs-top view. e) 3D model depicting the sub-model honeycomb structure for YSZ+DVC. f) 3D model exhibiting the sub-model honeycomb structure utilizing YSZ - GDZ +DVC. g) extracted DVC pillar from the central region of the honeycomb unit, presented in 3D, bottom view -one peak of the roughness at the center and four valleys at the corners. h) Three-dimensional pillar representation of YSZ +DVC, encompassing defects (pores, and cracks). i) Three-dimensional pillar representation of YSZ-GDZ +DVC displaying the multilayered encompassing defects (pores, and cracks). j) Cross-sectional view of the model presenting major dimensions of TBC model using YSZ and multilayer YSZ-GDZ. It includes the thickness of substrate, bond coat, TGO, and ceramic TBC. k) Sinusoidal profile used at the interfaces. For exemplification, the TGO is presented to describe the wavelength (lambda) and the amplitude (A)

Assembling process: boundary conditions, and meshing operations

Once the different layers are geometrically in contact, the interaction is defined as a “tie constraint”. This is useful as the two surfaces may have dissimilar meshes varying in size and/or type of elements. The formulation of tie surfaces requires the selection of a master and slave surface. The master surface controls the development of contact forces, while the slave surface adapts to the forces imposed by the master, adjusting its shape and position. Here, the stiffer material is declared as the master surface[27,28].

The boundary conditions vary subtly between global- and sub-models. In global models, the boundary condition is defined in the bottom surface of the Inconel 617 as an ENCASTRE condition which assures the

displacement and rotations (about x, y, z axes) to be zero. In the case of sub models, the same ENCASTRE condition is applied to the bottom surface of the entire geometry and the strain developed in the removed sections is imposed as boundary condition in the cut surfaces of the model (node-based sub modeling).

The meshing operations (element type, geometric order, and size) played a key role in ensuring good convergence and attaining reliable results. In the global models, a relatively coarse mesh is employed to conserve computational resources; however, it is sufficiently fine to capture the shapes of different material layers and their stress-strain behavior under thermal loads with element types that exhibits a favorable convergence rate under the imposed tie constraints. In the global models, the YSZ section adjacent to the TGO-YSZ interface is meshed with quadratic tetrahedral elements (C3D10) at an approximate element size of 20 to 50 µm, while the remaining YSZ section uses second-order quadratic brick elements (C3D20R) with an element size of about 24 µm. For YSZ + DVC models, the DVC section is meshed with C3D20R elements, each fixed at 50 µm. In YSZ-GDZ+DVC models, both the dense YSZ and GDZ sections use C3D10 elements (20 to 50 µm), while the GDZ+DVC section is meshed with C3D20R elements at a consistent size of 60 µm. Mesh refinement is applied in sub-models to accommodate reduced geometry sizes without compromising computational efficiency. In mesoscale models, C3D10 elements (10 to 50 µm) mesh YSZ and GDZ structures, while DVC structures use 20 µm C3D20R elements. In microscale models, C3D10 elements (1 to 5 µm) mesh the entire YSZ and GDZ structures.

Thermal loading

Thermal loading in global models and sub-models is applied using predefined fields. The simulations are structured into four consecutive time steps: initial, heating, holding, and cooling. In the initial step, the temperature field is set at 298 K and remains constant throughout the entire geometry. During the heating step, the temperature starts at 298 K and increases linearly to 1273 K over a five-minute interval. Subsequently, the holding step begins, maintaining the temperature at 1273 K for 120 minutes. Finally, in the cooling step, the temperature decreases linearly from 1273 K to 298 K in five minutes. It is noteworthy that the temperature in each time increment of each step is uniform throughout the entire geometry as isothermal.

Modeling of microstructural defects by polishing, imaging, image analysis, and CAD

To obtain the most representative microstructural defects and add them to the microscale models, a YSZ sample was carefully polished to obtain micrographs at several subsequent depths with known distance. Following ASTM E 1920-03 Method-[29], the metallographic guide for TS coatings, a polishing procedure was developed to achieve an optimum surface and eliminate imperfections. YSZ samples were mounted on epoxy resin and polished following best practices[30]. The grinding process was performed with a semi-automatic polisher, using 120, 240, 320, 400, and 600 grit sandpaper. Once the grinding process was finished, the polishing process continued using cloths of 9, 3 and 1 µm diamond solutions. The parameters used in the grinding and polishing of the samples can be seen in Table 2.

Table 2. Description of the procedure for sample preparation of YSZ coating for grinding and fine polishing. The depth-controlled polishing procedure allows to obtain images at known depths to reconstruct the defect microstructure in three dimensions.

Grinding and Polishing					
Surface	**Coolant/lubricant**	**Abrasive size/type**	**Time [min]**	**Force [N]**	**Surface speed [rpm]**
Abrasive paper	Water	120-240-320-400-600 grit	5	20	300
Soft cloth	Water-based suspension	9 µm-3 µm-1 µm diamond	5	20	300
Depth Controlled Polishing					
Surface	**Coolant/lubricant**	**Abrasive size/type**	**Time [min]**	**Force [N]**	**Surface speed [rpm]**
Soft cloth	Water-based suspension	3 µm-1 µm diamond	5	20	300

Each sample was indented three times on its polished surface using a Vickers hardness tester (Wilson Hardness Vickers 432 SVD) instrumented with a diamond indenter using a HV0.5 kg load, to obtain a reference of position and depth of the studied area. Then, the sample is coated by sputtering with a 4 nm layer of gold for SEM observation (JEOL LT300). The Vickers indentation mark is used to align subsequent photos, measure the depth of polishing, and trace the shape and size of defects identified in the images.

Once the first photo is taken, the polishing process is repeated using the soft cloths of 3 and 1 µm diamond water-based suspensions. A new photo is taken at a new depth which is estimated as one seventh of the average diagonals (depth = diagonal averages/7). The picture's depth changes between 5 µm and 10 µm. The SEM photos are aligned using the Vickers mark using ImageJ software, and a thresholding adjustment converting the photographs into an 8-bit -black and white- image to eliminate the background. This procedure is observed in Figure 2.

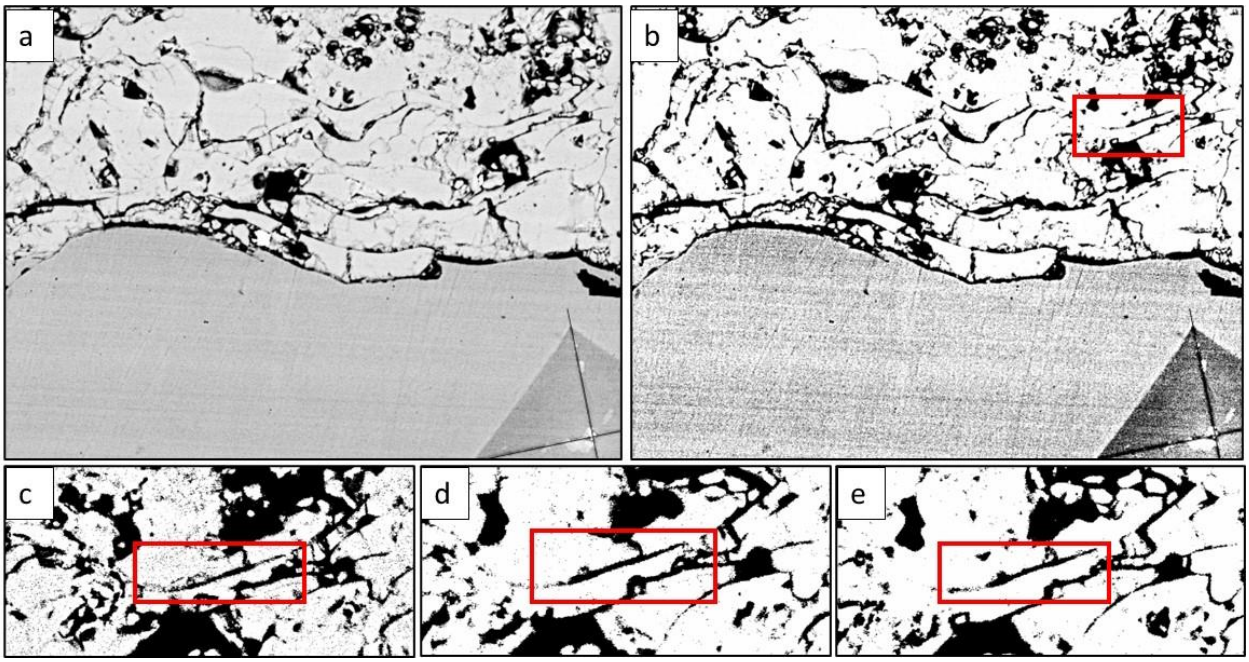

Figure 2. Microstructural defect analysis in TBC. a) Yttria-Stabilized Zirconia (YSZ) coating deposited via Air Plasma Spraying (APS), featuring a Vickers indentation in the bottom right corner. b) Image analysis of micrograph a) in black-and-white. c) Selection of a specific defect for detailed analysis and tracking. d) Image corresponding to the same defect as depicted in c), captured at a different depth. e) Image corresponding to the same defect as depicted in c) and d), captured at a different depth. Tracking of these defects (c, d, e) is facilitated by monitoring the positional changes and alterations in size of the Vickers indentation.

Defects of interest are isolated in the black&white images and traced using Autodesk AutoCAD. Several images of various individual defects were aligned at different depths on planes to be joined, creating a transitional shape between all the sketches in Autodesk Inventor. A solid of the defect is obtained in a 3D model. The procedure is illustrated in Figure 3 presenting 3 images out of the 8 used to reconstruct the crack.

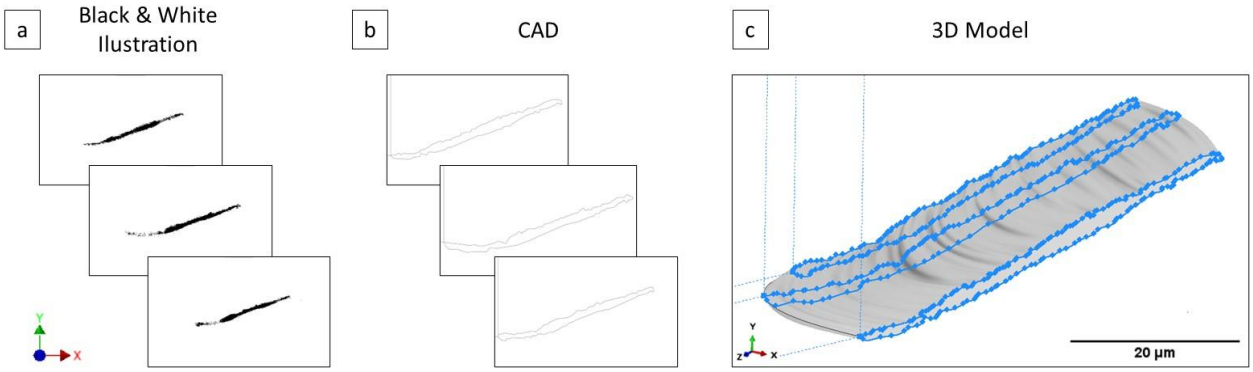

Figure 3. Horizontal crack reconstruction from eight images at varied depths. a) Illustration of three segmented images depicting the process of extracting the horizontal crack of interest. b) Computer-aided design (CAD) representation demonstrating the tracing of the defect on the tested images in a), and c) 3D model portraying the horizontal crack, offering a comprehensive visualization of its structural characteristics.

RESULTS

Modeling results in Global Models

In the 3D modeling of the TBC-YSZ dense structure, pronounced stress concentrations emerge near the TGO interface. Figure 4 illustrates highly compressive S22 stresses in the valleys of the TGO-YSZ interface, with lower residual stresses in the upper TBC towards the surface at the end of the cooling cycle. Notably, edge effects manifest due to computational constraints limiting the modeled section's size. Increased stresses are observed near edges and the center of the squared volume, particularly evident in the YSZ dense TBC. As depicted in Figure 4, contrastingly, DVC structures show reduced edge effects, thanks to vertical cracks accommodating stresses.

Figure 4 showcases cross-sectional views of three TBC models, each halved for clarity. These include a dense YSZ structure, a DVC YSZ, and a DVC YSZ-GDZ. Significantly, the stresses at the end of the cooling phase, specifically S22, play a pivotal role in the TGO-YSZ interface failure. Additionally, attention is directed towards the in-plane stresses, S11, crucial for understanding interactions with vertically oriented cracks, particularly in the case of DVC configurations. The accompanying presentation in Figure 4 also details the system's stored strain energy (shown as ESEDEN by Abaqus).

The typical behavior observed at the TGO interface of TBCs reveals high compressive stresses in the valleys and elevated tensile stresses at the peaks. This consistent pattern is evident across all three tested models. Notably, the cut representation emphasizes the lower valleys, with peaks appropriately offset to account for the profile amplitude. In the case of S11 stresses, concentrations manifest at the ends of vertical cracks, interacting with the stress profile produced by the interface. This interaction is observed at the TGO-TBC and YSZ-GDZ interfaces in the multilayer TBC. Regarding strain energy, the dense YSZ case concentrates energy closely to the TGO interface. Comparatively, the YSZ+DVC structure exhibits similar energy concentration values but in a larger volume, while the multilayer YSZ-GDZ structure displays lower magnitudes of strains near the TGO interface. The comprehensive assessment of stresses and energy highlights the multilayer YSZ-GDZ TBC structure as the optimal condition, with lower strain energy and a more evenly distributed high magnitude of stresses in larger volumes.

The magnitude of S22 in-plane stress spans from +80 to -300 MPa, while S11 stresses range from +100 to -280 MPa. Notably, both stress ranges fall within the bounds extensively assessed, measured, and reported in the literature[2,5,24]. In terms of strain energy, the maximum recorded value falls within the range of 2-7 MJ per cubic meter. It's important to highlight the use of the honeycomb-like structure of the DVC, with a lateral length (s) of 100 µm, reflecting the typical microstructures of DVCs. Additionally, the fixed width of the vertical crack (w) at 8 µm mirrors the actual sizes observed in microstructures. This attention to detail ensures a realistic representation of the studied structures.

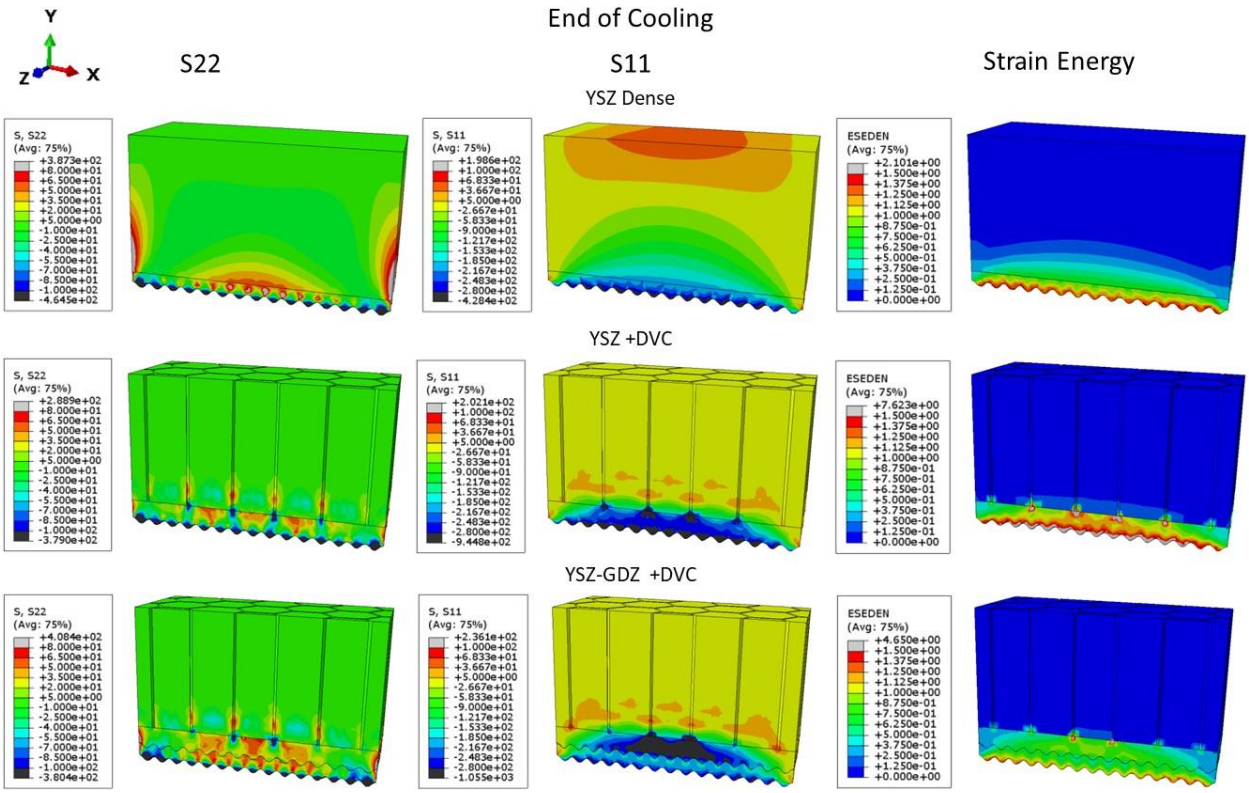

Figure 4: Stress analysis in global models post-cooling. Results showcase stress conditions at the end of the cooling phase. The original models are bisected to highlight stresses (S22, S11 – in MPa) and strain energy (ESEDEN by ABAQUS -in mJ/mm^3). The examined models encompass YSZ-Dense, YSZ+DVC, and YSZ-GDZ+DVC, the latest employ honeycombs with parameter *s* =100 µm, and spacing *w* = 8 µm in the DVC structures.

Figure 5 offers a bottom view of the TBCs, providing insight into the area in direct contact with the TGO. This perspective reveals compressive residual stresses in the valleys and tensile residual stresses at the peaks in S22. In the DVC structures, the bottom view illustrates the projection of the honeycomb-like structure, emphasizing its arrangement. Comparatively, the YSZ dense structure exhibits higher tensile stresses than the DVC-like structures, with the multilayer structure displaying the lowest S22 stresses. While the honeycomb-like structure does not notably reduce stresses in the TGO-TBC interface, a lower number of high tensile positions is recognized for the DVC coatings, especially for YSZ+DVC. Nonetheless, it's crucial to acknowledge that the honeycomb-like structure contributes to mitigating maximum tensile stresses.

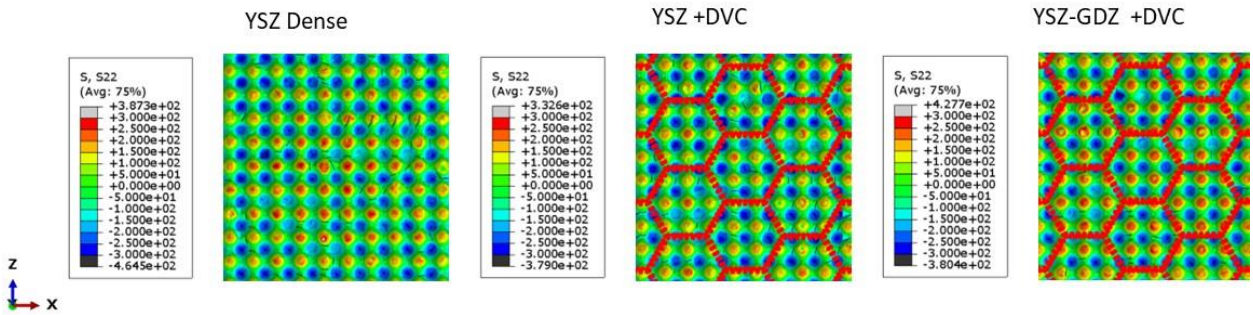

Figure 5. S22-Stresses in the YSZ -bottom view (in the YSZ-TGO interface) in post-cooling global models. The analyzed models include YSZ-Dense, YSZ+DVC, and YSZ-GDZ+DVC, with a specific focus on the latter to assess the impact of honeycombs on the stress distribution (honeycombs are projected on the interface).

During heating, tensile stress develops in the TBC until the bond coat yields at a certain temperature. Once this step is reached, a steady state ensues, maintaining stresses unchanged until the initiation of cooling, which elevates stresses to their maximum values near room temperature. Regarding S22 stress, it becomes highly tensile at the peak of the interface profile, increasing slightly at the cooling's onset, while the valley experiences low tensile stresses during heating that revert at yielding to a compressive steady state, reaching maximum compressive stress during cooling. Conversely, for S11 orientation, stresses shift slightly towards tensile until the bond coat yields, transitioning to a compressive state. During cooling, both peak and valley residual stresses shift to a compressive condition. Figure 6 illustrates these dynamics across positions 1 through 4, representing different depths through the middle of the peak, and position 5 extracted from the slightly offset valley. Stress maps in Figure 6 provide instantaneous readings at the end of the cooling stage for S11 and S22 stresses. These insights of the evolution of the stress with temperature are derived from the YSZ-TBC dense model and align with similar simulations conducted in 2D. Stresses in position 1-3 are often of negligible values. The edge-effects in these systems overestimate the stresses in points 1 and 3.

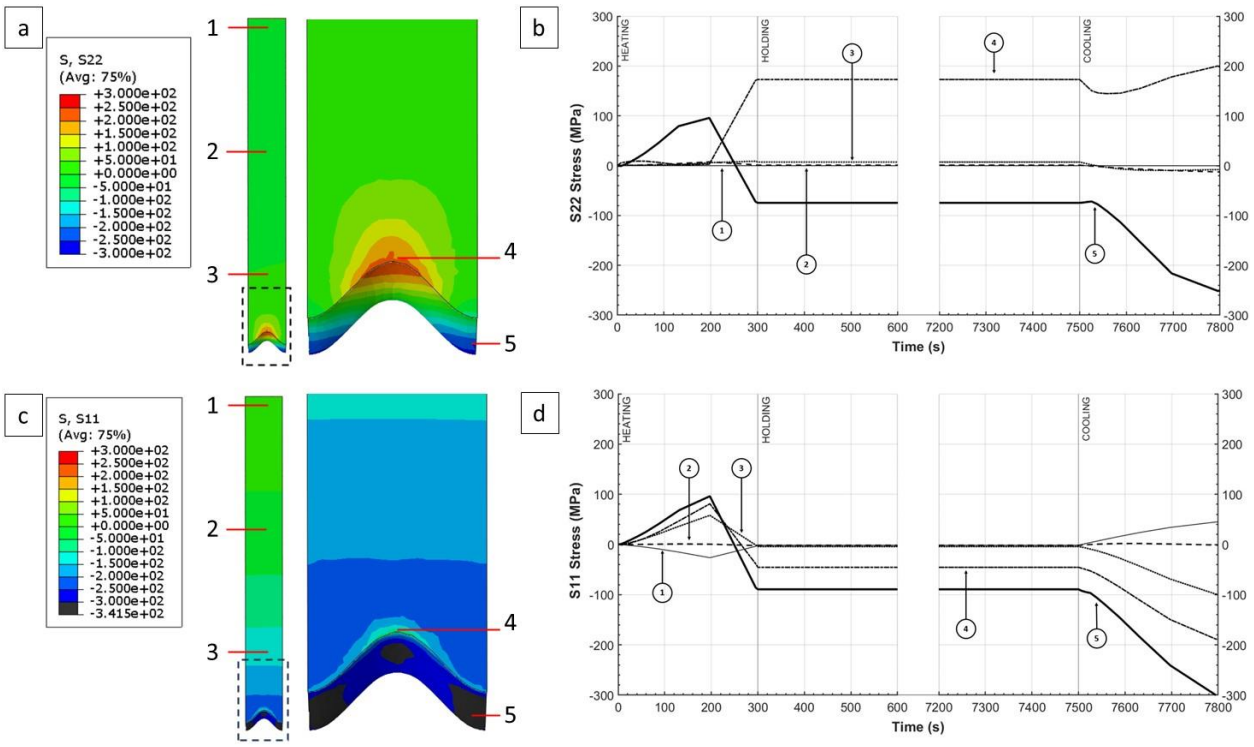

Figure 6: Stress analysis in various cross-sectional positions of dense YSZ global model TBC. a) Positions designated for S22 stress analysis, at the end of cooling. b) Temporal evolution of S22 stress across the stages of heating, holding, and cooling for designated positions 1 through 5. c) Positions designated for S11 stress analysis, at the end of cooling. d) Temporal evolution of S11 stresses across the stages of heating, holding, and cooling for designated positions 1 through 5.

Study of the honeycomb structure: size of the isles and width of vertical cracks

Vertically cracked structures in TBCs exhibit varying isles sizes determined by plasma spraying process parameters. Figure 7 explores the impact of isle size in global models. In Figures 7a, 50 µm, 100 µm, and 150 µm define honeycomb-like structures with different size parameters (the number represent the side length) for observation at various depths. Stress fields are analyzed at the edges of honeycomb-like isles, where deformation is not confined, in column 1. In column 2, stresses are presented within the aisles, showing larger S22 stresses for smaller isles. This is likely due to the need to accommodate thermal mismatch expansion deformation in a more confined space. In columns 1 and 2, stresses reveal significantly higher residual stresses at the isle edges as deformation is allowed here, contrasting with reduced stresses within the isles.

In Figure 7b, a noteworthy surge in S11 stresses is observed near the crack tips and edges. This increase significantly impacts the stress magnitude in the GDZ dense zone and the YSZ-GDZ interface. The concentration of stresses around the crack tips and edges underscores the critical influence of structural features on stress distribution, particularly in the GDZ dense zone and the interface with YSZ, revealing key areas of concern for potential failure mechanisms.

The horizontal view of S22 (Figure 7a, column 3) reveals a distinct pattern: in smaller isles -mud crack structures, tensile stresses intensify towards the center of the island. On the other hand, the horizontal view of S22 (Figure 7b, column 3) exhibits compressive stress concentration in the crack tips, and smaller isles present more area of crack tip. This observation highlights the nuanced relationship between island size and stress distribution in the context of mud crack structures, providing valuable insights for understanding and optimizing structural performance.

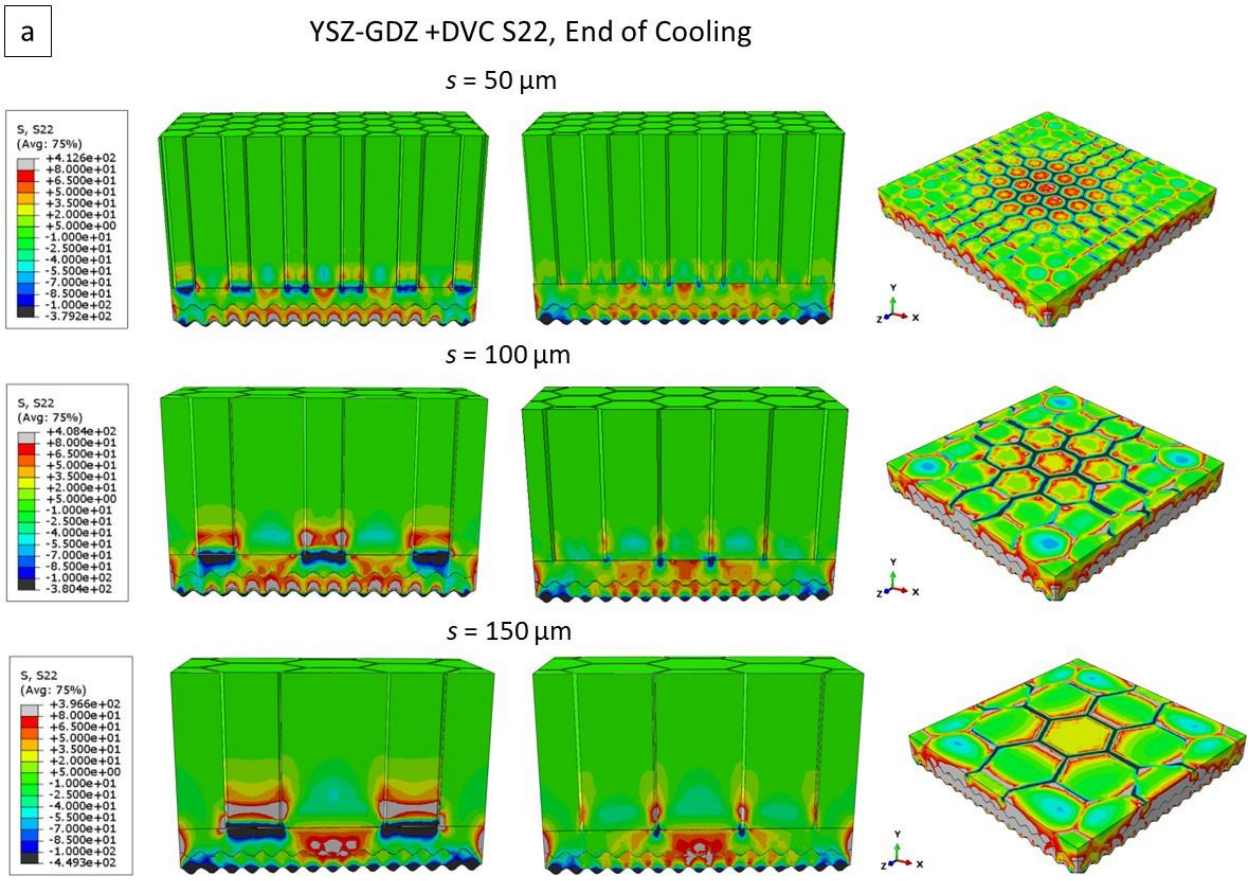

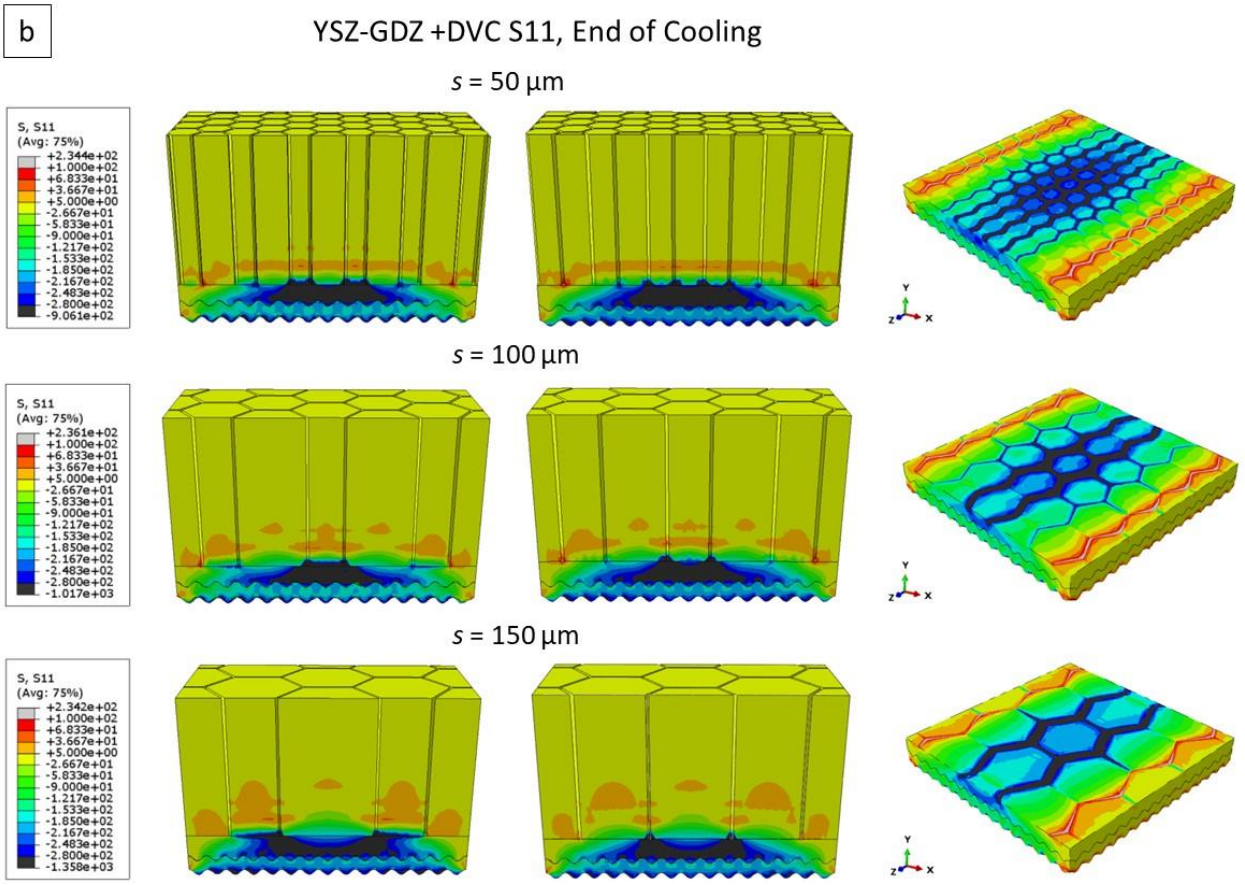

Figure 7. Stress analysis in global models of multilayer YSZ-GDZ+ DVC with honeycomb-like structures. Results depict stress conditions at the end of the cooling phase for models featuring honeycomb structures of varying parameters. Original models are dissected to emphasize a) S22- and b) S11-stresses at two distinct distances: firstly, at the edge of a side of the honeycomb, and secondly, across the entire honeycomb structure. Horizontal views are presented at a depth corresponding to the end of the vertical crack. The honeycomb parameter (*s*) (side of the hexagon) is systematically modified from 50 to 100 and 150 µm, while the spacing (*w*) is held constant at 8 µm.

Examining the TGO-TBC interface from the bottom in Figure 8, incorporating an overlapped projection of the mud crack structure reveals a discernible pattern. Larger honeycomb structures exhibit increased tensile stresses at the peaks of the profile. Conversely, smaller islands within the mud crack structure result in reduced stresses within the islands, specifically in S22 at the peaks. This reduction in peak stresses is advantageous, suggesting that structures with larger islands tend to approach the characteristics of the dense YSZ structure. This insight is pivotal for understanding the impact of island size on stress distribution at the interface, guiding the optimization of structural configurations.

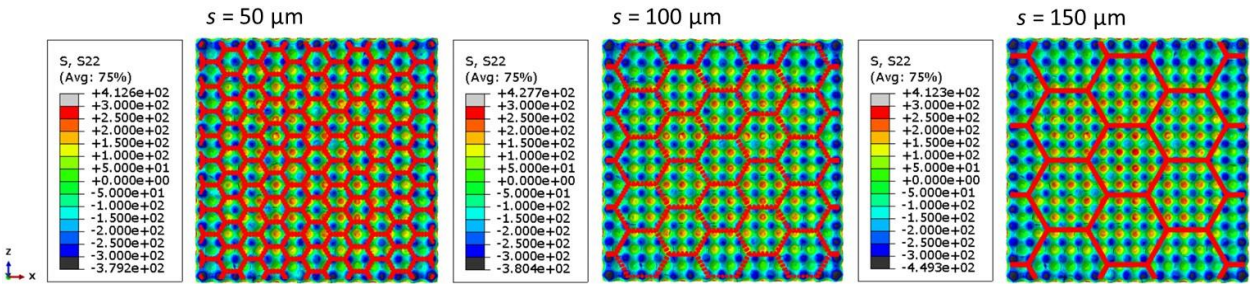

Figure 8. S22-Stresses in the YSZ -bottom view (in the YSZ-TGO interface) in post-cooling global models. The analyzed models include YSZ-GDZ+DVC, with a specific focus on the size of the honeycombs on the stress distribution (honeycombs are projected on the interface). The honeycomb parameter (*s*) (side of the hexagon) is systematically modified from 50 to 100 and 150 µm, while the spacing (*w*) is held constant at 8 µm.

Examining the impact of vertical crack width reveals interesting findings related to increased stress concentration in thinner cracks. Figure 9a demonstrates that reducing the width of the vertical crack results in decreased tensile S22 stresses within the island but increased compressive S22 stresses in the crack tip. On the other hand, the reduction in crack width corresponds with a slight increase in compressive S11 stresses within the islands and a larger increase (more compressive) in the crack tips. All attributed to the concentration of stresses caused by thinner cracks. This study underscores the model's importance in providing representative results, emphasizing the intricate relationship between crack width and stress distribution. Nevertheless, it's essential to acknowledge that in practical applications, the width of cracks may not be easily controlled during production.

It's noteworthy, as it will be depicted in Figure 15, that an element at the tip of the crack experiences tensile stresses during heating until the bond coat yields. With the continuation of the heat cycle, the crack tip undergoes compressive residual stresses in both the S11 and S22 directions. This shift to compressive stresses at the crack tips contributes to a reduction in the effect of failure due to stress concentration. However, it's crucial to emphasize that the width of cracks utilized in FEA plays a pivotal role in defining the magnitude of stresses. In other words, the model is sensitive to the widths of cracks incorporated, emphasizing the need for educated consideration of this parameter in the analysis.

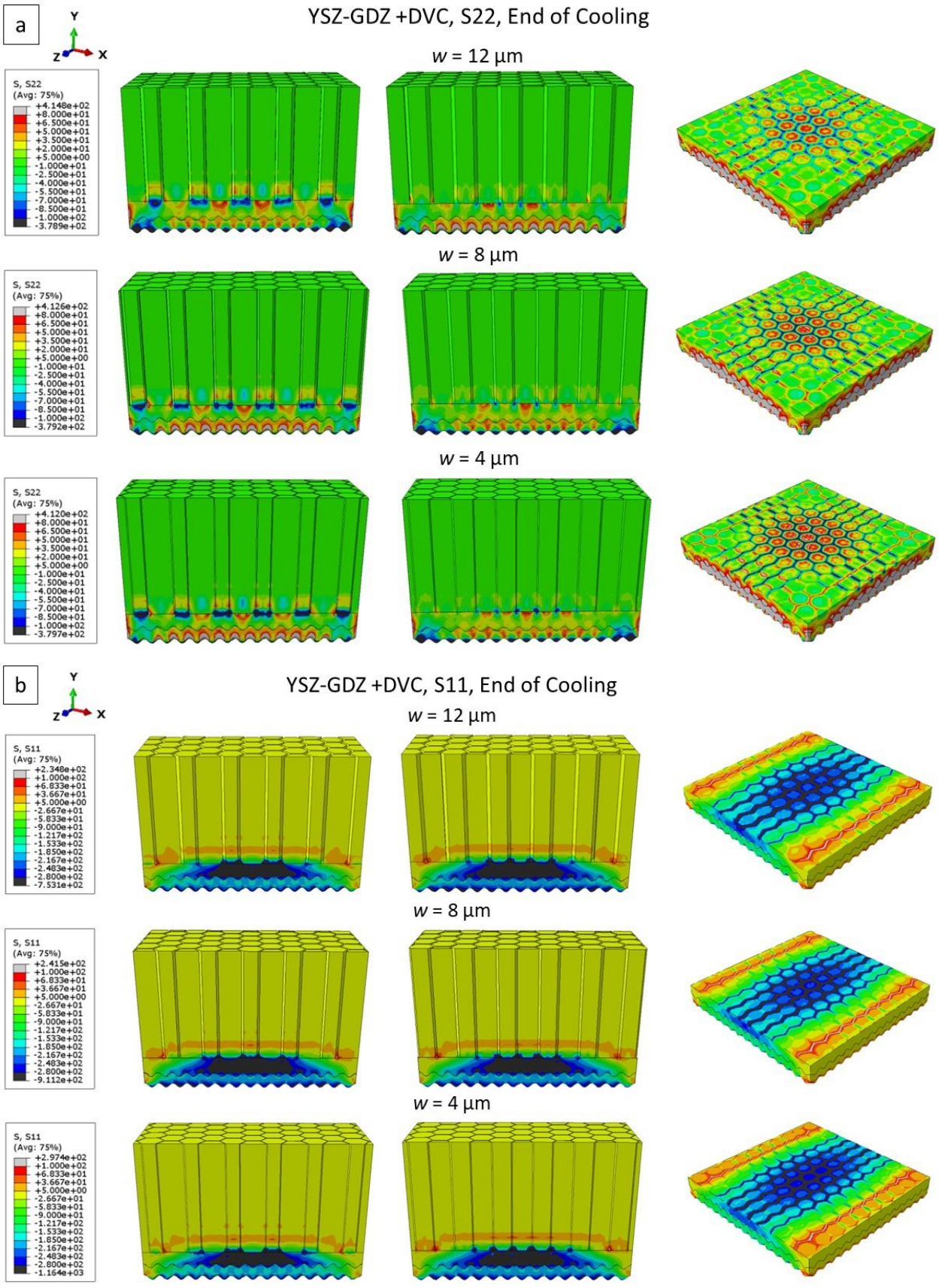

Figure 9. Stress analysis in global models of multilayer YSZ-GDZ+ DVC with honeycomb-like structures. Results depict stress conditions at the end of the cooling phase for models featuring honeycomb structures of varying width parameter of the vertical cracks. Original models are dissected to emphasize a) S22- and b) S11-stresses at two distinct distances: firstly, at the edge of a side of the honeycomb, and secondly, across the entire honeycomb structure. Horizontal views are presented at a depth corresponding to the conclusion of the vertical crack. The honeycomb width parameter (*w*) is systematically modified from 4 to 8 and 12 µm, while the parameter (*s*) is held constant at 100 µm.

Building upon previous observations, the bottom view of the interface in Figure 9 reveals the impact of varying crack widths. Confirming earlier findings, stresses within the islands, particularly S22, increase for thinner cracks. Consequently, the S22 stress at the peaks is elevated when compared to configurations with wider crack spacings. This underscores the intricate relationship between crack width and stress distribution at the interface, emphasizing the need for a nuanced understanding of these parameters for optimizing structural performance.

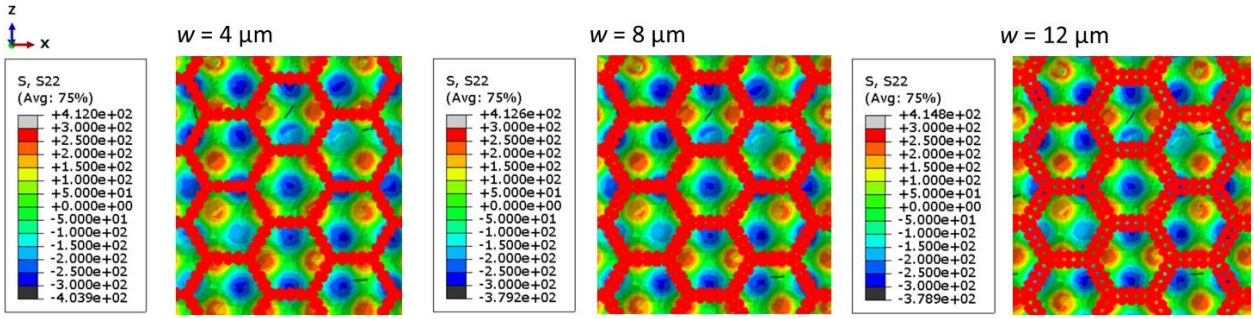

Figure 10. S22-Stresses in the YSZ -bottom view (in the YSZ-TGO interface) in post-cooling global models. The analyzed models include YSZ-GDZ+DVC, with a specific focus on the impact of the width of the vertical cracks on the stress distribution (honeycombs are projected on the interface). The honeycomb width parameter (*w*) is systematically modified from 4 to 8 and 12 µm, while the parameter (*s*) is held constant at 100 µm.

Interaction between vertical crack and roughness – proximity of crack end to the interfaces

Building on the prior discussions, the stress fields within the TBC volume are primarily defined by the TGO-TBC interface and the YSZ-GDZ interfaces, as well as the interaction of vertical cracks. In Figure 11, the proximity of the vertical crack end to the interfaces is investigated for both YSZ and multilayer YSZ-GDZ configurations, modeled with 7 honeycomb units. Notably, as the crack tip approaches the interface, there appears an interaction between the distribution of the stresses at the crack tip and the stresses produced at the profile. So as the crack approaches the interface, the interaction increases the stresses in the surroundings of the isles. In the case of the YSZ-TBC coating, it is observed that as the crack tip approaches the interface with the bond coat, the S22 stresses exhibit an increase, Figura 11a. For the YSZ-GDZ, Figura 11b, as the crack tips approach the YSZ-GDZ interface, similar behavior is observed that S22 stresses increase as the crack tip approaches the interface.

This nuanced analysis sheds light on the intricate relationship between crack positioning and stress distribution within the TBC volume. As the crack tip approaches the interface, a dynamic interaction unfolds between the stress distribution at the crack tip and the stresses generated at the profile. This interaction intensifies stresses in the vicinity of the isles as the crack nears the interface. This insight further underscores the importance of understanding the interplay between crack positioning and interface interactions in influencing stress patterns within the TBC structure.

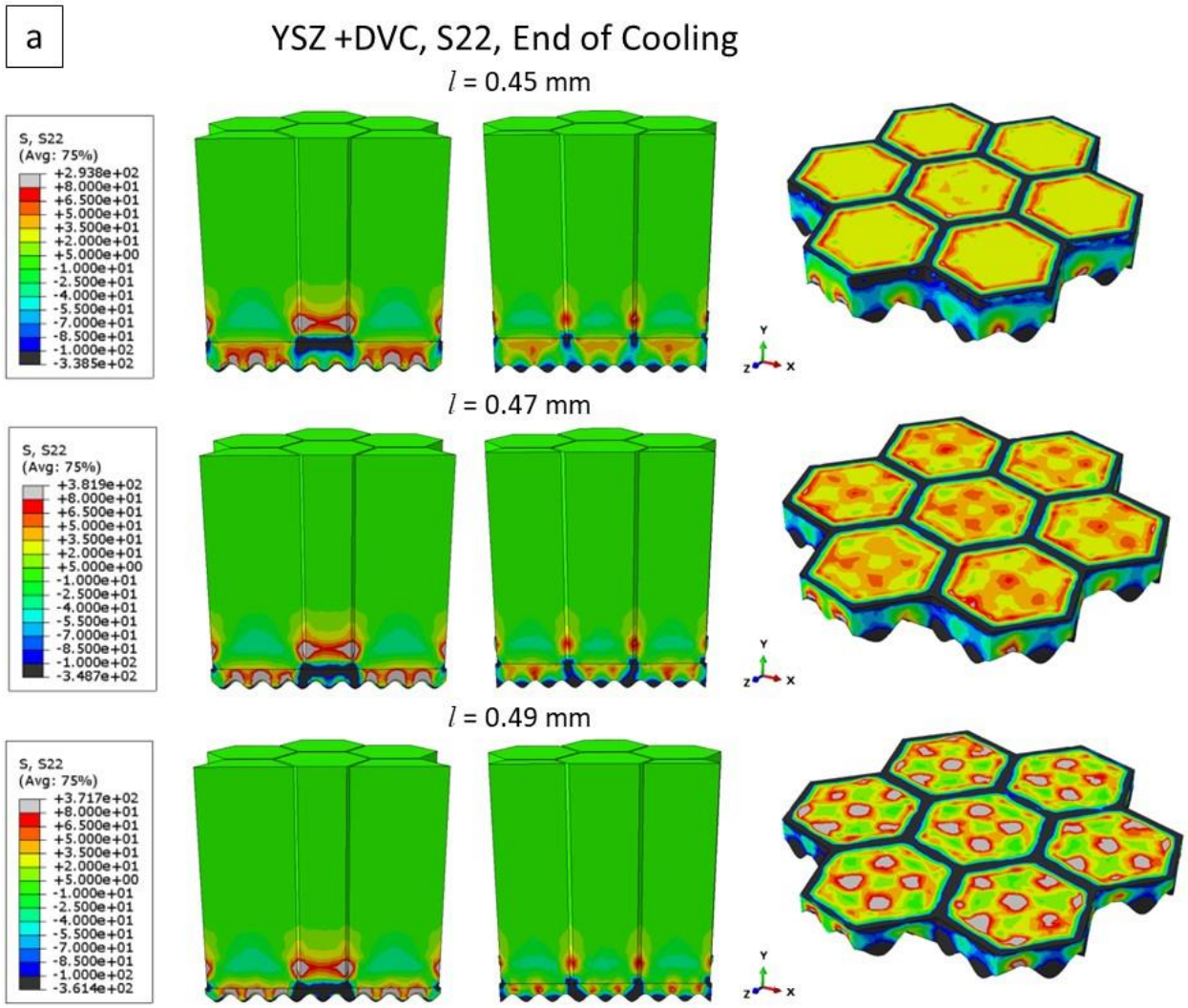

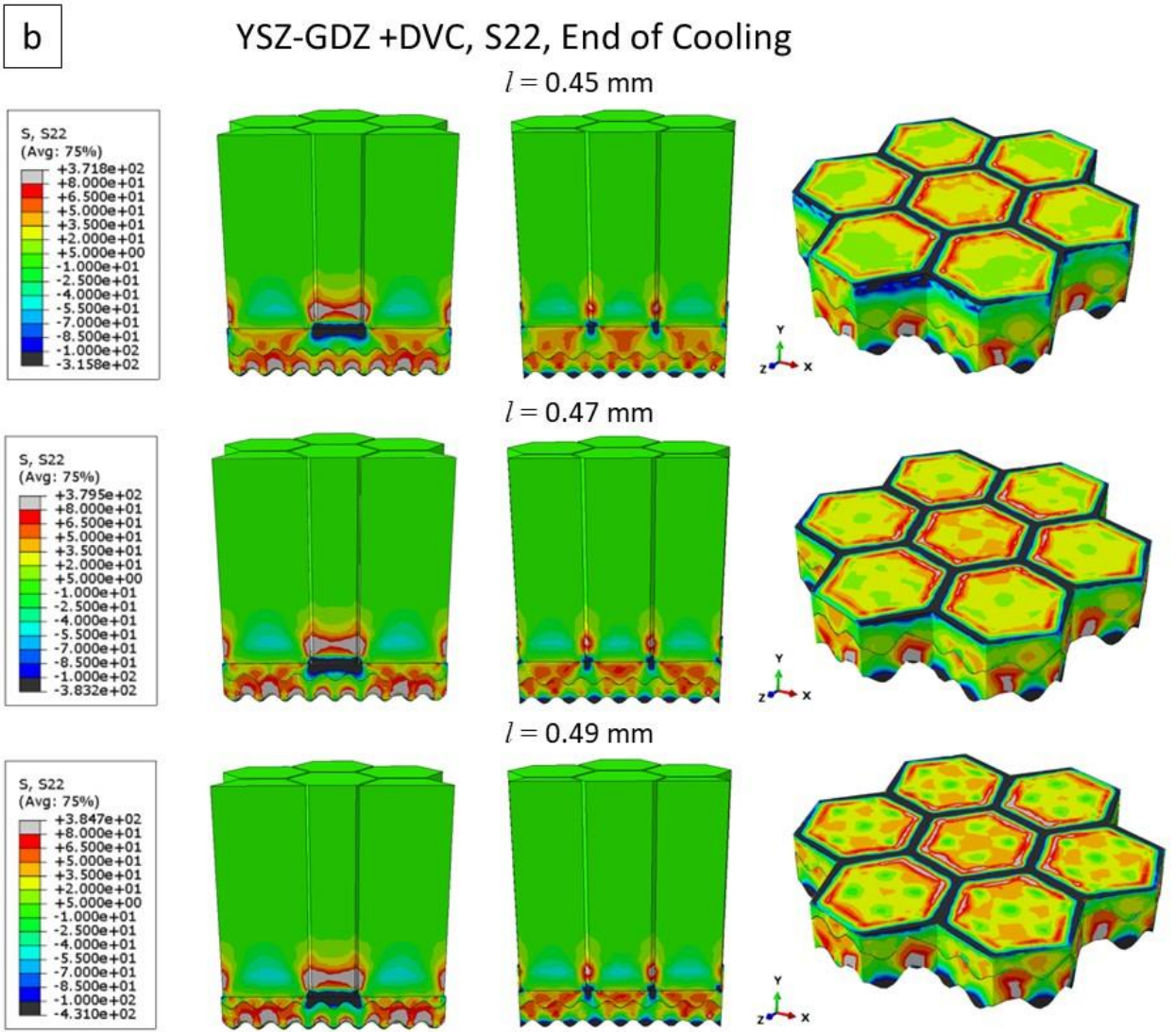

Figure 11. Analysis of stresses varying vertical crack length in mesoscale models of multilayer YSZ-GDZ+ DVC with honeycomb-like structures. Results illustrate stress conditions at the end of the cooling phase for models incorporating honeycomb structures with varying vertical crack length. The original models are sectioned to emphasize a) S22- and b) S11-stresses at two distinct distances: firstly, at the edge of a side of the honeycomb, and secondly, across the entire honeycomb structure. Horizontal views are presented at a depth corresponding to the vertical crack's conclusion. The honeycomb length parameter (*l*) is systematically modified from 0.45 to 0.47 and 0.49 mm, while the parameter (*s*) is held constant at 100 µm, and (*w*) at 8 µm.

Examining the stresses on the interfaces with TGO and between YSZ and GDZ from a bottom view, a consistent pattern emerges, Figure 12. As the crack approaches the interface, the S22 stresses at the peaks amplify for both YSZ and the multilayer YSZ-GDZ at both interfaces. This finding is crucial, highlighting that the interaction of crack tips with interfaces augments stresses at the peaks. In practical terms, this implies it is advantageous to design vertical cracks through processing, that commence farther away from multi-material interfaces. This strategic approach can contribute to optimizing stress distributions within the TBC structure. This strategy has been the one adopted in this paper as developed by Viswanathan et al.[21].

In Figure 12, a comparative analysis is conducted on the proximity of crack tips to the TGO interfaces for both the YSZ-DVC coating and the multi-layer YSZ+GDZ-DVC coating. Although the magnitude of stresses appears similar in both coatings, a notable distinction arises in their effects. Particularly, in the YSZ coating, the impact of proximity is significantly more pronounced as the cracks approach the TGO interface. In contrast, for the multi-layer configuration, where crack tips approach the interface between the two zirconates, the effect over the TGO interface to increase stresses is comparatively smaller. In both cases, the stress range spans from -300 MPa up to +400 MPa, but for the interface between zirconates, stresses range between +180 to about -30 MPa. Regardless, a consistent trend is observed: as the tip of the vertical crack approaches the interface, S22 stresses escalate in magnitude. This trend poses potential challenges for the longevity of the two interfaces, emphasizing the need for careful consideration in designing and managing stress concentrations in these critical regions.

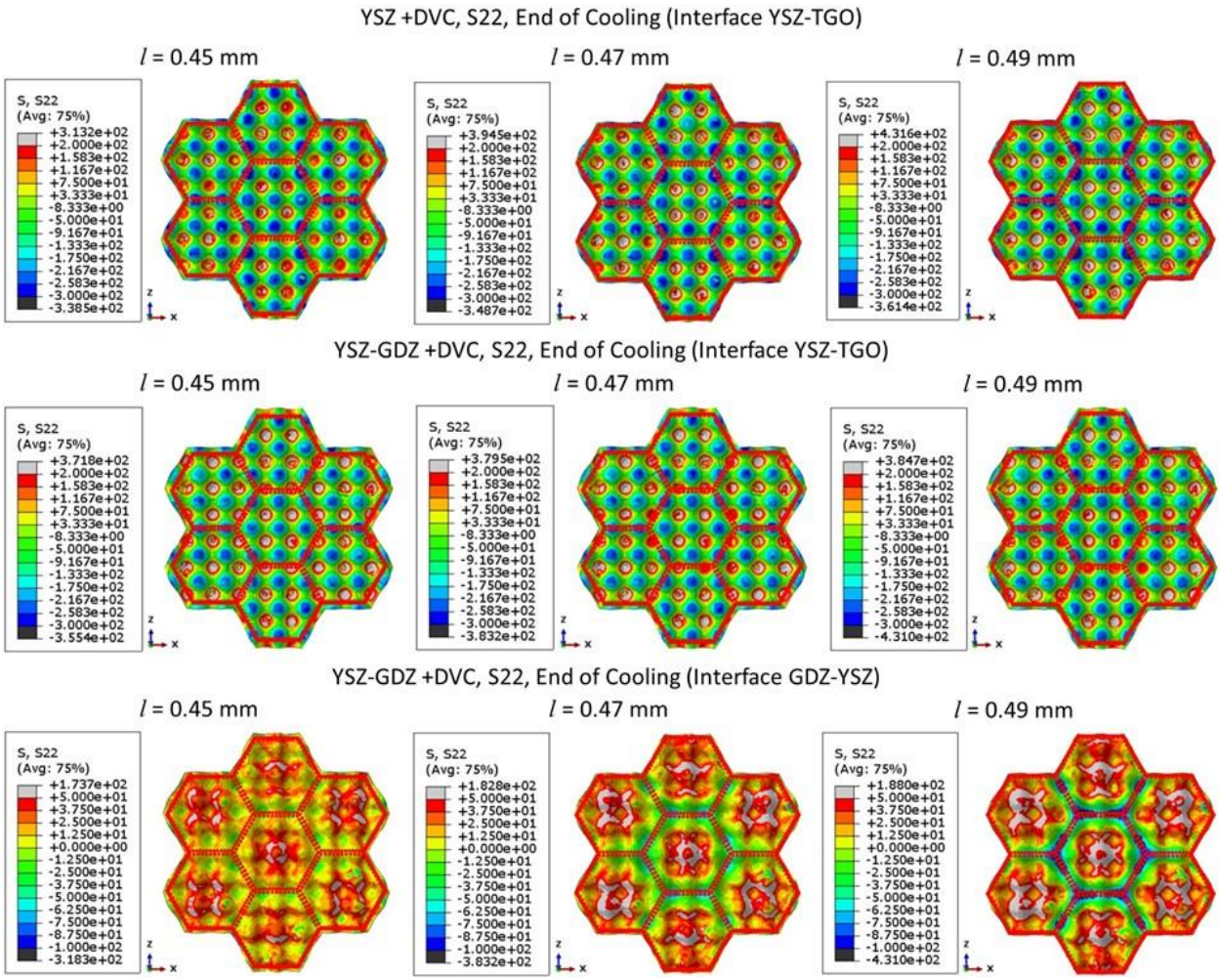

Figure 12. S22-Stresses in the YSZ -bottom view in post-cooling mesoscale models. The analyzed models include YSZ-DVC (in the TGO-YSZ interface), YSZ-GDZ+DVC (in the TGO-YSZ interface), and YSZ-GDZ+DVC (in the YSZ-GDZ interface), with a specific focus on vertical crack's length on the stress distribution (honeycombs are projected on the interface). The honeycomb length parameter (*l*) is systematically modified from 0.45 to 0.47 and 0.49 mm, while the parameter (*s*) is held constant at 100 µm, and (*w*) at 8 µm.

Effect of defect presence with the TBCs (increasing percentage of defects)

To mitigate the substantial computational demands associated with simulating small defects within the microstructure of TBCs, experiments were conducted on a sub-model of minimal dimensions of the YSZ-GDZ. This sub-model incorporates various defects such as cracks and pores, randomly distributed at varying levels. Figure 13 illustrates four distinct outcomes: the first serves as a reference, depicting a unit comprising a peak and four valleys extracted from the center of a honeycomb, devoid of any defects. The subsequent three models exhibit an escalating percentage of defects, namely 10%, 20%, and 30%, providing a comprehensive overview of the impact of defect concentration on the structural characteristics. The evaluation of microstructure defects is performed in micro-models featuring refined meshing to accommodate defect placement. These defects are reconstructed based on the analysis of real defects observed in 2D sequential images, as outlined in the methodology, ensuring an accurate representation of the microstructure in three dimensions. In Figure 13, the consistent location of defects across successive microstructures is maintained until it reaches a 30% defect presence (this 30% is measured in a 2D image section as this is the common metallography practice).

In Figure 13a, the S22 stresses range from approximately +300 MPa to -300 MPa, with the distinctive pattern of high tensile stresses in the peak and high compressive stresses in the valleys of the interface profile. The image depicts the primary half-cut of the unit and the projection of the valleys at the bottom. The introduction of cracks alters the stress distribution, particularly for cracks oriented perpendicular to the out-of-plane direction of S22 stresses. Horizontal cracks and crack tips in this orientation exhibit heightened interaction, causing a redistribution of stresses in the surrounding volume, amplifying their magnitude. For instance, in the 20% and 30% case, a large horizontal crack near the peak significantly alters the stress distribution. As illustrated in Figure 14 (bottom view of the four units), this large crack diminishes S22 stresses around its opening, reducing the occurrence of the highest tensile stress at the center of the peak and displacing it to the sides. Additionally, note the horizontal orientation of crack tips, concentrating significant S22 stresses.

Figure 13b illustrates a similar behavior in S33 stresses (S11 equivalent), showcasing compressive stresses near the TGO interface that transition to tensile stresses as TBC approaches the surface. The introduction of cracks and defects induces a redistribution of stresses within the sections, particularly with vertically running microcracks being influenced by the S33 stress. Interestingly, when observed from the bottom, Figure 14b, the presence of defects, including the large horizontal crack impacting the S22 stresses, does not affect significantly the region of the interface for S33 stresses. The distinct behaviors of S22 and S33 stresses highlight the intricate influence of defects and their location, orientation and percentage, on stress redistribution within the TBC microstructure.

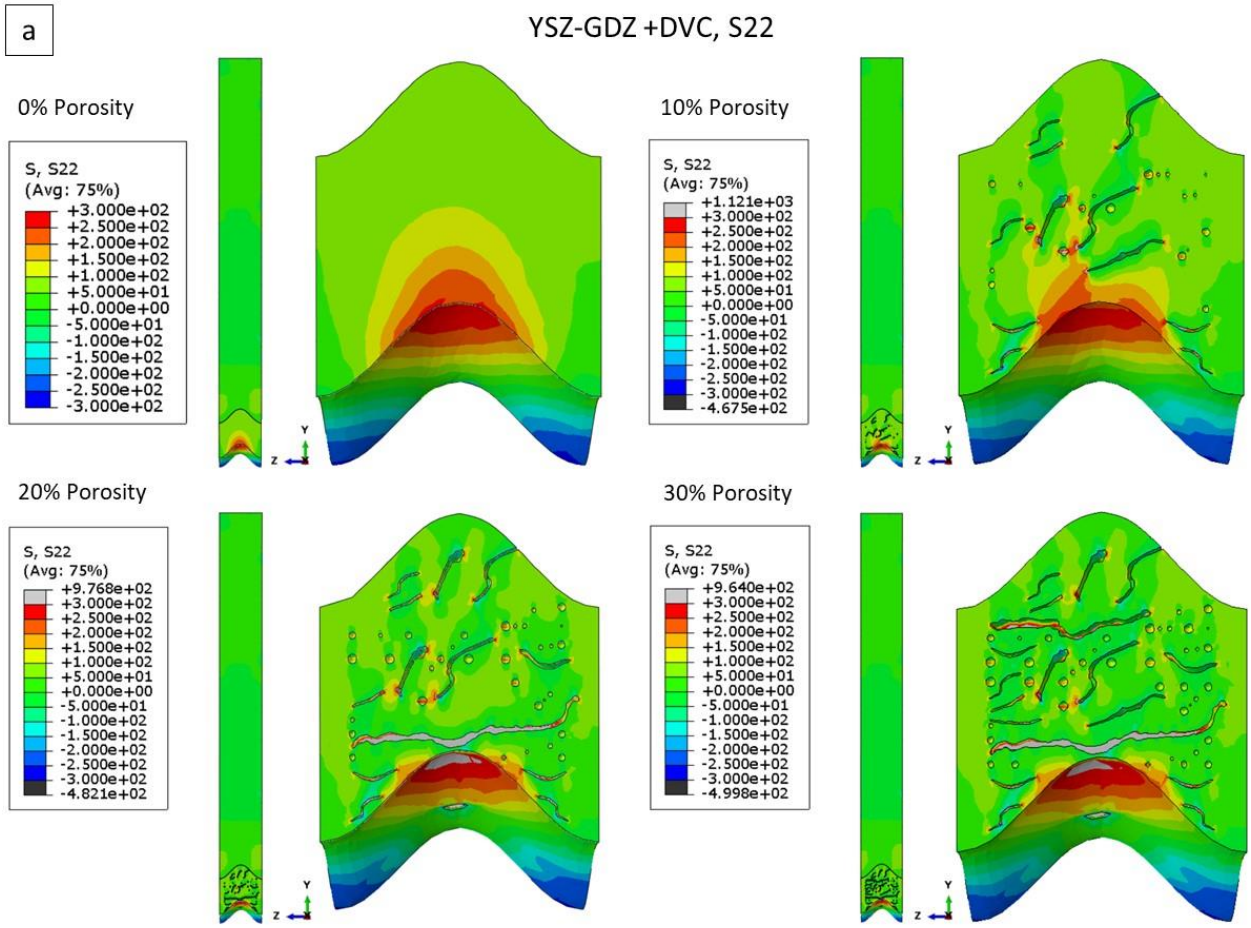

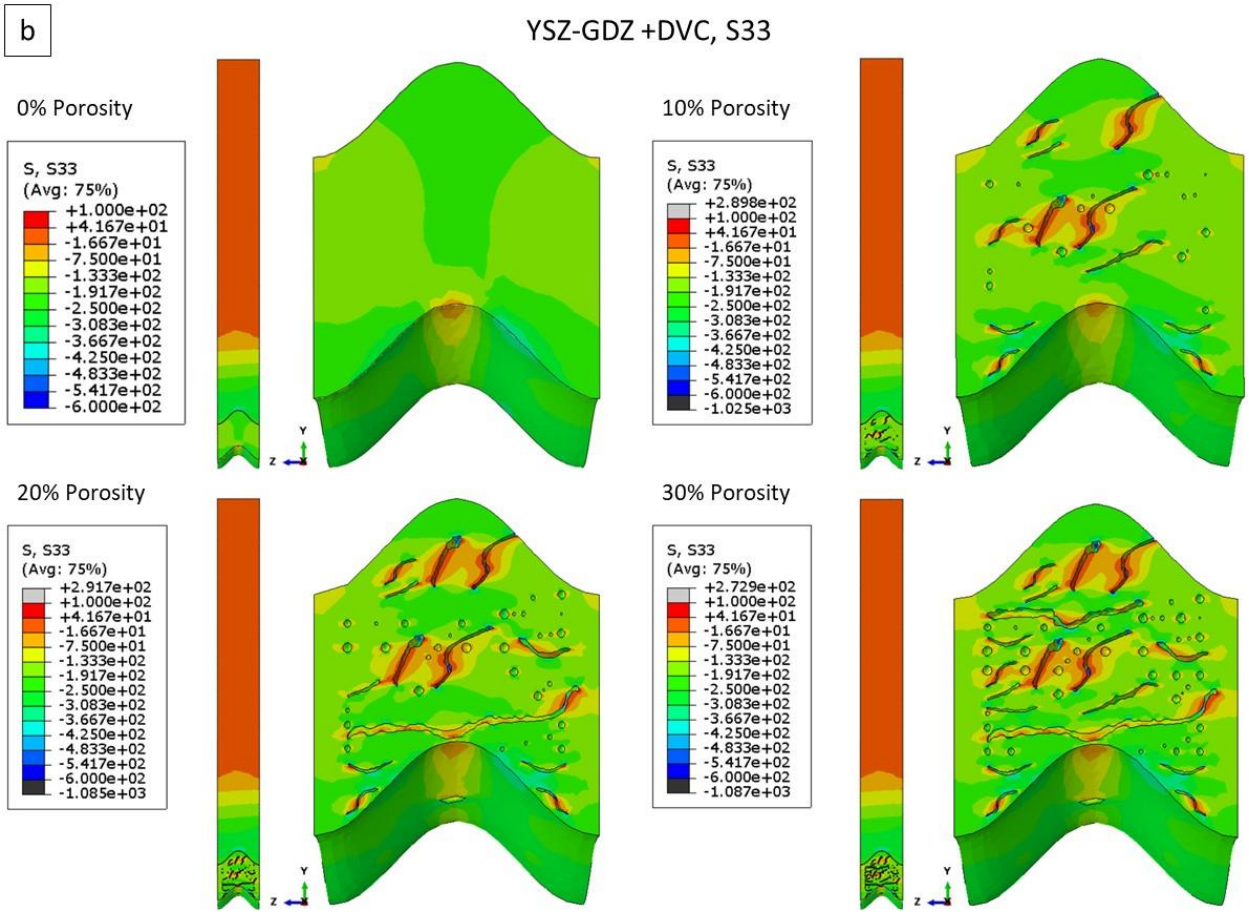

Figure 13. Stresses analysis in microscale models of multilayer YSZ-GDZ+ DVC with varying defect percentage. Results illustrate stress conditions at the end of the cooling phase for models extracted from honeycomb structures with systematically varied percentages of defects (pores and cracks). Original models are partitioned to underscore a) S22- and b) S33-stresses at half the minimal unit, inclusive of a peak and four valleys. Post-cut, the image presents the peak at the top and the projection of two valleys in the bottom corners. The defect percentage is incrementally adjusted from 0 to 10, 20, and 30%. Defects, randomly distributed, are derived from actual microstructures and digitized for insertion into the model, progressively added to enhance model complexity.

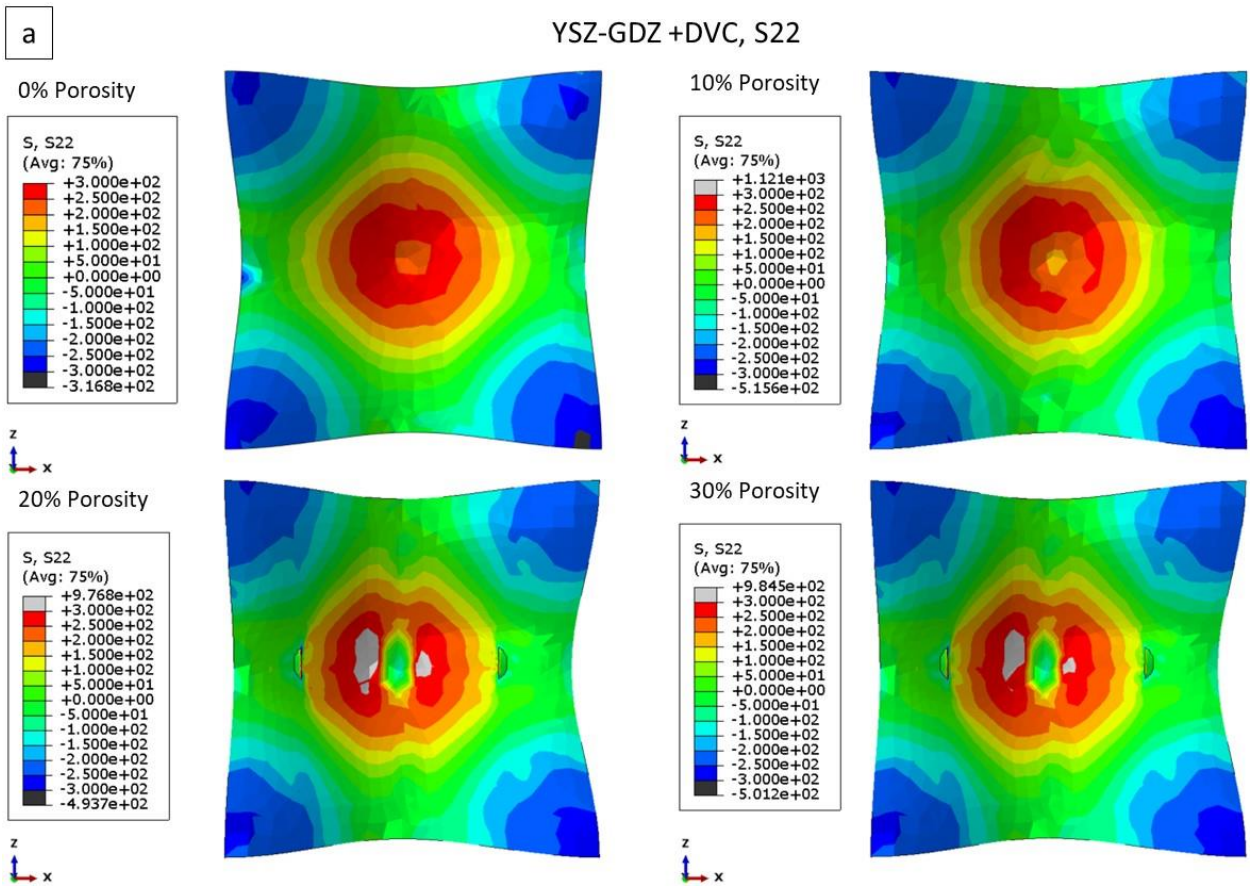

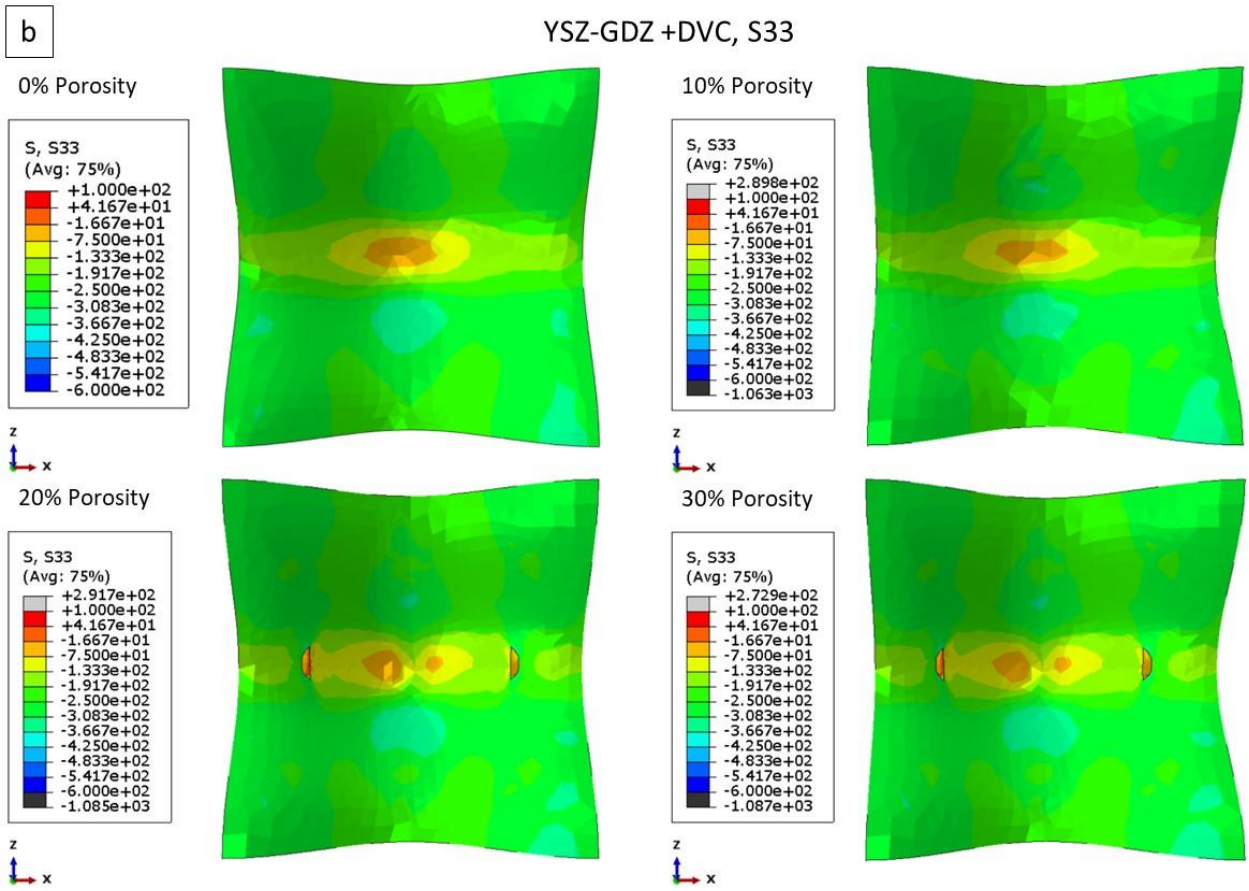

Figure 14. Stresses Analysis in YSZ at the TGO-YSZ interface within microscale models of multilayer YSZ-GDZ+ DVC with varying defect percentage. Results show the stress field from the bottom view at the end of the cooling phase with systematically varied percentages of defects (pores and cracks). Models present a) S22- and b) S33-stresses, inclusive of a peak and four valleys. The defect percentage is incrementally adjusted from 0 to 10, 20, and 30%.

In Figure 15, the analysis akin to Figure 6 is extended, focusing on the evolution of stresses throughout distinct phases: heating, holding, and cooling. However, the emphasis shifts to a detailed examination of a honeycomb structure representing the multilayer YSZ-GDZ +DVC. This analysis encompasses the dynamics of stress across six distinct positions. Position 1 resides near the top surface, positions 2 and 3 are strategically located near the YSZ-GDZ interface—position 2 at the peak and position 3 in the valley. Similarly, positions 4 and 5 represent the peak and valley of the YSZ-GDZ interface, with position 6 serving as a reference point at the tip of the vertical crack. This analysis involves two distinct sets of results: one derived from the center line of the honeycomb structure, depicting the TBC without defects; the other set serves for comparison, illustrating stress patterns at the same positions when the microstructure incorporates a 30% defect rate. This comparative approach offers valuable insights into the impact of defects on stress distribution within the multilayer YSZ-GDZ TBC.

In Figure 15a, the S22 stress dynamics is presented, with position 1 exhibiting nearly negligible stresses. Interestingly, this position in S22 and S11 contrasts with Figure 6, where slightly larger stresses were observed, potentially attributed to edge effects in the global model. However, given the unit reference as one honeycomb in this analysis, the likelihood of edge effects is substantially reduced. Positions 2 and 3

demonstrate opposing stress trends during heating. At the peak (position 2), stresses are marginally compressive and increment slightly post-yielding, while position 3 experiences an incremental increase in compressive stresses throughout the heating phase, growing more pronounced post-yielding. Peaks and valleys (positions 4 and 5) of the TGO-YSZ exhibit a similar trend during heating, with a more substantial increment observed for the peak compared to the valleys. Concerning the TGO interface, the anticipated high tensile stresses in the peaks and corresponding compressive stresses in the valleys are evident. Notably, the difference in tensile stresses is markedly reduced in materials with presence of defects, indicating a stress reduction on the tensile side. Conversely, the impact on the compressive side is marginal, suggesting that defects in a small volume of the valley have limited influence.

On the other hand, at the YSZ-GDZ interface, the observation of tensile stresses at the peaks and compressive stresses in the valleys is apparent. However, the magnitudes of these stresses are notably smaller compared to the TGO-YSZ interface. Despite their reduced magnitude, the possibility of delamination near this interface, as documented in the literature[5,24], persists—particularly in the GDZ as this TBC exhibits lower fracture toughness compared to YSZ. The origin of different magnitudes of stresses at the interfaces is likely linked to differences in stiffness: in YSZ-GDZ, where GDZ is stiffer than YSZ, and in TGO-YSZ, where the underlying material is stiffer. This underscores the nuanced interplay between material properties and stress distribution, crucial in understanding potential failure mechanisms.

In Figure 15b, an akin analysis is presented, specifically S11 stresses that are tensile in most positions during heating, excluding those at position 4, situated in the valley of TGO-YSZ interface, until the elastic-plastic transition of the bond coat prompts a comprehensive shift towards compressive stresses. Position 1, distanced from the interfaces, exhibits negligible stresses. Notably, at position 2 (the peak), higher compressive stresses manifest in the YSZ-GDZ interface than in position 3 (the valleys), contrasting with the YSZ-TGO interface, where position 4 (the peak) records less compressive stresses than position 5 (the valleys). Minimal divergence between stress sets from the 0% defects and 30% defects scenarios are observed.

Remarkably, point 6, corresponding to the vertical crack's end (from a global model), registers pronounced tensile and compressive stresses. The yielding of the bond coat induces a significant shift—while heating sees the highest tensile stresses due to stress concentration and crack opening, cooling transforms this position into a safer domain. The yielding instills compressive stresses, fortifying the integrity of this point and highlighting its resilience during the cooling phase.

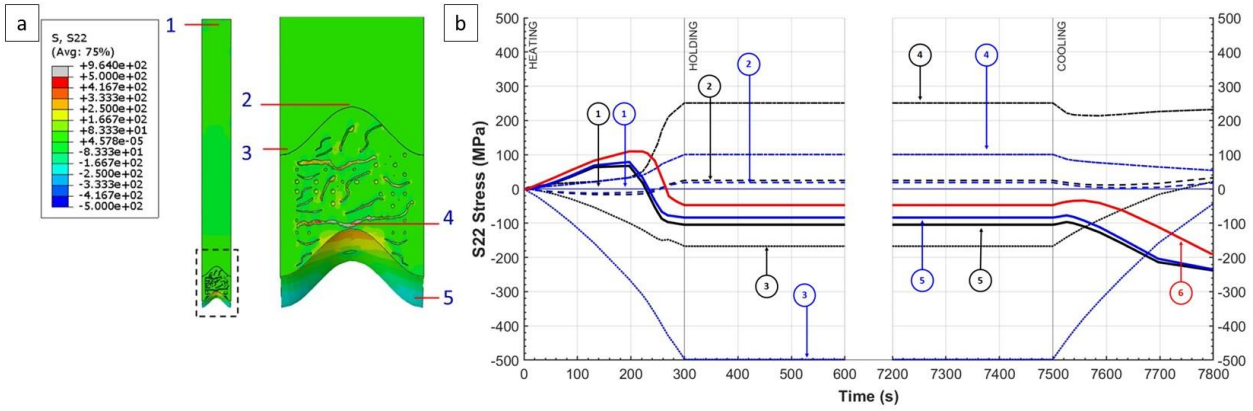

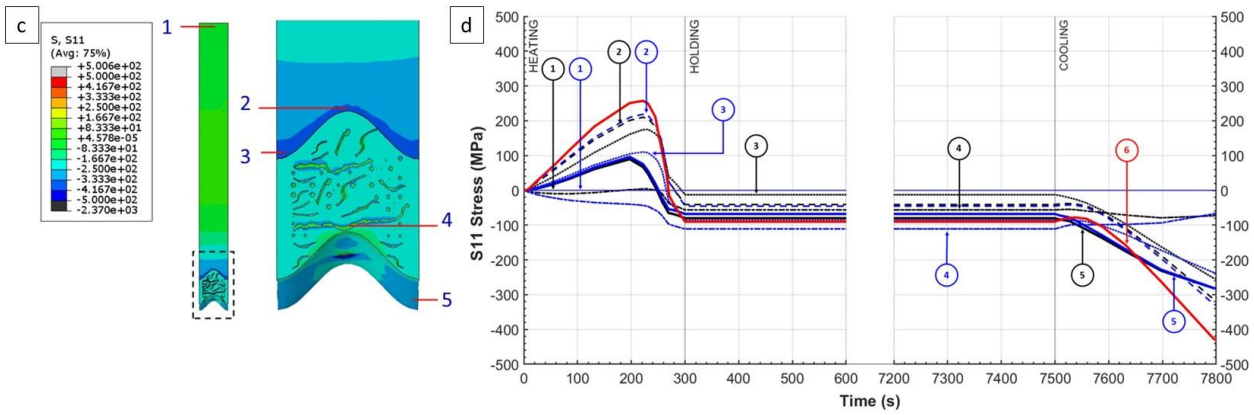

Figure 15: Stress analysis in various cross-sectional positions of YSZ-GDZ+DVC microscale model TBC. a) Positions designated for S22 stress analysis (snapshot at the end of cooling). Position 2 and 3 correspond to a peak and valley, respectively, in the YSZ-GDZ interface, whereas positions 4 and 5 correspond to a peak and valley, respectively, in the TGO-YSZ interface. b) Temporal evolution of S22 stress across the stages of heating, holding, and cooling for designated positions 1 through 5. c) Positions designated for S33 stress analysis (snapshot at the end of cooling). d) Temporal evolution of S33 stresses across the stages of heating, holding, and cooling for designated positions 1 through 5. Position 6 corresponds to a vertical crack's tip in the honeycomb like-DVC mesoscale model (YSZ-GDZ+DVC) for comparison and reference.

DISCUSSION

In elucidating the outcomes of the simulations and scrutinizing the intricate interplay among thermal stresses, material stiffness, defects such as pores and cracks, and the distinctive mud-cracking-like structure inherent in DVC-TBCs, the merits of employing a multi-scale analysis through the FEM emerge prominently. This approach proves advantageous in capturing the genuine microstructure present in gas turbines, constructed on a millimeter scale (1.000 µm). Notably, strategically integrated coatings in multiple layers are also captured on a scale measured in hundreds of micrometers (100 µm). Given that the defects influencing TBCs' thermal conductivity and mechanical resistance reside in the range of 100 µm to 1 µm or less, incorporating this multitude of minute imperfections into the microstructure and extrapolating to the actual scale of turbine blade production poses a considerable computational demand.

To surmount this challenge, a judicious strategy of breaking down the problem into distinct scales was successfully employed. This involved initially solving a global model at the millimeter scale to capture overarching thermomechanical phenomena. Subsequently, this information is transposed into smaller mesoscale models, facilitating the precise observation of mud-crack and vertical crack formations in TBCs. Furthermore, introducing minute defects into these mesoscale models enables the meticulous tracking of stresses, thereby refining calculations to attain detailed stress values at the minute crack geometries. This iterative process yields remarkable benefits, offering a comprehensive understanding of the thermomechanical intricacies at varying scales and facilitating advancements in coated turbine blade production.

The simulations and resultant data reveal prevalent engineering challenges, notably the occurrence of elevated S22 stresses at the YZ-TGO interface and stress concentrations not only at the tip of the vertical cracks within the DVC structure but also at the tips of inter-splat cracks. Our study underscores analogous manifestations of stress enhancement at the other material interface, YSZ-GDZ, where the rough interface introduces points susceptible to failure owing to heightened stresses. The avoidance of combinations resulting in high stresses—arising from factors such as interface disparities, vertical cracks, stress concentration at crack tips, or stress redistribution proximal to a crack opening—is imperative to prolong coating lifespan and avert delamination-induced failure.

This investigation uniquely delves into strategic insights, emphasizing the necessity for vertical crack tips to remain insulated from the influence of interface roughness profiles. Furthermore, the presence of cracks is explored as a potential means to mitigate stresses, counteracting scenarios where other components or phenomena contribute to stress escalation. Notably, the study accentuates not only the significance of stress magnitude but also the directional orientation, elucidating how S11 stresses interact specifically with vertical cracks and S22 stresses exhibit interactions with horizontal cracks. Notably, also, the yielding of the bond coat layer determines most of the mechanical behavior at elevated temperatures of the TBC layers at the various positions studied.

The utilization of a multiscale approach has yielded stress values of comparable magnitudes across the three scales. However, the global model exhibits heightened sensitivity to edge effects. Conversely, the mesoscale model captures intricate details within the interaction of peaks, valleys, and the honeycomb structure. The microscale provides further detail, enabling the observation of effects from microstructural defects at a finer level. The presence of defects diminishes stress magnitudes by enhancing material compliance, although variations are contingent upon measurement locations, i.e. proximity to a microcrack tip.

The TGO-YSZ interface manifests significant thermal mismatch effects among the metallic alloy substrate, TGO, and YSZ. Tensile stresses in the S22 direction range between +150 to +200 MPa in peaks, while valleys exhibit a similar order of magnitude in compression. Notably, S22 tensile stresses are identified as increasing the risk of coating failure. The S11 in-plane direction registers compressive stresses of -150 to -200 MPa in peaks and more pronounced compression of -250 to -300 MPa in valleys. Examining the YSZ-GDZ interface for the multilayer system, S22 stresses are relatively low, ranging from +20 to +40 MPa in peaks and tensile stresses between +5 to +40 MPa in valleys. Contrarily, S11 exhibits significantly high compressive stresses, ranging from -300 to –350 MPa in peaks and -200 to -250 MPa in valleys. Despite the similar coefficients of expansion and elastic modules of the two ceramic materials, Figure 15 illustrated substantial stress effects attributable to the interaction with the metallic alloy substrate. This comprehensive stress magnitude assessment is important, given that failures in TBC configurations are often observed at the interfaces. In conclusion, the consistent influence of stress mismatches between substrates and coatings, coupled with roughness profiles, emerges as a primary locus for observed failures.

While acknowledging that this study does not comprehensively address the entire spectrum of fundamental physics inherent in TBCs—such as modifying the amplitude and wavelength of stress profiles, ratcheting, creep, sintering, or in-situ TGO growth—the acquired results serve as a foundational step toward grasping the three-dimensional actuality of TBC structures. Significantly, these findings propose new routes for designing optimal multi-layer and multi-material TBCs, where variations in composition yield diverse properties and confer chemical, thermal, or mechanical advantages to produce superior

TBCs. Thus, this study points out the potential to customize TBCs by adjusting factors like the thickness of each layer, the presence of defects, the use of graded structures, or modifying the mud-crack structure. Such modifications offer opportunities for tailoring TBC properties to specific requirements, paving the way for advancements in the design and engineering of robust and high-performance TBCs.

Conclusions

In this investigation, comprehensive 3D simulations employing a multiscale strategy were undertaken, incorporating a detailed recreation of actual defects through metallography. Notably, the model facilitated a nuanced exploration of interface effects, mud cracking –dense vertically cracked DVC structures, isle sizes, yielding effects, vertical crack length, percentage of porosity, and other pertinent parameters. Using ABAQUS software, the models underwent isothermal tests to elucidate the repercussions of thermomechanical stress arising from the thermal expansion and elastic modulus disparities within the materials.

The triad of 3D simulations encompassed TBCs comprising YSZ dense material, YSZ+DVC, and a multilayer YSZ-GDZ +DVC. Notably, the latter exhibited diminished strain energy and fewer instances of high stresses, particularly evident in S22 stresses at the peaks of the TGO-YSZ interface. This suggests a potential enhancement in performance with the incorporation of GDZ atop and YSZ beneath. Nevertheless, the introduction of the YSZ-GDZ interface necessitates careful consideration, as stress intensifications were observed due to the profile causing stress increments.

Significant stress concentrations were observed at interfaces and crack tips, specifically correlating to interlamellar horizontal microcracks and vertical cracks from DVCs. Incidences of S11 stresses were observed at vertical crack tips, while S22 stresses manifested at horizontal cracks. Special emphasis is placed on advocating the avoidance of stress field interactions between the tips of vertical cracks and the stress fields at interfaces.

In summation, this study successfully delineates a systematic multiscale approach, coupled with an endeavor to capture microstructural intricacies. It sheds light on the magnitude of stresses imperative for the design of coatings geared toward superior performance, making a significant contribution to the understanding of TBC behavior in the 3-dimensional space.

Acknowledgement
The authors gratefully acknowledge the financial support of AFOSR-SOARD, with grant number FA9550-20-1-0075-3D Thermo-mechanical Modeling of Multilayered TBCs for gas turbine engines."

References:

1. Evans, A. G., Clarke, D. R. & Levi, C. G. The influence of oxides on the performance of advanced gas turbines. *J. Eur. Ceram. Soc.* **28**, 1405–1419 (2008).

2. Poerschke, D. L., Jackson, R. W. & Levi, C. G. Silicate Deposit Degradation of Engineered Coatings in Gas Turbines: Progress Toward Models and Materials Solutions. *Annu. Rev. Mater. Res.* **47**, 297–330 (2017).

3. Clarke, D. R., Oechsner, M. & Padture, N. P. Thermal-barrier coatings for more efficient gas-turbine engines. *MRS Bull.* **37**, 891–898 (2012).

4. Sampath, S., Schulz, U., Jarligo, M.O. and Kuroda, S. Processing science of advanced thermal-barrier systems. *MRS Bull.* **10**, 903–915 (2012).

5. Evans, A. G., Mumm, D. R., Hutchinson, J. W., Meier, G. H. & Pettit, F. S. Mechanisms controlling the durability of thermal barrier coatings. *Prog. Mater. Sci.* **46**, 505–553 (2001).

6. Levi, C. G. Emerging materials and processes for thermal barrier systems. *Curr. Opin. Solid State Mater. Sci.* **8**, 77–91 (2004).

7. Vassen, R., Stuke, A., Sto, D. & Ju, F. Recent Developments in the Field of Thermal Barrier Coatings. *J. Therm. Spray Technol.* **18**, 181–186 (2009).

8. Cao, X. Q., Vassen, R. & Stoever, D. Ceramic materials for thermal barrier coatings. *J. Eur. Ceram. Soc.* **24**, 1–10 (2004).

9. Li, C. *et al.* Understanding the residual stress distribution through the thickness of atmosphere plasma sprayed (APS) thermal barrier coatings (TBCs) by high energy synchrotron XRD; digital image correlation (DIC) and image based modelling. *Acta Mater.* **132**, 1–12 (2017).

10. Li, C. *et al.* Residual stress distribution analysis of heat treated APS TBC using image based modelling. *Data Br.* **13**, 557–561 (2017).

11. Bumgardner, C., Croom, B. & Li, X. High-temperature delamination mechanisms of thermal barrier coatings: In-situ digital image correlation and finite element analyses. *Acta Mater.* **128**, 54–63 (2017).

12. Kulkarni, A. a. *et al.* Advanced Microstructural Characterization of Plasma-Sprayed Zirconia Coatings Over Extended Length Scales. *J. Therm. Spray Technol.* **14**, 239–250 (2005).

13. Tan, Y., Longtin, J. P. & Sampath, S. Modeling Thermal Conductivity of Thermal Spray Coatings: Comparing Predictions to Experiments. *J. Therm. Spray Technol.* **15**, 545–552 (2006).

14. Wang, L. *et al.* Modeling of thermal properties and failure of thermal barrier coatings with the use of finite element methods: A review. *J. Eur. Ceram. Soc.* **36**, 1313–1331 (2016).

15. Bäker, M. & Seiler, P. A Guide to Finite Element Simulations of Thermal Barrier Coatings. *J. Therm. Spray Technol.* **26**, 1146–1160 (2017).

16. Wei, Z. Y., Chai, Y. J., Yi, P., Meng, G. H. & Zhang, W. W. Stress profile and crack evolution in a three-dimensional (3D) thermal barrier coatings during isothermal cyclic test. *Ceram. Int.* **48**, 30606–30620 (2022).

17. Jinnestrand, M. & Sjöström, S. Investigation by 3D FE simulations of delamination crack initiation

in TBC caused by alumina growth. *Surf. Coatings Technol.* **135**, 188–195 (2001).

18. Mahade, S. *et al.* Erosion Performance of Gadolinium Zirconate-Based Thermal Barrier Coatings Processed by Suspension Plasma Spray. *J. Therm. Spray Technol.* **26**, 108–115 (2017).

19. Jonnalagadda, K. P. *et al.* Hot Corrosion Mechanism in Multi-Layer Suspension Plasma Sprayed Gd2Zr2O7 /YSZ Thermal Barrier Coatings in the Presence of V2O5 + Na2SO4. *J. Therm. Spray Technol.* **26**, 140–149 (2017).

20. Zhou, D. *et al.* Thermal cycling performances of multilayered yttria-stabilized zirconia / gadolinium zirconate thermal barrier coatings. 2048–2061 (2020) doi:10.1111/jace.16862.

21. Viswanathan, V., Dwivedi, G. & Sampath, S. Multilayer, multimaterial thermal barrier coating systems: Design, synthesis, and performance assessment. *J. Am. Ceram. Soc.* **98**, 1769–1777 (2015).

22. Abaqus. Creating the submodel boundary condition. *Abaqus* at https://docs.software.vt.edu/abaqusv2022/English/SIMACAECAERefMap/simacae-t-advsubmodelingbc.htm.

23. Guven Gok, M. & Goller, G. State of the Art of Gadolinium Zirconate Based Thermal Barrier Coatings: Design, Processing and Characterization. in *Methods for Film Synthesis and Coating Procedures* (Intechopen, 2019). doi:10.5772/intechopen.85451.

24. Aktaa, J., Sfar, K. & Munz, D. Assessment of TBC systems failure mechanisms using a fracture mechanics approach. *Acta Mater.* **53**, 4399–4413 (2005).

25. Bejarano, M. L., Valarezo, A., Lara-Curzio, E. & Sampath, S. Dilation Behavior of Thermal Spray Coatings. *J. Therm. Spray Technol.* (2019) doi:10.1007/s11666-019-00927-4.

26. Yang, F. Electrical and thermal properties of yttria-stabilized Zirconia (YSZ)-based ceramic materials. **26**, 173 (2011).

27. Assistant, C. Questions And Answers - CAE Assistant. *CAE Assistant* at https://caeassistant.com/questions/question/master-slave-surfaces-basic-rules.

28. Systémes, D. *Abaqus 6.9 Theory Manual*. *Dassault Systémes Simulia Corp., RI, USA* (2009).

29. ASTM E1920-03(2021). *Standard Guide for Metallographic Preparation of Thermal Sprayed Coatings*. (2021).

30. Society, A. T. S. Accepted Practice for Recognizing Artifacts in Air Plasma Spray Thermal Barrier Coating Microstructures. in *Thermal Spray Technology* 55–68 (ASM International, 2022). doi:10.31399/asm.tb.tstap.t56040055.

de la Roche, J., Alvarado-Orozco, J. M., Gómez, P. A., Cano, I. G., Dosta, S., & Toro, A. (2022). Hot corrosion behavior of dense CYSZ/YSZ bilayer coatings deposited by atmospheric plasma spray in Na2SO4 + V2O5 molten salts. *Surface and Coatings Technology*, *432*, 128066. https://doi.org/10.1016/J.SURFCOAT.2021.128066

Gildersleeve, E., Viswanathan, V., & Sampath, S. (2019). Molten silicate interactions with plasma sprayed thermal barrier coatings: Role of materials and microstructure. *Journal of the European Ceramic Society*, *39*(6), 2122–2131. https://doi.org/10.1016/J.JEURCERAMSOC.2019.01.023

Appendix 2:

Manuscript of paper:
THERMO-MECHANICAL MODELING OF MULTILAYERED TBCs FOR GAS TURBINE
ENGINES

CÍRCULO DE CUMBAYÁ. P.O.BOX: 17-12-841 QUITO-ECUADOR
T.: (593 2)297-1700 AL 708. FAX.: (593 2)289 0070.
WWW.USFQ.EDU.EC

THERMO-MECHANICAL MODELING OF MULTILAYERED TBCs FOR GAS TURBINE ENGINES

Alfredo Valarezo, Samantha Criollo, Diego Morales, Yupanki de la Cruz, Pedro Reina, Marco León, Lorena Bejarano

Institute for Energy and Materials, Department of Mechanical Engineering, Universidad San Francisco de Quito, Quito, Ecuador

* Corresponding Author: E-mail: alfredo.valarezo@gmail.com ;
Tel: +593-2971700 ext. 1048

ABSTRACT

In this paper, we assess coating effective thermal conductivity and thermomechanical stresses of multilayered TBC´s using image analysis and the finite element method employing OOF-2 and ABAQUS FEA software. Coatings consist of layers of Yttria Stabilized Zirconia (YSZ), and Gadolinium Zirconates (GDZ) deposited by air plasma spray to produce coatings with different combinations of microstructures: dense, porous, or dense vertically cracked (DVC) type. A detailed procedure for image analysis (IA) and modeling of five different multilayered/multi-material TBC microstructures is presented. The contribution to the effective thermal conductivity of individual layers and defects (globular pores, and horizontal and vertical cracks) are discussed and compared to experimental results. The thermal conductivity is predicted with a high level of confidence. On this premise, thermomechanical simulations were carried out to evaluate in-plane S11 and out-of-plane stresses S22, as well as elastic strain energy. The results show two interfaces of higher potential of failure, the YSZ-TGO and GDZ-YSZ interface. The computational results identify that GDZ fails at lower strain energy (30-40 J/m^2) than YSZ (>50 J/m^2), producing premature failures. The results highlight that the longest lifetime was for coating “C” (failure at YSZ-TGO interface), and its performance is correlated to a combination of high fracture toughness of the dense-YSZ layer in the interface and low stresses at the GDZ-YSZ interface. It is presented that the method works satisfactorily to capture the microstructural defects on thermo-mechanical stresses that drive the failure of multilayer TBCs.

Introduction

Thermal barrier coatings (TBCs) allow gas turbine engines to work at higher operating temperatures. Higher efficiency and higher output power can be achieved with TBCs of lower thermal conductivity, good chemical stability, and high fracture toughness. Currently, most turbines engines use TBCs composed of Yttria Stabilized Zirconia (YSZ) deposited onto a Ni-superalloy blade with a bond coat (typically an M-CrAlY alloy). The current TBCs using YSZ have reached their performance limit. Thus, depositing multilayers is considered an industrial option to benefit transport and defense aircraft. Here, Gadolinium Zirconate ($Gd_2Zr_2O_7$ -GDZ) coatings are proposed as a topcoat layer to take advantage of its better chemical resistance against CMAS, and its lower thermal conductivity. However, its incompatibility with the TGO at the bond coat interface and its lower fracture toughness than YSZ raises the need to deposit a bottom layer of YSZ whose advantageous performance at that spatial position is demonstrated, here.

Recent investigations [1]–[3] denote that the multilayering strategies demand in-depth analysis of stresses to discover potential failures that affect coating lifetime. The study of thermomechanical stress on coatings demands the use of computational tools such as finite element analysis (FEA) and object-oriented finite element (OOF-2) software for image recognition to capture accurately the microstructural defects. The in-plane stresses caused by the thermal expansion mismatch are affected by transitions between layers, cracks (vertical and horizontal), porosity, and roughness. Therefore, determining the stress field is not a trivial problem, and computational tools are a need.

Several studies have demonstrated the applicability of OOF to microstructure recognition in TBCs and prediction of the thermal conductivity and thermal residual stresses ([4]–[8]. Gupta et al. [8] pioneered the utilization of this approach for analyzing YSZ with varying morphologies and dual-layer systems. The authors found that finite element analysis is a powerful tool for predicting the performance of different coating technologies, despite its tendency to overestimate properties due to the limitations of two-dimensional models. Moreover, they discovered that materials with globular pores combined with cracks perform better, as this combination leads to lower thermal conductivities and lower Young's modulus, resulting in coatings with a longer lifetime. Torkashvand et al. took a step further in advancing this field by integrating (OOF) analysis with image processing and experimental techniques. Their research was primarily dedicated to precisely quantifying the influence of porosity on the thermal conductivity of Thermal Barrier Coatings (TBCs). In their study, the authors emphasized the effectiveness of employing an object-oriented finite model within the finite element method. This model takes into careful consideration the presence of pores, defects, and the interplay of phases between different layers of the coatings. Their findings led to a significant conclusion: if there exists a random distribution of pores within the TBCs, the thermal conductivity will exhibit a continuous decrease, irrespective of how these pores are distributed. However, it's crucial to note that the determination of conductivity faced certain limitations due to the reliance on a two-dimensional approach. This method tended to magnify the decrease in thermal conductivity attributed to variations in pore volume fraction. Ganvir et al. harnessed OOF to predict how porosity and crystallite structure influence the thermal conductivity of TBCs created through axial suspension plasma spraying. Additionally, Poursaeidi et al. leveraged OOF analysis to assess the effects of CMAS (CaO-MgO-Al2O3-SiO2) on TBC thermal conductivity. Their research successfully projected the influence of CMAS penetration on the thermal conductivity of coatings, concluding that it leads to an increase in thermal conductivity, thereby diminishing the insulating properties of TBCs.
On the other hand, studies related to multilayered TBCs have boomed over the latest years to highlight their applicability and advantages. In the realm of thermal barrier coatings (TBCs) for gas turbine applications, recent advancements have been made to address challenges faced by Yttria-stabilized zirconia (YSZ). Satyapal Mahad et al. propose a solution in the form of double-layered TBCs, utilizing YSZ as the intermediate layer and pyrochlore as the top layer, deposited through suspension plasma spray. Comparative analyses reveal that these multi-layered TBCs exhibit favorable columnar microstructures, lower thermal

conductivity, and increased thermal cycling life at high temperatures compared to single-layer YSZ coatings. Meanwhile, M. Tamura et al. focus on enhancing oxidation resistance in land-based gas turbine components by introducing a triplex TBC, incorporating an aluminized layer. This novel design demonstrates superior durability in thermal cycle tests and resistance to oxidation compared to conventional duplex TBCs. In a parallel study, Viswanathan et al. [1] investigate the role of processing and microstructure in the durability of plasma sprayed TBCs. Their approach involves strategic bilayer architectures, aiming to provide a balance between high toughness and low thermal conductivity, showcasing the adaptability of plasma spray technology for multifunctional coatings. These studies collectively contribute to the state-of-the-art understanding of TBCs, offering insights into improved microstructures, enhanced durability, and tailored designs for specific turbine components.
However, there are no previous studies using the finite element method to analyze multilayered TBCs capturing several types of microstructures in detail, and that can relate the stress analysis to the failure by heat cycles.

We aim to study five multilayered TBCs deposited by atmospheric plasma spraying (APS) that were modeled and simulated by FEA, using ABAQUS and the OOF-2 tool. A broad experimental characterization of these samples has been published by Viswanathan et. al [1] including data on thermal conductivity measurements, elasticity, and coating lifetime in furnace cycles tests at 1100°C. This set of samples presents an interesting combination of microstructures to test the computational procedure towards improving efficacy and accuracy of the models. From (a) to (e), Figure 1 presents the combination of YSZ bottom layers and GDZ top layers with dense, porous, or dense vertically cracked (DVC) structures. The purpose of such combinations for the TBC is to take advantage of the different properties of the materials. YSZ has very low thermal conduction, but not as good resistance to CMAS attack as GDZ which is thus proposed as an alternative top layer. The use of YSZ at the bottom of the TBC in a form of a dense coating (b,c,d) and DVC (a,d) enhances the fracture toughness at the region known for the highest thermal strain mismatch. The mechanical compliance of the coatings is increased through the thickness by producing porous, DVC-YSZ and DVC-GDZ coatings, and their combination. The DVC-GDZ structure at the top layers (b, c, d, e) assured “strain tolerance”.

The first approach in the simulation is to obtain the effective thermal conductivity of the multilayers by FEA to compare with the experimental results. This single property allows the fine tuning of the model before assessing thermomechanical residual stresses that cannot be experimentally examined. Furnace cycle tests produced coating failures in the GDZ-YSZ interface or YSZ-TGO interfaces of the proposed coatings. The simulation results showed that the best performing coatings present lower strain energy at the GDZ by the GDZ-YSZ interface, and higher strain energy at the YSZ by YSZ-TGO interface. Since YSZ has a higher fracture strength, this case presented an extended lifetime under furnace cycle testing, coating type “C”.

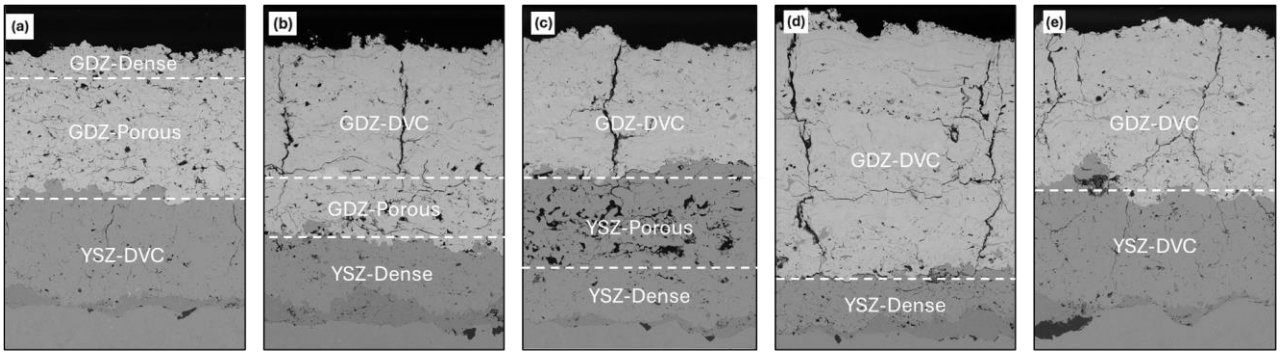

Figure 1. Microstructures of five multilayered/multi-material TBCs adopted from Viswanathan et. al [1]

In this paper, we present in detail the procedure to analyze the TBC images and import the different phase information into the OOF-2 models and FEA. We then apply properties and simulate heating cycles to produce the results of effective thermal conductivity and residual stresses. The TBC, TGO and substrate materials are considered elastic, while the bond coat is elastic-plastic, including creep. The presence of the TGO is assumed in the coatings and included by image modification. The simulation and experimental results suggest that keeping a dense YSZ layer near the TGO-bond coat interface and following by a strain tolerant YSZ porous and GDZ-DVC is the best configuration to manage the residual stresses through-the-thickness.

Materials and Methods

Multilayered Coatings

Viswanathan et al. [1] introduced multiple layers and material TBC configurations with an ample characterization of mechanical properties, microstructure, and thermal properties. Here, we study the microstructure images of four micrographs per each of those five configurations of multilayered coatings from Viswanathan et al. The common configuration of TBCs consisting of a topcoat, a bond-coat, and a thin oxide layer (TGO) developed from the oxidation process of the bond coat is followed as baseline.
Five types of GDZ and YSZ combinations [1] are modeled and simulated here. Coatings of reference were deposited on a Rene 80 substrate with a thin bond-coat layer of NiCoCrAlYHfSi composition. The five multilayers are constituted from top to bottom, as follows (Figure 1):

a. Top layer: dense GDZ (low porosity). Mid-layer: porous GDZ. Bottom layer: DVC-YSZ.
b. Top layer: DVC GDZ. Mid layer: porous GDZ. Bottom layer: dense YSZ.
c. Top layer: DVC GDZ. Mid layer: porous YSZ. Bottom layer: dense YSZ.
d. Top and Mid layer: DVC GDZ. Bottom layer: dense YSZ.
e. Top layer: DVC GDZ. Mid and bottom layer: DVC YSZ.

Microstructure Image Processing

Four distinct SEM images with a magnification of 300x of each of the above-mentioned configurations were processed in a TIFF format. The images had a resolution of 1280x950 pixels. A python code was used to delimit each of the layers of the micrograph by applying contrast, stretching, equalization and denoising operations on the image. The code was also employed to transform the images from grayscale to binary with a threshold criterion based on the gray level difference of the YSZ, GDZ, bondcoat, and substrate materials; and to separate the pores and cracks (vertical and horizontal) into another image, by applying a mask with a threshold based on the gray level of each layer, to ease image processing. It is important to acknowledge that the threshold criterion is selected between a color range of grayscale of 35-45 for defects, 50-130 for the bond coat, and 140-200 for GDZ, depending on the clarity and quality of the image. Thus, it can be subjective to the analyst judgement to improve the discretization. The resin and the substrate materials are identified by discarding from the other regions.

Vertical cracks, horizontal cracks and globular pores were segmented on each image and layers, using ImageJ (v1.54f) Shape Filter Plugin. For this process, the angle of the defects and circularity was considered as a discretizing criterion. Angle ranges from 0° to 45° and from 135° to 180° were used for horizontal crack segmentation, whereas angle ranges from 45° to 135° were used for vertical crack segmentation. For globular pores segmentation, the circularity of the defects was considered, using a criterion from 0 to 1 which assures that only defects that resemble a circular geometry enter this category. After segmentation, images are processed on Sketchbook, a raster graphic software in which the layers margins are traced manually. Finally, the images with differentiated coating layers and defects are merged as graphical layers. Figure 2 shows an example of the analysis of multilayered coating C, where the segmentation of different layered materials can be observed together with the identification of defects (cracks, pores, etc.). In Figure 2, (*a*) shows the original SEM microstructure image; (*b*) is the same image after stretching, equalization, denoising, and tracing; (*c*) through (*f*), show the microstructure with the three types of defects in separated images, thus: (*c*) all defects, (*d*) globular pores only, (*e*) vertical cracks only, and (*f*) horizontal cracks only.

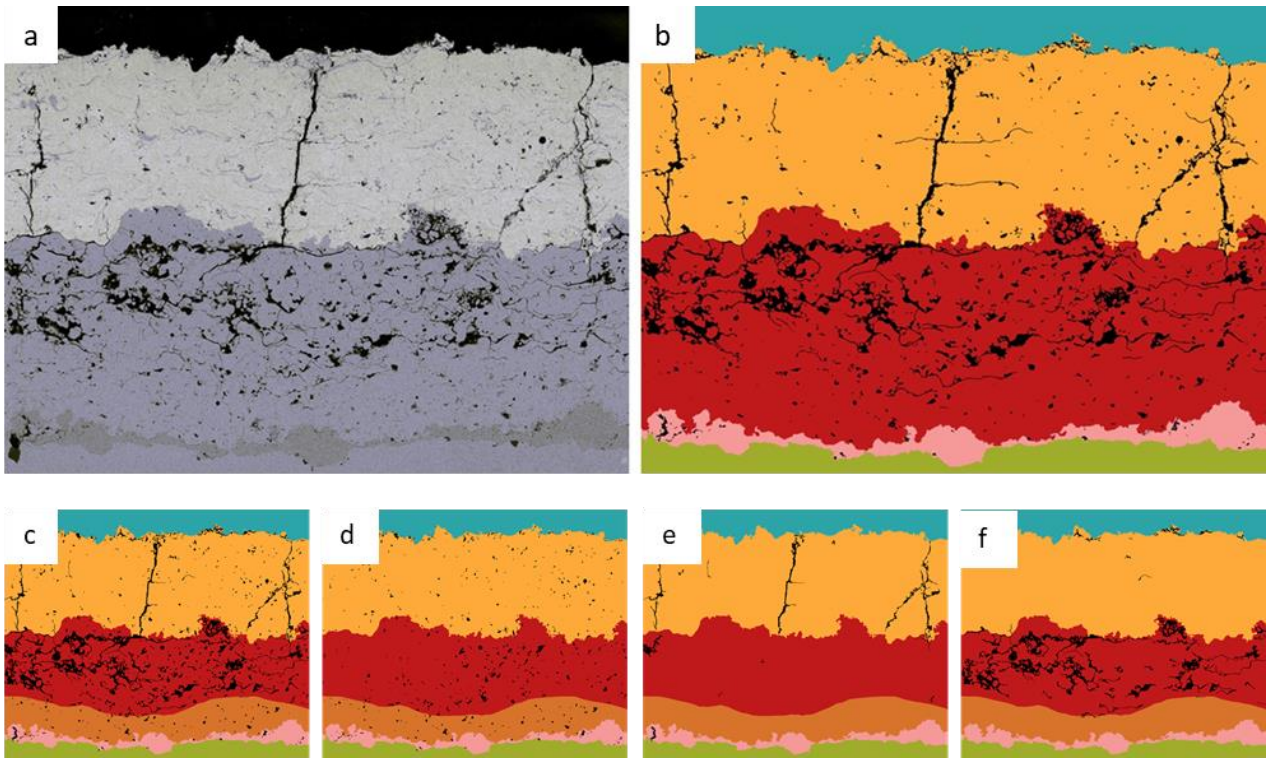

Figure 2. Image processing of coating type-C, TBC configuration. (a) Original gray scaled image followed by the processed image (b) after stretching, equalization, denoising, and tracing, (c) compounded image with each of its layers, (d) segmented image of globular pores, (e) segmented image of vertical cracks, (f) segmented image of horizontal cracks.

Finite element model and simulation for effective thermal conductivity

After the image-processing has been conducted, a finite element (FE) object-oriented package, OOF2 (version 2.1.19), was employed to create meshes for each layer and the corresponding defects. OOF2 is a C++ and Phyton package that recognizes in the image different areas that can be assigned with their respective material properties. Figure 3 shows the flowchart for the analysis of the microstructures and later, prediction of properties using FEA.

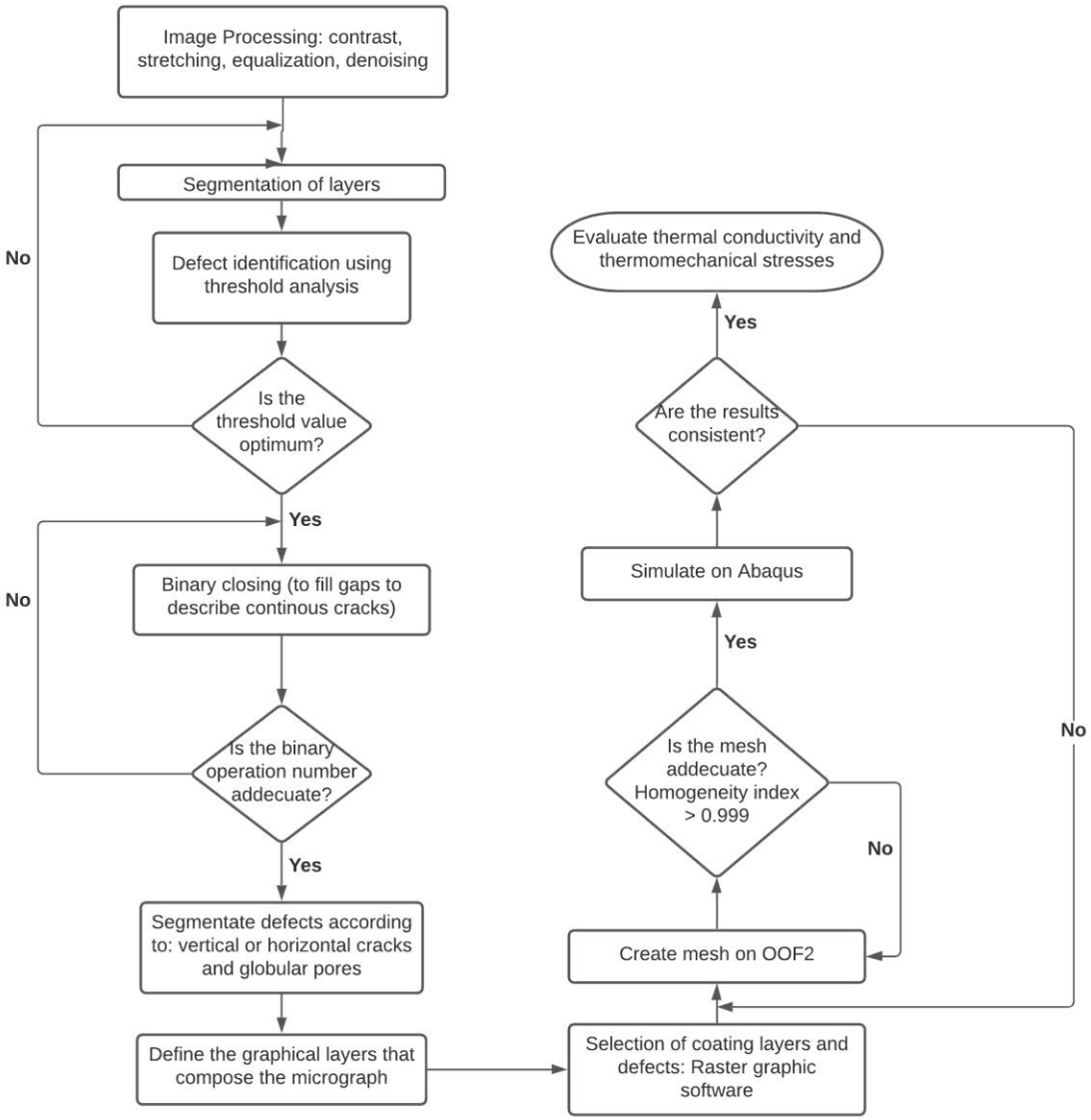

Figure 3. Flow chart for image analysis towards producing well-identified and meshed phases to simulate thermal conductivity and residual stresses of TBCs by means of finite element analysis FEA.

Abaqus (version 2022) was used for the FEA to predict the effective thermal conductivity of single and multilayered TBCs. For a single TBC layer, the mesh is created with three segments, one defined as a top block, followed by the TBC, and then a bottom block, all of them defined with the same material properties. In a multilayered case, the segments are similar, one as a top block, then the two layers (YSZ-GDZ), and the bottom block. In this case, the top and bottom segments adopt the material properties of the TBC that is sharing nodes with. This condition helps to distribute the heat transfer in a better way, avoiding issues with the profile (peaks and valleys) inherent of the micrograph's top and bottom boundary limits. The boundary nodes in the top and bottom are identified in the meshed micrograph as limits, assigning them the initial loads of 400°C and 25°C respectively. Also, a predefined field of 25°C is assigned to the entire model. Material properties for bulk materials are assigned according to Table 1.

The effective thermal conductivity, (k_{eff}) is calculated using the Fourier equation, as follows:

$$Q = k_{eff} * \left(\frac{\Delta T}{H}\right) \left[\frac{w}{m^2}\right] \quad \text{equation 1}$$

Where (Q) represents heat flux in the y-direction (through-the-thickness of the coatings), (k_{eff}) the effective thermal conductivity, (ΔT) the temperature gradient, and (H) thickness of the section in study. To calculate (k_{eff}), the image is divided into one hundred and fifty vertical paths, and the average heat flux in each path is considered in Fourier´s equation accounting for the precise temperature difference and distance between the top and bottom nodes. The top and bottom boundaries are considered isothermal, and the right and left boundaries are adiabatic. The high number of paths allow us to obtain a representative value of thermal conductivity.

Heat flux is low on pores and cracks due to air low conductivity [4] and thus, cracks and pores have a high influence on thermal resistance by reducing the flux. Figure 1S(a) shows an example of the heat flux in the multilayered coating C where low flow of heat is observed near cracks and pores, whereas Figure 1S(b) shows the results of (k_{eff}) for those one hundred and fifty paths.

Table 1. Thermo-mechanical properties of bulk materials used in the simulation, density (ρ), heat capacity (C) and thermal conductivity (*k*), Coefficient of Thermal Expansion (CTE), Young´s Modulus (E), Poisson´s ratio (*v*). [4], [9], [10]

Material	T [°C]	ρ [kg/m^3]	C [J/kg K]	K [W/m K]	CTE x10^{-6}, [mm/mm]	E [GPa]	B [1/(sMPa^n)]	*v*
GDZ	25	6320	-	1.6	8.65+0.00285T (80-1100°C)	40	-	0.276
	400		430				-	
	800		470				-	
	1000		520				-	
YSZ	25	5960	434	2.2	10.53+0.001T (100-1100°C)	50	-	0.2
	400	-	578				-	-
	800	-	617				-	-
	1000	-	626				-	0.2
Bond Coat	25	7380	450	10.8	9.848 + 0.013T-0.000007T^2 (50-600°C)	250	6,54e-19 (n=4.57)	0.3
	200					220		0.3
	400					200		0.3
	600	-	-	-		180		0.3
	700	-	-	-		165	2.2e-12 (n = 2.99)	0.3
	800	-	-	-		155	1.84e-7 (n=1.55)	0.3
	1000	7030	980	32.1		120	2.15e-8 (n=2.45)	0.3
Air	25	1.225	1006	0.025	-	-	-	-
TGO	25	3984	755	33	6.7596+0,0022T (300-900°C)	380	-	0.23
	300	-	-	-		-	-	-
	600	-	-	-		350	-	0.23
	800	-	-	-		340	-	0.25
	900	-	-	-		-	-	-
	1000	3868	1285	6.7		315	-	0.25
Inconel 617	20	8360	419	13.4	-		-	
	25		419	13.4	11.6	211	-	0.3
	400		515	19.3	13.6	188	-	0.3
	800		611	25.5	15.4	149	-	0.3
	1000		662	28.7	16.3		-	

Finite element simulation for thermo-mechanical residual stresses

For the thermomechanical residual stress analysis, representative sections of each microstructure model were carefully selected. The model and methodology considered for the analysis is illustrated in Figure 4. To account for the oxidation effect of the bond-coat, a layer of thermally grown oxide (TGO) was incorporated between the YSZ layer and the bond-coat. This TGO layer of 4 µm in thickness was introduced during the segmentation of the images. In the model, temperature-dependent material properties were considered, according to Table 1. By incorporating temperature-dependent properties, the model can effectively capture the viscoelastic behavior of the bond coat which plays a significant role in absorbing and dissipating stresses during the thermal cycle.

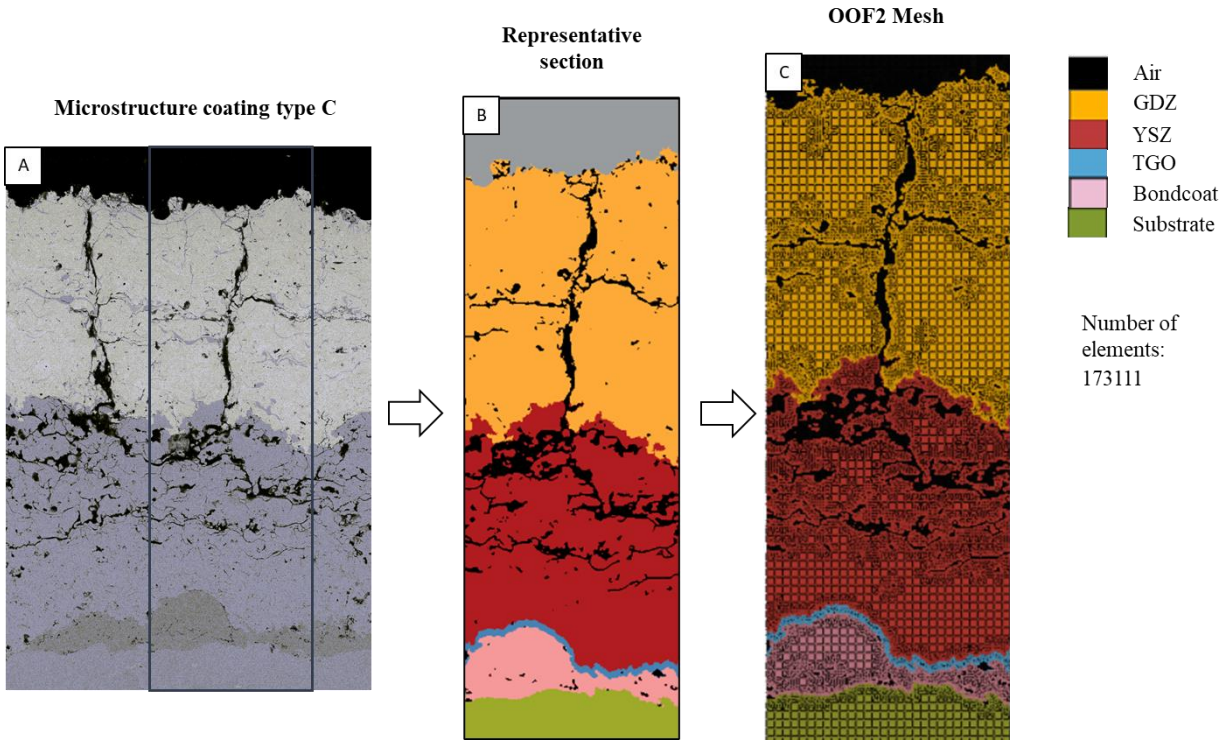

Figure 4. Image processing for thermal conductivity and thermomechanical analysis. (a) Original SEM Image in backscattering of the multilayered coating C, (b) Segmented image including substrate (in green), bond coat (in pink), TGO (in blue), and three layers of TBC –dense YSZ in the bottom (in red), porous YSZ in the middle (also in red), GDC-DVC in yellow. (c) Meshed image with identification of each layer, and finer mesh in the interfaces. The number of elements is 173,111 for this image. Air is identified in the top of the microstructure and in the pores and cracks as opened spaces. Homogeneity index: 0.999

The heat cycle analysis was carried out in three stages. The first one involved heating the model from an initial temperature of 25°C to 1000°C within 300 seconds. Subsequently, the temperature was maintained at 1000°C for 7200 seconds in the holding stage. Finally, the cooling phase was implemented, decreasing the model's temperature from 1000°C to 25°C, over 300 seconds. For the holding stage, a creep model was integrated to account for the viscoelastic behavior, time dependent plastic strain of the bond coat at temperature. The creep follows the Norton model:

$$\dot{\varepsilon}_{eq}^{cr} = B * \left(\sigma_{eq}\right)^{n} \quad \text{equation 2}$$

Where ($\dot{\varepsilon}_{eq}^{cr}$) is the von Mises equivalent creep strain, (σ_{eq}) is the von Mises equivalent stress, (*B*) and (*n*) are temperature-dependent properties of the materials that are listed in Table 2. The values of the property (*B*) at the temperatures in-between those given in Table 2 are interpolated logarithmically according to Aktaa et al. [10]

Table 2. Temperature dependent parameters of Norton creep considered for bond coat

T [°C]	$B\left[\frac{1}{s\,MPa^n}\right]$	*n*
≤ 600	6.54×10^{-19}	4.57
700	2.20×10^{-12}	2.99
800	1.84×10^{-7}	1.55
≥ 850	2.15×10^{-8}	2.45

The 2D models in this section are considered as in plane-strain. Regarding boundary conditions, the left side is designated as symmetrical, with movement restricted in the *x*-direction, and similarly, the bottom is symmetrical with movement restricted in the *y*-direction. In line with parameters from prior studies, a periodic boundary condition is established between the left and right edges to ensure seamless connectivity between corresponding nodes. This condition is mathematically expressed as:

$$u_r - u_l = u_b - u_a \qquad \text{equation 3}$$

Here, *a* and *b* represent the corner bottom nodes, while *r* and *l* denote each subsequent on the right and left sides after *a* and *b*, respectively. The variable *u* signifies degrees of freedom, which, in this case, are two (x and y). To maintain an equal number of nodes on both sides, a mirror condition in the y-z plane was instituted in the assembly part and subsequently merged in the instance.

The simulation heat cycle is organized into four consecutive time steps: initial, heating, holding, and cooling. In the initial step, the stress is set to zero, and the temperature field to 298 K. As the simulation progresses to the heating step, the temperature linearly increases from 298 K to 1273 K over a five-minute interval. Subsequently, the holding step ensues, maintaining the temperature at 1273 K for 120 minutes. Finally, during the cooling step, the temperature decreases linearly from 1273 K to 298 K in five minutes. It is essential to note that the temperature is uniformly distributed throughout the entire geometry in each time increment of each step, ensuring an isothermal condition. The heating cycle is visually depicted in Figure 5, with the conclusion of the heating phase labeled as H1, the end of the holding phase as H2, and the conclusion of the cooling phase as C. This codification will be utilized to present the thermomechanical results.

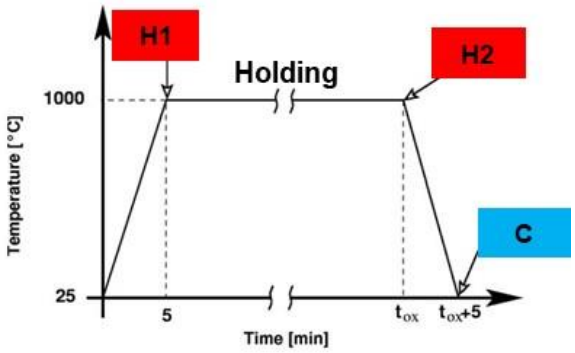

Figure 5. Visualization of the heat cycle. In the initial step, the stress is set to zero, and the temperature field to 298 K. In the heating step, the temperature linearly increases from 298 K up to 1273 K (H1-end of heating step) over a five-minute interval. Subsequently, the holding step ensues, maintaining the temperature at 1273 K for 120 minutes (H2-end of holding step). Finally, the temperature decreases linearly from 1273 K to 298 K in five minutes (C-end of cooling).

Results and Discussion

Effective Thermal Conductivity Results – Analysis in Single- and Multi-layer TBCs

The thermal conductivity simulation results were compared with experimentally determined coating-property values obtained by Viswanathan et al. using the laser flash technique on free-standing samples. Figure 6 and Table S1 present a comprehensive comparison between the experimental and simulated thermal conductivities of the various combinations of YSZ and GDZ. Table S1 specifically outlines the deviation from experimental values, which spans from 4% to 55%. It is noteworthy that certain intricacies, such as small cracks, pores, interlamellar interfaces, or partially bonded splats, might not be fully captured by image analysis. This characteristic was particularly evident in previous simulation results for YSZ coatings [4], [5]. However, despite these challenges, the comparison across the five structures and the combination of materials and defects exhibits a consistent trend relative to the experimental values, as illustrated in Figure 6.

It is crucial to emphasize that, while the simulation may not capture all microscopic details, the trends observed align closely with the experimental outcomes. Notably, the simulated values consistently demonstrate a similar standard deviation, remaining below 5% for the largest standard deviation observed. This consistency underscores the precision and reliability of the image analysis procedure applied across various regions and structures, revealing a relatively low deviation.

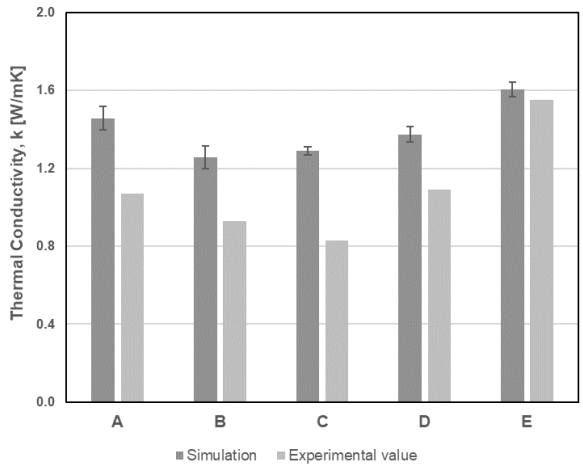

Figure 6. Simulation and experimental results of effective thermal conductivity of various multilayer TBCs.

The deviation between simulated results and reported experimental values can be attributed to several factors. These include: (a) the oversight of contact resistance among splats of both similar and dissimilar materials; (b) the utilization of user-defined threshold values for image processing, introducing subjectivity in separating pores and cracks; (c) a two-dimensional approximation of the model, which, given the three-dimensional nature of thermal conductivity, introduces limitations when adapting the model to a 2D microstructure; and (d) an insufficient number of elements in the mesh, leading to an inaccurate representation of cracks, pores, and material transitions that impact heat flow barriers. In this study, a quantitative method has been rigorously employed to address the issue of image processing, identifying defects and phases with defined ranges for shapes and grayscale to minimize user bias in the analysis. Additionally, the OOF-2 tool has been instrumental in meshing interfaces between defects and bulk material, as well as between dissimilar materials, contributing to a more accurate representation of the complex thermal barrier coating system.

As depicted in Figure 6, coatings B and C exhibit the lowest thermal conductivity, primarily attributed to the high porosity of the porous GDZ and YSZ layers, respectively, serving as effective thermal barriers to heat flow. In contrast, configurations A and E display higher conductivity due to a reduced number of defects. Configuration E demonstrates the highest thermal conductivity, likely owing to its low porosity percentage and overall high density [1]. Supporting this observation, Table 3 provides the percentage of defects per configuration, while Figure 6 illustrates the temperature distribution. The average defect percentage has been categorized into horizontal cracks, vertical cracks, and globular pores, with horizontal cracks identified as the defects most influential in relation to heat flow in the through thickness direction.

Table 2. Average defects percentage measured by Image Analysis on multilayers A-E. Dark black regions are compared to the coating area to obtain the percentage of defects of each composite. Nominal values of the general percentage of defects are comparable to typical TBCs.

	Percentage of defects (%)			
Group	General	Horizontal cracks	Vertical Cracks	Globular Pores
A	4.46 ± 1.24	0.91 ± 0.13	1.11 ± 0.27	2.48 ± 0.25
B	6.15 ± 0.72	2.62 ± 0.27	1.91 ± 0.29	1.67 ± 0.13
C	6.70 ± 0.18	3.68 ± 0.21	1.52 ± 0.27	1.54 ± 0.10
D	3.30 ± 0.48	0.67 ± 0.16	1.56 ± 0.12	1.07 ± 0.14
E	2.58 ± 0.31	0.29 ± 0.08	1.20 ± 0.18	1.26 ± 0.04

Figure 7 illustrates the image analysis and simulation of thermal gradients in the various multi-layer coating systems. The figure comprises original SEM images, followed by image analysis, segmentation, and defect identification. Subsequently, segments are meshed using the OOF-2 tool, depicting thermal gradient results through the thickness. The top boundary of the TBC is fixed at 400°C, while the bottom boundary remains fixed at 25°C. The thermal gradient reveals an intensified effect of thermal resistance due to horizontal micro-cracks. Notably, in cases A, B, and C, elevated temperatures persist in regions preceding the appearance of numerous horizontal defects. This effect is most pronounced in B and C, whereas in cases D and F, temperatures distribute more uniformly or linearly from top to bottom in a steady state.

This analysis highlights the significant variation in thermal gradients among different coatings, potentially influencing thermal stresses. While this study does not address thermal gradients in thermomechanical stresses, it emphasizes that the presence of defects can markedly alter the thermal barrier effects of various coatings in preserving substrate materials.

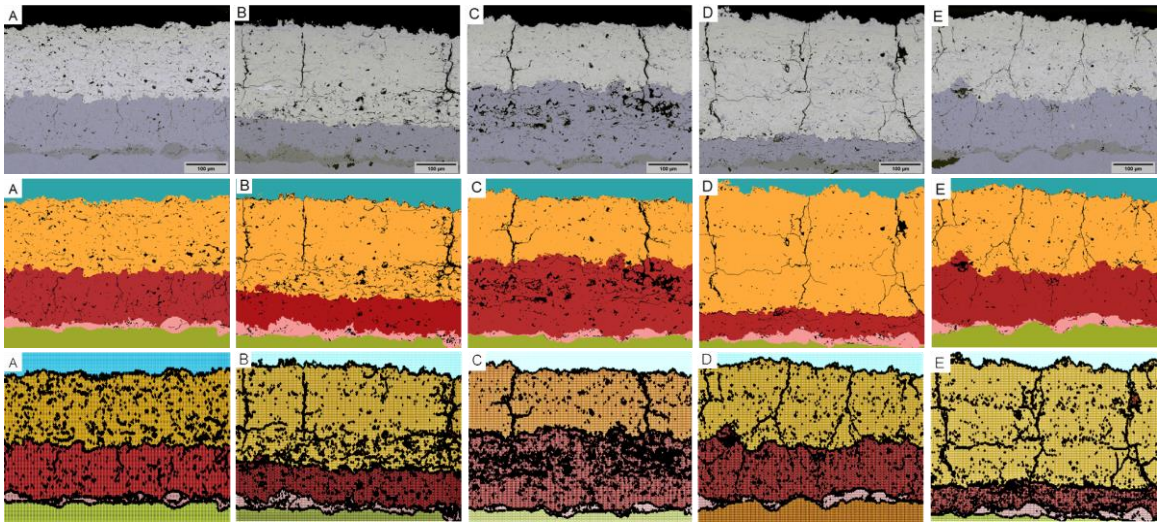

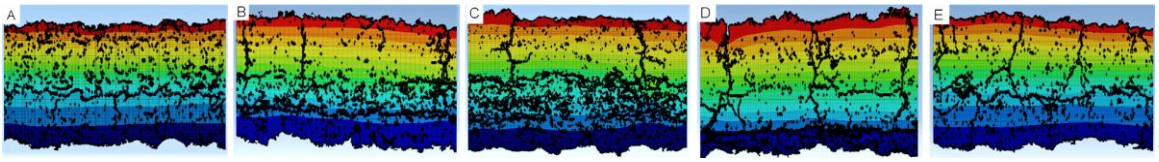

Figure 7. Image analysis and simulation of thermal gradients in multilayer/multimaterial coating system A-E, including their respective thermal conductivities and pore-crack architecture. The temperature is fixed in the top boundary layer at 400°C and at the bottom boundary layer at 25°C. The first row shows the original version of the images, second row presents the image analysis including segmentation and defect identification. The third row shows the images with their respective mesh using OOF-2 tool, and the fourth row shows the FEA results of the temperature gradient through the thickness considering the influence of thermal conductivity of the materials, and thermal resistance of cracks and pores.

Observations of thermal gradients indicate that distinct regions within the multilayered TBC serve as varying thermal barriers, with different defects playing specific roles as thermal resistors. Through modeling and image segmentation, a more in-depth analysis becomes possible, allowing each contributing factor to be quantified in terms of reduced thermal conductivity.

Figure 8 exemplifies this approach, focusing on the thermal conductivity of sample C (**top layer**: dense vertically cracked GDZ-DVC; **mid-layer:** YSZ porous, **bottom layer:** YSZ dense). The impact of each type of defect within a single layer can be precisely analyzed, shedding light on their individual effects on the overall thermal conductivity.

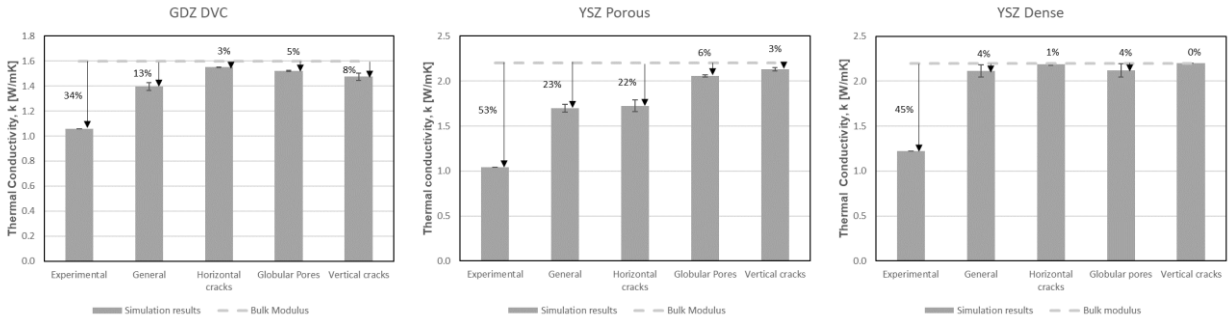

Figure 8. Effect on thermal conductivity by type of defect in all the layers of the multilayer-C (top layer: dense vertically cracked GDZ-DVC; mid-layer: YSZ porous, bottom layer: YSZ dense).

Figure 8 illustrates the decrease in thermal conductivity compared to bulk conductivity as a reference (dotted line), with experimental results of thermal conductivity for individual layers published by Viswanathan et al. [1]provided for comparison. In Figure 8a, it is evident that vertical cracks contribute the most to the decrease in conductivity, primarily due to their abundance in the image and the branching nature of these defects, which creates horizontal barriers. The overall impact ranges from 8% to a maximum of 13% when considering all defects. Notably, the experimental value for this single layer is lower than the simulation result (34% of the bulk), a deviation attributed to the factors discussed earlier.

For the layer composed of porous YSZ, as depicted in Figure 8b, horizontal cracks exert the most significant effect on thermal conductivity reduction (22%), while vertical cracks and globular pores have minimal influence. The total predicted reduction is 23%, whereas the measured thermal conductivity indicates a 53% reduction compared to the bulk. Moving to Figure 8c, the dense YSZ layer, where image analysis predominantly identifies globular pores, the simulation underscores the predominance of these pores as thermal barriers. The reduction in bulk property measured in a single layer was 45%, while the predicted reduction was only 4% less than the bulk. This layer presents a potentially less accurate prediction from simulation.

From the finite element analysis (FEA), it is observed that horizontal defects have the most significant impact on conductivity decrease when they are present in large percentages (Figure 8b). Although similar trends cannot be conclusively drawn from the other layers, this analysis enables the identification of deviations from different sources per layer. Considering that the decrease in thermal conductivity due to various defects is a complex phenomenon given the nature of heat flow and the presence of barriers that determine varying temperature fields, the modeling work by FEM approaches remains one of the best predictions for property and performance assessment, despite the acknowledged limitations.

To ensure methodological consistency, Figure 9 assesses the predicted thermal conductivity for identical layers deposited in various multi-layer systems, allowing for cross-system comparisons. In Figure 9a, the thermal conductivity of GDZ-TBC is analyzed across systems A-E. Likewise, Figure 9b examines YSZ dense, and Figure 9c focuses on YSZ-DVC. While there remains a notable disparity between the simulated and experimentally measured thermal conductivity, a relatively strong consistency is evident in the simulation results across different coatings and layers. The observed variation falls within acceptable standard deviations. Assuming optimal similarity in processing conditions for depositing these diverse layers, the research procedures employed in this paper demonstrate a notably high consistency in the analysis between images from different coating systems and within images or portions of the same multi-layer system.

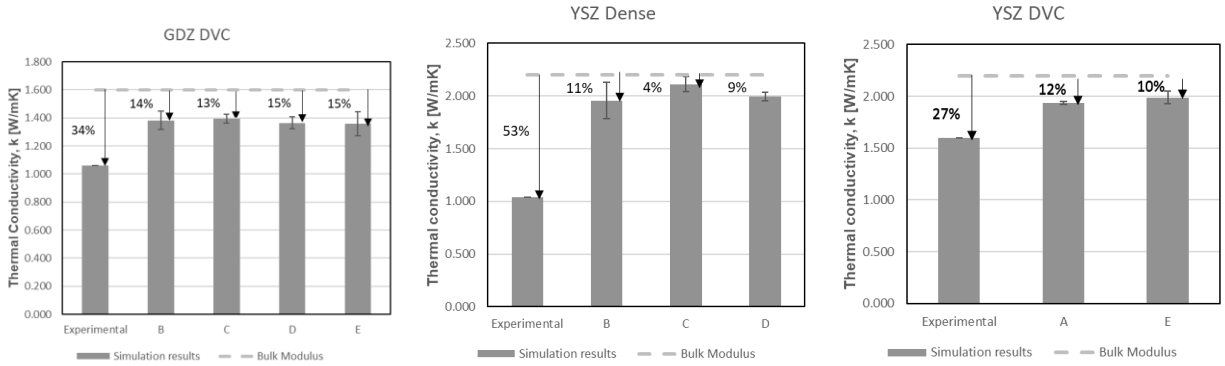

Figure 9. Comparison of the thermal conductivity based on the material of the multilayer configuration

While the methodology has demonstrated high performance in predicting the reduction of thermal conductivity attributable to various structural elements (defects -pores, microcracks, vertical cracks, dissimilar materials, etc.), it acknowledges the inherent challenge of predicting perfect property values. Nevertheless, the research methods employed, coupled with comparisons to actual properties, instill confidence in progressing to the next analysis of thermomechanical stresses. In this context, where direct property comparisons may be unfeasible, the prediction of stresses will be correlated with performance tests (burner rig test), as presented in the subsequent section.

Thermomechanical FE Simulations

In Figure 10, the thermomechanical stress analysis unfolds throughout the heating cycle, considering the expansion of the substrate material, bond coat, TGO, and TBC, and accounting for their inherent expansion mismatches, resulting in thermal residual stresses. The model, symmetric with respect to the left-hand axis, undergoes a rightward displacement of nodes on the right-hand side during heating. Expansion is also considered along the *y*-positive axis, causing nodes to move upwards (not presented here for brevity).

The *x*-positive axis displacement is visually represented by the rightward movement of nodes until the conclusion of heating (H1), with subtle variations persisting by the end of the holding time (H2). During the cooling phase, the displacement diminishes (C). Notably, inelastic phenomena occur in the bond coat, contributing to a residual change in displacement and generating residual stresses. The representation in Figure 10, corresponding to the multilayered sample “C”.

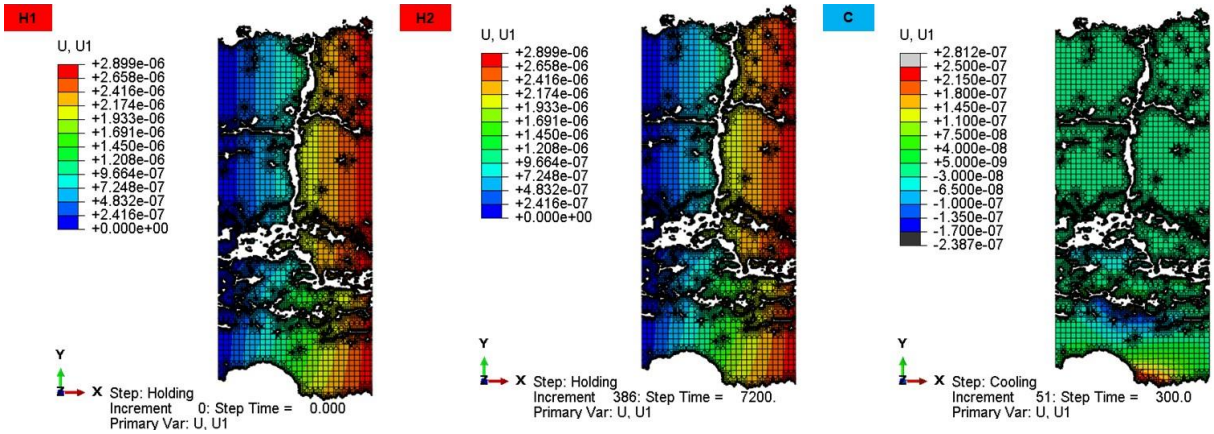

Figure 10. Simulation results of *x*-axis displacement for coating sample C. The illustration depicts rightward movement of nodes, progressing from the initiation of heating (H1) through the end of the holding time (H2) and concluding at the end of the cooling phase (C)

In Figure 11, the presentation of residual stresses and strain energy corresponding to the multilayered sample C is presented. S11 stresses, representing in-plane stresses, predominantly exhibit tension, attributed to the larger expansion of the substrate material compared to the TBCs. This tension is further influenced by the yielding and creep of the bond coat, resulting in high tensile stresses in the TBC near the TGO and marginal compressive stresses in the coating at the end of heating. Throughout the holding period, slight stress variations occur due to bond coat creep, and by the end of cooling, the stresses predominantly transition into compression, driven by the substrate material contracting more than the ceramic TBC. Stress concentrations are notable near the TGO interface, with tensile stresses at the TBC-TGO interface peak and compressive stresses in the valley zone.

Regarding S22 stresses in the through-thickness direction, values are nearly null or negligible at the end of heating and holding, except near the TBC-TGO interface. By the end of cooling, stresses grow significantly at the TBC-TGO interface peak in tension and in compression in the valley zone. The coating's structure, inclusive of porosity, microcracks, and vertical cracks, influences the distribution of S22 stresses, diminishing almost to negligible levels away from the TBC-TGO interface.

Examining strain energy, concentration occurs near the TBC-TGO interface, notably increasing by the end of cooling. Both S22 stresses and strain energy play a key role in causing delamination at the peak of the roughness profile, as the literature provides evidence.

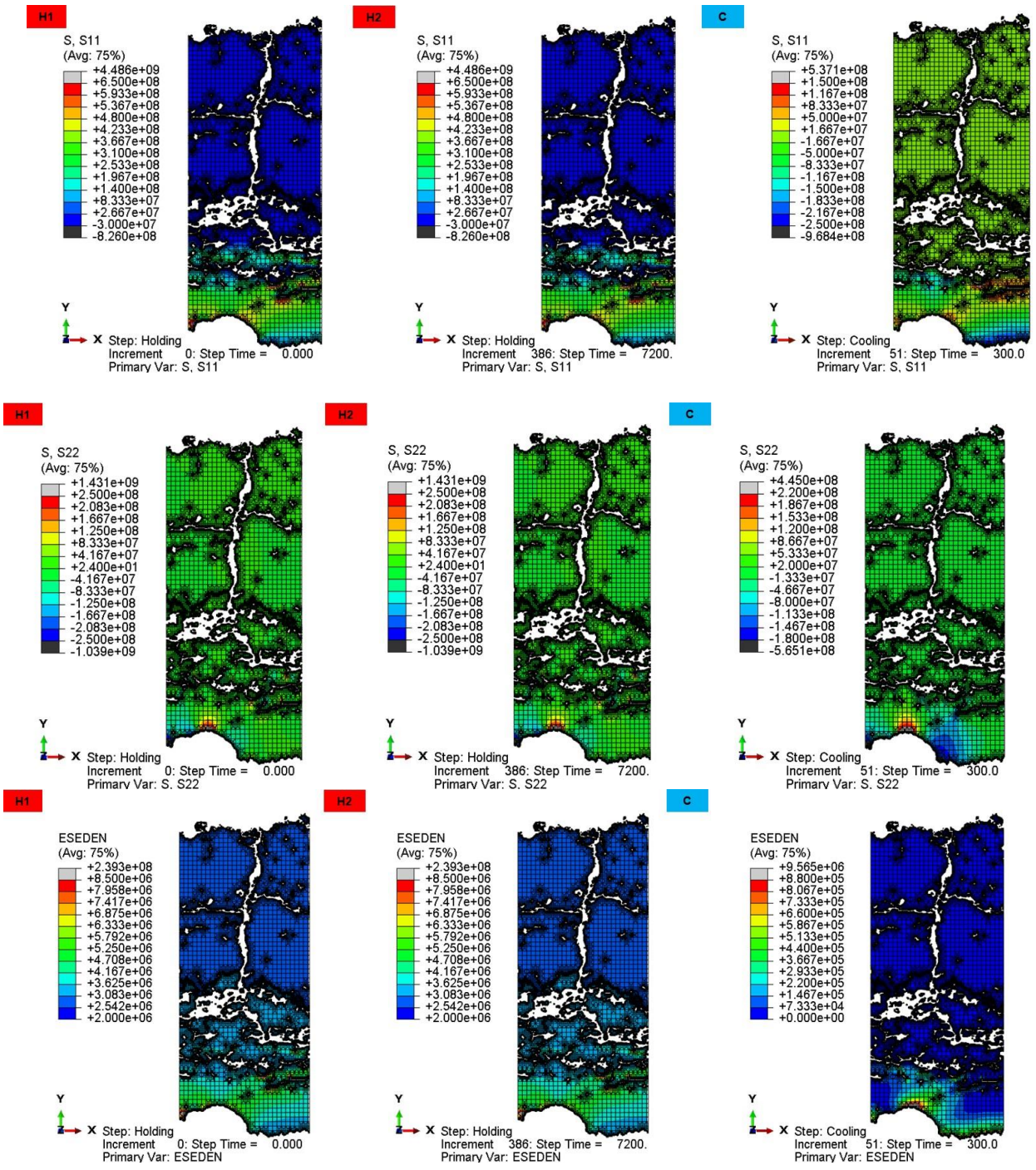

Figure 11. Simulation results illustrating S11 and S22 stresses, along with strain energy (ESEDEN by Abaqus), for multilayered coating C. The presented data corresponds to the end of the heating stage (H1), the end of the holding time (H2), and the conclusion of the cooling stage (C).

In Figures 12 and 13, the analysis of S11-S22 stress and strain energy is presented for coatings A and B, respectively. For the sake of brevity, the analysis for coatings D and E is not presented here. In Figure 12, the coating, structured with a DVC bottom layer followed by a porous layer, exhibits distinct behavior. The presence of the vertical crack allows for significant deformation or compliance, resulting in compressive stresses near the crack during heating, while the top layer experiences tension. Near the TBC-TGO interface,

stress concentrations, particularly near the crack end, are evident. By the end of cooling, S11 stresses become nearly negligible, except in proximity to the interface. S22 stresses exhibit some concentration near the vertical crack, its ends, and the TGO interface during heating and holding stages. At the end of cooling, stresses diminish, with high tensile stresses at the peak of the roughness profile and high compressive stresses in the valleys, specifically at the interface. Strain energy in the DVC region is lower due to the compliance provided by the cracked deformation, whereas strain energy increases in the top layer. By the end of cooling, strain energy concentrates primarily at the TGO-TBC interface.

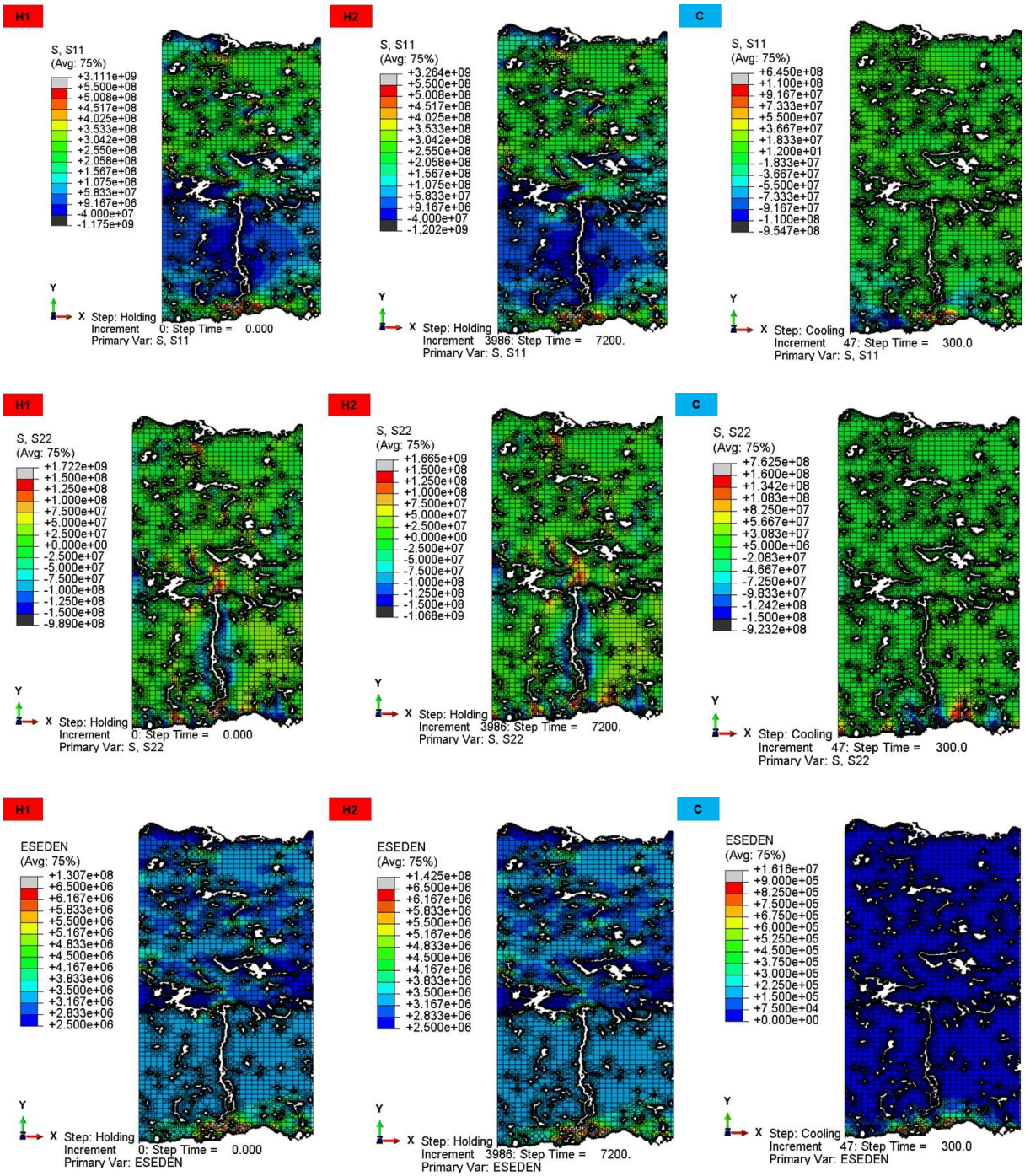

Figure 12. Simulation results illustrating S11 and S22 stresses, along with strain energy (ESEDEN by Abaqus), for multilayered coating A. The presented data corresponds to the end of the heating stage (H1), the end of the holding time (H2), and the conclusion of the cooling stage (C).

In Figure 13, coating B undergoes a similar analysis. For S11 stresses, a pattern akin to coating C is observed. However, the transition between the dense first layer and the porous layer exhibits a distinct feature due to the material shift from YSZ to GDZ. Tensile stresses manifest in the YSZ, sharply transitioning at the YSZ-GDZ interface to compressive. In the top DVC-GDZ layer, compressive stresses are observed. The behavior remains largely similar during holding, while during cooling, stresses concentrate at the TBC-TGO profile, where S11 compressive stresses concentrate in the valleys while some tensile stresses concentrate at the peaks.

Concerning S22 stresses, concentration occurs primarily near the TBC-TGO interface, resembling the previously described behavior. Peaks exhibit compressive tensile stresses, and valleys display compressive stresses, intensifying towards both more compressive and more tensile states by the end of cooling. The strain energy during heating and holding concentrates in the dense YSZ, with larger values at the TBC-TGO interface. This strain reduces during cooling while retaining significant strain energy at the TBC-TGO interface, recognized as the critical point for failure.

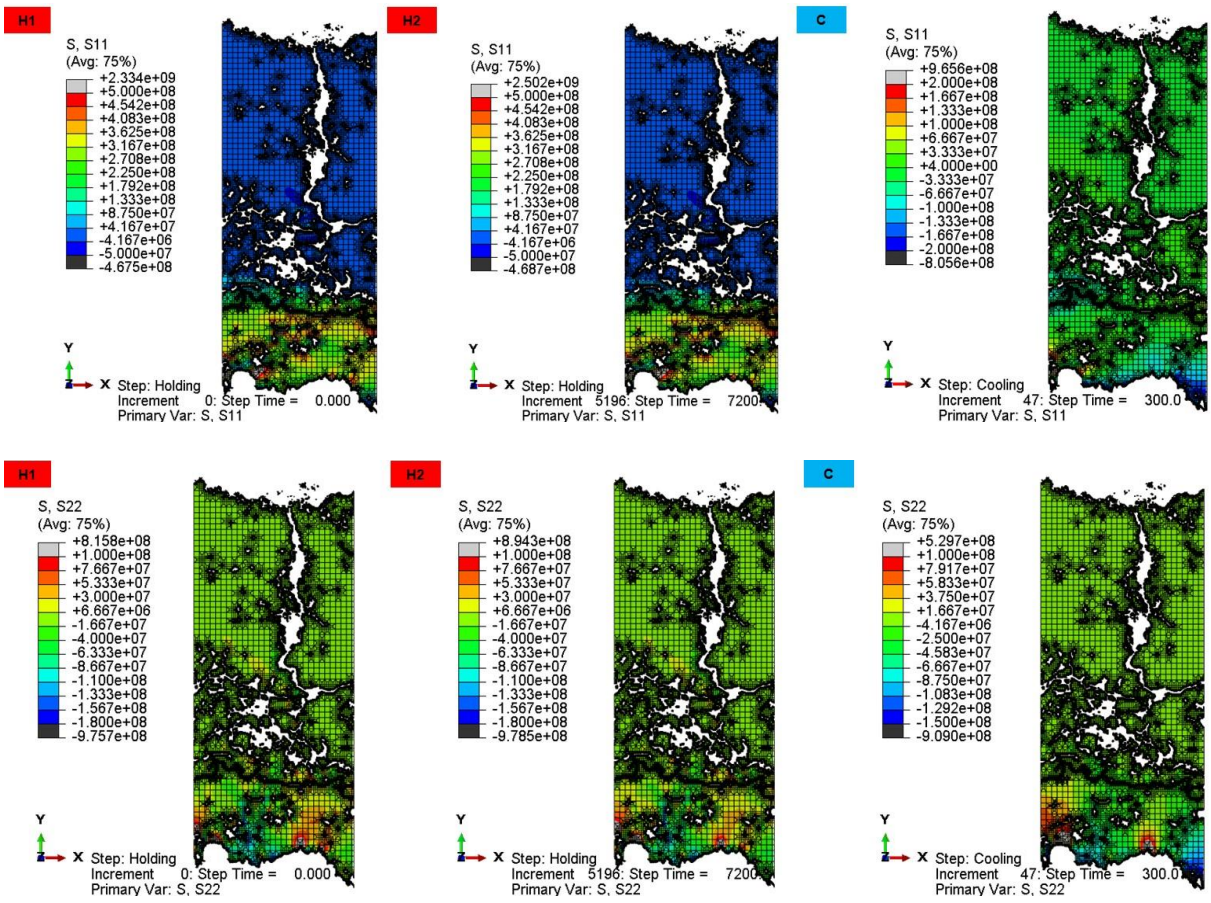

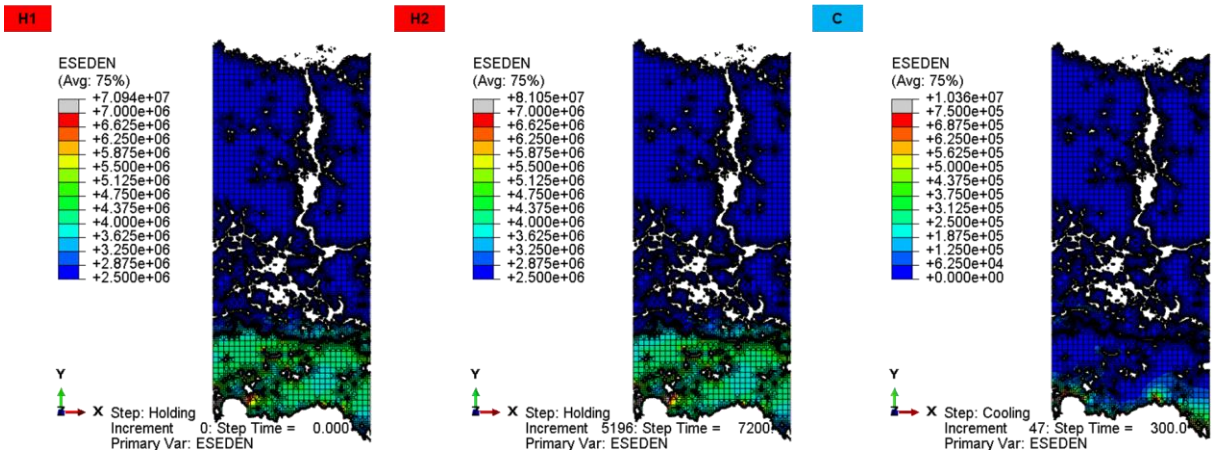

Figure 13. Simulation results illustrating S11 and S22 stresses, along with strain energy (ESEDEN by Abaqus), for multilayered coating B. The presented data corresponds to the end of the heating stage (H1), the end of the holding time (H2), and the conclusion of the cooling stage (C).

In Figure 14, the discussion centers on the relationship of the failure locus of coatings A, B, and C in relation to the elastic strain energy computed as average values obtained from the strain energy maps. Coatings A and B experience failure at the GDZ-YSZ interface, with this interface registering strain energy values between 30 to 40 J/m^2. In contrast, coating C, failing at the YSZ-TGO interface, exhibits remarkably low strain energy in the GDZ at the same GDZ-YSZ interface.

According to the burner-rig tests, coating C demonstrates a significantly longer lifetime compared to B and A, as per Viswanathan et al.'s results [1]. Coating A, identified as the least performing before the tests, registers the highest strain energy at the GDZ-YSZ interface among the three coatings. Given GDZ's lower fracture toughness, it is hypothesized that once GDZ reaches a threshold of elastic strain energy, along with other potential factors such as large S22 tensile stresses during heating, the coating may undergo delamination.

In coatings B and C, both featuring GDZ-DVC top layers, the transition for C occurs from a porous YSZ to a DVC-GDZ, while for B, the transition is from dense YSZ to porous GDZ. It is hypothesized that the porous GDZ, with lower fracture toughness, may delaminate at this transition point, reaching the threshold of strain energy. Coating C endures longer as strain energy is concentrated in the denser YSZ coating, expected to possess higher fracture toughness. Transitions from one material to another, especially through a porous YSZ in this case, significantly reduce strain energy at the interface of two dissimilar materials (YSZ-GDZ). Those being the reasons why coating C has an improved performance even compared to traditional single layer YSZ-TBCs.

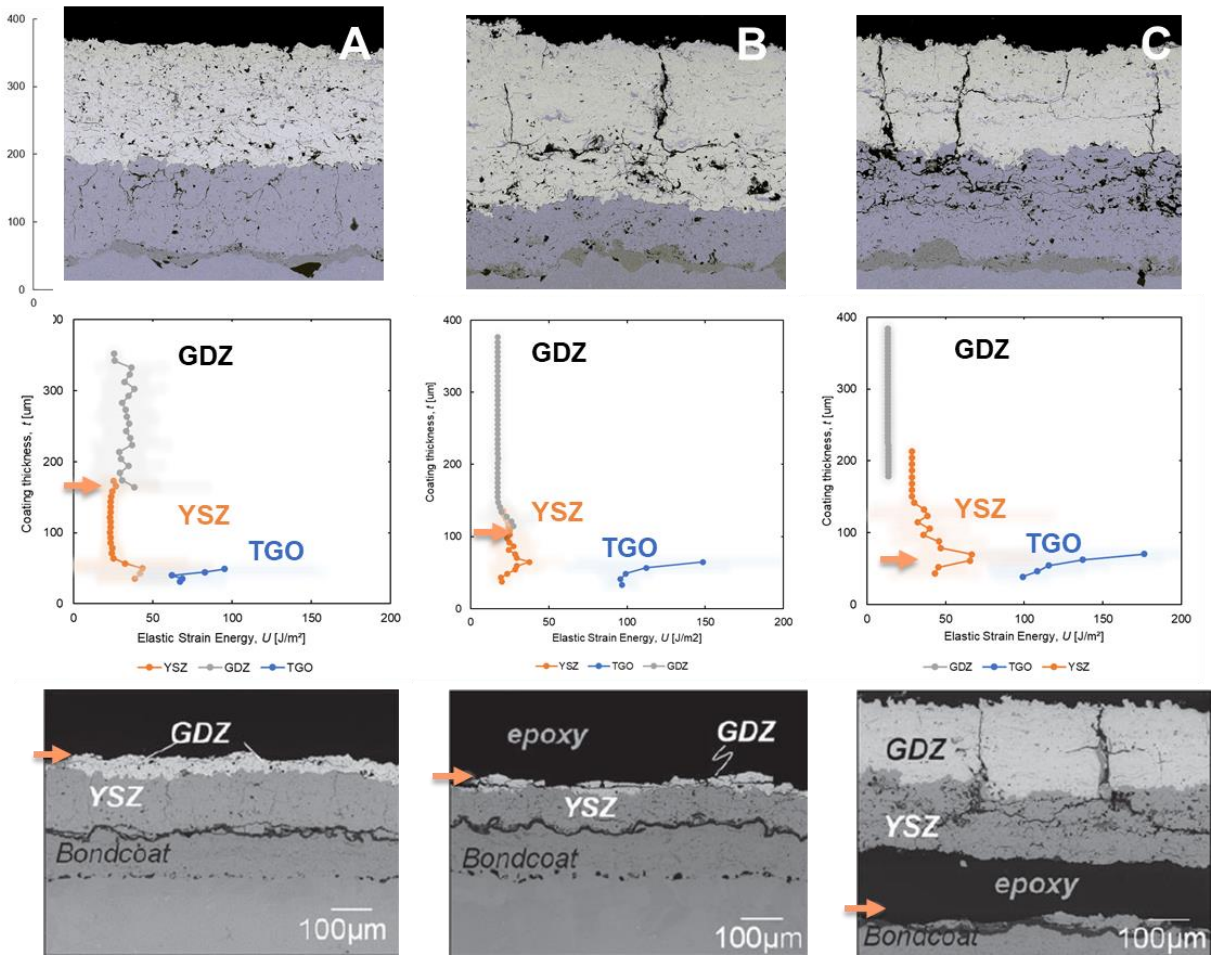

Figure 14. Comparative analysis of multilayered coatings A, B, and C. The figure includes original SEM images showing the distance through the thickness; the elastic strain energy changes through the thickness in the TGO, YSZ, and GDZ materials; and the locus of failure, as per Vaishak et al., to illustrate the region of failure.

The current FEA analysis, characterized by a detailed examination of the microstructure encompassing material segmentation, interface identification, and the discernment of features such as vertical cracks, microcracks, and pores, significantly enhances our comprehension of the underlying factors driving the failure of TBC coatings. The thorough depiction of various microstructural elements contributes to a nuanced understanding of residual stress and strain energy distributions throughout the coating thickness. It is emphasized that each microstructural feature plays a role in redistributing stresses and strain energy, particularly important at the material interfaces where the mismatch of thermal expansion heightens the likelihood of failure.

The application of FEA is critical in revealing sharp transitions between areas with distinct characteristics, overcoming limitations inherent in previously employed analytical methods [1]. Although the current approach does not include certain concurrent phenomena, such as sintering, TGO growth, or thermal gradients, its demonstrated potential in unraveling the mechanics of the coating empowers designers to make informed judgments for the development of enhanced performance designs.

Conclusions

This paper introduces an effective procedure for image processing and subsequent FEA to determine the effective thermal conductivity and thermal residual stresses in five distinct multilayered TBCs. The applied procedures enable the investigation of the impact of various defects (horizontal microcracks, vertical cracks, globular pores, and interfaces) on reducing thermal conductivity. The analysis successfully predicts the overall trends in thermal conductivity, aligning with experimental results. Notably, horizontal cracks emerge as the predominant defect responsible for reducing through-the-thickness thermal conductivity while simultaneously introducing mechanical compliance that mitigates thermal residual stresses.

The thermomechanical analysis identifies zones prone to failure, in concordance with experimental results, particularly at the material interfaces YSZ-TGO and YSZ-GDZ. Stresses (S11 and S22) and strain energy concentrate at these interfaces, with a more significant impact observed at the YSZ-TGO interface due to larger thermal expansion mismatch and compliance differences. Importantly, the lower fracture toughness of GDZ compared to YSZ means even smaller stress or lower strain energy can precipitate failure at the GDZ interface (on the GDZ side) first. The results validate the adequacy of the computational procedures and highlight the methodology's strength in identifying potential failure zones.

References

[1] V. Viswanathan, G. Dwivedi, and S. Sampath, “Multilayer, multimaterial thermal barrier coating systems: Design, synthesis, and performance assessment,” *J. Am. Ceram. Soc.*, vol. 98, no. 6, pp. 1769–1777, 2015, doi: 10.1111/jace.13563.

[2] D. Zhou, D. Sebold, D. Emil, M. Emine, O. Guillon, and R. Vaßen, “Thermal cycling performances of multilayered yttria-stabilized zirconia / gadolinium zirconate thermal barrier coatings,” no. September 2019, pp. 2048–2061, 2020, doi: 10.1111/jace.16862.

[3] P. G. Lashmi, P. V Ananthapadmanabhan, G. Unnikrishnan, and S. T. Aruna, “Journal of the European Ceramic Society Present status and future prospects of plasma sprayed multilayered thermal barrier coating systems,” *J. Eur. Ceram. Soc.*, vol. 40, no. 8, pp. 2731–2745, 2020, doi: 10.1016/j.jeurceramsoc.2020.03.016.

[4] Y. Tan, J. P. Longtin, and S. Sampath, “Modeling Thermal Conductivity of Thermal Spray Coatings: Comparing Predictions to Experiments,” *J. Therm. Spray Technol.*, vol. 15, no. December, pp. 545–552, 2006, doi: 10.1361/105996306X147216.

[5] A. a. Kulkarni *et al.*, “Advanced Microstructural Characterization of Plasma-Sprayed Zirconia Coatings Over Extended Length Scales,” *J. Therm. Spray Technol.*, vol. 14, no. 2, pp. 239–250, 2005, doi: 10.1361/10599630523818.

[6] R. Ghafouri-Azar, J. Mostaghimi, and S. Chandra, “Modeling development of residual stresses in thermal spray coatings,” *Comput. Mater. Sci.*, 2006, doi: 10.1016/j.commatsci.2005.02.007.

[7] P. Michlik and C. Berndt, “Image-based extended finite element modeling of thermal barrier coatings,” *Surf. Coatings Technol.*, vol. 201, no. 6, pp. 2369–2380, 2006, doi: 10.1016/j.surfcoat.2006.04.003.

[8] A. Ganvir, C. Kumara, M. Gupta, and P. Nylen, “Thermal Conductivity in Suspension Sprayed Thermal Barrier Coatings: Modeling and Experiments,” *J. Therm. Spray Technol.*, vol. 26, no. 1–2, pp. 71–82, 2017, doi: 10.1007/s11666-016-0503-8.

[9] M. Guven Gok and G. Goller, “State of the Art of Gadolinium Zirconate Based Thermal Barrier Coatings: Design, Processing and Characterization,” in *Methods for Film Synthesis and Coating Procedures*, Intechopen, 2019. doi: 10.5772/intechopen.85451.

[10] J. Aktaa, K. Sfar, and D. Munz, “Assessment of TBC systems failure mechanisms using a fracture mechanics approach,” *Acta Mater.*, vol. 53, no. 16, pp. 4399–4413, 2005, doi: 10.1016/j.actamat.2005.06.003.

List of Symbols, Abbreviations and Acronyms

TBCs	Thermal Barrier Coatings
YSZ	Yttria Stabilized Zirconia
GDZ	Gadolinium Zirconate
OOF	Object oriented finite element.
FEA	Finite element analysis
DVC	Dense Vertically Cracked
CMAS	Calcium-Magnesium-Aluminosilicates

Appendix 3:

Presentation at International Materials Research Conference, August 15th 2023. Cancún Mexico. Entitled:
RESIDUAL STRESSES AND ELASTIC STRAIN ENERGY IN MULTILAYERED/MATERIAL TBCS: THEIR RELATIONSHIP TO FAILURE.

CÍRCULO DE CUMBAYÁ. P.O.BOX: 17-12-841 QUITO-ECUADOR
T.: (593 2)297-1700 AL 708. FAX.: (593 2)289 0070.
WWW.USFQ.EDU.EC

COLEGIO DE CIENCIAS E INGENIERÍAS

Universidad San Francisco de Quito

Residual Stresses and Elastic Strain Energy in Multi-layered/material TBCs: Their Relationship to Failure

Prof. Alfredo Valarezo

Universidad San Francisco de Quito - Ecuador

Prof. M. Lorena Bejarano, Prof. Marco León, Samantha Criollo, Pedro Reina, Pedro de la Cruz, Diego Morales, Krutskaya Yépez

Collaborations: Prof. Sanjay Sampath, Stony Brook University; Tinker Air Force Base, Consortium of Thermal Spray Technology

IMRC International Materials Research Conference

Cancún, México. August 15th, 2023

USFQ

Ceramic Coatings for Combustion- and Gas Turbine-Engines

Commercial Aviation

Space trips for Civilians

Millitary Aviation

Defense weapons

Power Plants

Batmovil

Industry-Academia Consortium Strategies – Innovation Hub

Consortium is operated by the Center for Thermal Spray Research at Stony Brook University

Jun 2018

Materials in the combustion zone

Modern gas turbines rely on ceramic & ceramic coatings to protect structural components along the hot gas path.

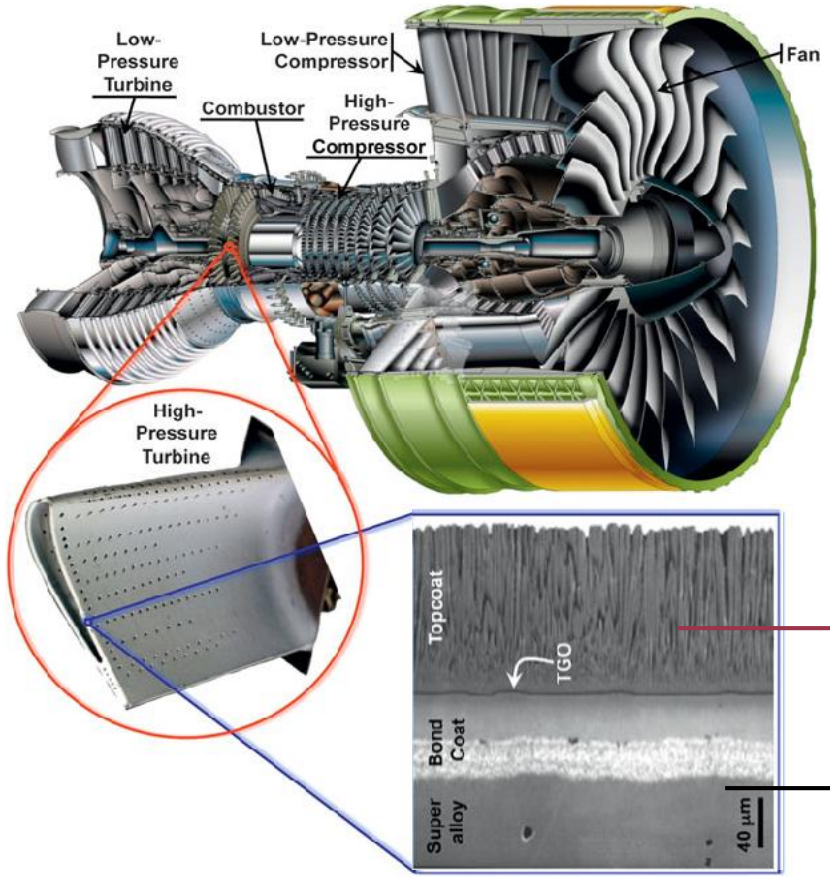

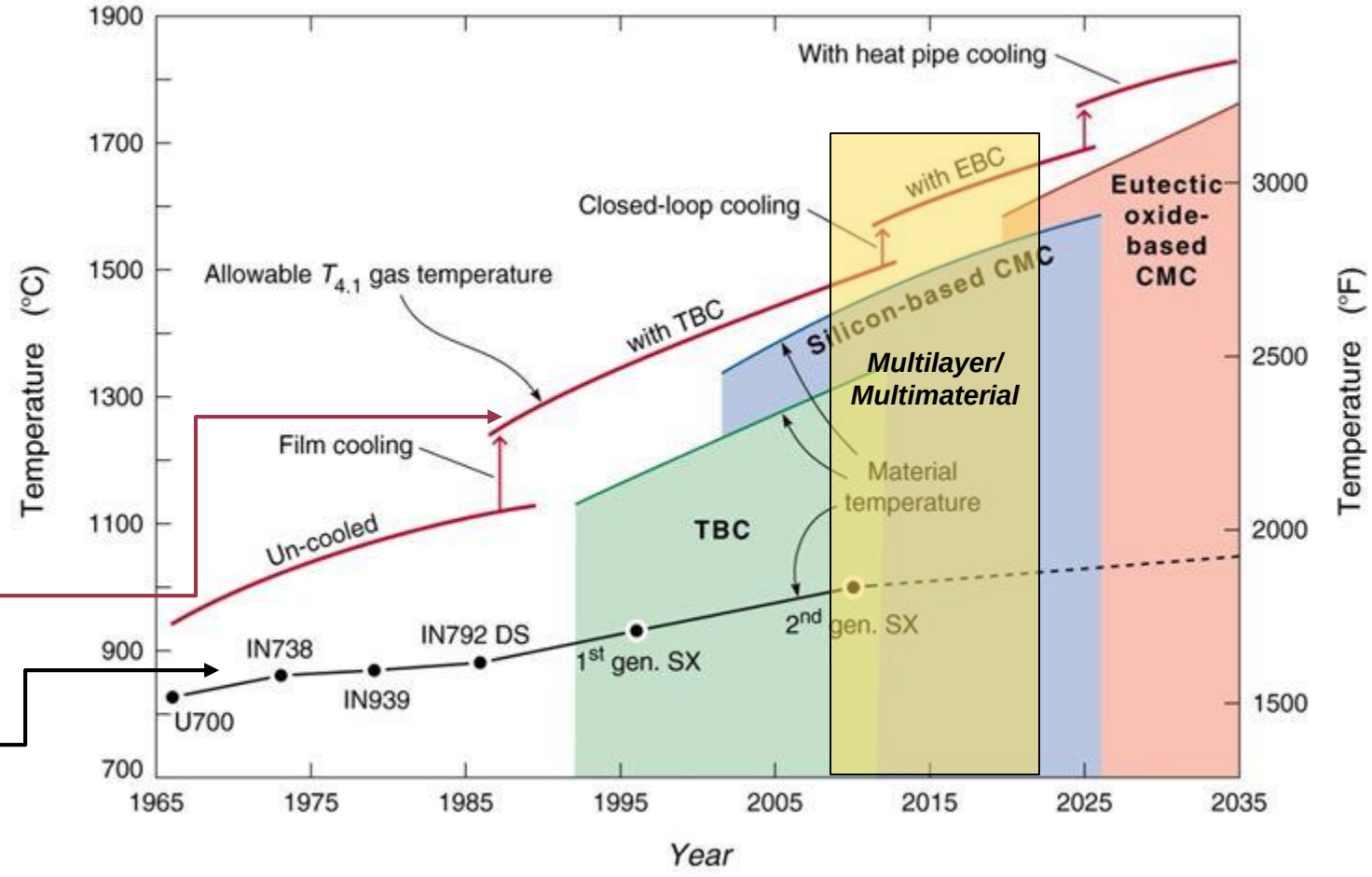

The CMAs Problem

CMAS: term coined to represent compositions involving primarily Ca/Mg/Al/Si oxides, which are, along with Fe oxides, the main components of the earth's crust

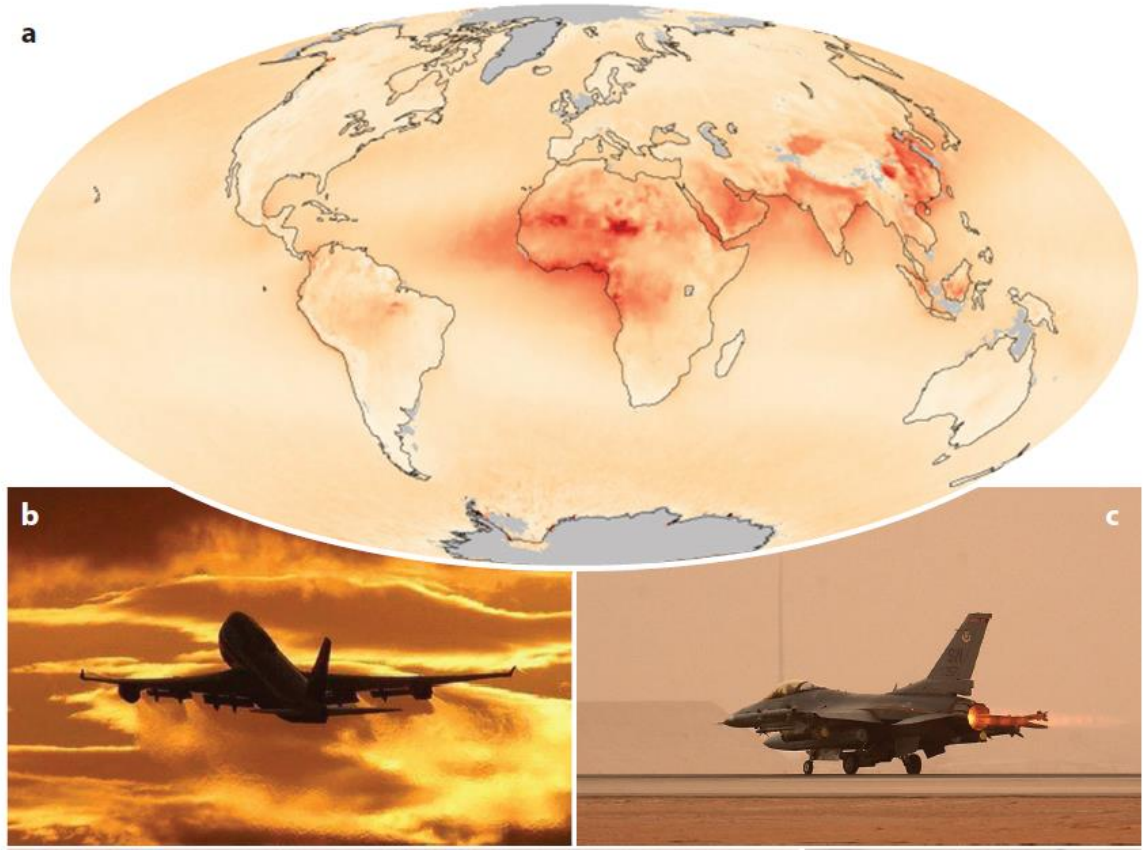

This deposit-induced coating degradation has become increasingly relevant due to increased engine operating temperatures and the growth of air transport within and through the Middle East and Asia.

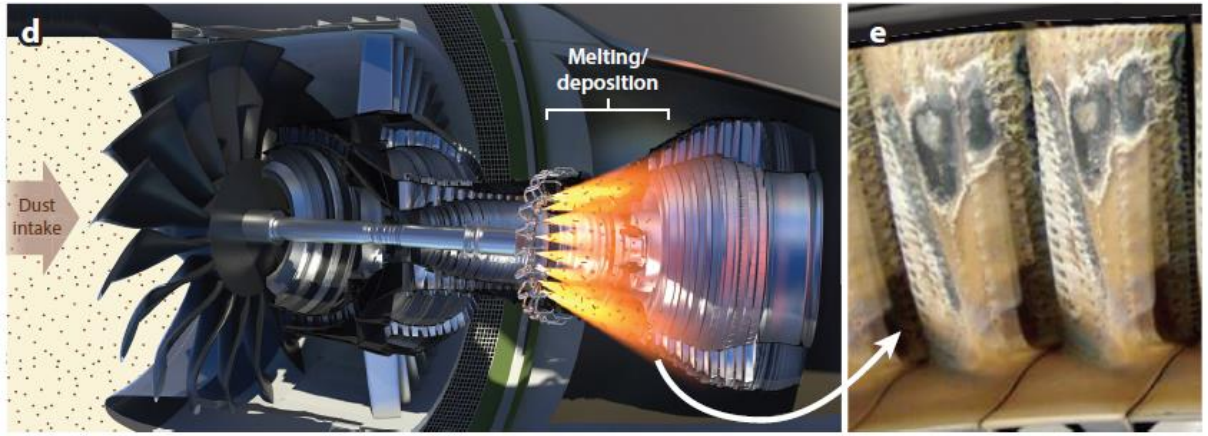

(a) The map in panel, shows average atmospheric aerosol distribution from 2000 to 2010; red indicates the highest concentrations. Image from NASA/Robert Simmon. Engines on (*b*) commercial and (*c*) military aircraft
(d) aircraft regularly ingest particulate debris, which (*d*) melts and deposits on hot section components
(*e*) accelerates coating failure

Plasma Spray Technique to deposit TBC´s

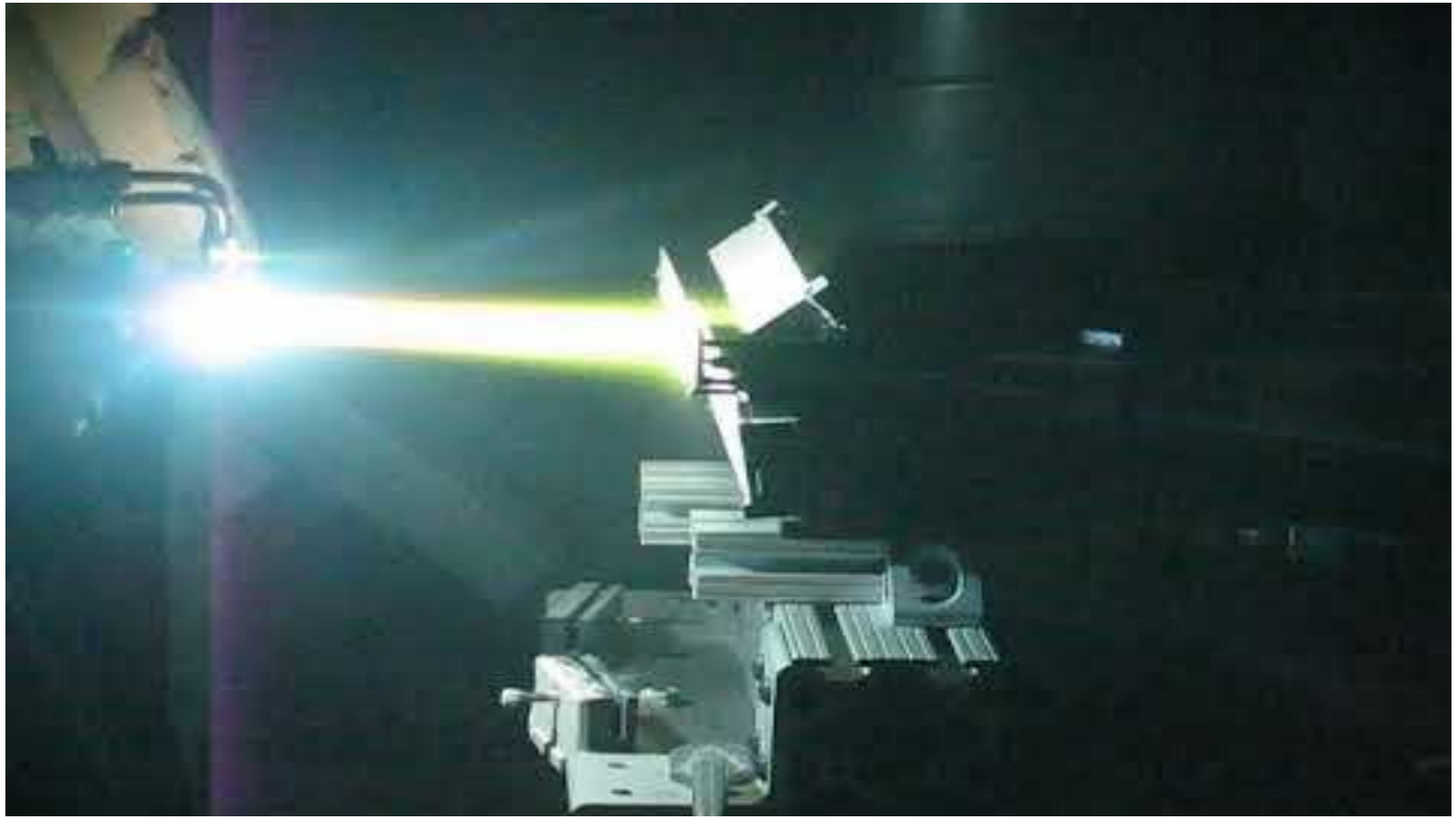

https://youtu.be/zxeFSpKSFMI

Single and Multilayered Strategies with Plasma Spraying

- Newer developments on TBC´s by multilayer design and new material compositions allow to increase the engine efficiency by increasing the operational temperatura beyond the capabilities of Yttria-stabilized zirconia (YSZ).

- Gadolinium Zirconate (GDZ)-based pyrochlore oxides offer lower thermal conductivity, and ability to resist attack by silicate deposits (CMAS). However, GDZ is incompatibility with the TGO layer.

- Multilayer architectures, YSZ–GDZ system, have been proposed by plasma spraying.

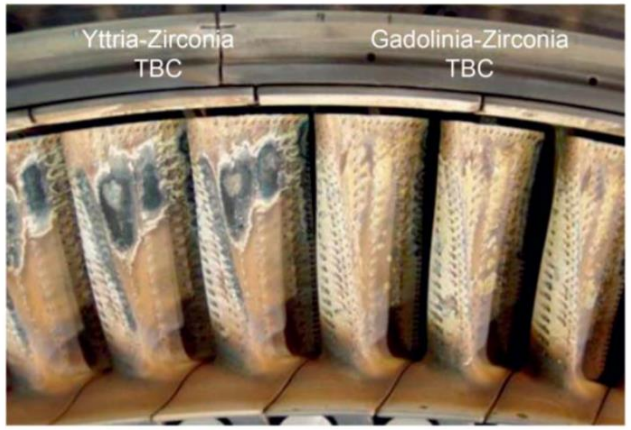

@Pratt-Whitney

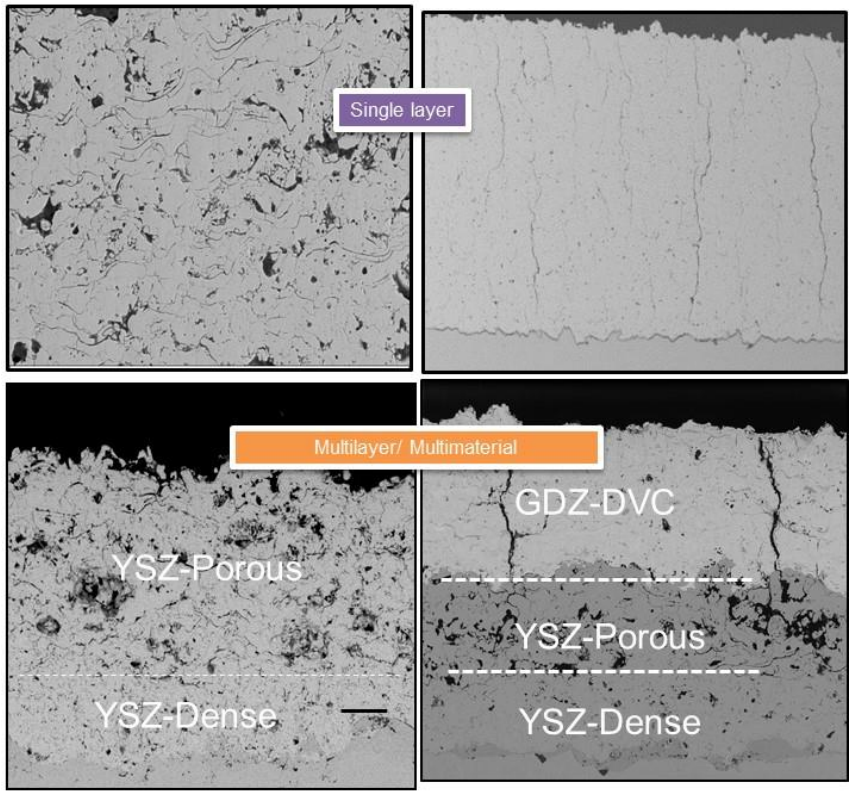

Objective of the Study

Goal of the study

- Determine and analyze the thermo-mechanical behavior of various configurations of multilayered/multimaterial TBCs, using modeling and simulation.

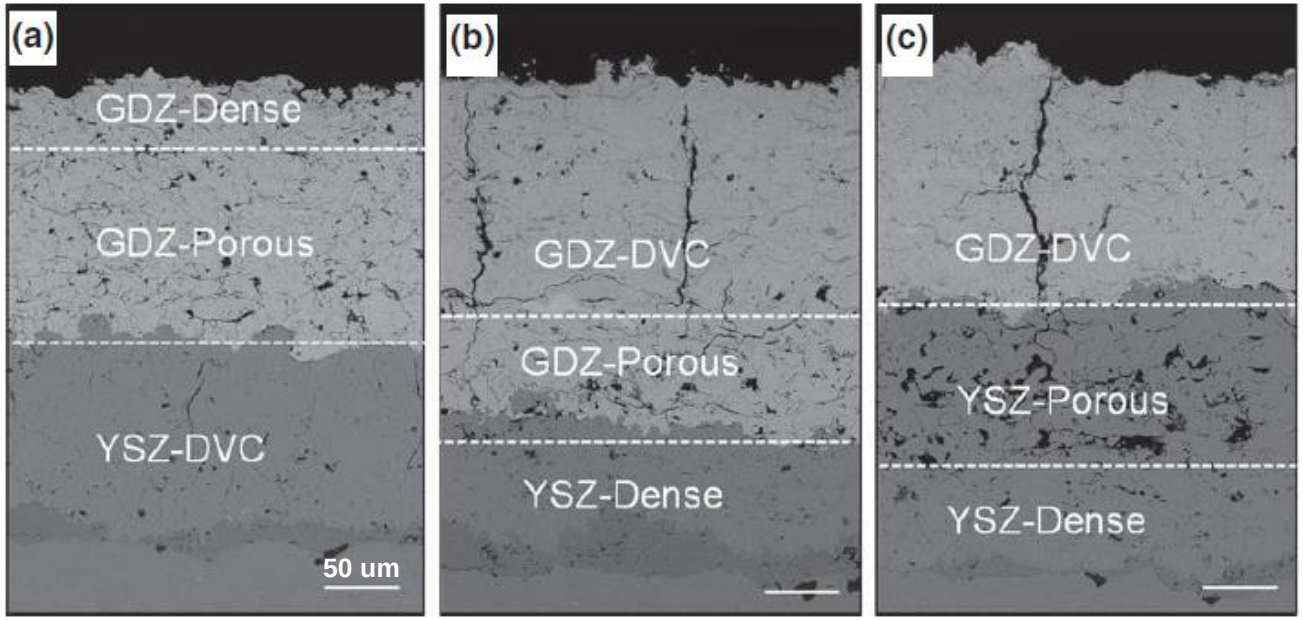

As-sprayed microstructures of the multilayer variants. Three types of YSZ and GDZ microstructures (porous, dense and DVC). GDZ is always on top to offer erosion and CMAS resistance. The micrometer bar represents 50 um.

Specific Objectives

- Determine a correlation between coating lifetime and the thermo-mechanical behavior in regards to the thermo-mechanical loading
- Understand the functionality of the different multilayer configurations of the TBCs, proposed by Viswanathan, et al.
- Test the model to predict the effective thermal conductivity.
- Compare OOF2-ABAQUS simulation to experimental results, and propose failure mechanisms

Viswanathan, et al. Multilayer, Multimaterial Thermal Barrier Coating Systems: Design, Synthesis, and Performance Assessment. J. Am. Ceram. Soc., 1–9

General Method: OOF2, scrypting and ABAQUS

Image Processing

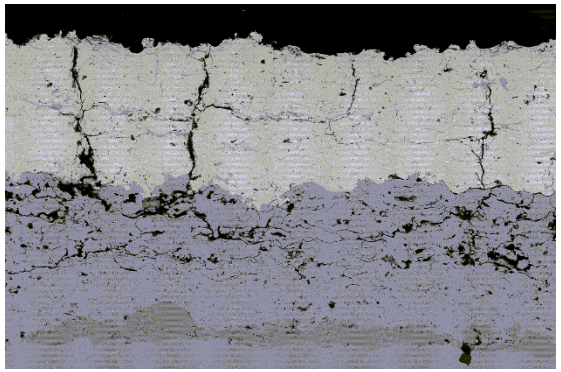

1. TBC multilayer Micrograph

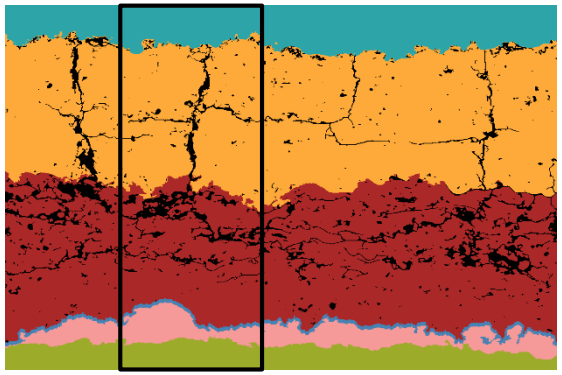

2. Segmented Image

Finite Element Analysis

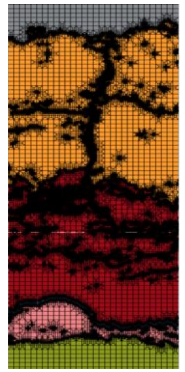

3. Mesh

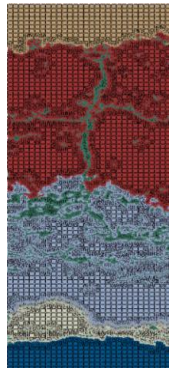

4. Assignment of Properties

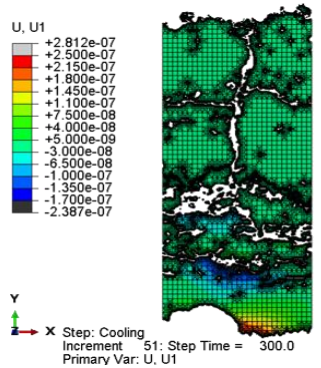

5. Results evaluation

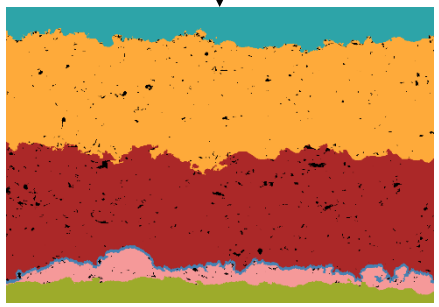

A. Pores

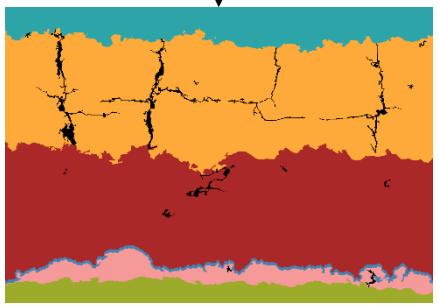

B. Vertical cracks

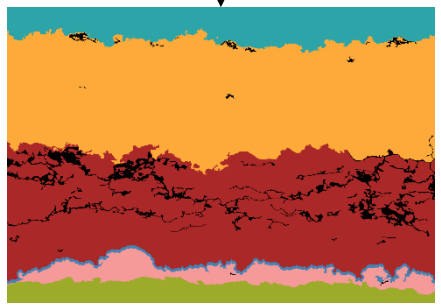

C. Horizontal cracks

Cracks segmentation

Sample C-example: YSZ Dense+GDZ porous and DVC

Image Analysis + OOF2 + FEA

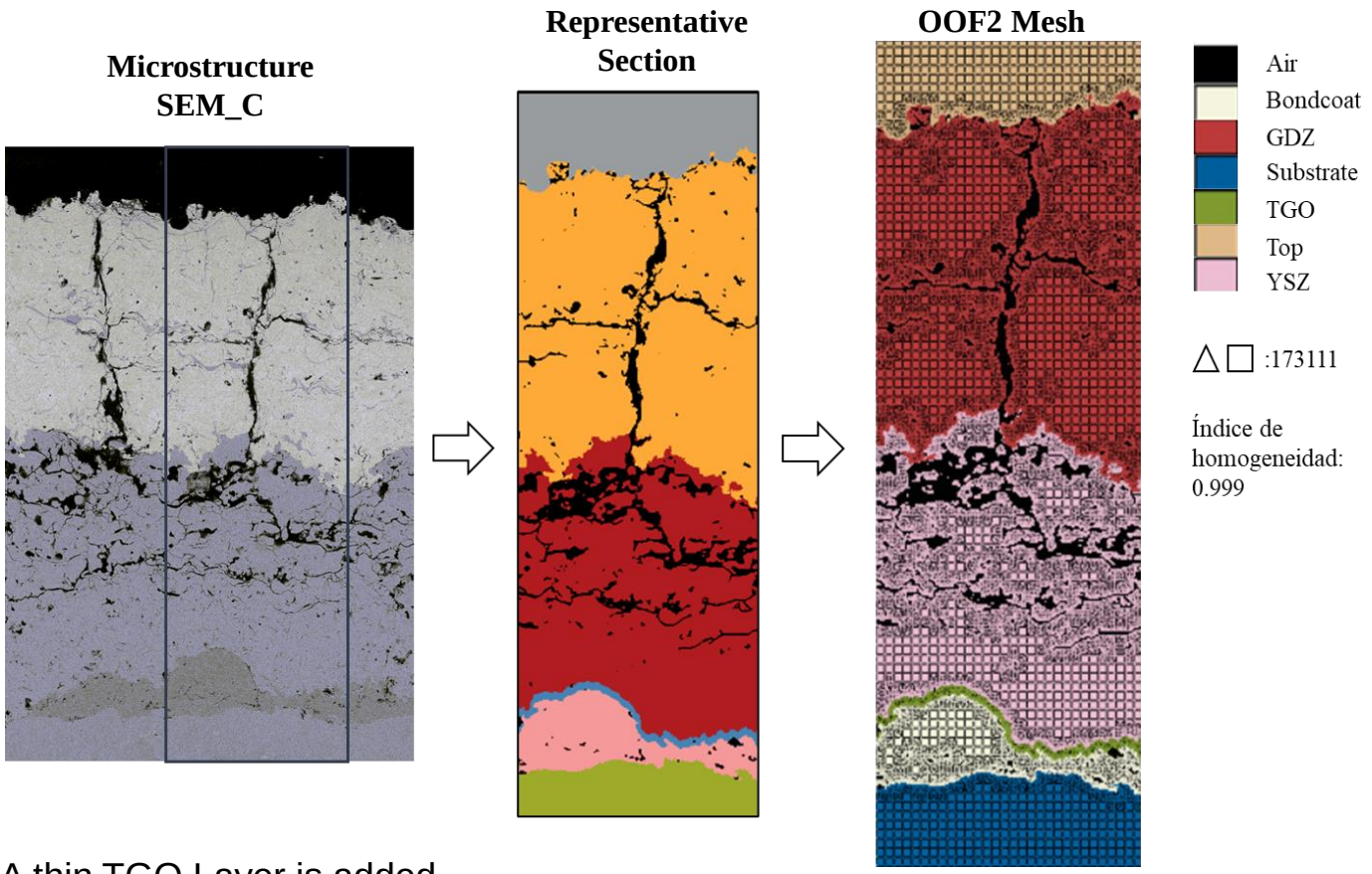

*A thin TGO Layer is added
*A periodic boundary condition (PBC) was set to link the displacement of opposing boundaries in one direction.

Specific Data & Thermal Loading Cycle

Temperature dependent properties

Purely Elastic Materials

- GDZ: Gadolinium Zirconate
- YSZ: Yttria-stabilized zirconia
- TGO: Al2O3
- Substrate: Inconel 617

Elastic Plastic Materials

- Bond Coat: NiCoCrAlY (also stationary creep – Norton Type)

$\dot{\varepsilon}_{eq}^{cr} = B\sigma_{eq}^{n}$ with ε_{eq}^{cr} and σ_{eq} being the von Mises equivalent creep strain and stress, respectively.

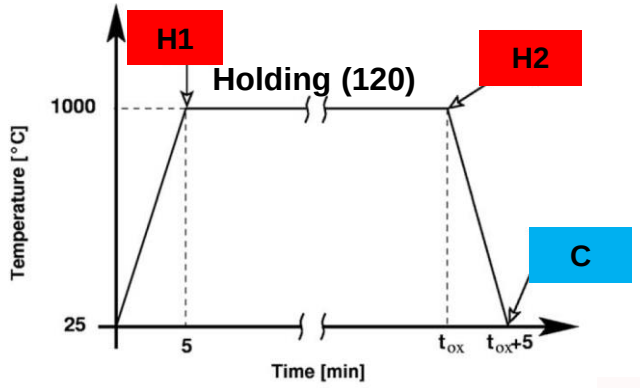

Image Analysis- Result for Configuration “C”

Identification of layers and defects

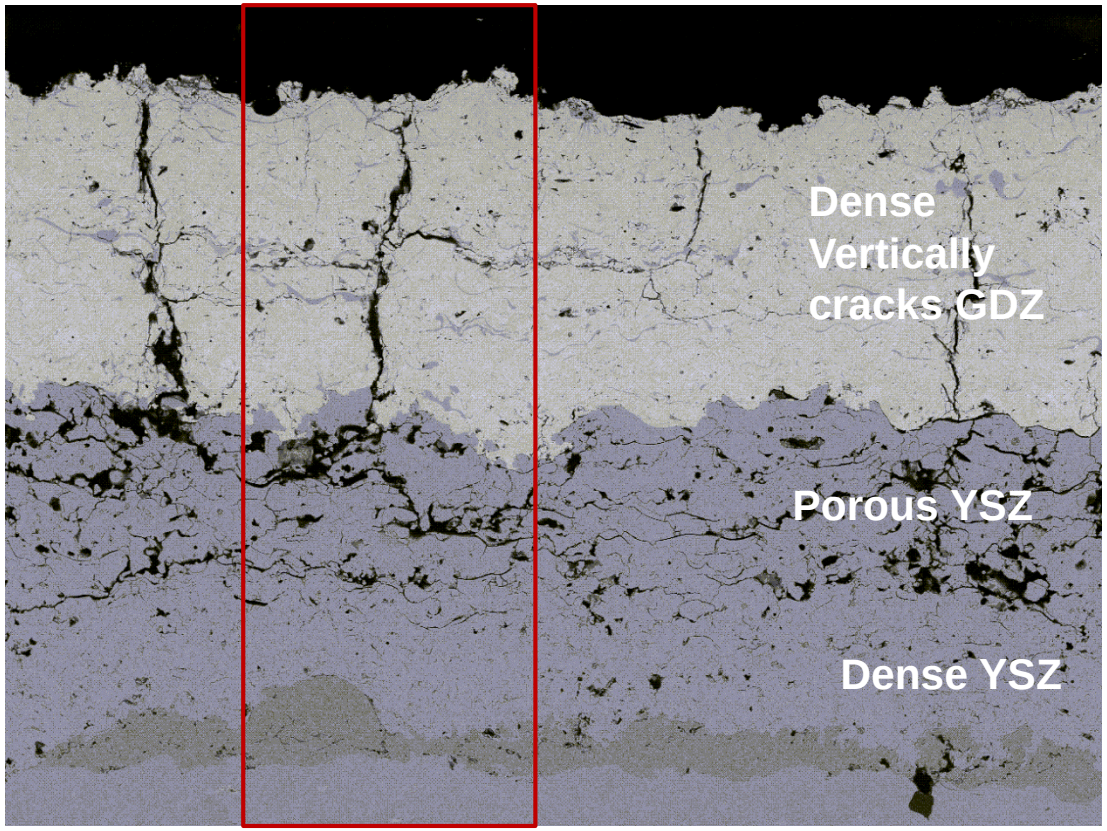

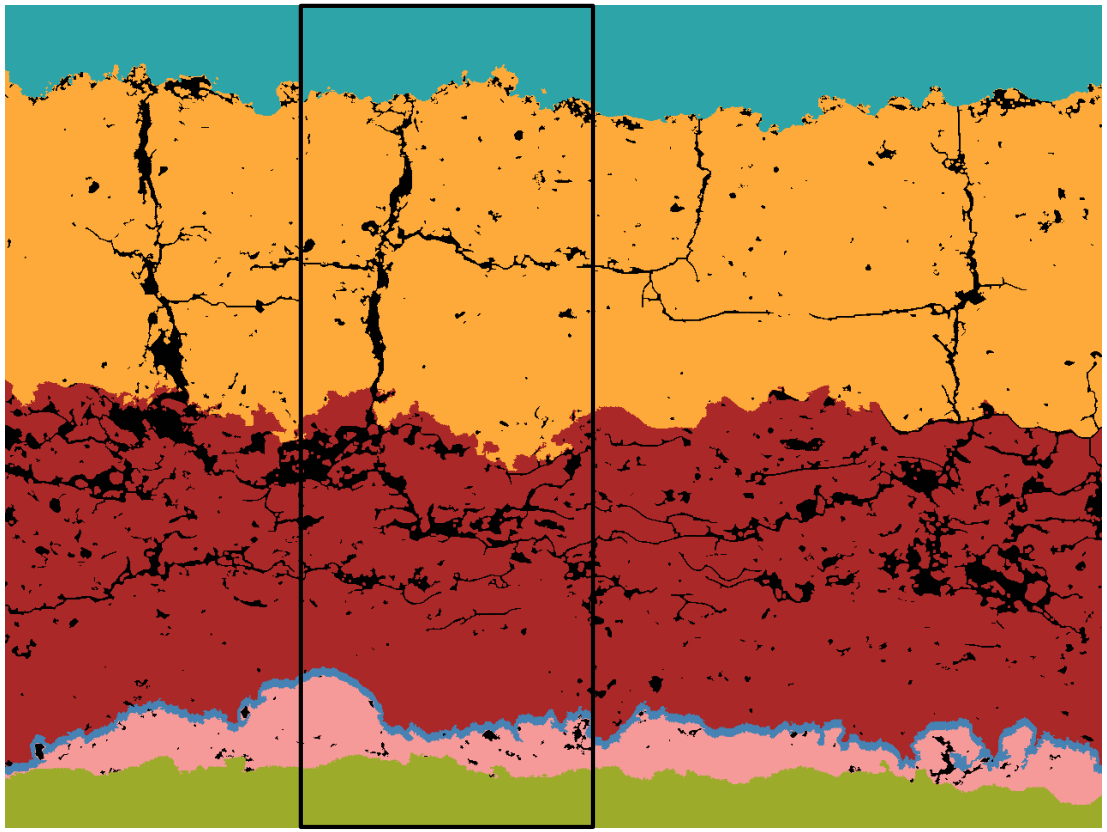

Displacement: Result for Configuration “C” – GDZ-YSZ

Displacement in [m] towards positive x

H1

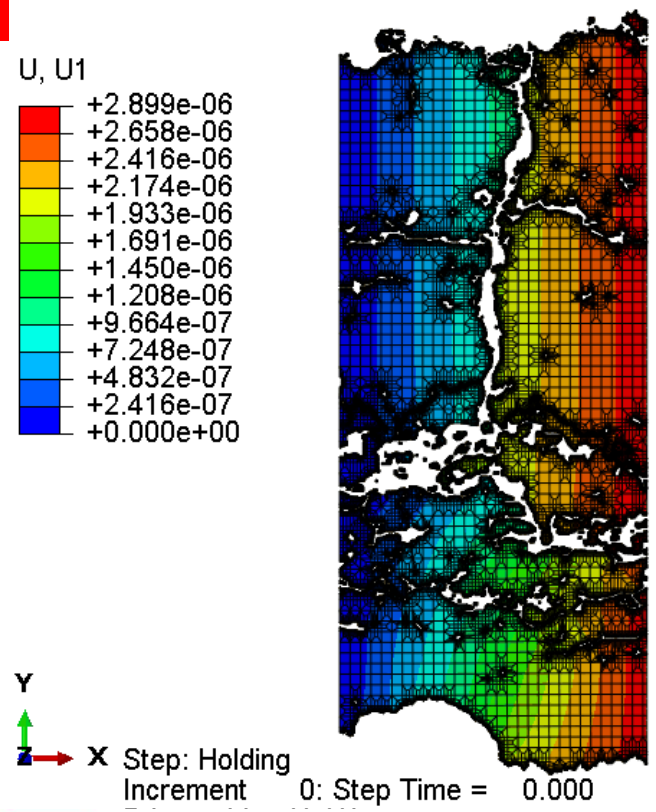

H2

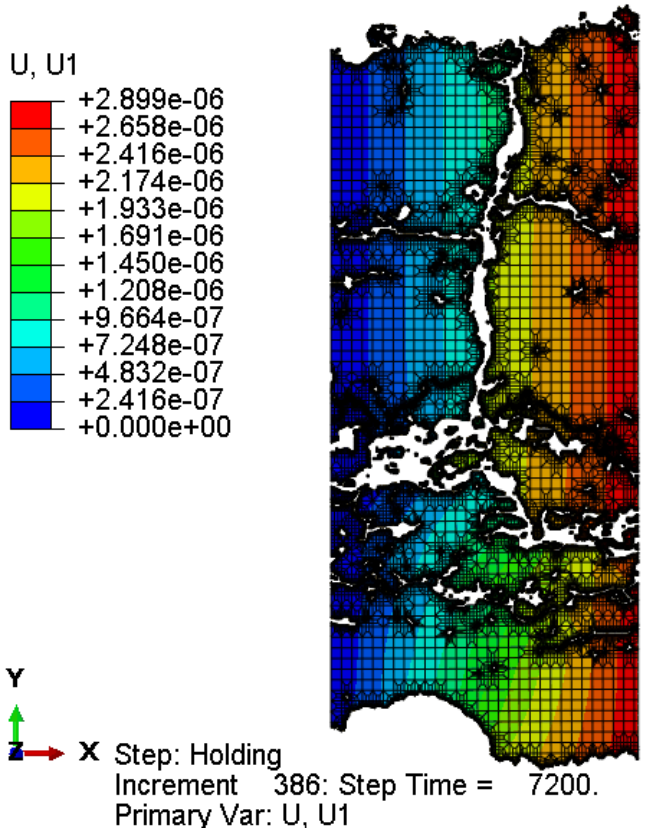

C

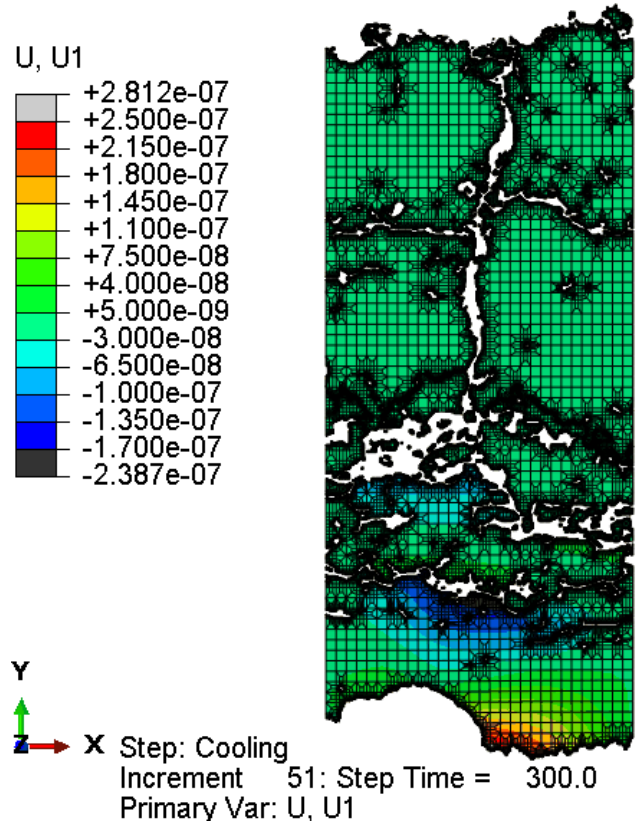

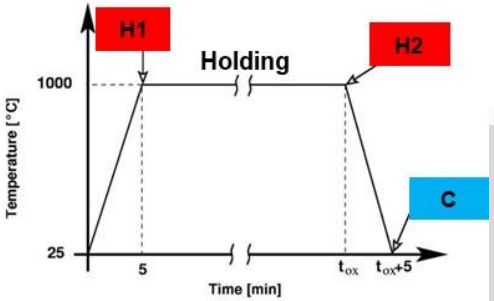

Thermal Stresses: Result for Configuration “C” – GDZ-YSZ

S11 Stresses in [Pa]

H1

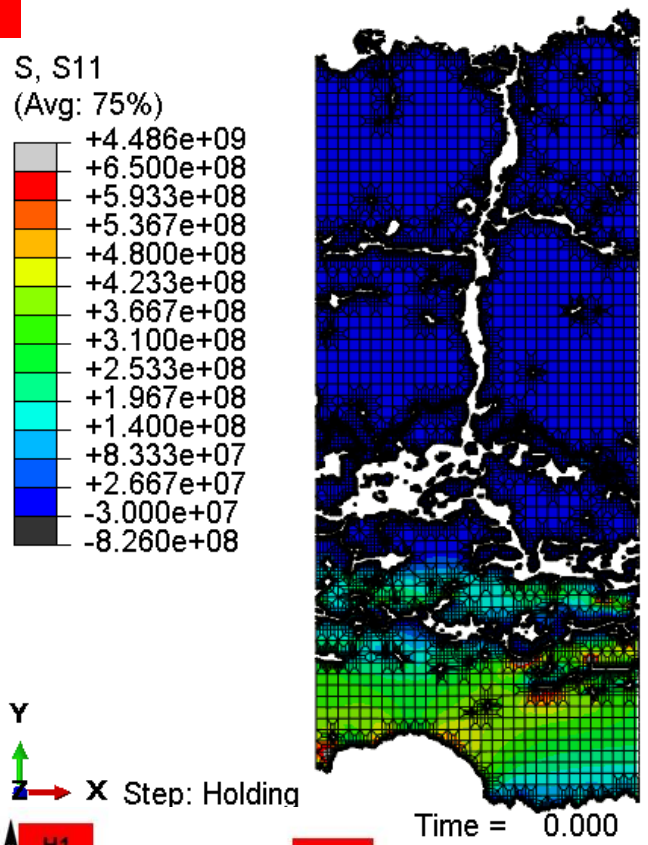

H2

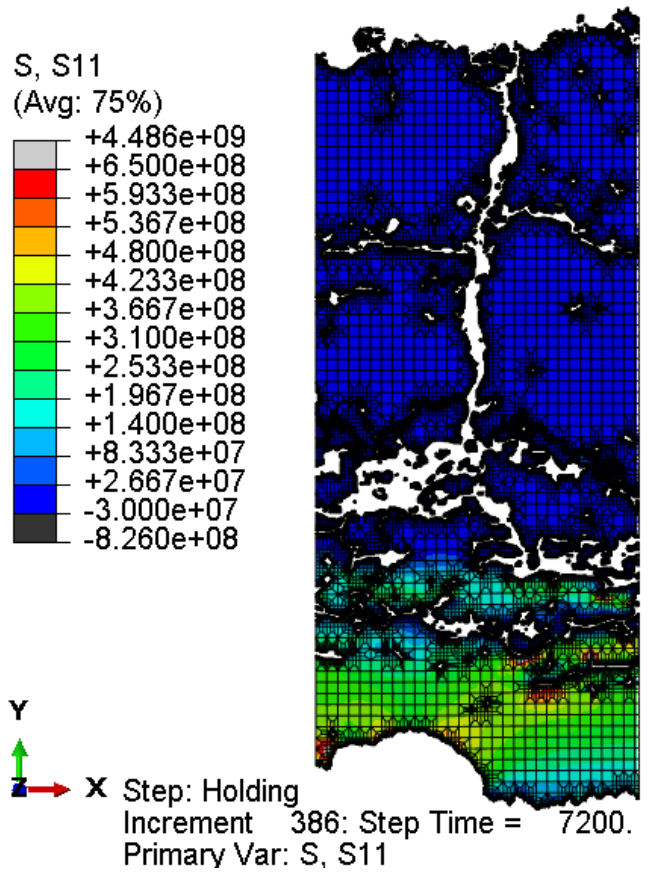

C

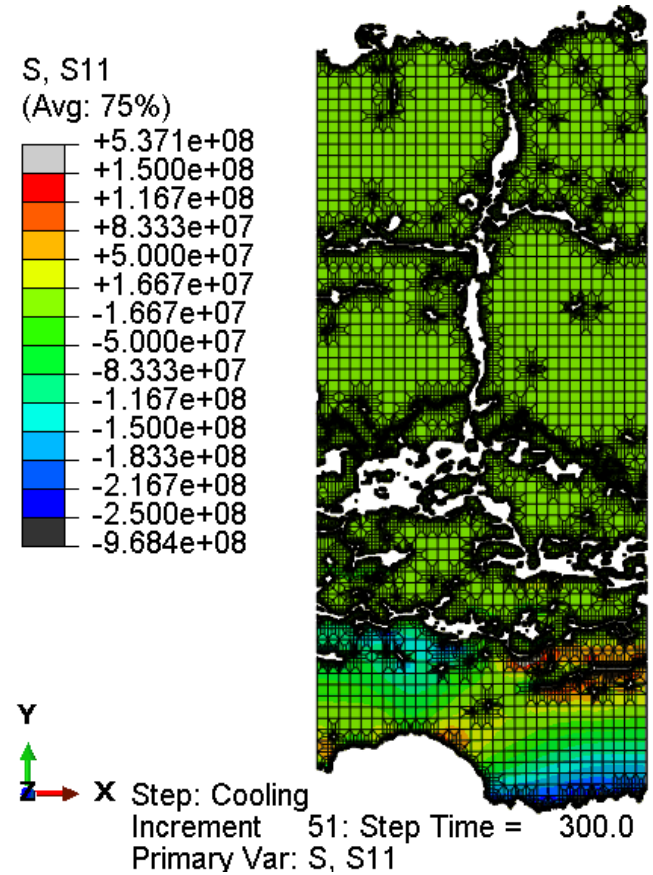

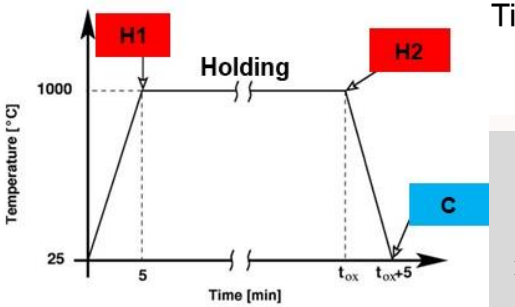

Thermal Stresses: Result for Configuration “C” – GDZ-YSZ

S22 Stresses in [Pa]

H1

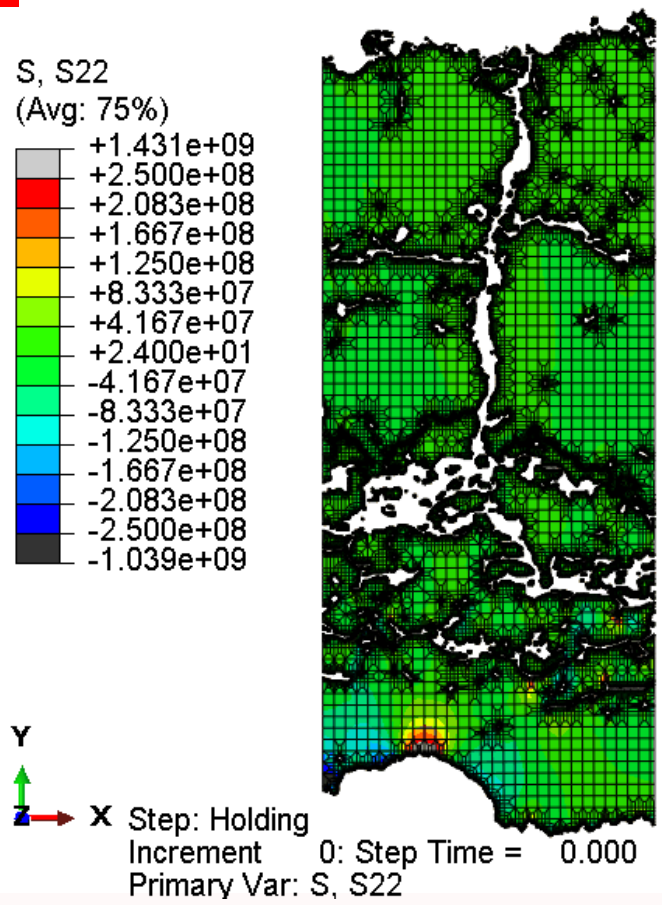

H2

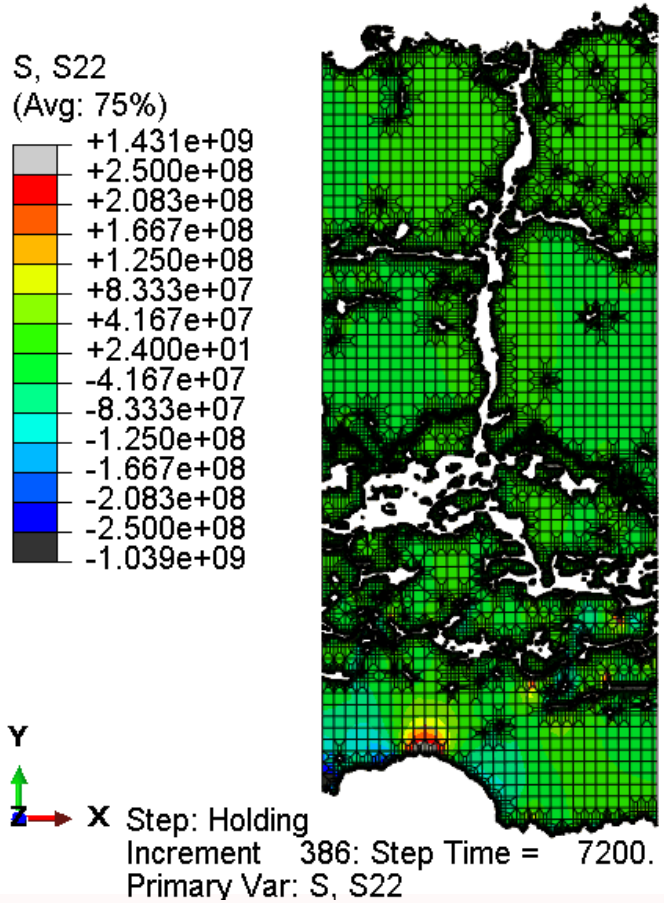

C

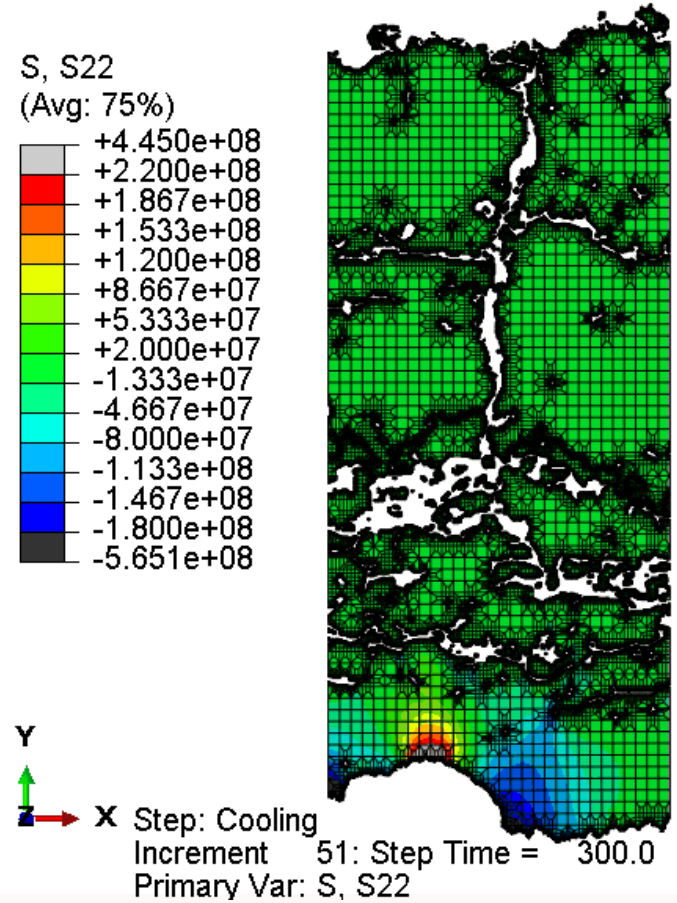

Strain Energy Density: Result for Configuration “C” – GDZ-YSZ

Strain Energy Density is the driving force for crack openning

H1

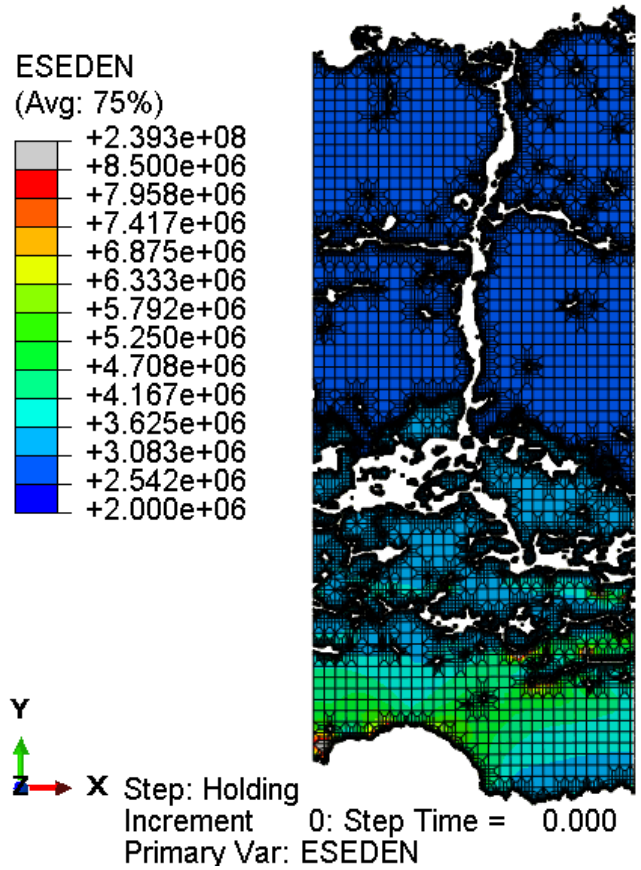

H2

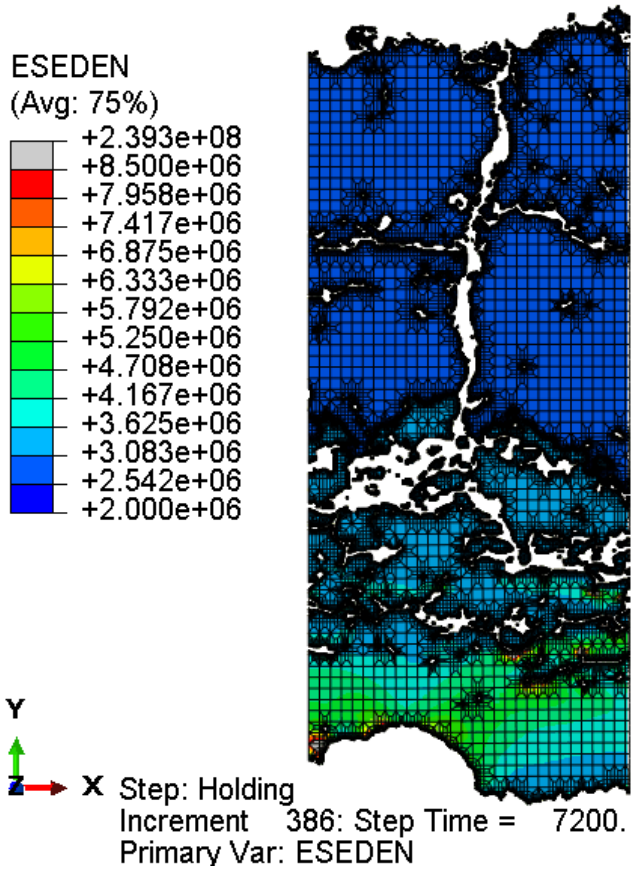

C

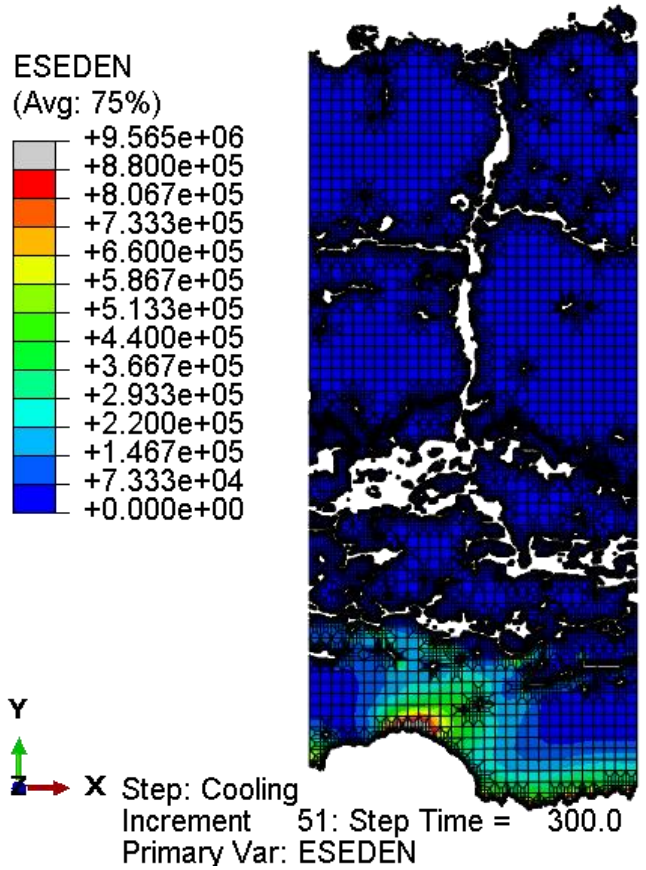

Failure Assessment in multilayers by FCT

Furnace Cycle Testing with a 24h cycle was conducted in a box-furnace at 1100°C in air.

A criterion of 20% or more spallation of top-coat was used to identify coating failure.

The loci of failure is near the bond-coat and top-coat interface (adhesive failure)

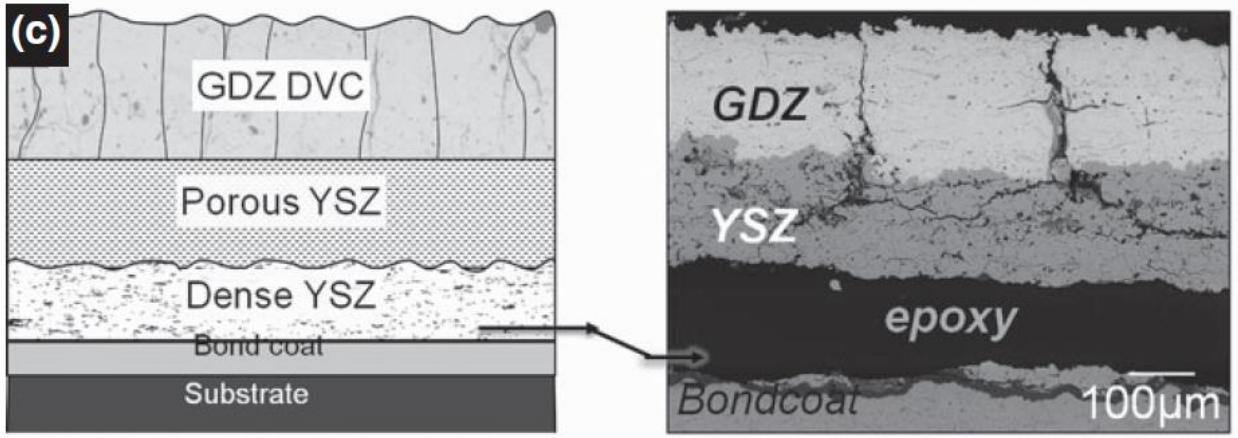

TBC Lifetime Assessment

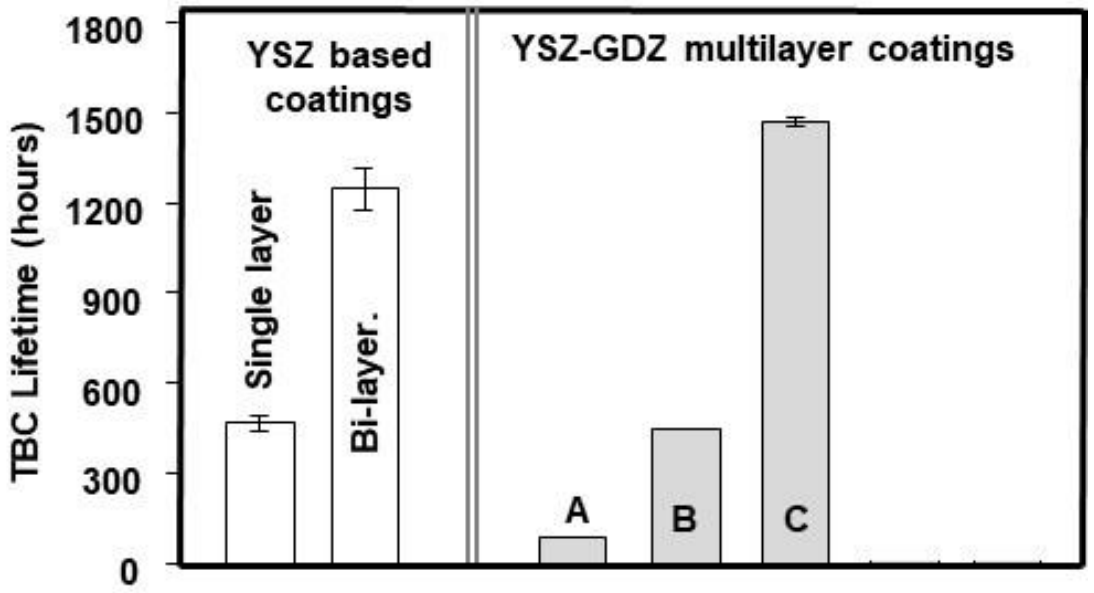

Viswanathan, et al. Multilayer, Multimaterial Thermal Barrier Coating Systems: Design, Synthesis, and Performance Assessment. J. Am. Ceram. Soc., 1–9

Image Analysis- Result for Configuration “A”

Identification of layers and defects

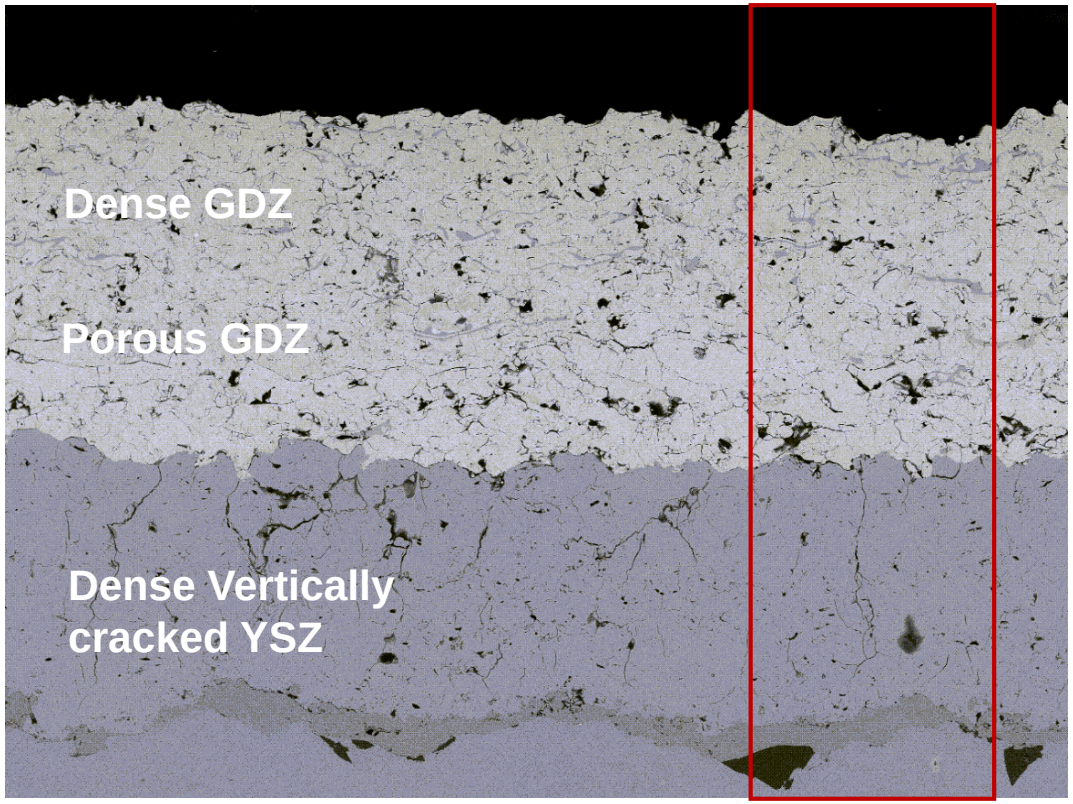

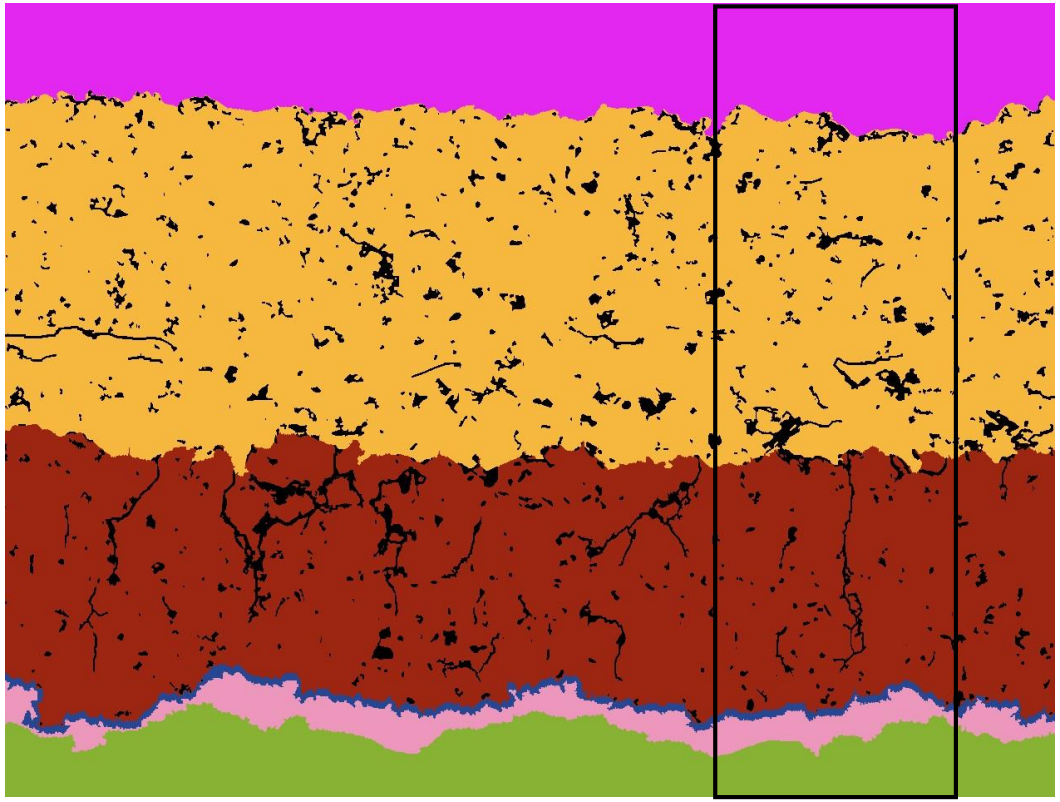

Thermal Stresses: Result for Configuration “A” – GDZ-YSZ

S11 Stresses in [Pa]

H1

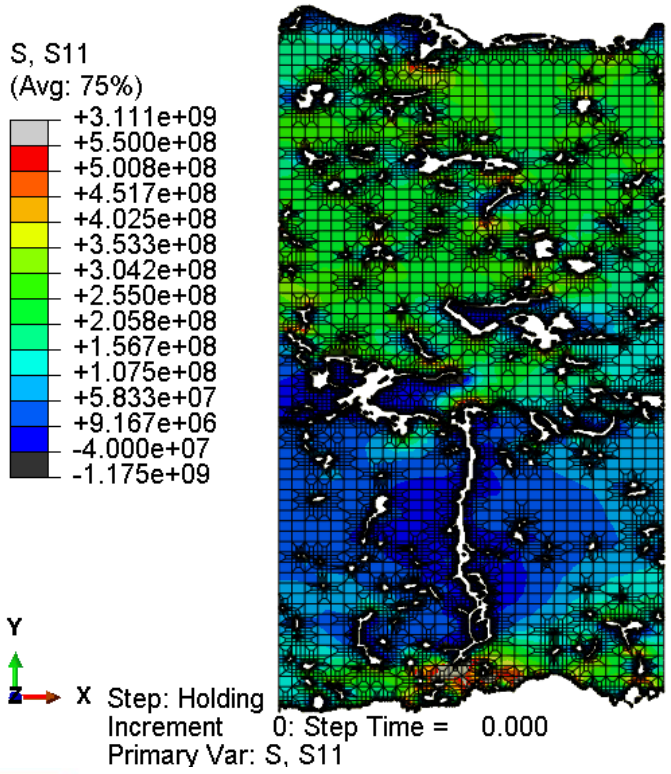

H2

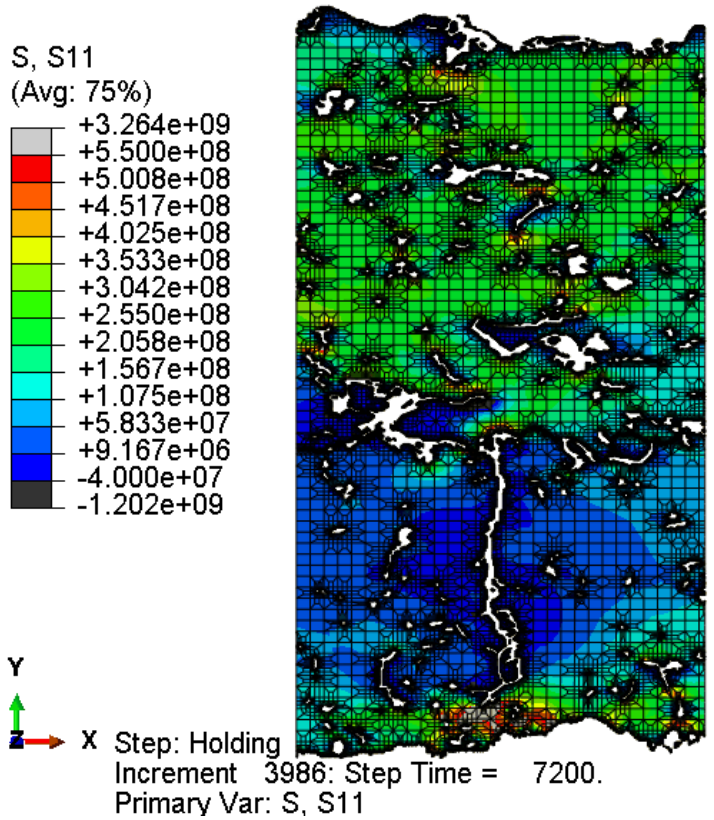

C

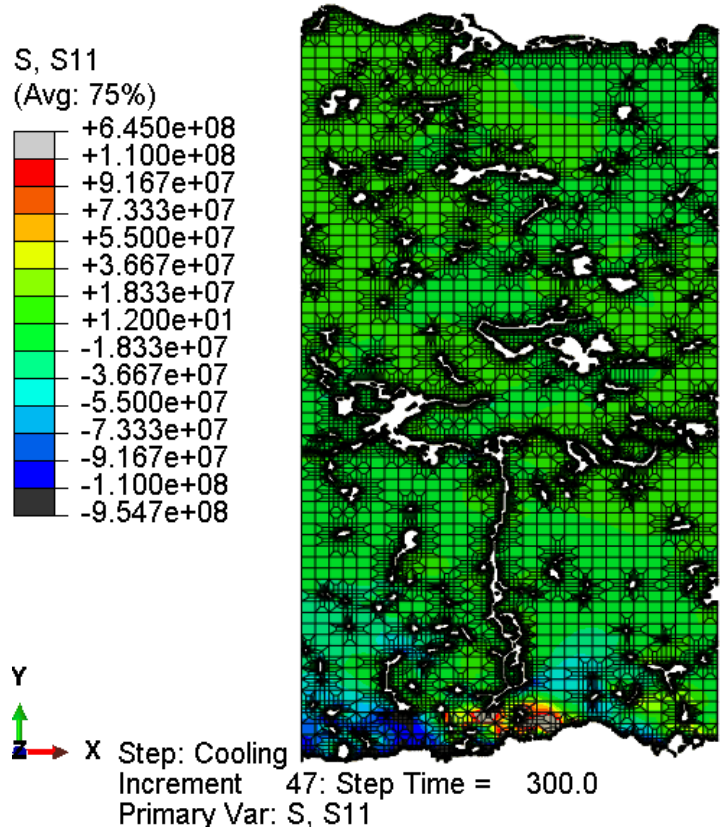

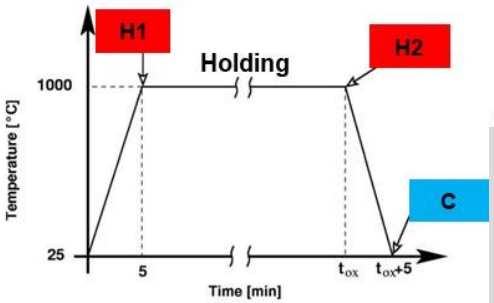

Thermal Stresses: Result for Configuration “A” – GDZ-YSZ

S22 Stresses in [Pa]

H1

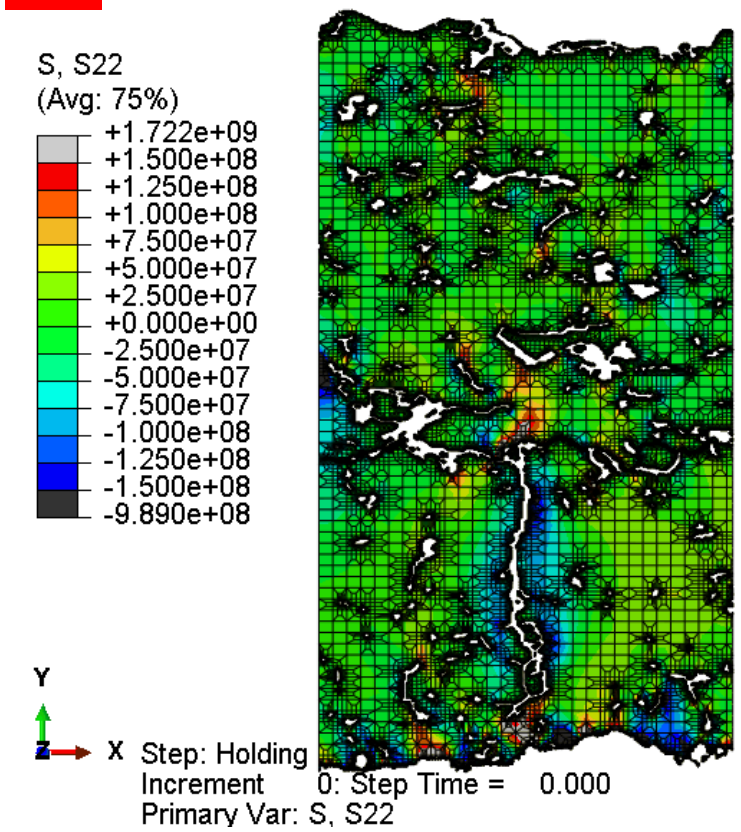

H2

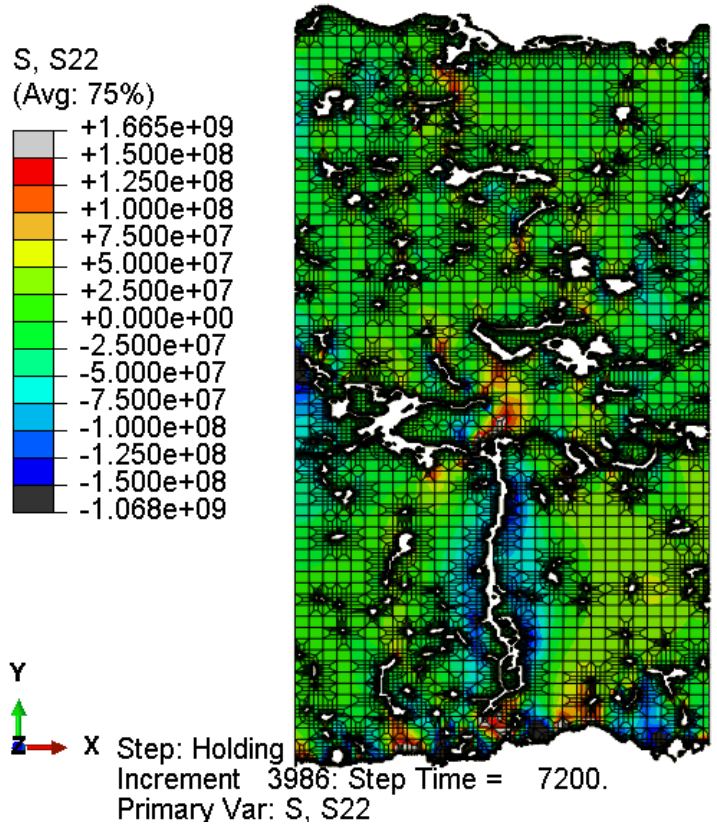

C

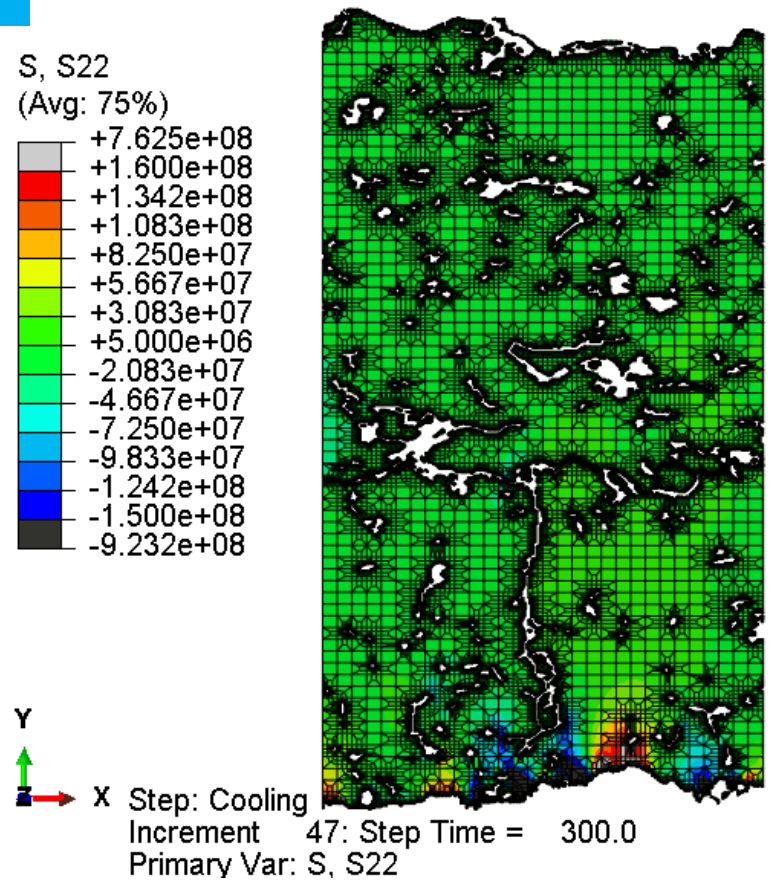

Strain Energy Density: Result for Configuration “A” – GDZ-YSZ

Strain Energy Density is the driving force for crack openning

H1

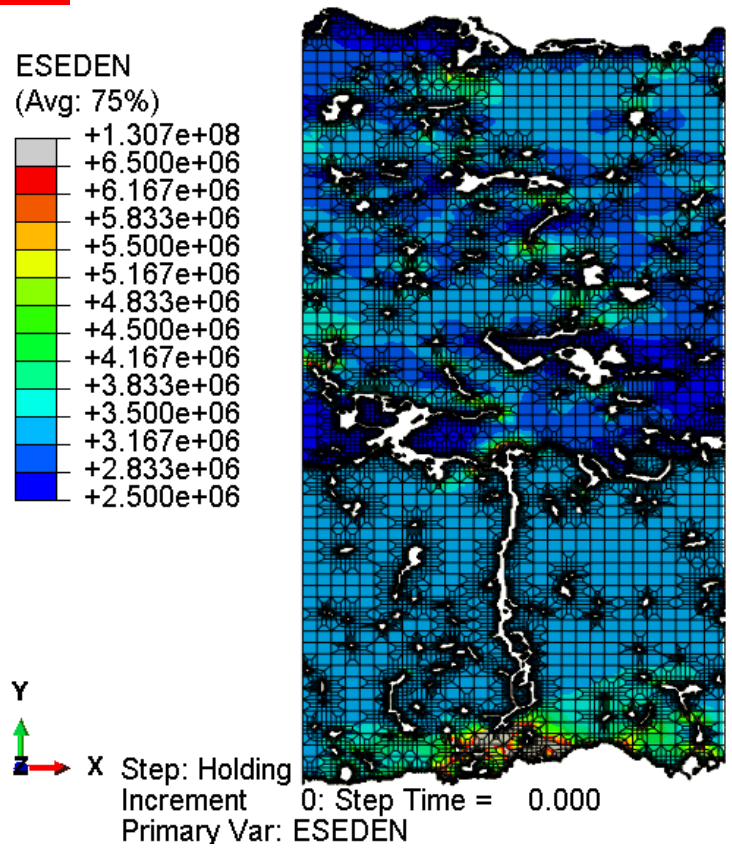

H2

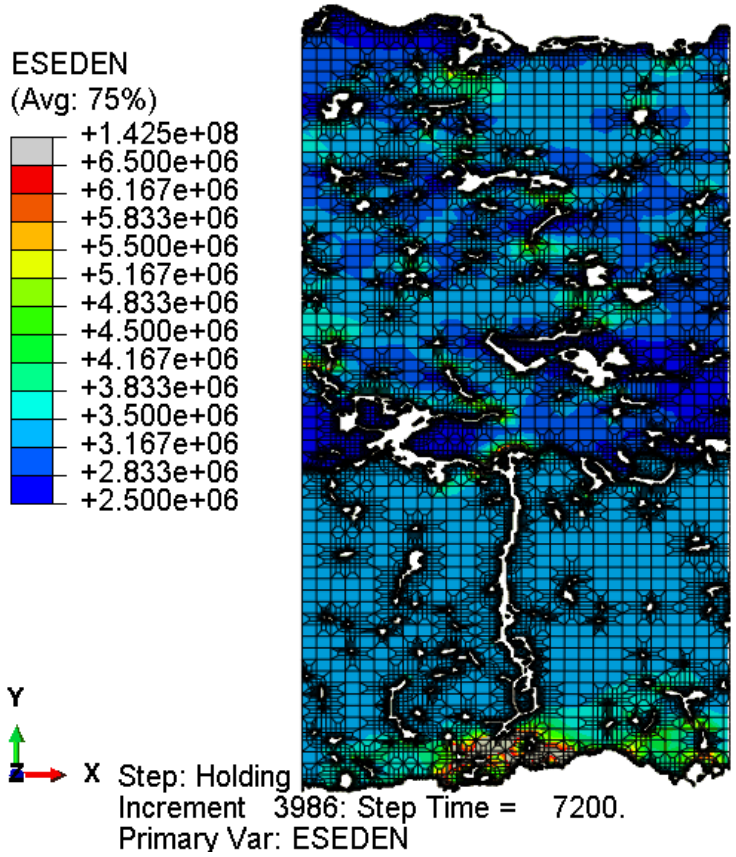

C

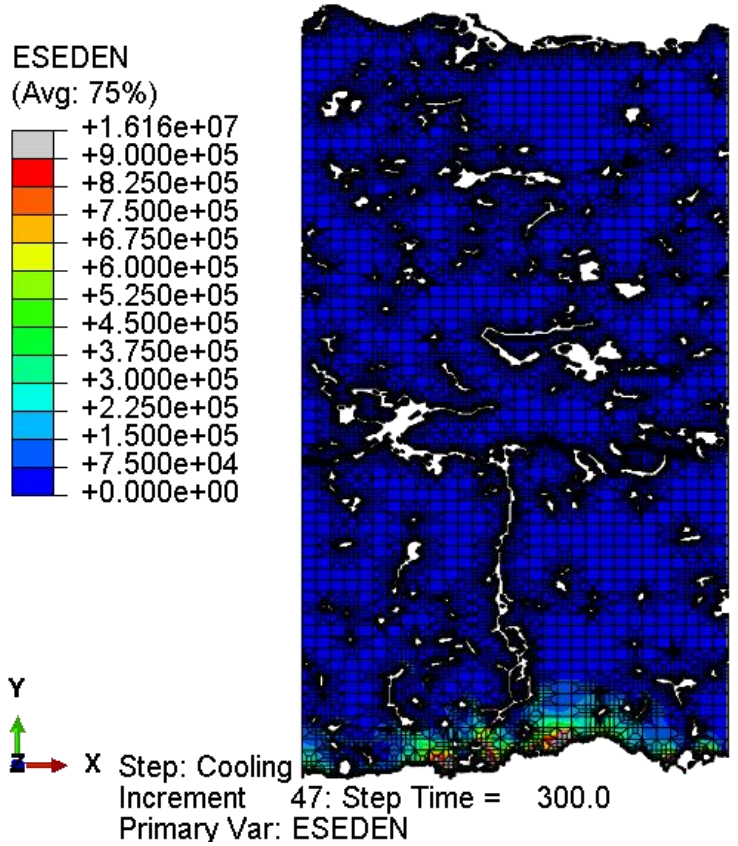

Failure Assessment in multilayers by FCT

The loci of failure is near the GDZ – YSZ interface (cohesive failure)

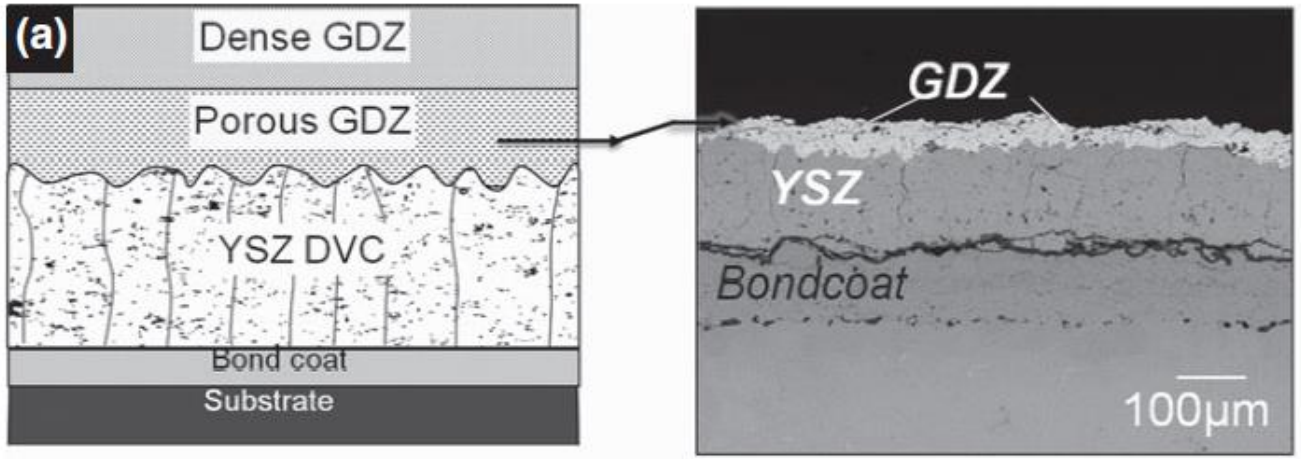

TBC Lifetime Assessment

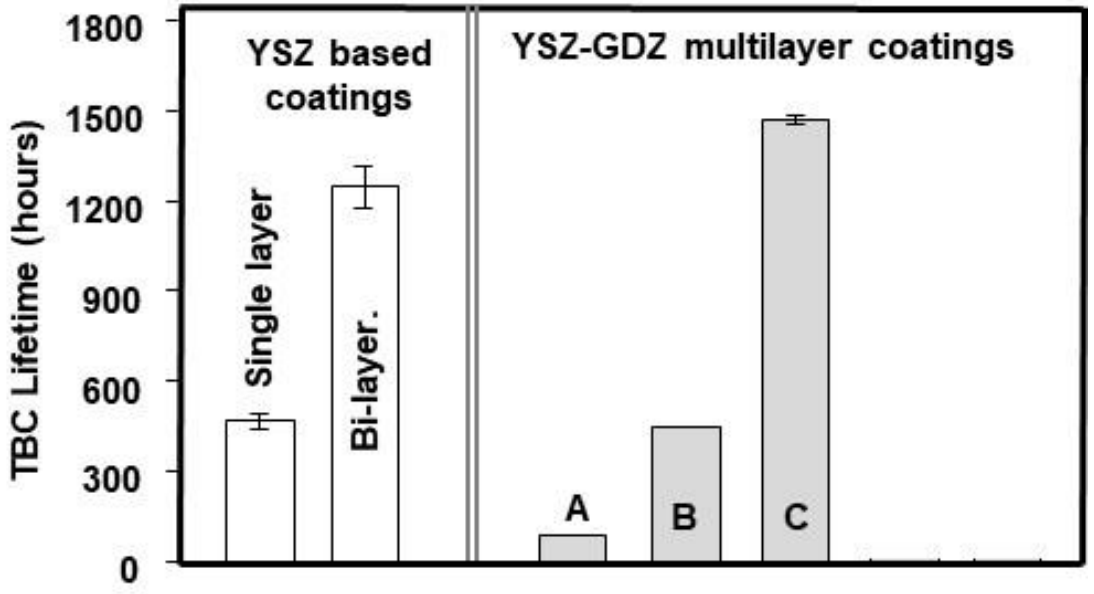

Viswanathan, et al. Multilayer, Multimaterial Thermal Barrier Coating Systems: Design, Synthesis, and Performance Assessment. J. Am. Ceram. Soc., 1–9

Image Analysis- Result for Configuration “B”

Identification of layers and defects

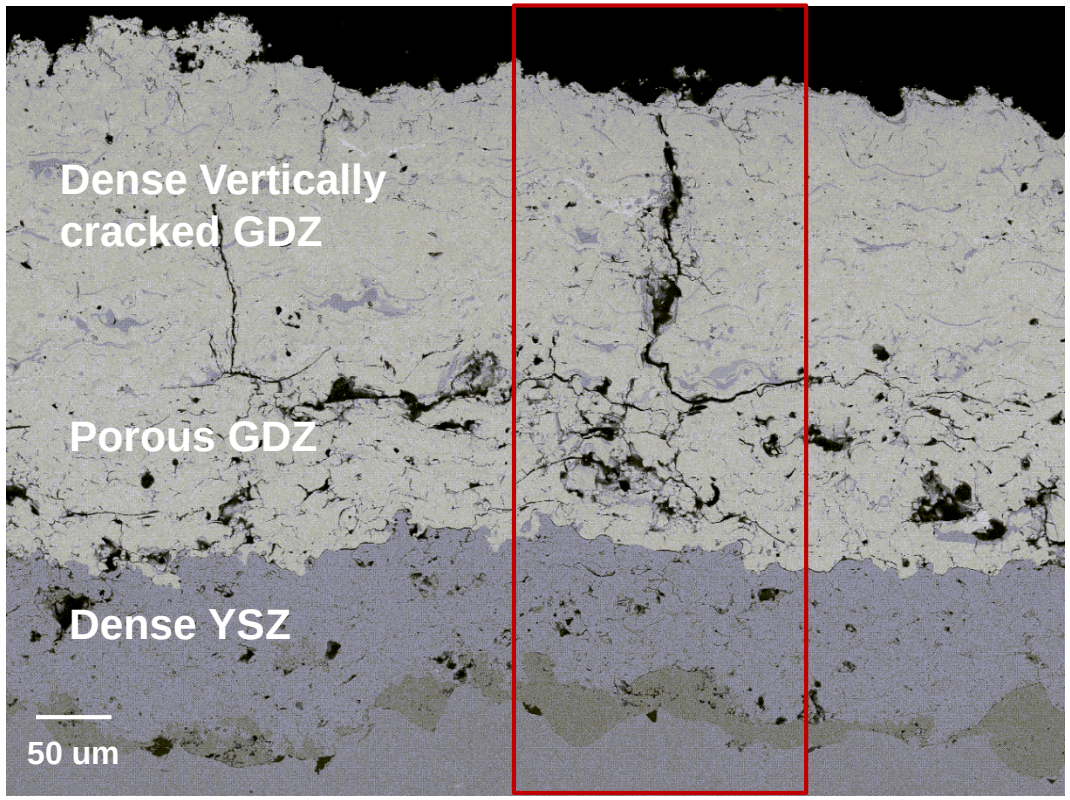

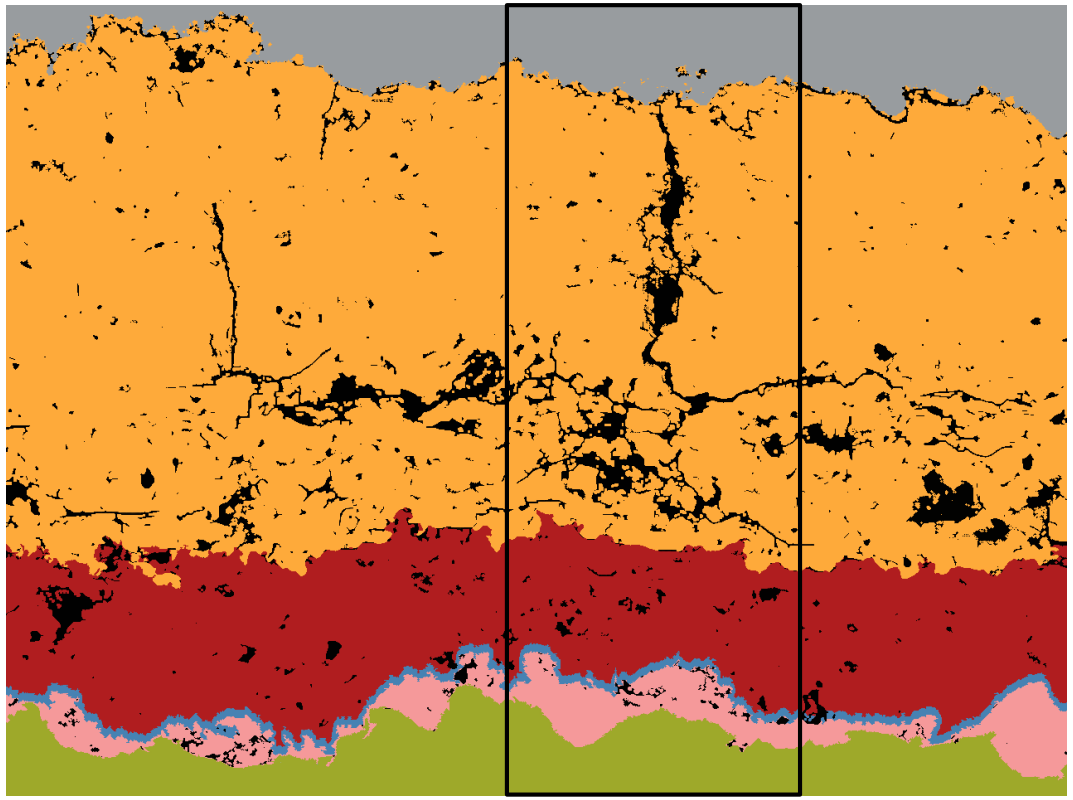

Thermal Stresses: Result for Configuration “B” – GDZ-YSZ

S11 Stresses in [Pa]

H1

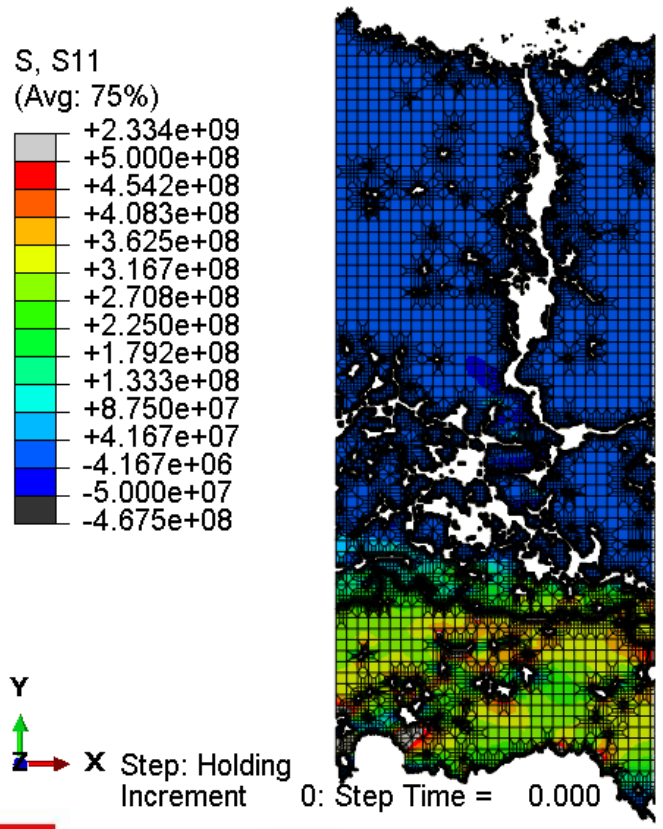

H2

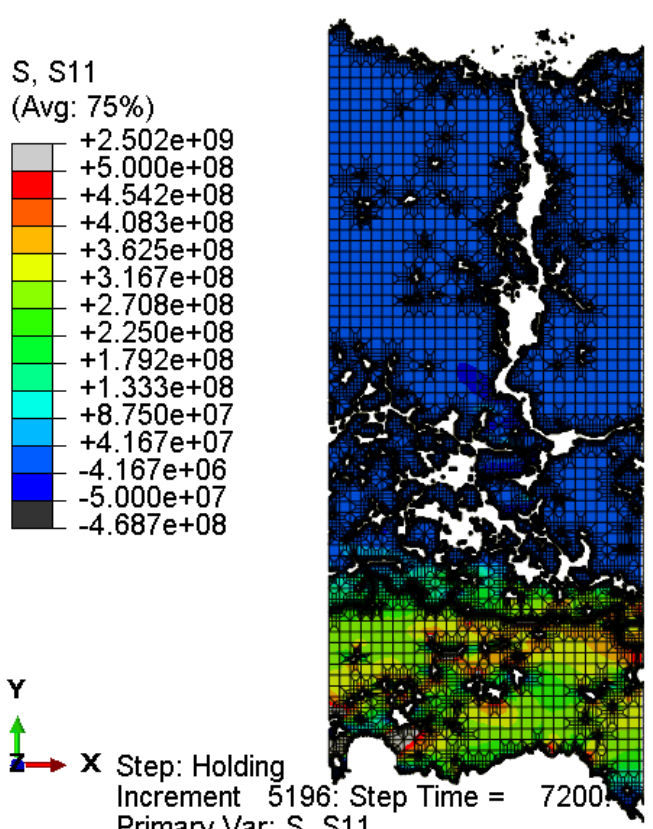

C

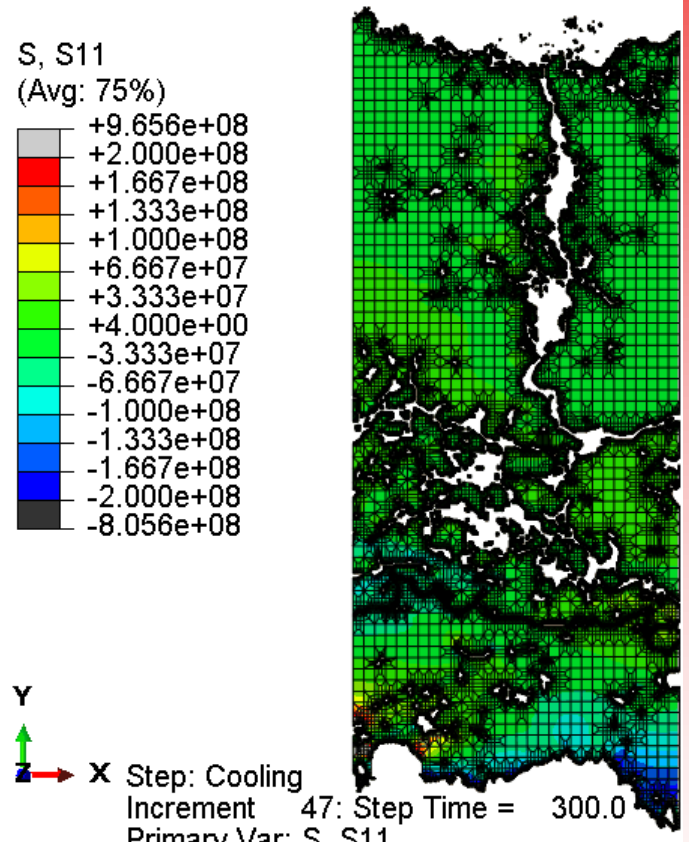

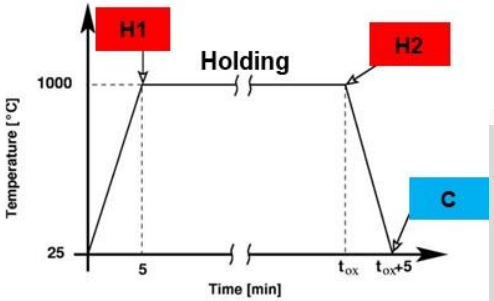

Thermal Stresses: Result for Configuration “B” – GDZ-YSZ

S22 Stresses in [Pa]

H1

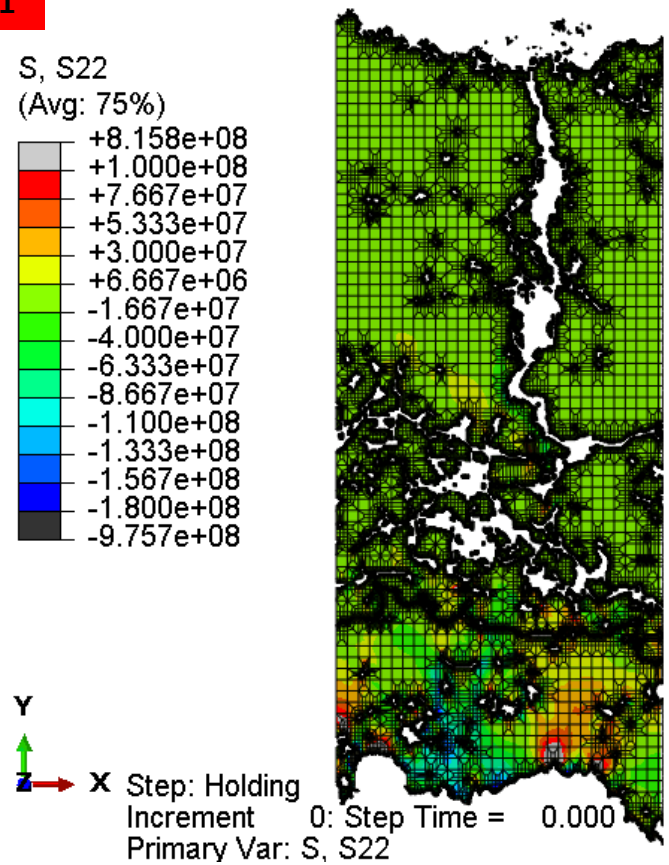

H2

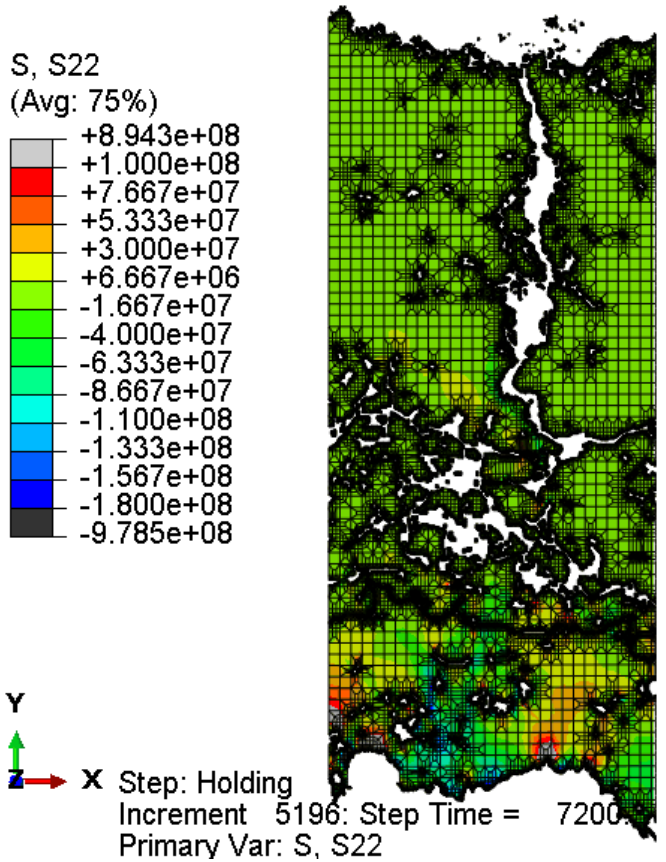

C

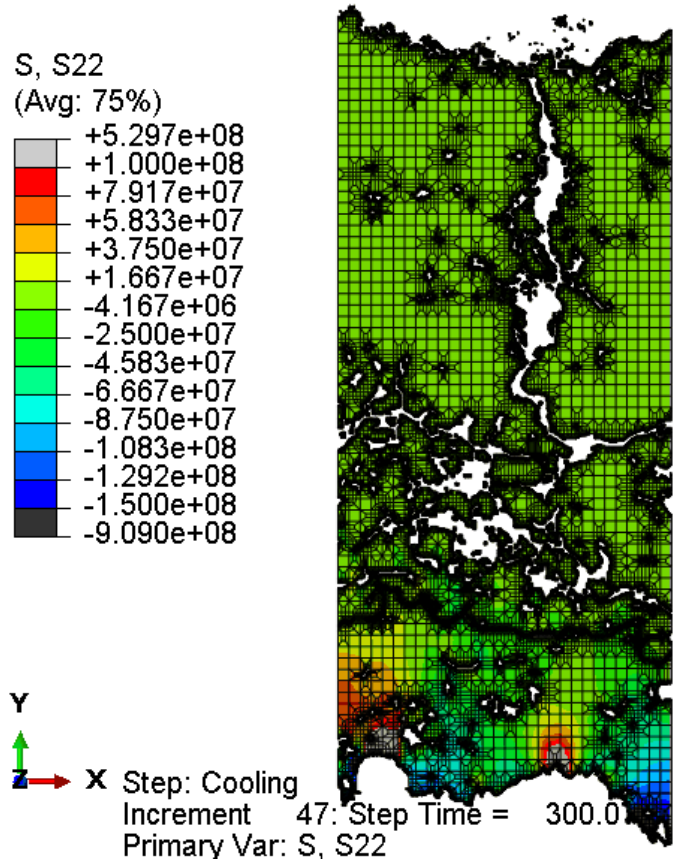

Strain Energy Density: Result for Configuration “B” – GDZ-YSZ

Strain Energy Density is the driving force for crack openning

H1

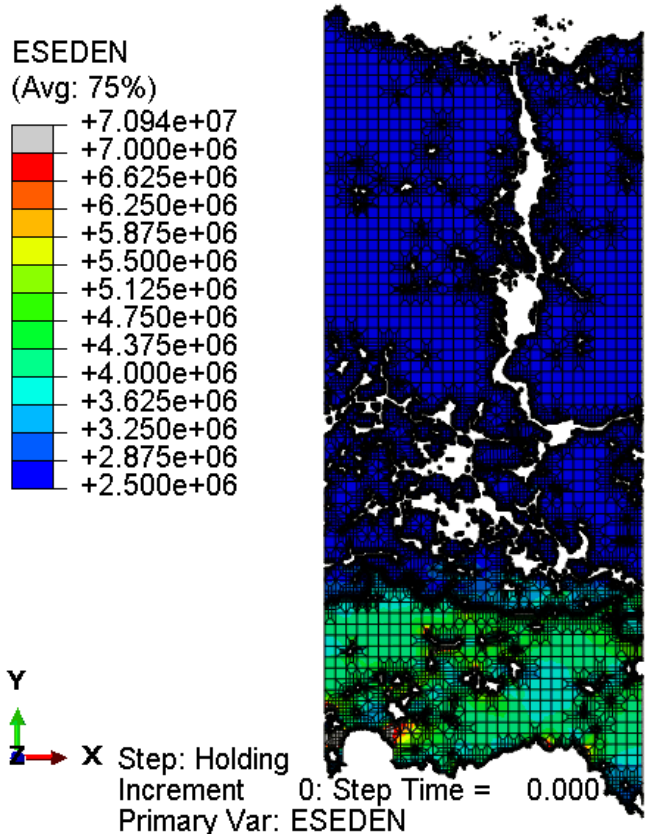

H2

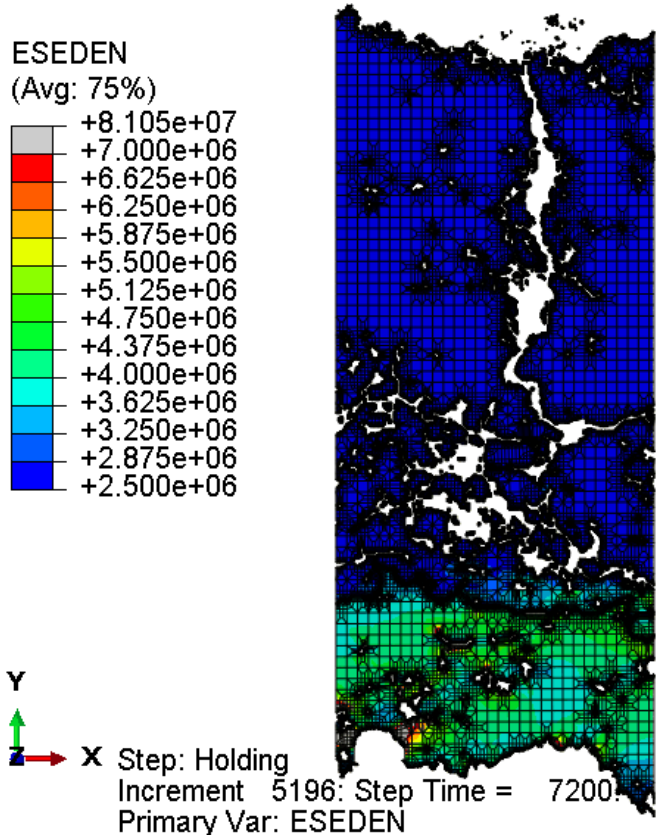

C

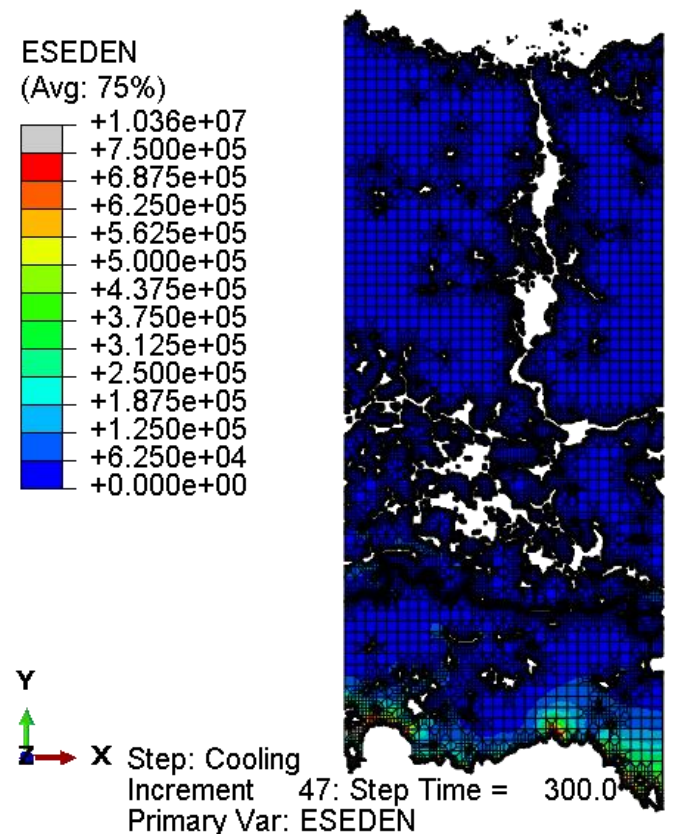

Failure Assessment in multilayers by FCT

The loci of failure is near the GDZ – YSZ interface (cohesive failure)

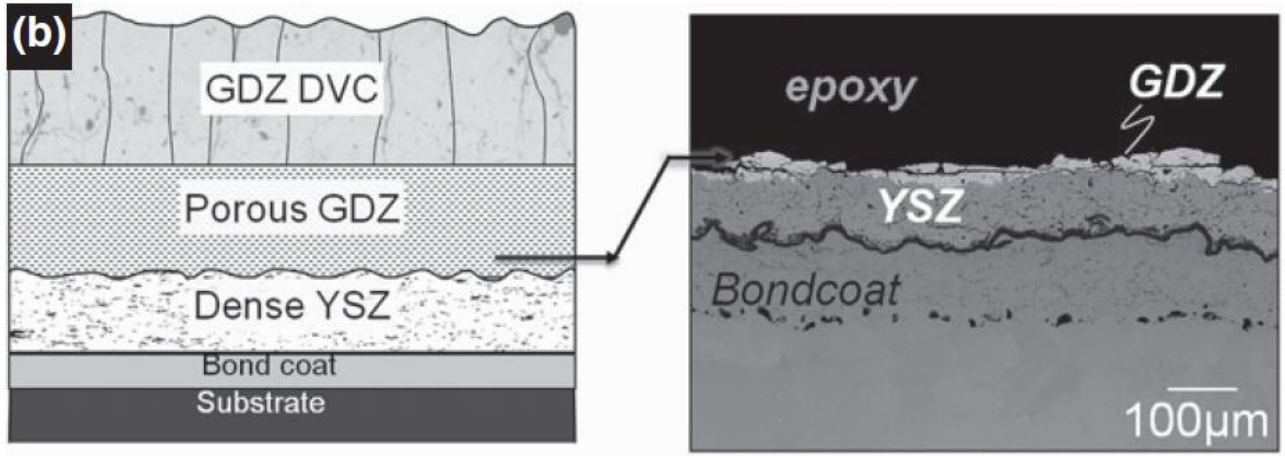

TBC Lifetime Assessment

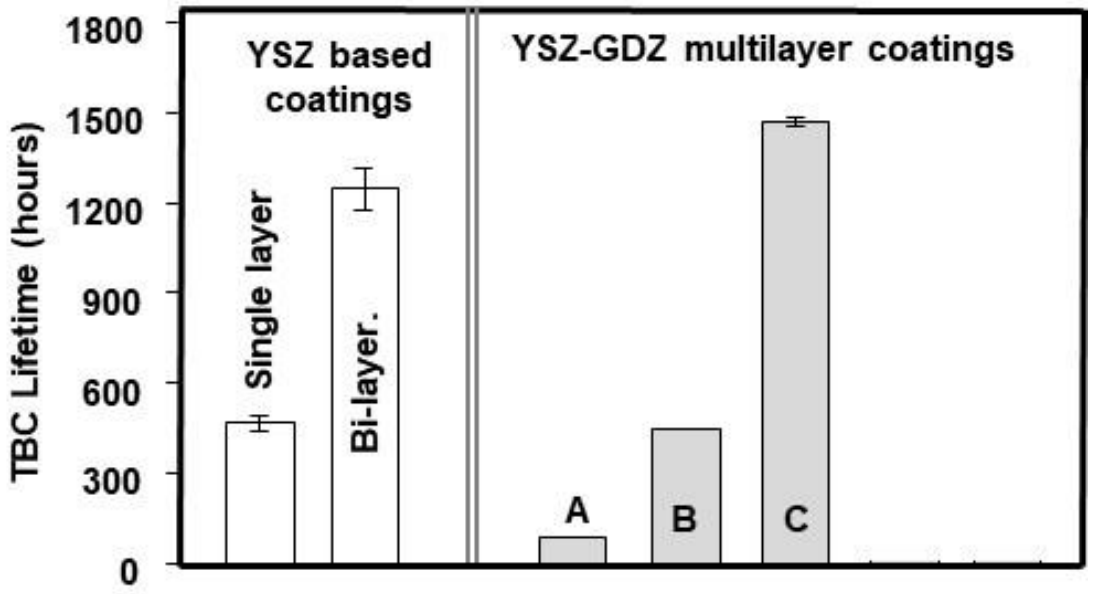

Viswanathan, et al. Multilayer, Multimaterial Thermal Barrier Coating Systems: Design, Synthesis, and Performance Assessment. J. Am. Ceram. Soc., 1–9

Summary of Results

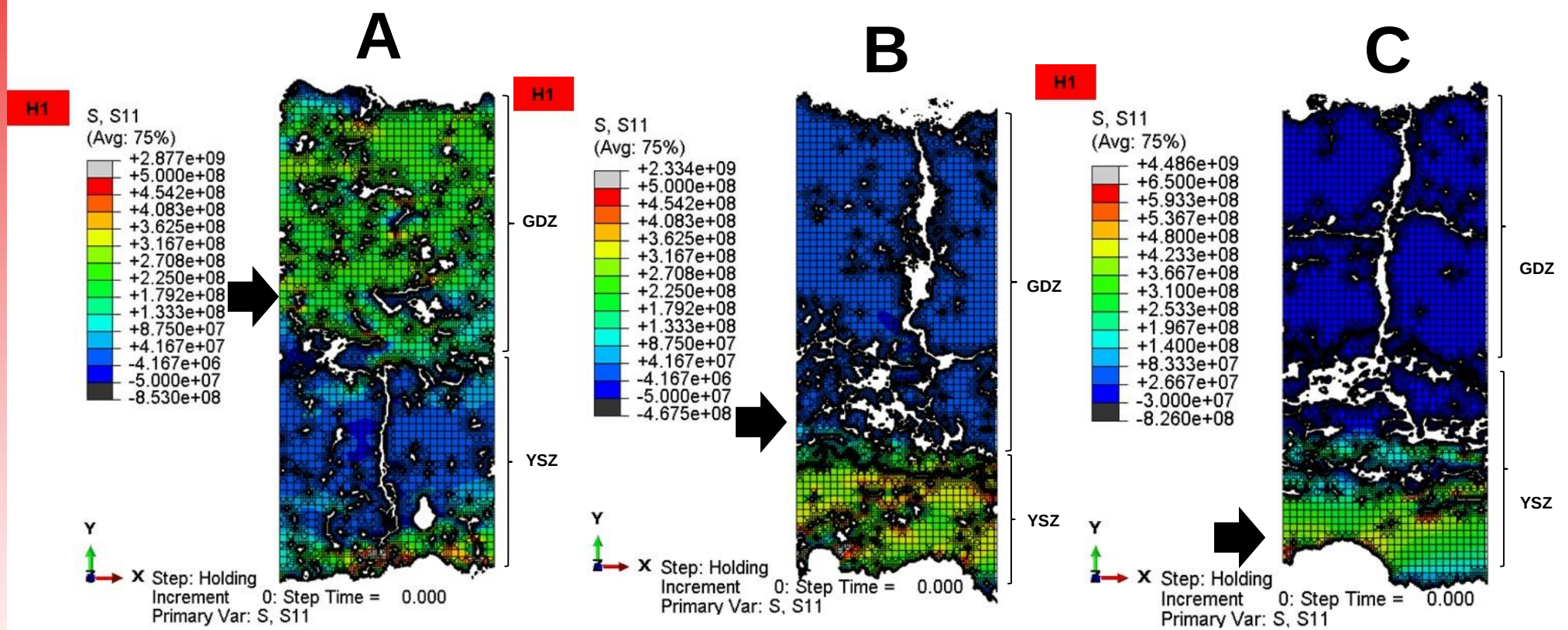

TBC Lifetime Assessment

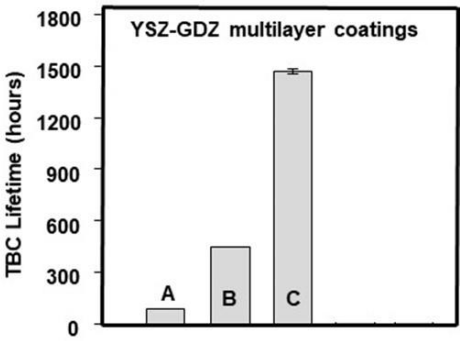

Failure: Occurs at the region of maximum stress and low fracture toughness

Summary of Results - Ctnd

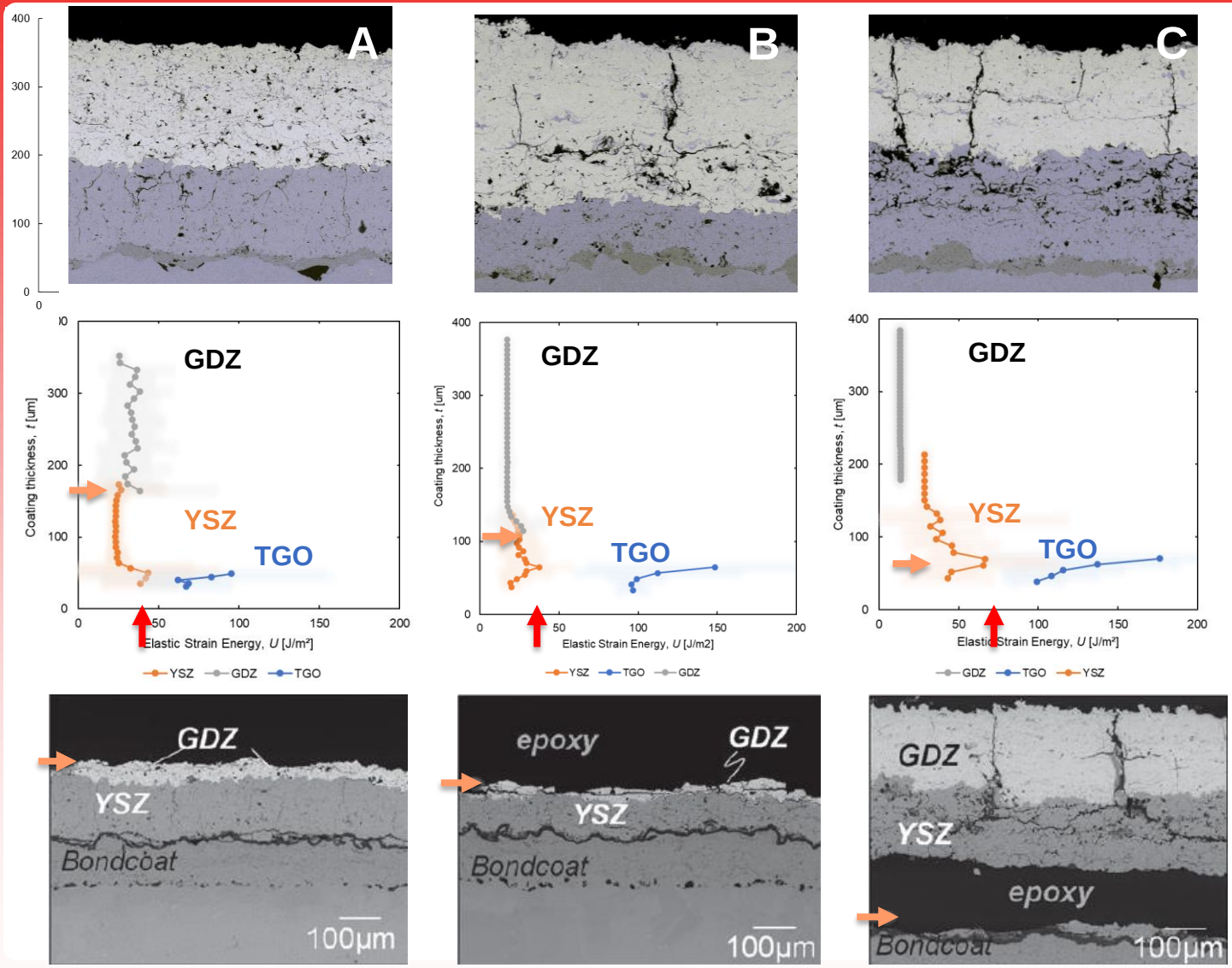

A and B

- Fail in the GDZ-YSZ interface with a strain energy of about 30-40 J/m2 in the GDZ which is of lower fracture toughness
- YSZ-TGO interface is subjected to about 40 J/m2 which does not make it fail.

C

- Fail in the YSZ-TGO interface with a strain energy of about 70 J/m2 in the YSZ despite its large fracture toughness
- In the YSZ-GZ interface, the strain energy in GDZ is low (10 J/m2) which assures that GDZ does not fail.

Strain distribution and roughness in the INTERFACES are key for failure

Conclusion

- There is a **continuous interest in improving the efficiency** of turbine engines by depositing TBC coatings of higher temperature resistance, lower thermal conductivity, high chemical resistance, an elevated fracture toughness.
- **Implementation of new materials and process induced structures** (defects, etc) is one of the routes to improve engine efficiency with great impact over fuel consumption.
- **Modeling thermomechanical stresses by FEA and capturing the microstructure (by OOF-2) allows the understanding of residual stresses** and strain energies that can only be predicted in a environment where measuring stresses is imposible.
- **The presented model is able to capture regions of high stresses** and strain energies **which drive the failure** in zones of relative low fracture toughness.

Center for Thermal Spray Research

Universidad San Francisco de Quito

Grant FA9550-20-1-0075

THANKS !!

avalarezo@usfq.edu.ec

Acknowledgment

USFQ

Appendix 4:

Presentation at International Materials Research Conference, August 15th 2023. Cancún Mexico.
3D MODELING OF THERMAL STRESSES IN MULTI-LAYER/MATERIAL TBCS FOR GAS TURBINE ENGINES

Círculo de Cumbayá. P.O.Box: 17-12-841 Quito-Ecuador
T.: (593 2)297-1700 al 708. Fax.: (593 2)289 0070.
www.usfq.edu.ec

COLEGIO DE CIENCIAS E INGENIERÍAS

Universidad San Francisco de Quito

3D Modeling of Thermal Stresses in Multi-layer/material TBCs for Gas Turbine Engines

Prof. Alfredo Valarezo

Universidad San Francisco de Quito - Ecuador

Westly Castro, Samantha Criollo, Emilio Bonilla, Diego Morales, Krutskaya Yépez, Prof. Marco León, Prof. Lorena Bejarano,
Collaborations: Prof. Sanjay Sampath, Stony Brook University; Tinker Air Force Base, Consortium of Thermal Spray Technology

31st International Materials Research Congress - IMRC2023

Cancún, Mexico. August 15th, 2023

Grant FA9550-20-1-0075

USFQ

Industry-Academia – AFRL – USFQ – Stony Brook University Collaboration

Materials in the combustion zone

Modern gas turbines rely on ceramic & ceramic coatings to protect structural components along the hot gas path.

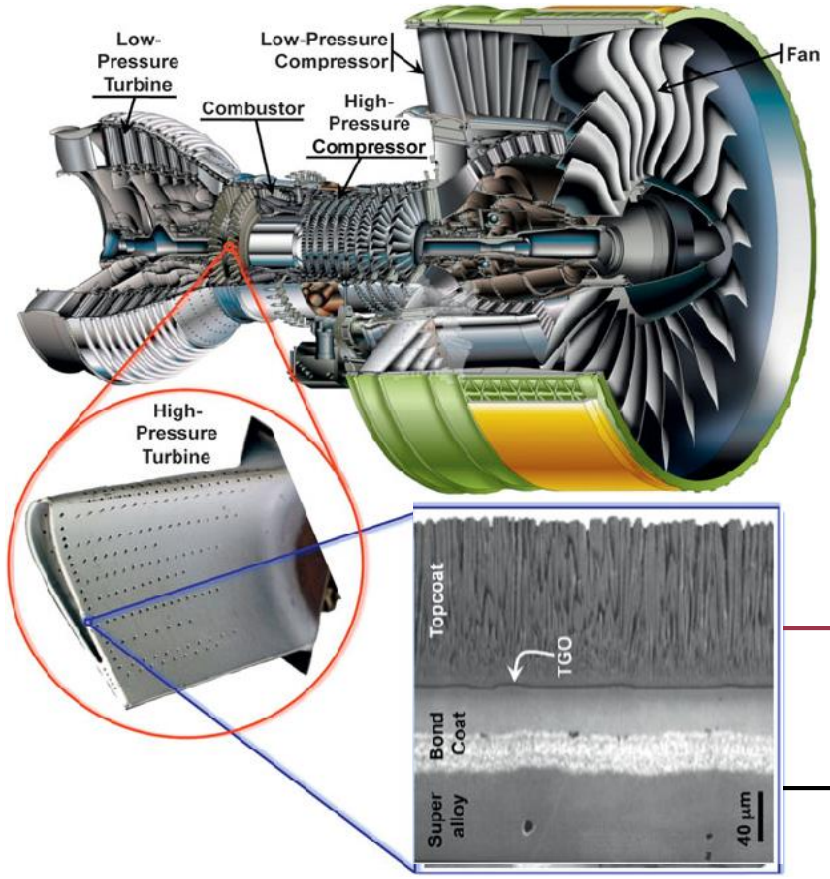

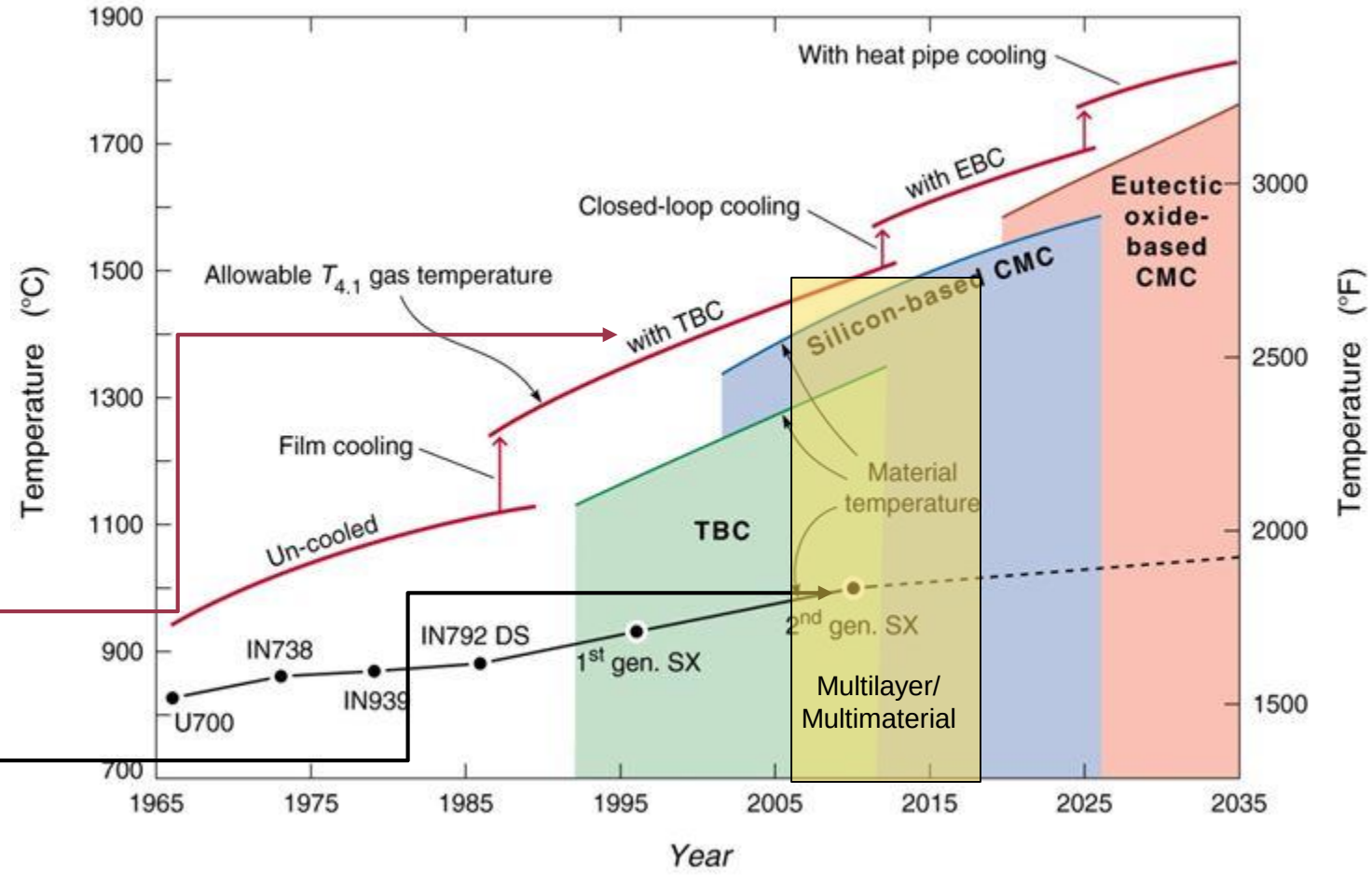

The Engineering Problems of TBC´s to successfully stand high temperatures

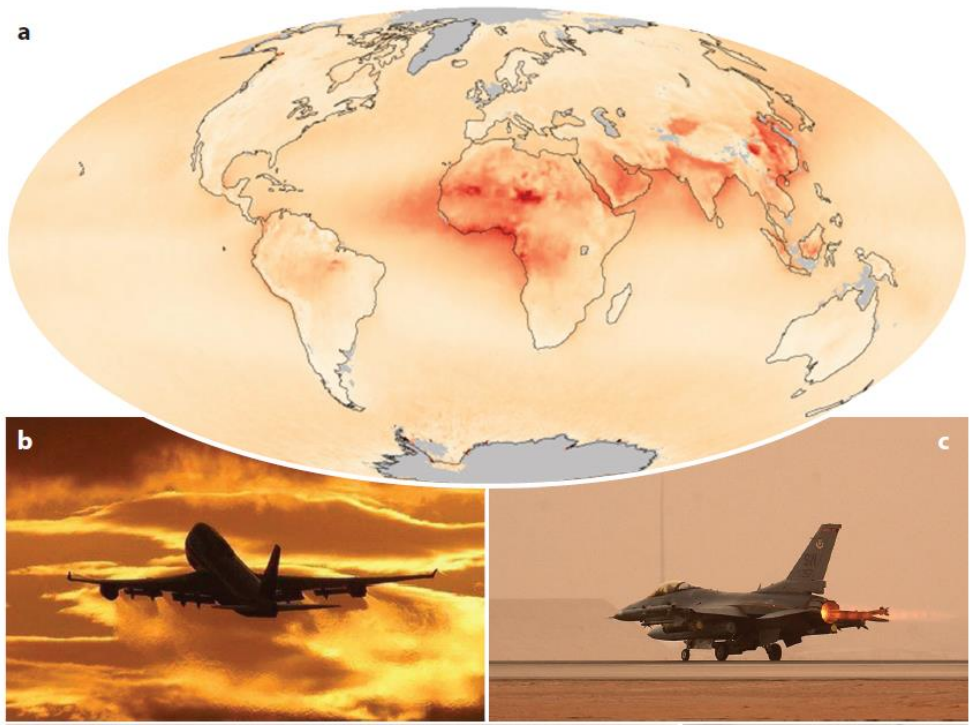

(a) The map in panel, shows average atmospheric aerosol distribution from 2000 to 2010; red indicates the highest concentrations. Image from NASA/Robert Simmon. Engines on (*b*) commercial and (*c*) military aircraft
(d) aircraft regularly ingest particulate debris, which (*d*) melts and deposits on hot section components
(*e*) accelerates coating failure

Among the challenges to design heat resistant coatings, the following considerations need to be addressed:

- Matching thermal expansion coefficients
- Oxidation resistance of bond coat layer
- Low thermal conductivity
- High fracture toughness and delamination resistance.
- CMAS resistance (chemical attack and mismatch stresses)
- Sintering, densification and creep of materials.
- Erosion resistance
- Environmental barriers (water vapor protection)
- TGO growth: swelling and rumpling

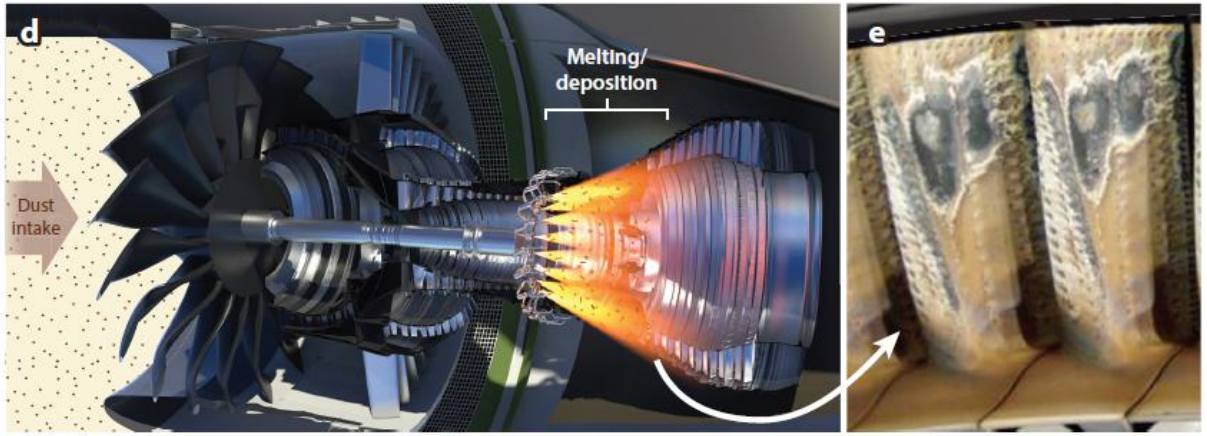

CMAS: term coined to represent the effect of droplets of ash/sand composed of primarily Ca/Mg/Al/Si oxides, which are deposited onto the TBCs in liquid form and solidify on during cooling. They containing Fe oxides as well, constituting the main components of the earth's crust

Plasma Spray Technique to deposit TBC´s

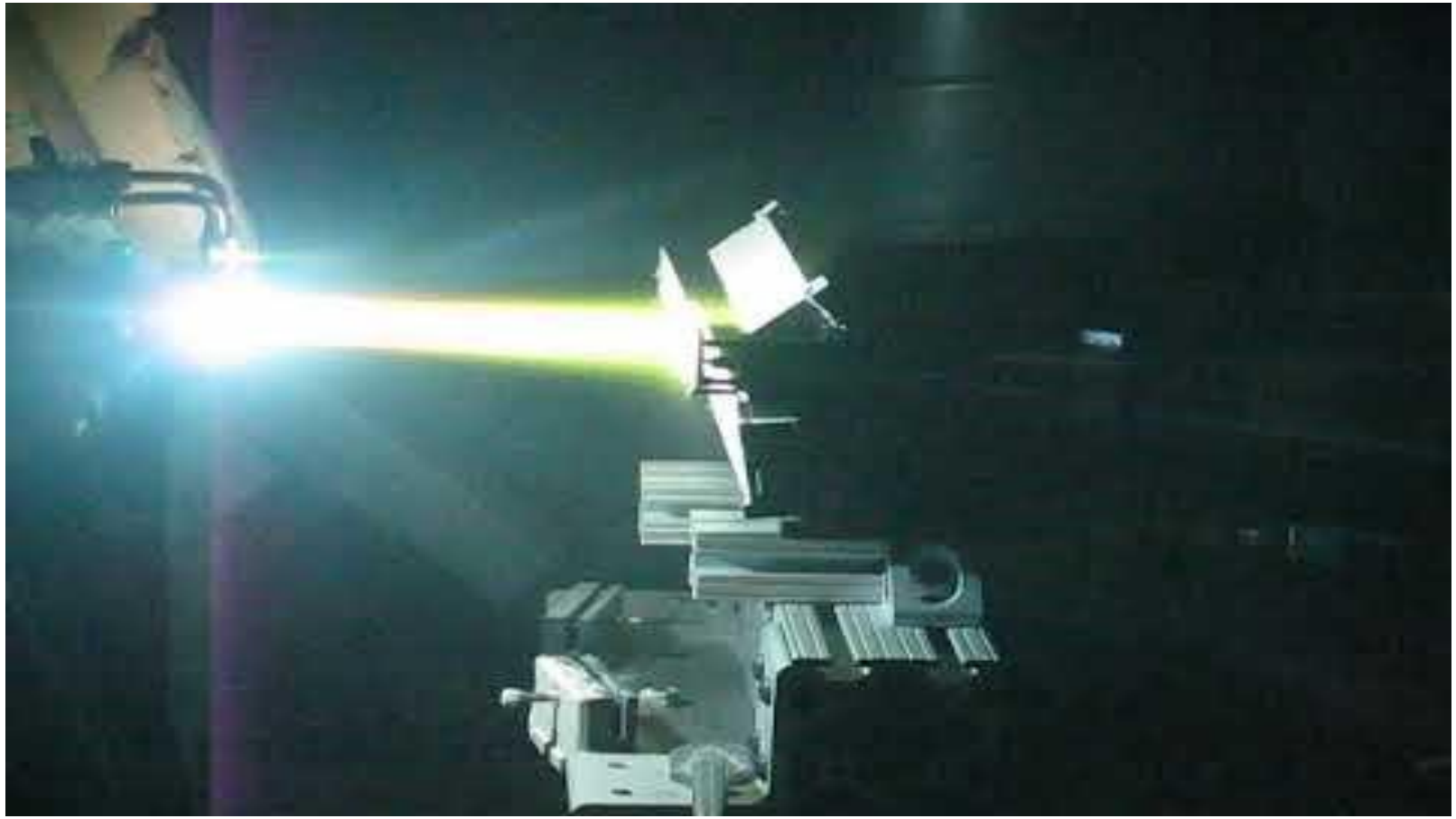

https://youtu.be/zxeFSpKSFMI

Objective of the Study

Goal of the study

- Determine and analyze the 3D thermo-mechanical behavior of various configurations of multilayered/multimaterial TBCs, using modeling and simulation.

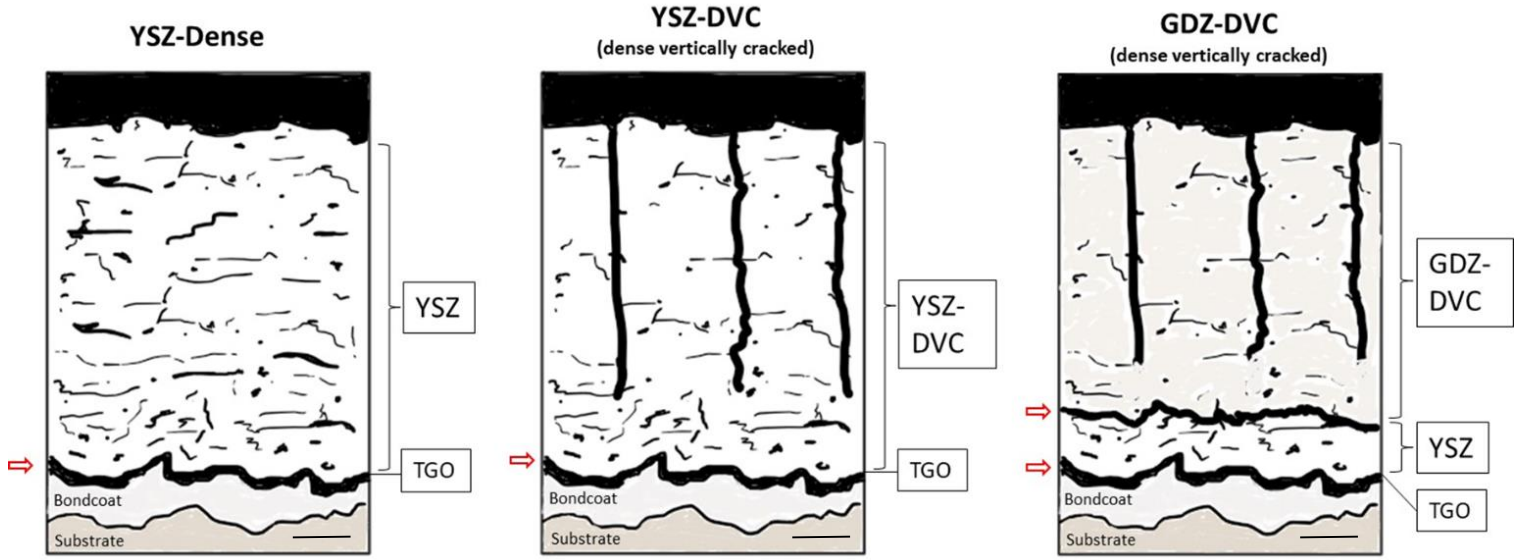

Suggest microstructures of the TBCs vs multilayer variant. Three types of YSZ and a GDZ microstructures (porous -right, and DVC-dense vertically cracked YSZ and GDZ). GDZ is required to be on top to offer erosion and CMAS resistance. The micrometer bar represents 50 um.

Specific Objectives

- Develop a multi-scale model to understand thermal stresses and suggest optimum TBC configurations in terms of thickness, compliance, toughness, etc.
- Understand the functionality of the different multilayer configurations of the TBCs, and optimize such configuration.
- Determine a correlation between coating lifetime and the thermo-mechanical behavior in regards to the thermo-mechanical loading

Viswanathan, et al. Multilayer, Multimaterial Thermal Barrier Coating Systems: Design, Synthesis, and Performance Assessment. J. Am. Ceram. Soc., 1–9

Failure Assessment in multilayers by FCT-Furnace Cycle testing

Furnace Cycle Testing with a 24h cycle was conducted in a box-furnace at 1100°C in air.

A criterion of 20% or more spallation of top-coat was used to identify coating failure.

The loci of failure is near the bond-coat and top-coat interface (adhesive failure)

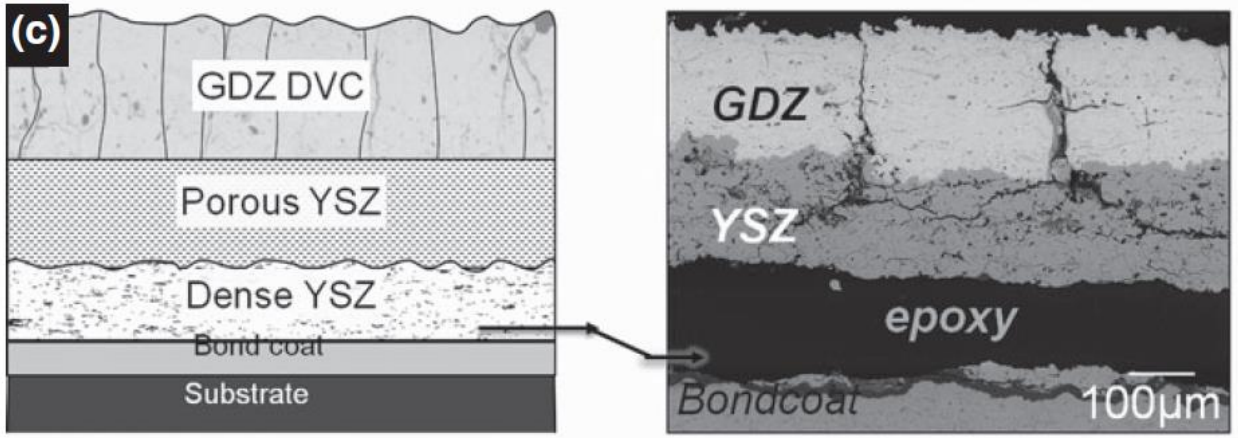

TBC Lifetime Assessment

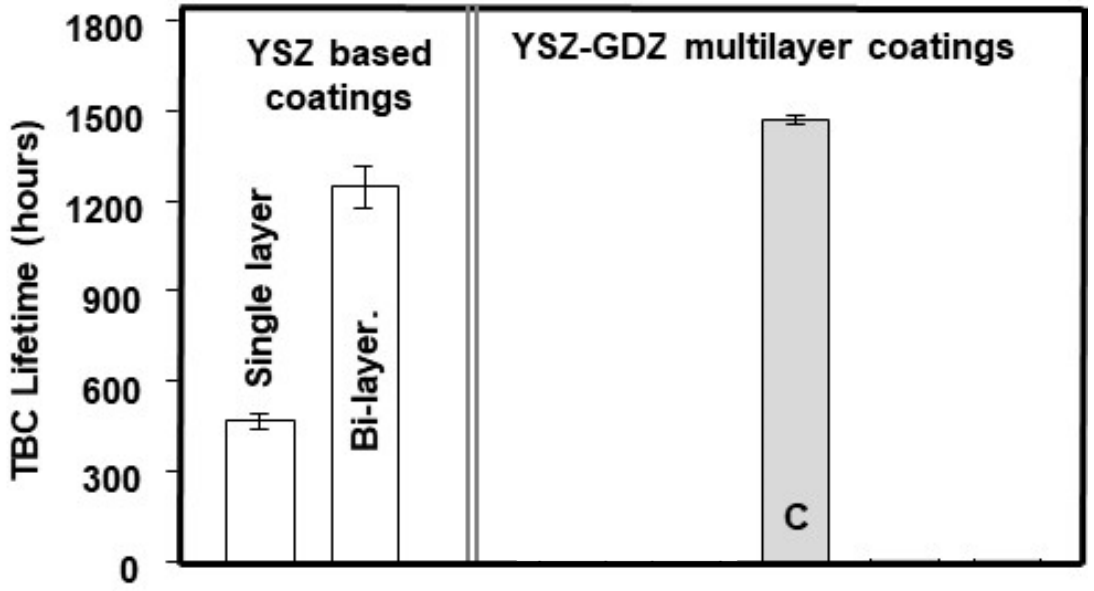

Viswanathan, et al. Multilayer, Multimaterial Thermal Barrier Coating Systems: Design, Synthesis, and Performance Assessment. J. Am. Ceram. Soc., 1–9

Microstructure of Porous and Vertically Cracked Coatings – the 3D Need

Real 3D YSZ microstructures

Traditionally, Thermal Barrier Coatings (TBCs) have been modeled as 2D structures with infinitely large in-plane dimensions. However, the presence of defects, specifically pores, horizontal cracks and vertical cracks make the three-dimensional (3D) assessment of particular interest.

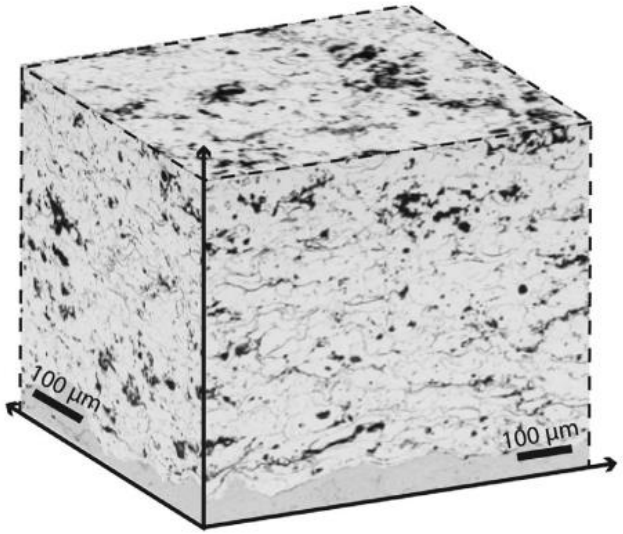

Porous microstructure

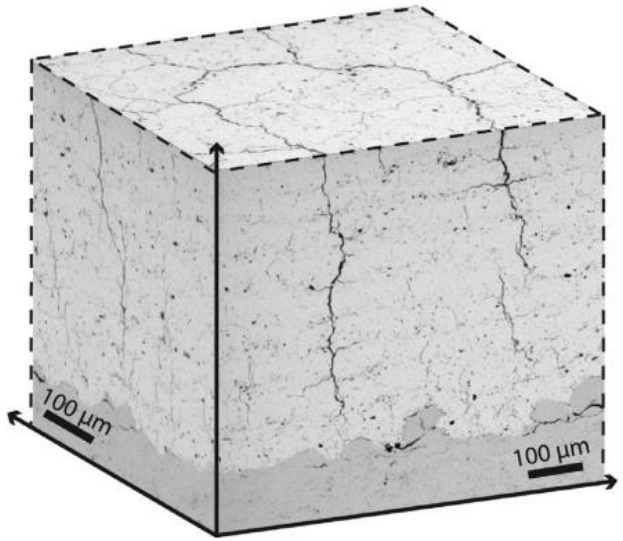

Dense Vertically Cracked

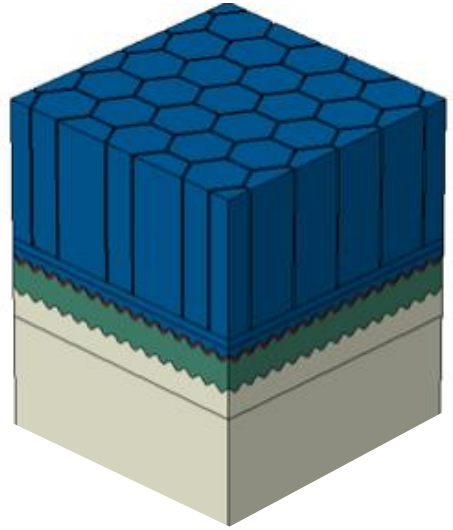

HoneyComb-like (inverted) Structure

Shinde, S. V., Gildersleeve V, E. J., Johnson, C. A. & Sampath, S. Segmentation crack formation dynamics during air plasma spraying of zirconia. Acta Mater. 183, 196–206 (2020). Courtesy Stony Brook University

Intro – 2D vs 3D modeling: TGO-TBCs interface are key zones

2D-research

Mechanisms controlling the durability of TBCs

Evans, Hutchinson, Levy, Clark, Vassen, Sampath

Assessment of TBC systems failure mechanisms using a fracture mechanics approach. Aktaa et al.

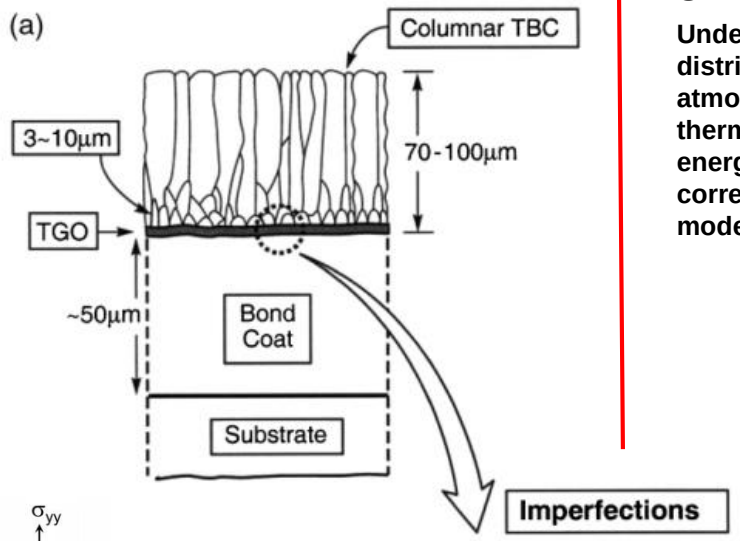

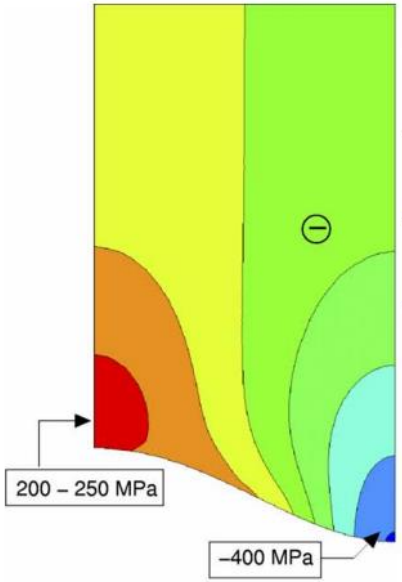

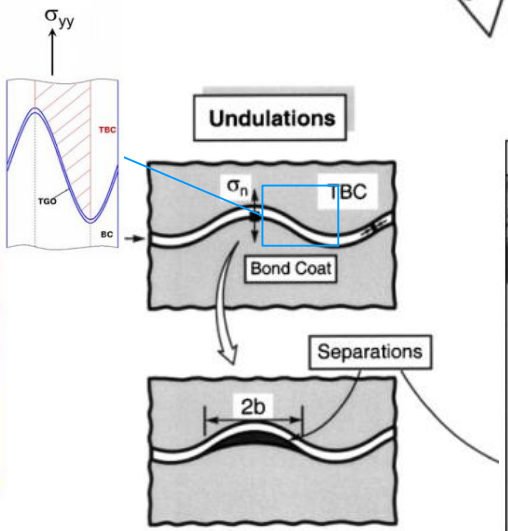

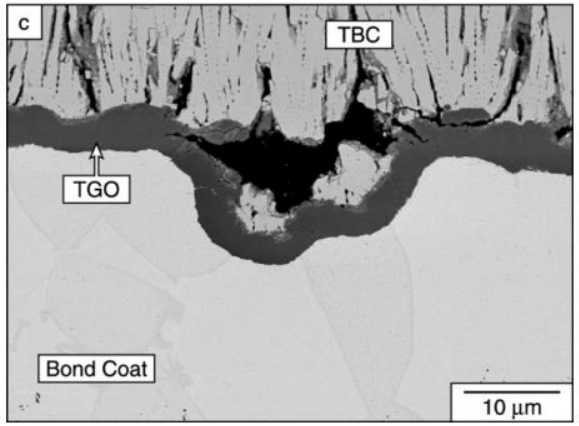

3D-research

Understanding the residual stress distribution through the thickness of atmosphere plasma sprayed (APS) thermal barrier coatings (TBCs) by high energy synchrotron XRD; digital image correlation (DIC) and image based modelling

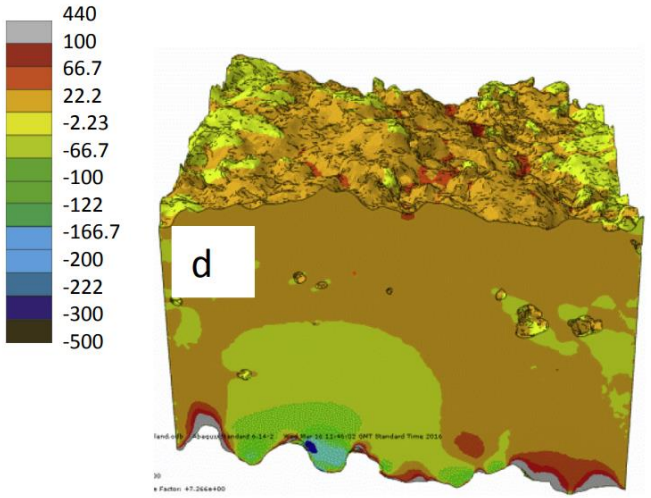

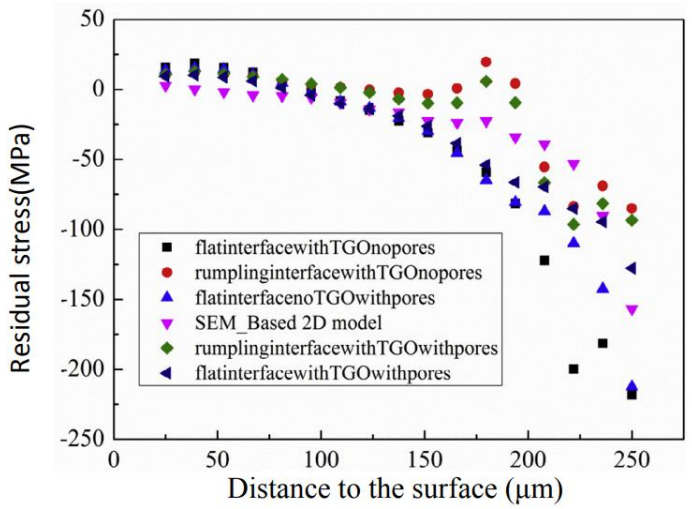

Aktaa et al. Assessment of TBC systems failure mechanisms using a fracture mechanics approach. doi:10.1016/j.actamat.2005.06.003

Li et al. Understanding the residual stress distribution through the thickness of atmosphere plasma sprayed (APS) thermal barrier coatings (TBCs) by high energy synchrotron XRD; digital image correlation (DIC) and image based modelling doi.org/10.1016/j.actamat.2017.03.044

Model Definition of the 3D Structure - Global Model : Dense YSZ

Model Definition

3D-VIEW

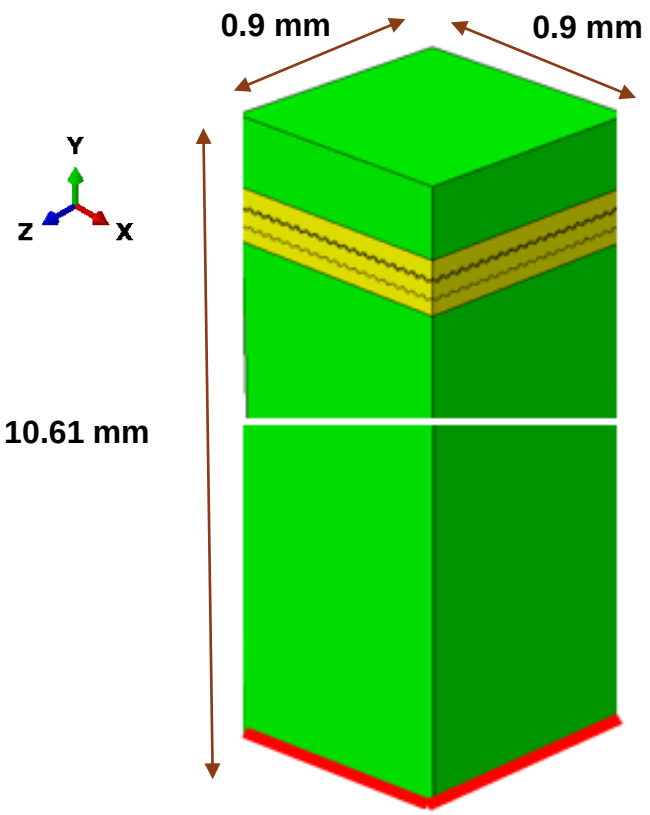

FRONT VIEW

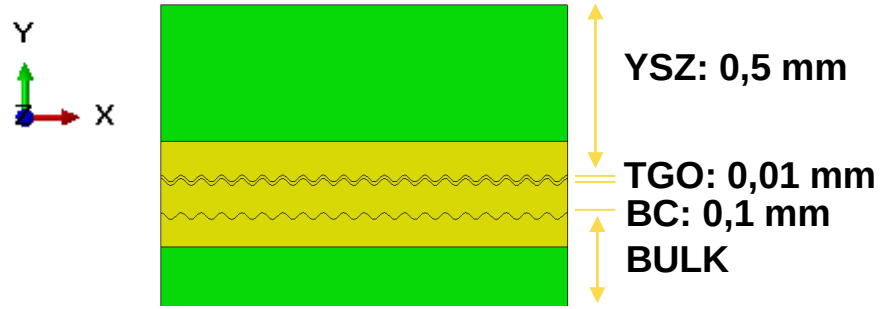

CONTACT SURFACE PROFILE

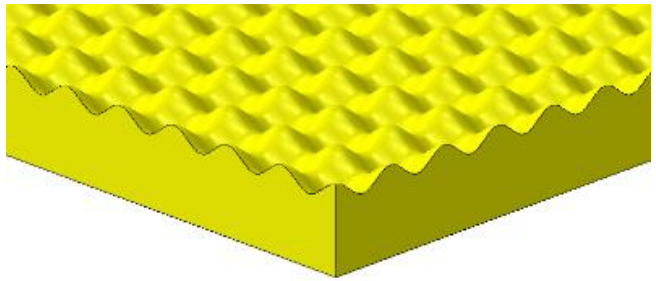

TEMPERATURE PROFILE

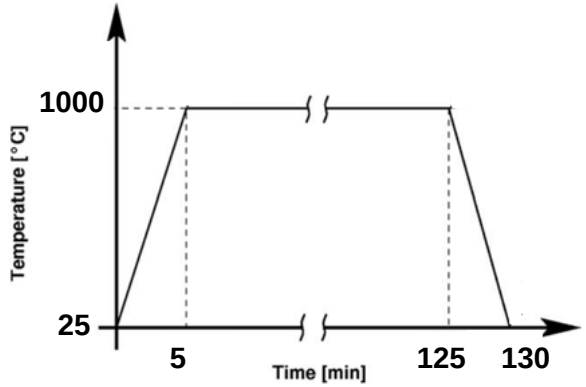

A = 0,01 mm $\lambda = 0,06\ mm$

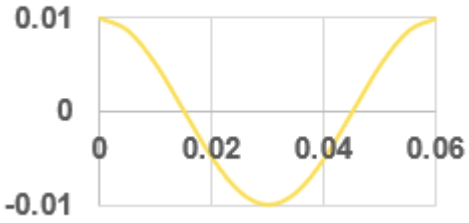

Mesh Definition of the 3D Structure - Global Model: Dense YSZ

Model Definition : Meshing and Boundary Conditions

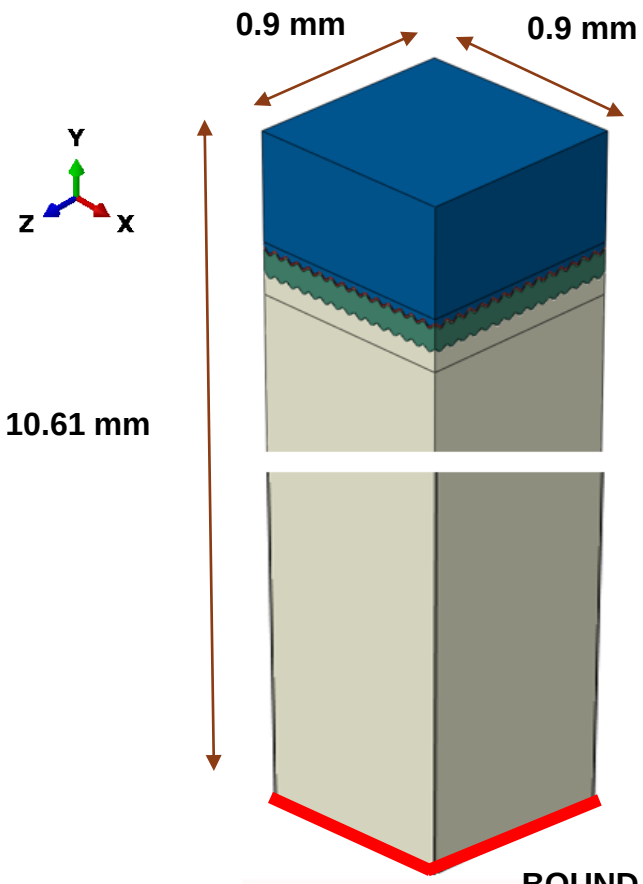

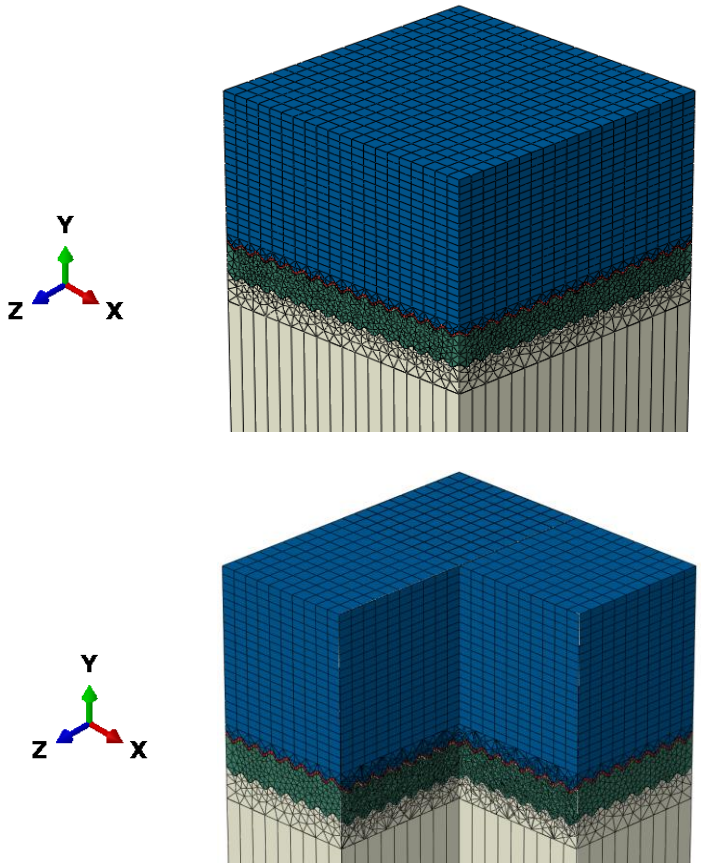

SECTION	ELEMENT TYPE	NUMBER OF ELEMENTS	ELEMENT SIZE (APROX.)
YSZ TOP	HEX	29805	0.045 mm
YSZ BOT (INTERFACE)	TET		0,05 mm
TGO	WEDGE	26242	0,05 mm
BC	TET	137551	0,05 mm
BULKTOP (INTERFACE)	TET	44587	0,05 mm
BULK BOT	HEX		0,5 mm

BOUNDARY CONDITION: ENCASTRE
U1=U2=U3=UR1=UR2=UR3=0

Model Definition of the 3D Structure - Global Model: YSZ DVC

Model Definition

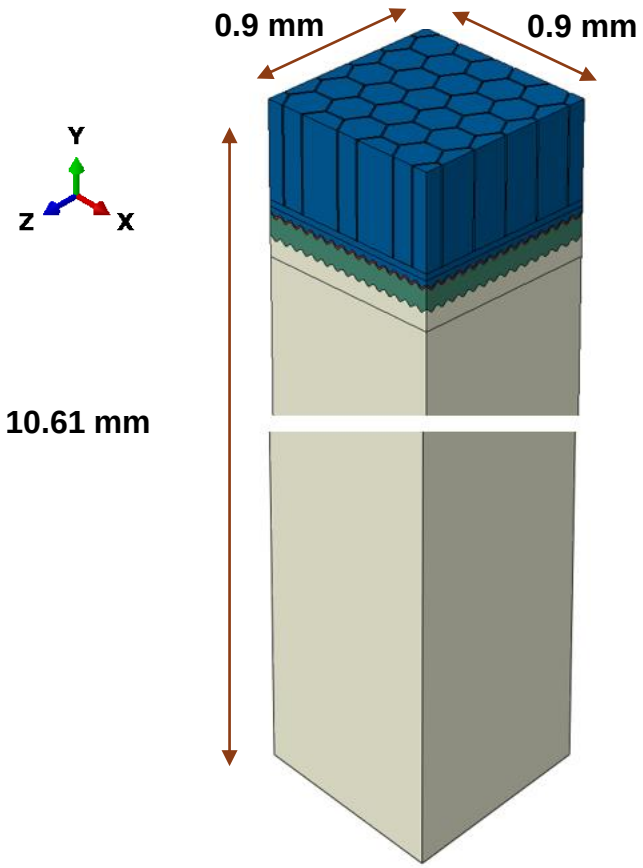

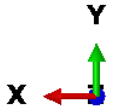

FRONT VIEW

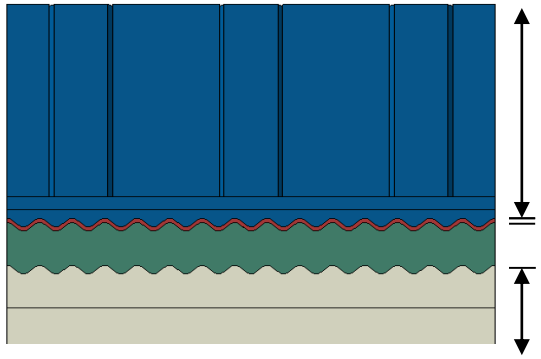

PROFILE OF CONTACT SURFACES

A = 0,01 mm $\lambda = 0,06\ mm$

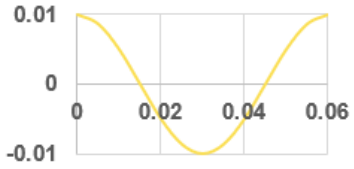

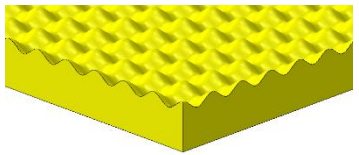

TEMPERATURE PROFILE

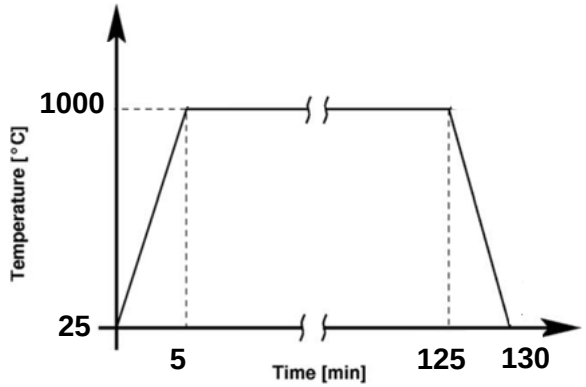

Dense Vertically Cracked microstructure (DVC)

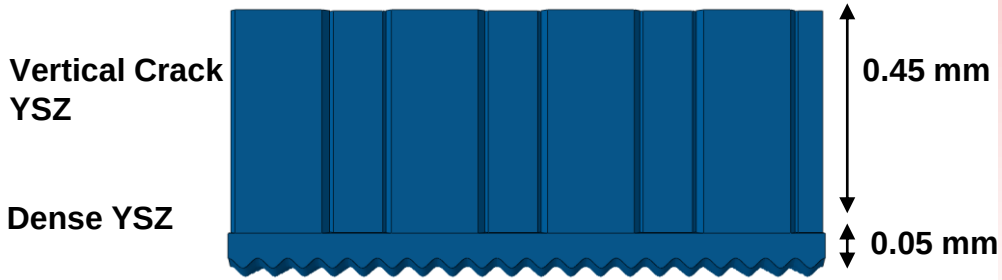

Model Definition of the 3D Structure - Global Model: YSZ + GDZ DVC

Model Definition

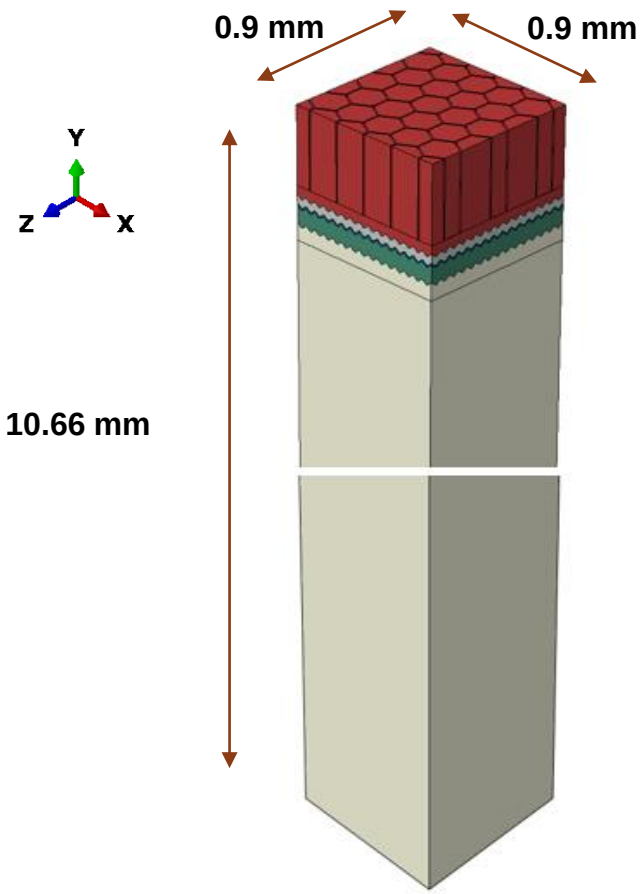

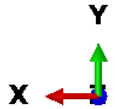

FRONT VIEW

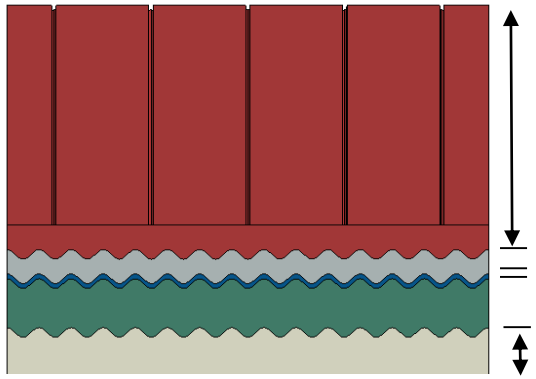

GDZ: 0,5 mm

YSZ: 0,05 mm
TGO: 0,01 mm
BC: 0,1 mm
BULK: 10 mm

PROFILE OF CONTACT SURFACES

A = 0,01 mm $\lambda = 0,06\ mm$

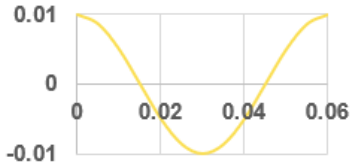

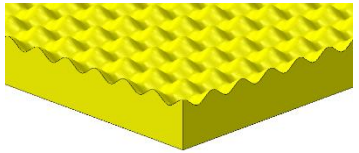

TEMPERATURE PROFILE

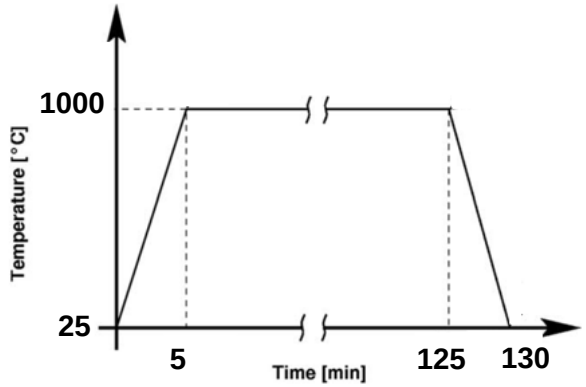

Dense Vertically Cracked microstructure (DVC)

Vertical Crack GDZ

Dense GDZ

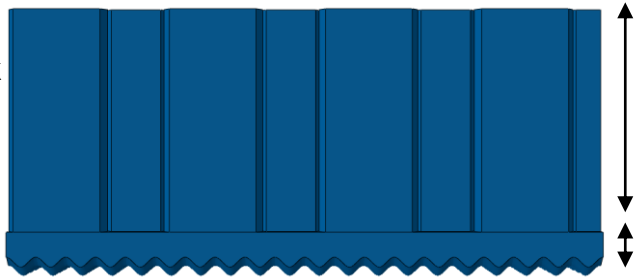

Multiscale analysis model and submodel – the 3D Approach

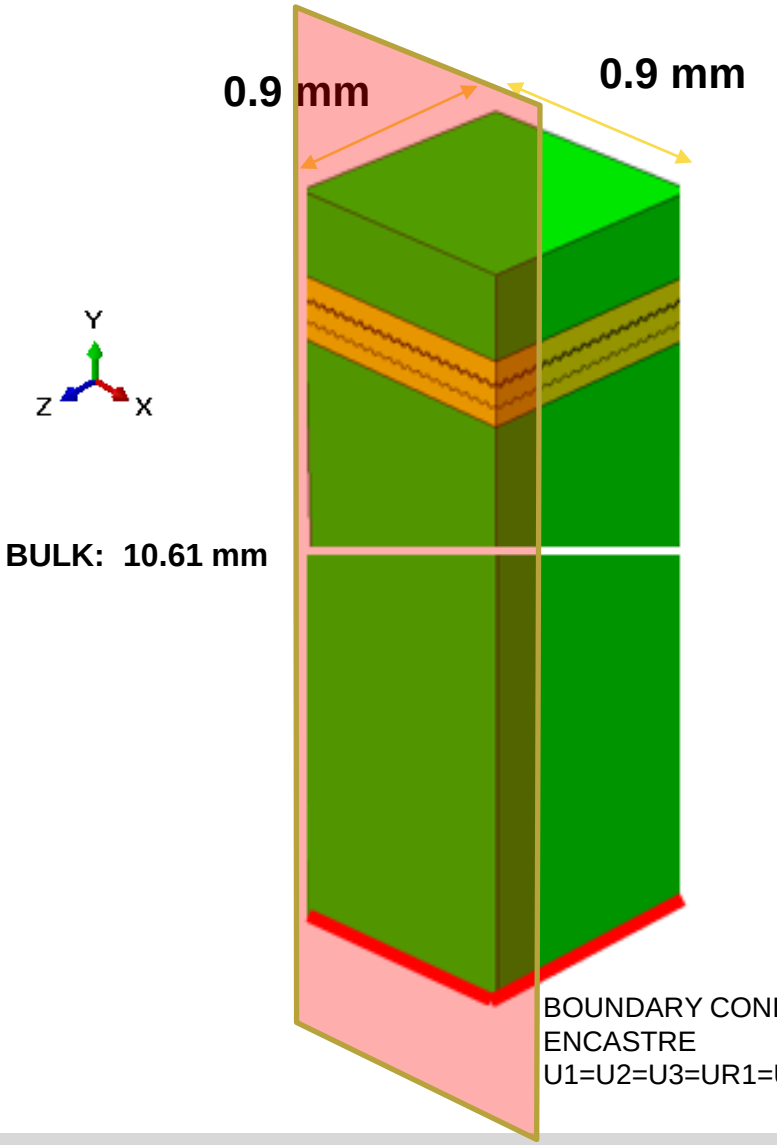

BOUNDARY CONDITION:
ENCASTRE
U1=U2=U3=UR1=UR2=UR3=0

In this approach, the entire simulation model (global) is cut to reduce its size. The resulting model (sub model) receives the information of the deleted elements and nodes through boundary conditions.

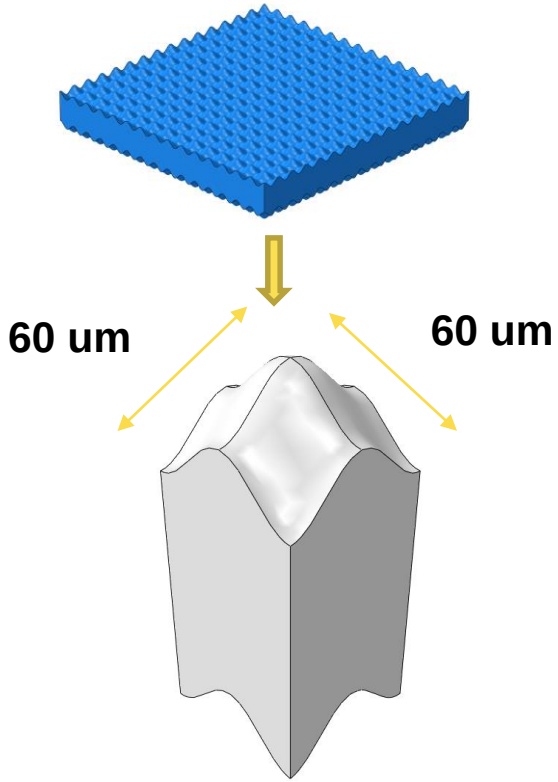

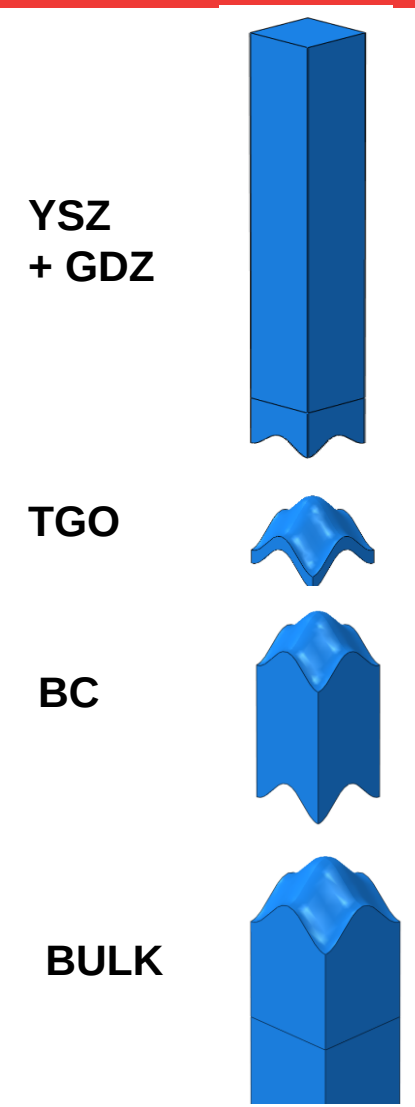

Multiscale analysis model and submodel – the 3D Approach

The interface between materials is a sine 3D wave surface with the next properties:

A = 0,01 mm $\lambda = 0,06\ mm$

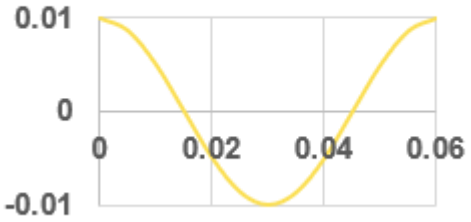

In our study, the simulation unit (sub model), is composed by a 3D peak and four valley quarters in reference to YSZ geometry.

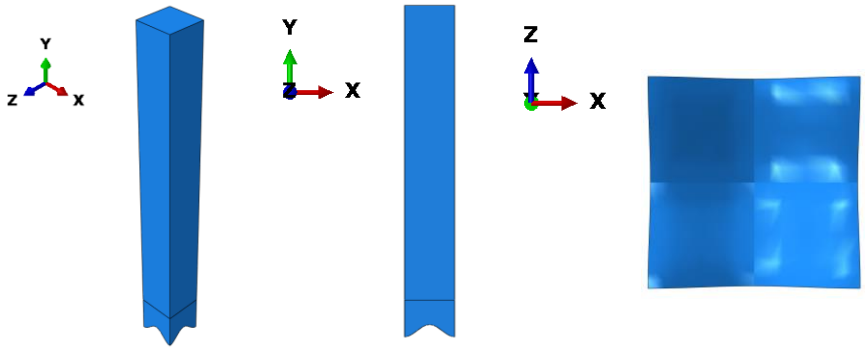

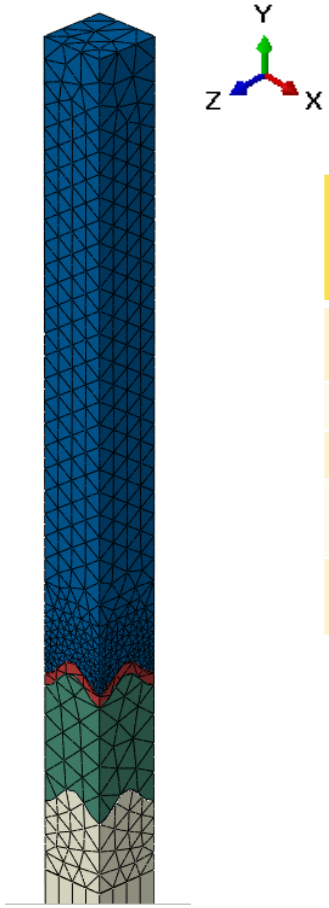

SECCIÓN	TIPO DE ELEMENTO	NUMERO DE ELEMENTO	APROX. TAMAÑO DE ELEMENTO
YSZ	TET	5681	0,01 mm
TGO	TET	116	0,01 mm
BC	TET	390	0,01 mm
BULK (SUPERIOR)	TET	914	0,01 mm
BULK (INFERIOR)	HEX		0,5 mm

3D simulation of YSZ Dense - Biaxial In-plane Stresses

Simulation Results (S11, End of Cooling)

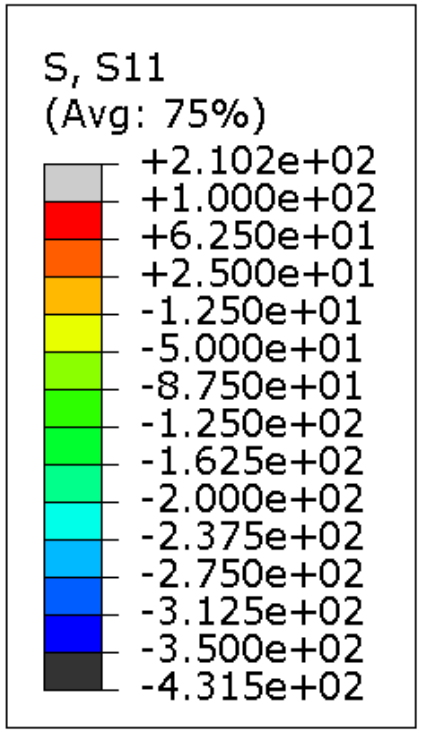

100,-350

GEOMETRY MID CUT VIEW

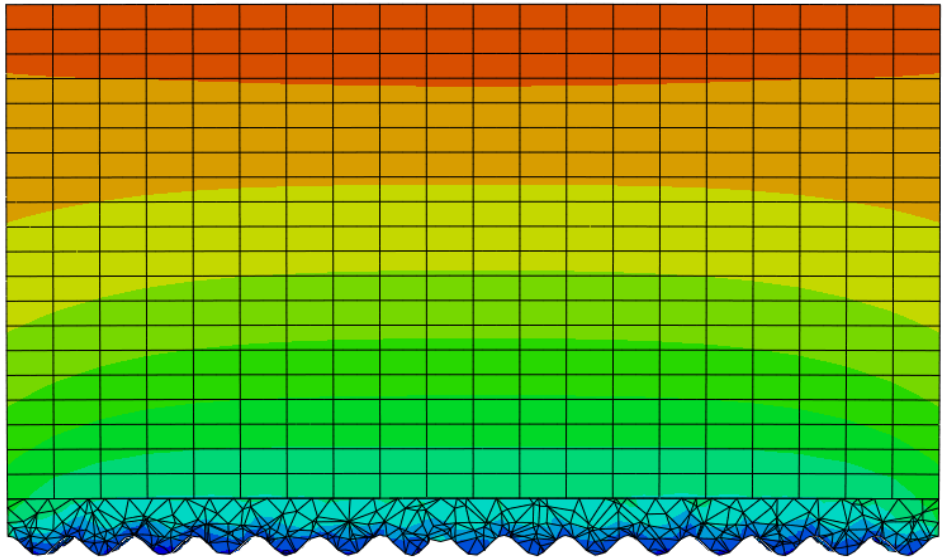

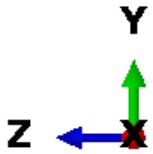

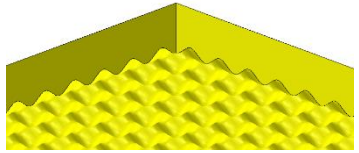

BOTTOM VIEW

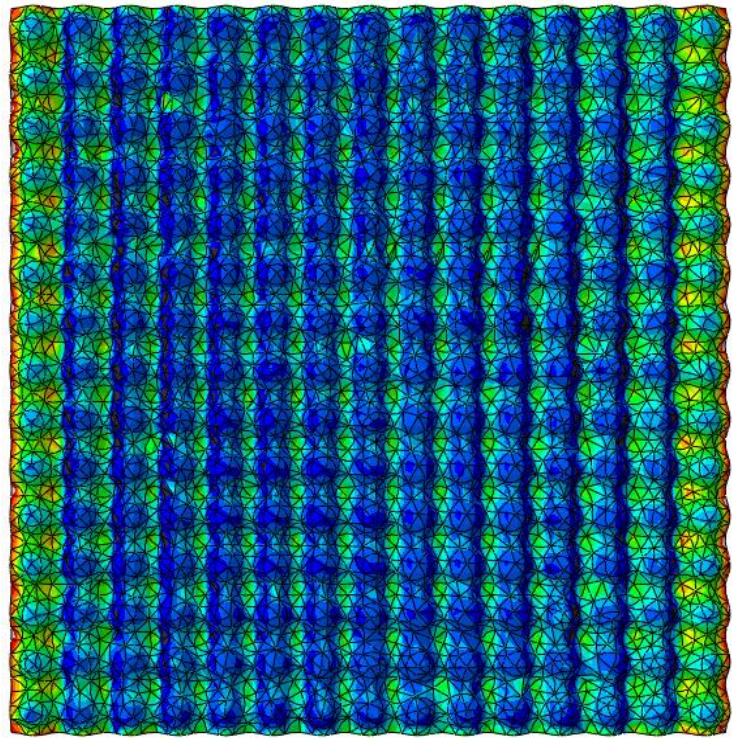

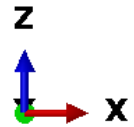

3D simulation of YSZ Dense - Biaxial In-plane Stresses - Ctnd

Simulation Results (S11)

GEOMETRY MID CUT VIEW (END OF HOLDING)

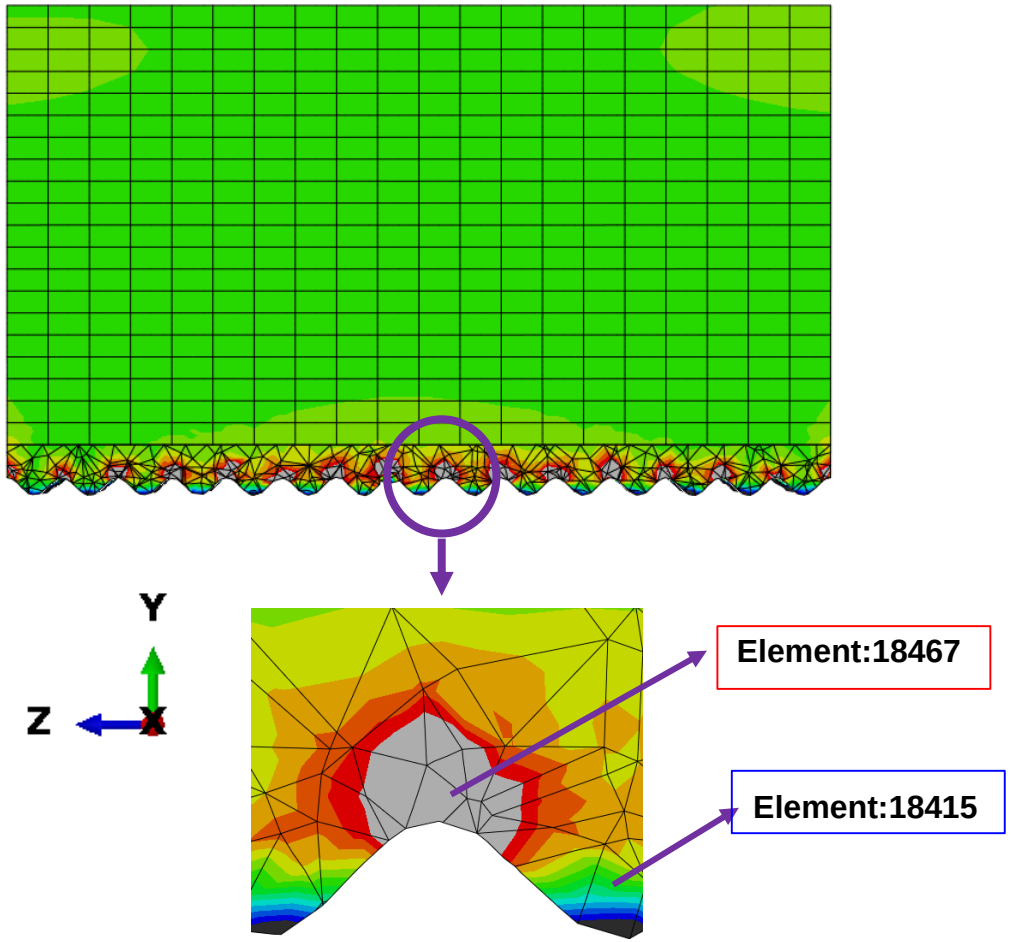

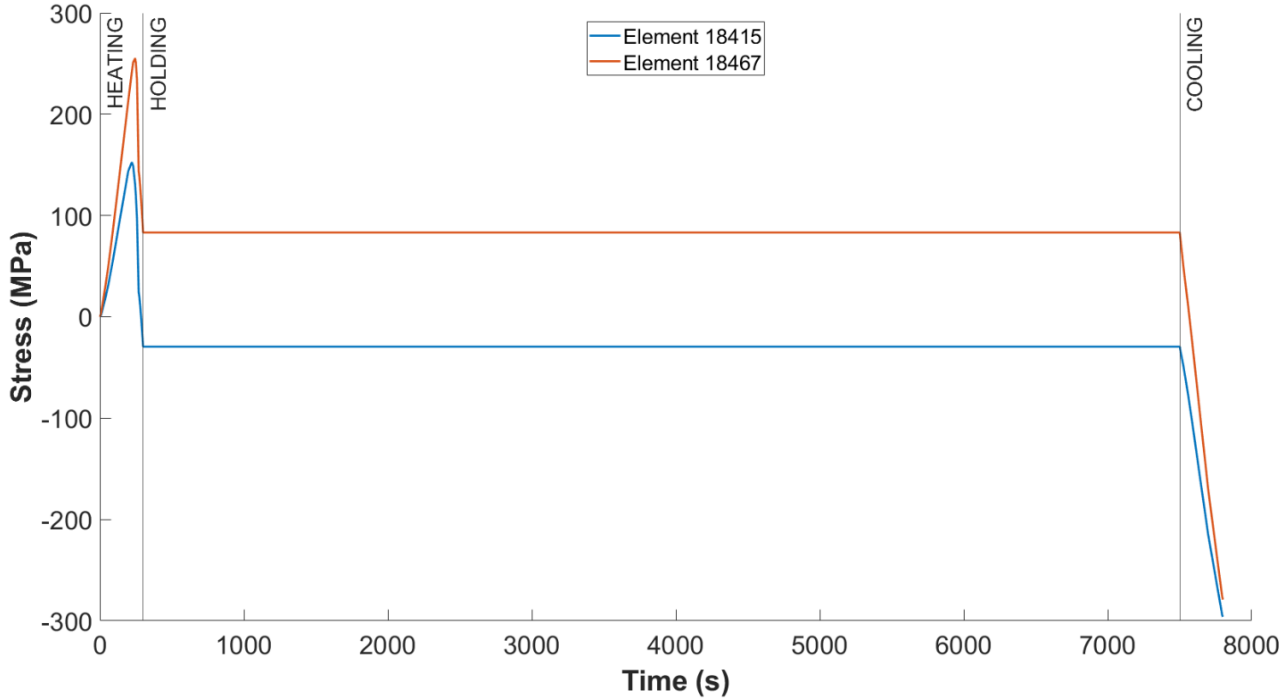

3D simulation of YSZ Dense - Through-thickness out of plane Stress

Simulation Results (S22, End of Cooling)

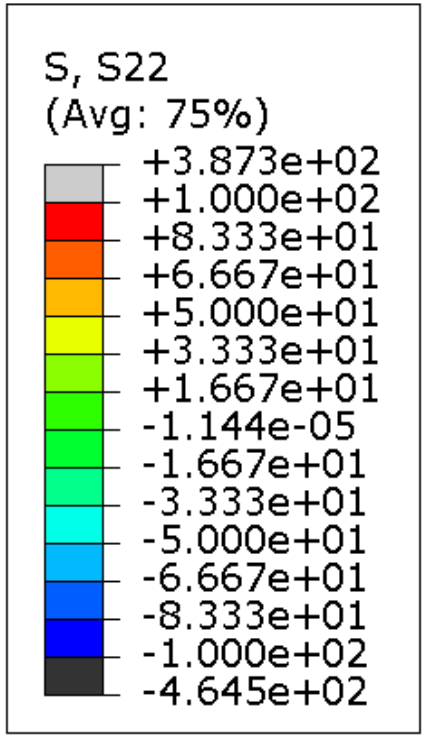

100,-100

GEOMETRY MID CUT VIEW

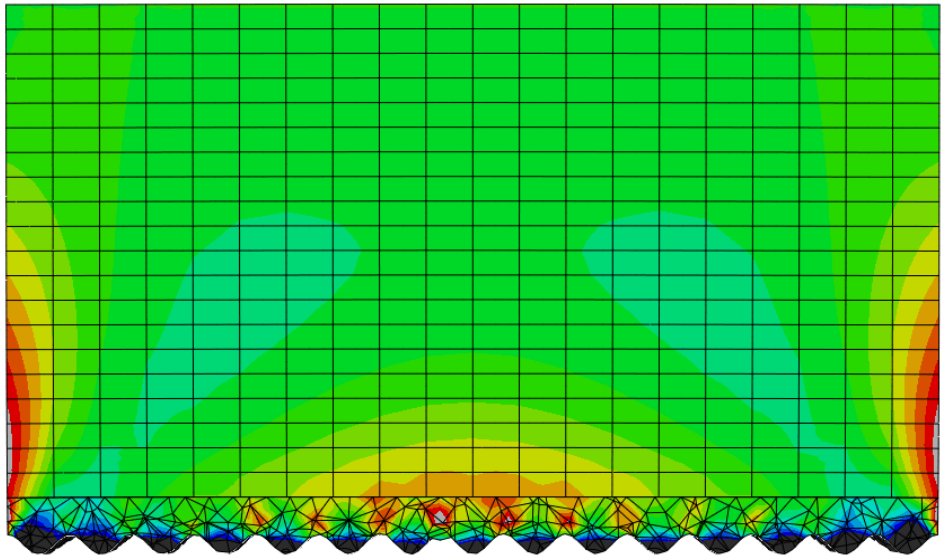

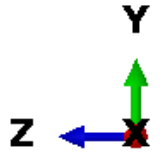

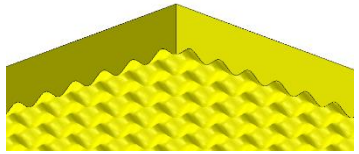

BOTTOM VIEW

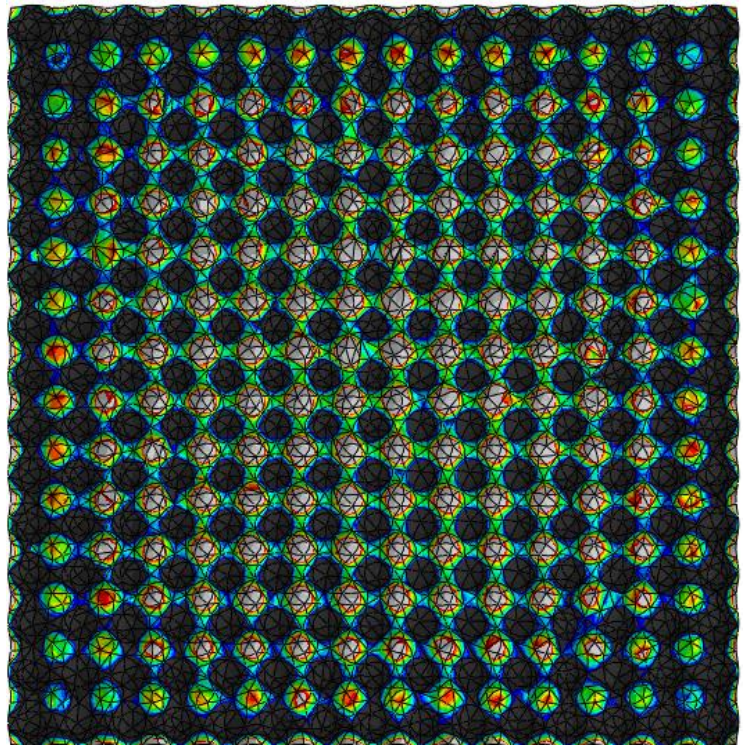

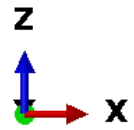

3D simulation of YSZ Dense - Through-thickness out of plane Stress - Ctnd

Simulation Results (S22)

GEOMETRY MID CUT VIEW (END OF HOLDING)

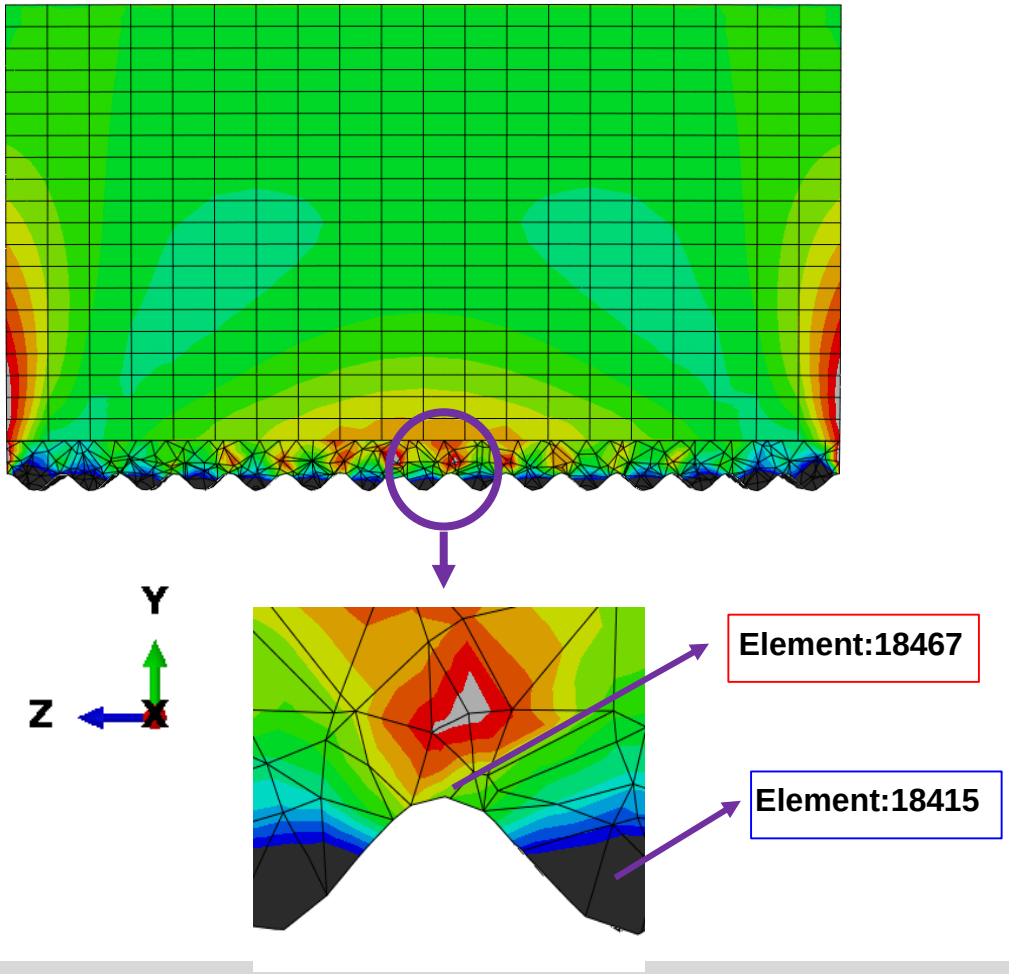

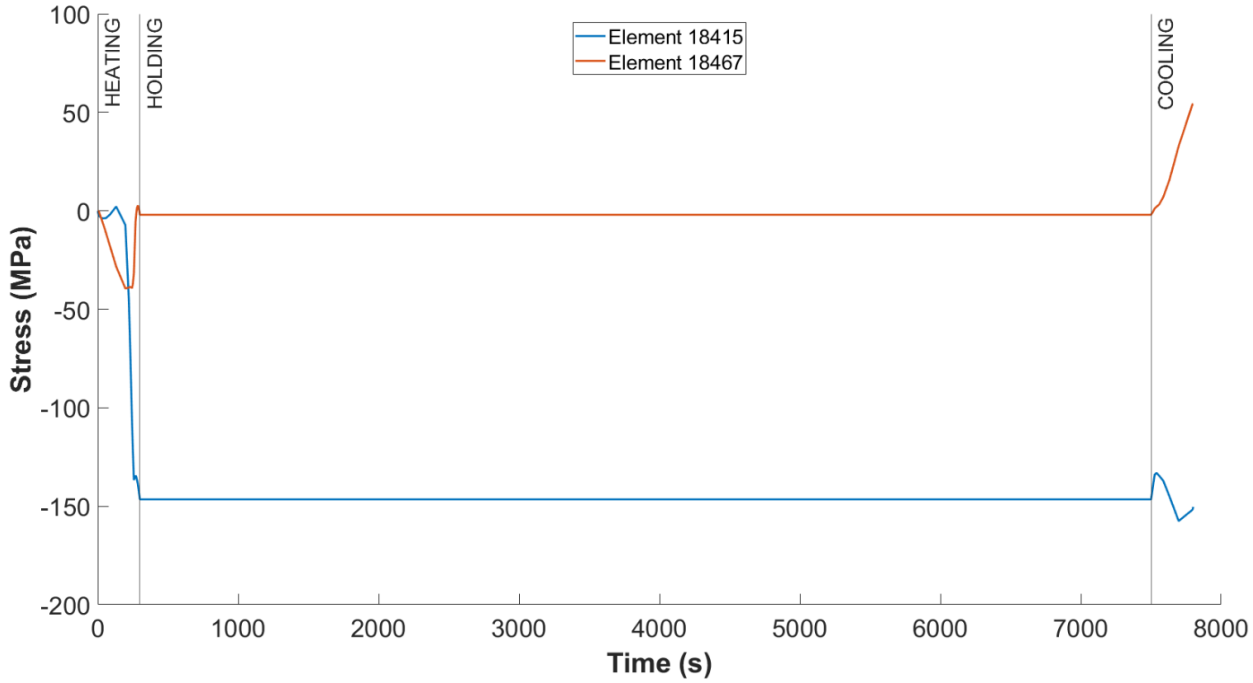

3D simulation of YSZ DVC - Bi-axial in-plane stress

Simulation Results (S11, End of Cooling)

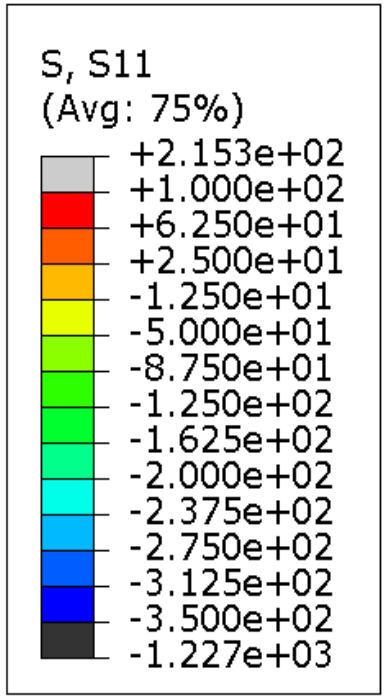

100,-350

GEOMETRY MID CUT VIEW

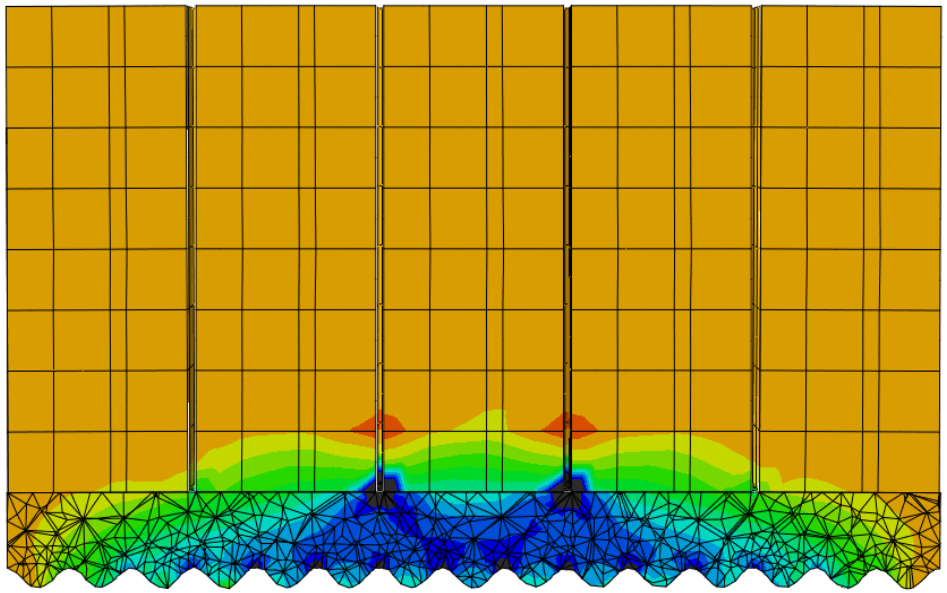

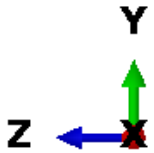

BOTTOM VIEW

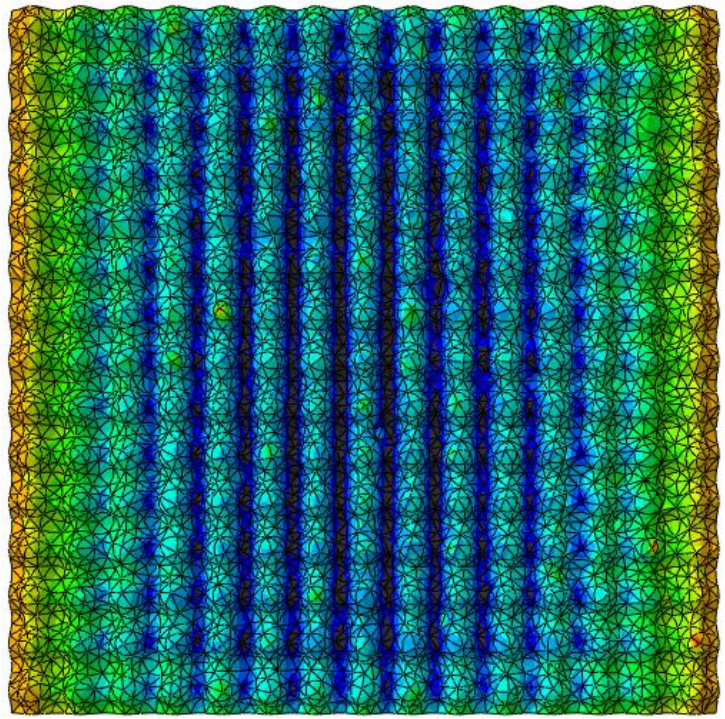

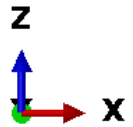

3D simulation of GDZ-DVC - Bi-axial in-plane stress

Simulation Results (S11, End of Cooling)

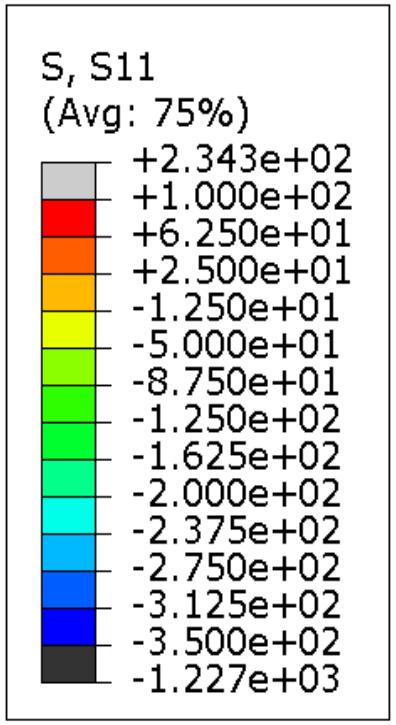

100,-350

GEOMETRY MID CUT VIEW

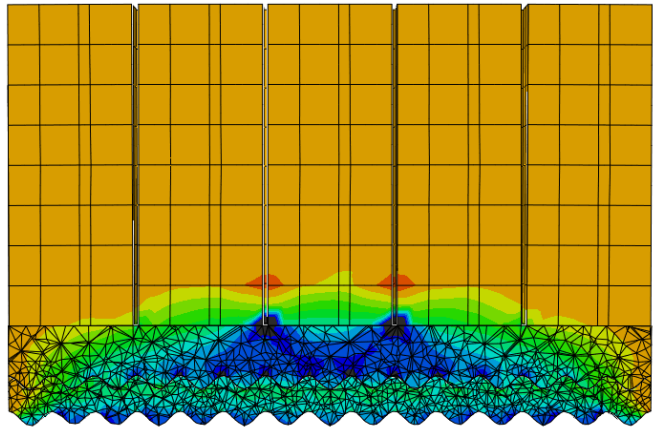

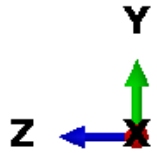

BOTTOM VIEW YSZ

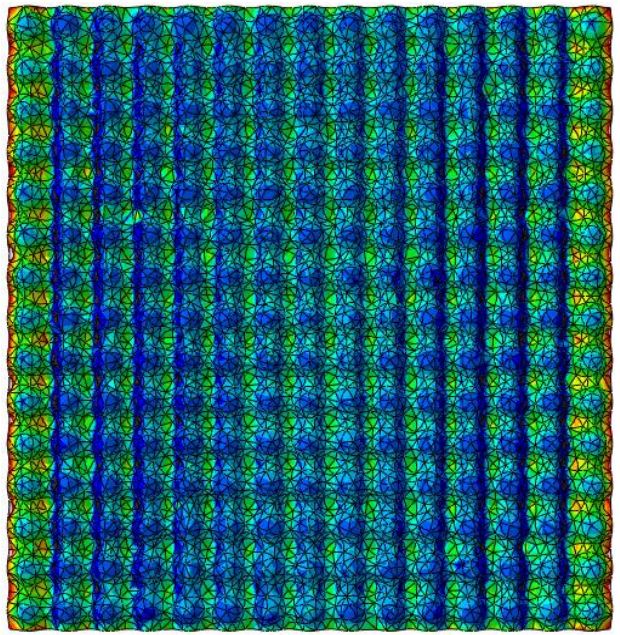

BOTTOM VIEW GDZ

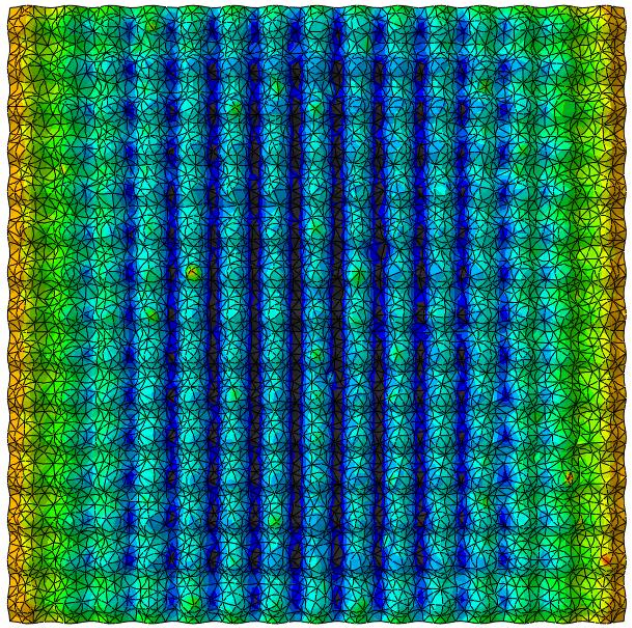

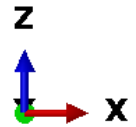

3D simulation of GDZ-DVC - Through the thickness- out of plane

Simulation Results (S22, End of Cooling)

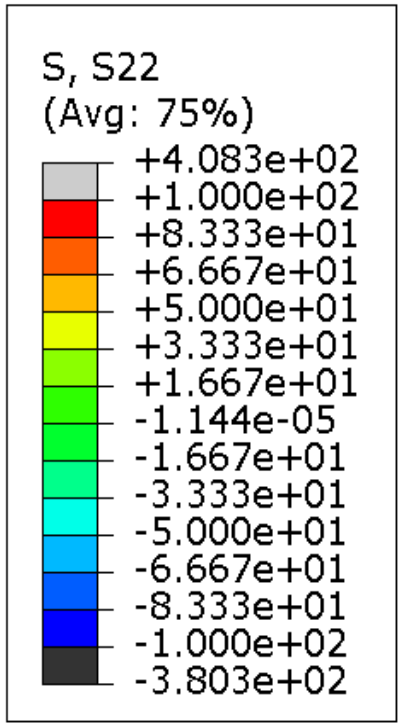

100,-100

GEOMETRY MID CUT VIEW

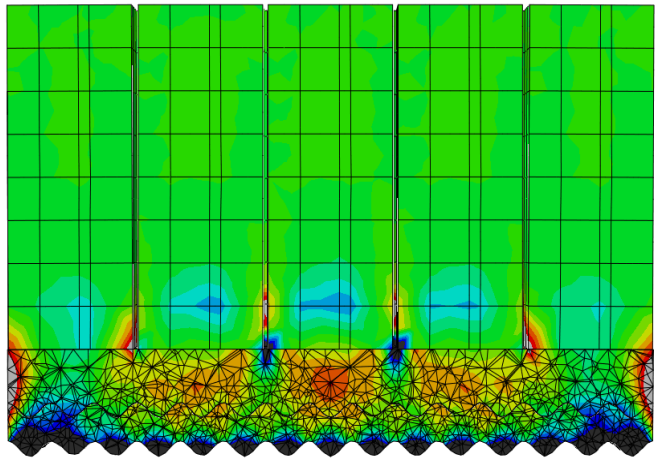

BOTTOM VIEW YSZ-TGO

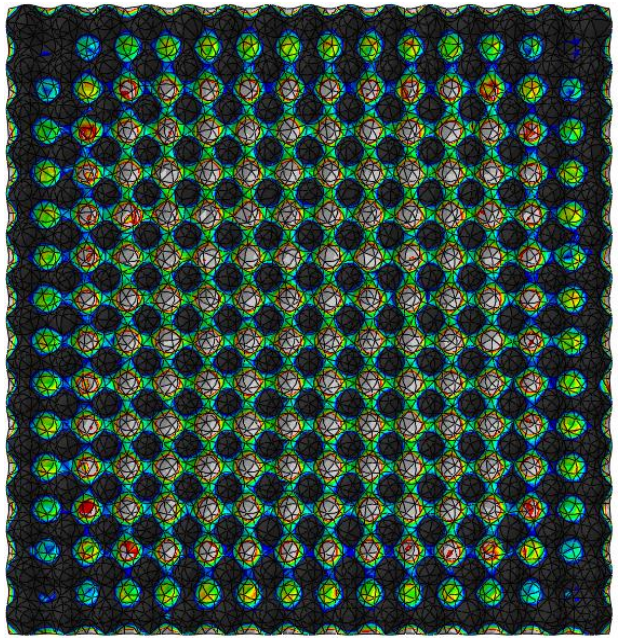

BOTTOM VIEW GDZ-YSZ

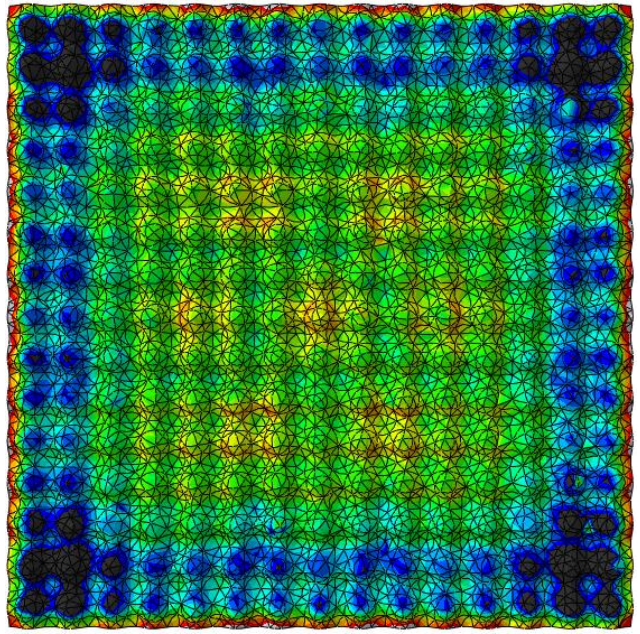

Comparison 3D simulation of YSZ Dense and YSZ DVC - Through thickness stress

Simulation Unit - S22 out of plane stress

YSZ Dense

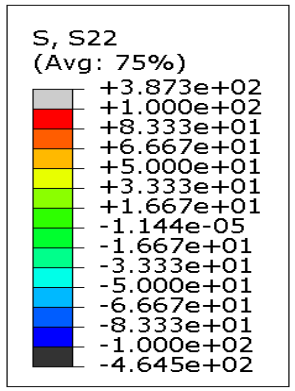

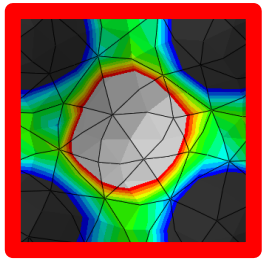

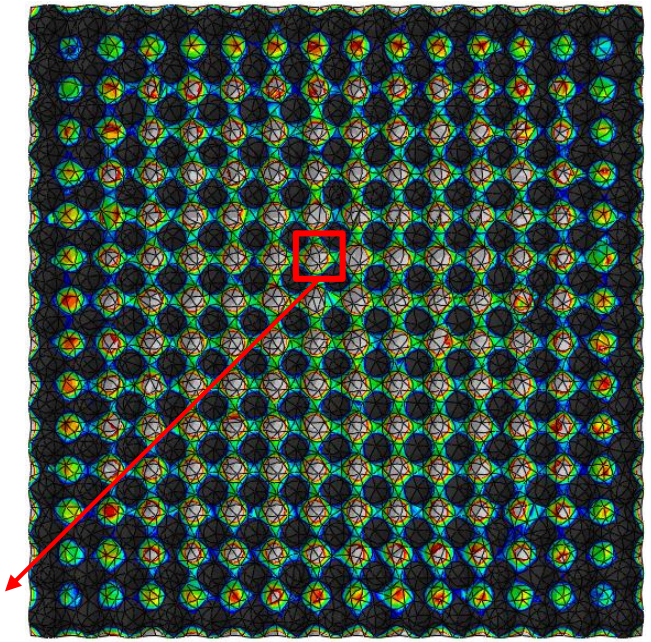

YSZ DVC

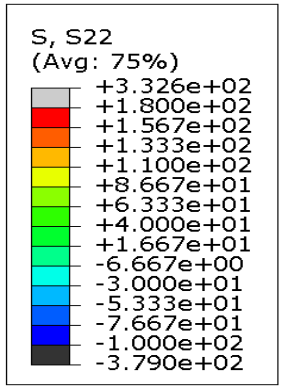

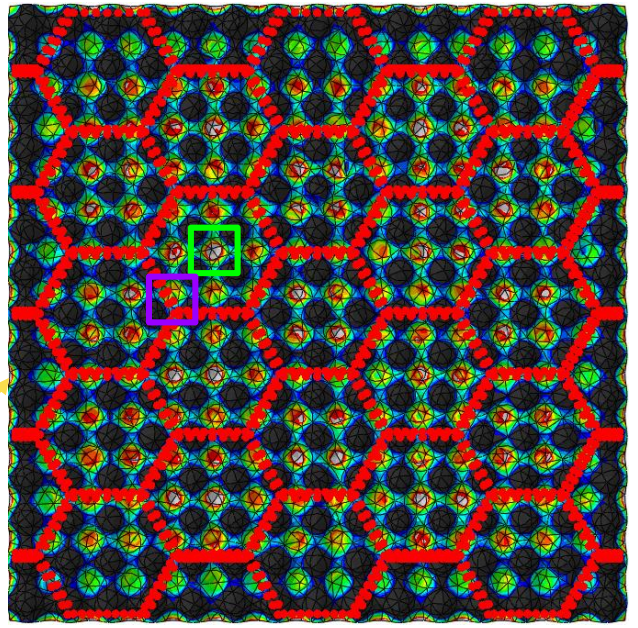

High Stress

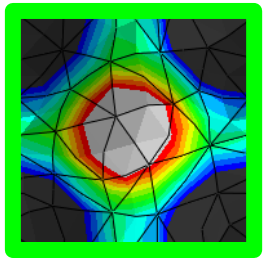

Low Stress

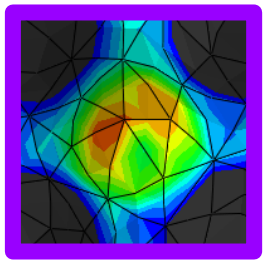

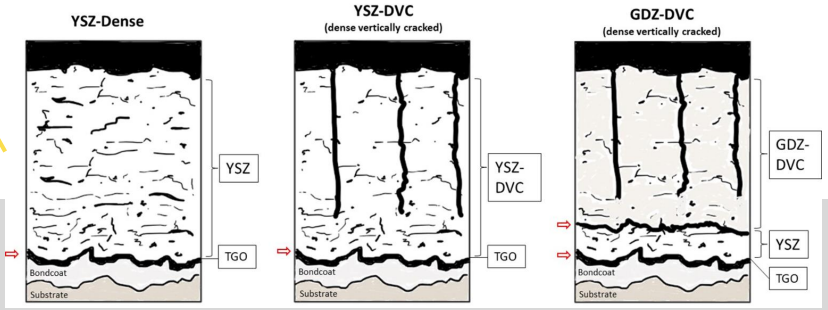

100,-100,-100,180

Comparison 3D simulation of GDZ DVC - Through thickness stress

Simulation Unit

YSZ and TGO Interface

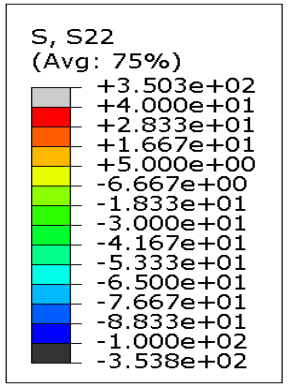

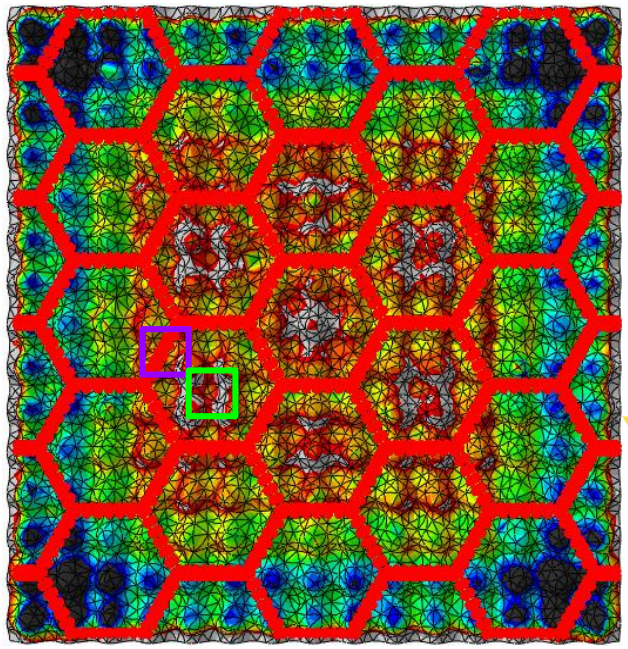

40,-100,200,-150

GDZ DVC + YSZ Dense

GDZ and YSZ Interface

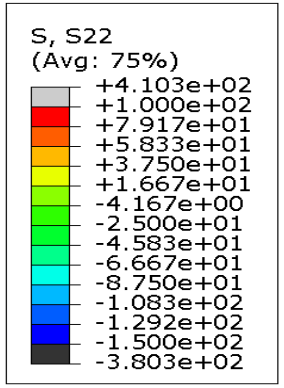

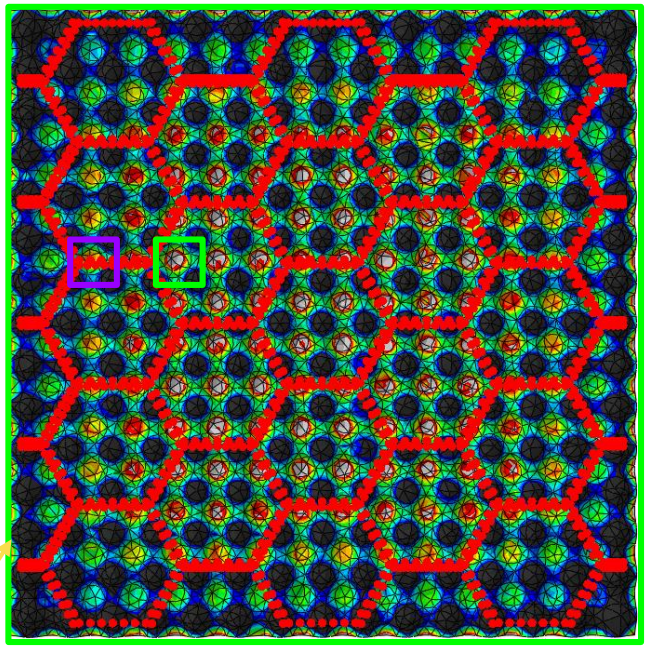

High Stress

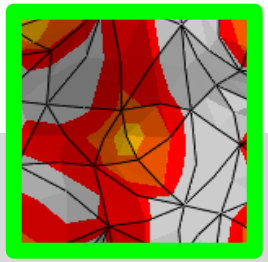

Low Stress

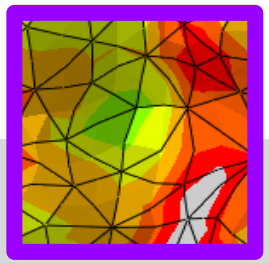

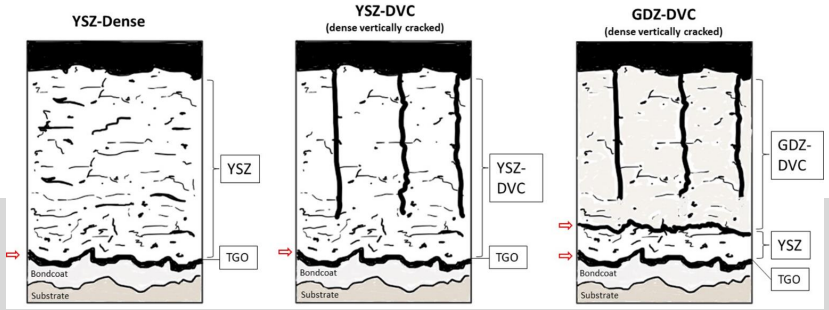

High Stress

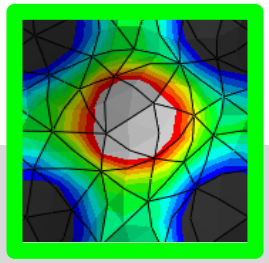

Low Stress

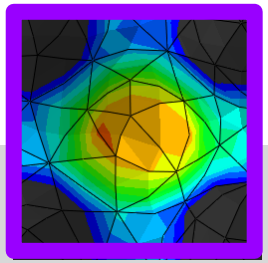

Mesh refinement

SUBMODELS

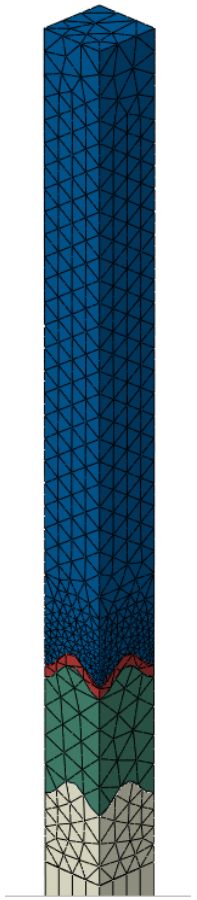

3D simulation of YSZ Dense, YSZ DVC, GDZ DVC: submodel

Simulation Results (S22, End of Cooling)

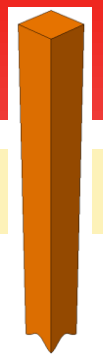

Simulation Unit

YSZ Dense-TGO

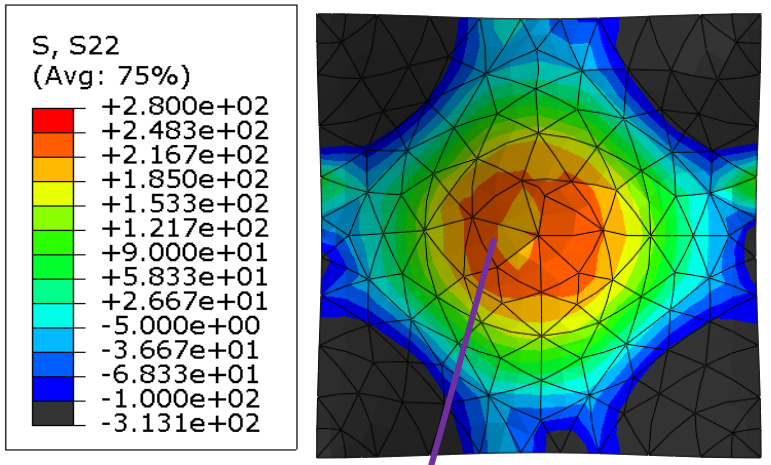

Element:5511

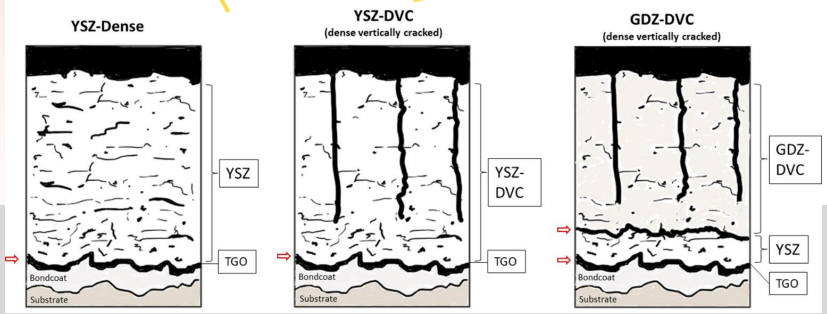

YSZ DVC - TGO

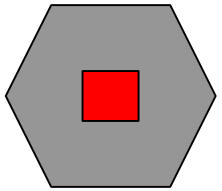

Middle of the island

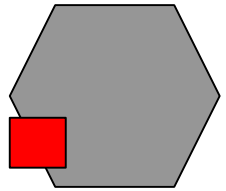

Near an edge

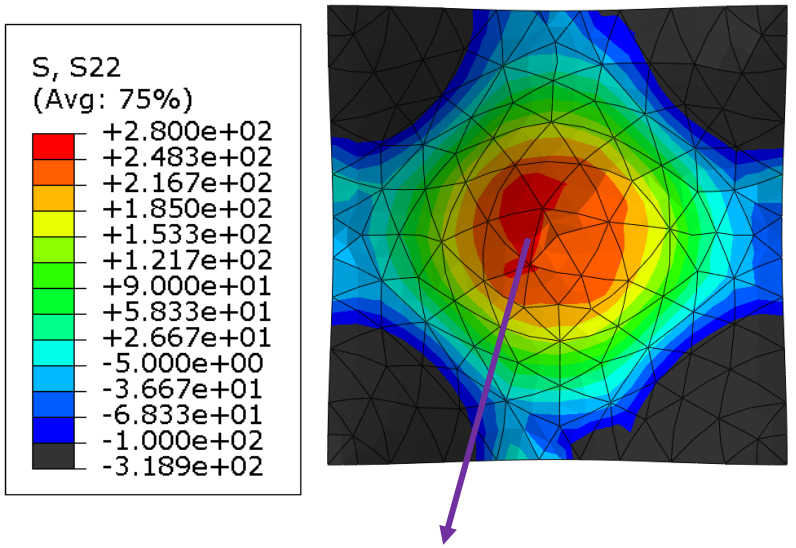

Element:4306

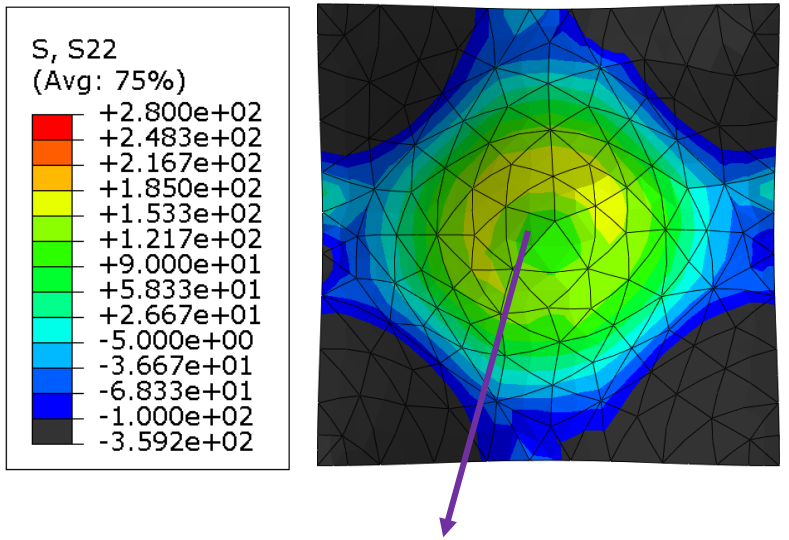

Element:4984

We find similar magnitude of stresses in the middle of the island but quite lower near the cracks projection, which decreases the number of failure points

3D simulation of YSZ Dense, YSZ DVC, GDZ DVC: submodel

Simulation Results (S22, End of Cooling)

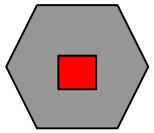

Middle of the island

GDZ DVC

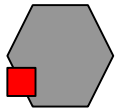

Near an edge

YSZ Dense-TGO

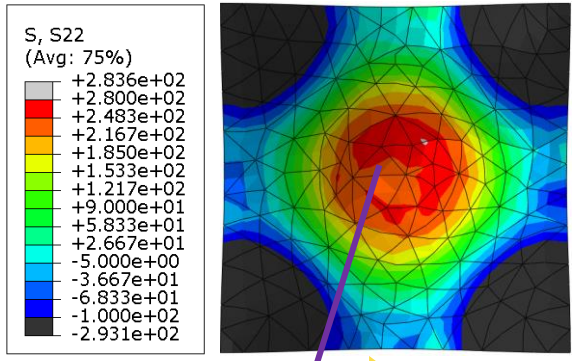

GDZ DVC- YSZ

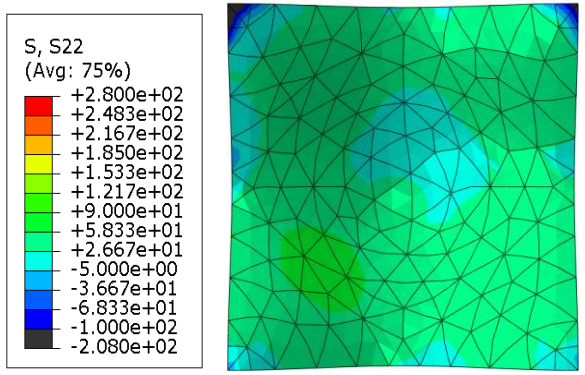

Element:1854

YSZ Dense-TGO

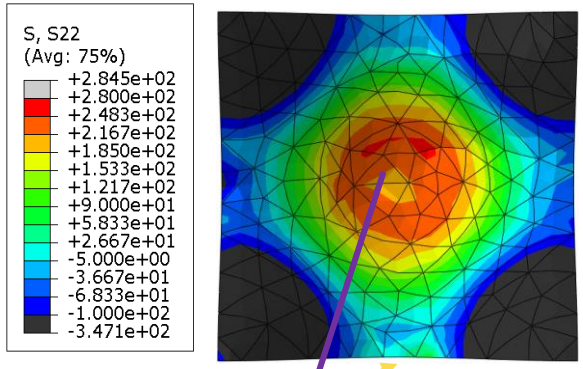

GDZ DVC- YSZ

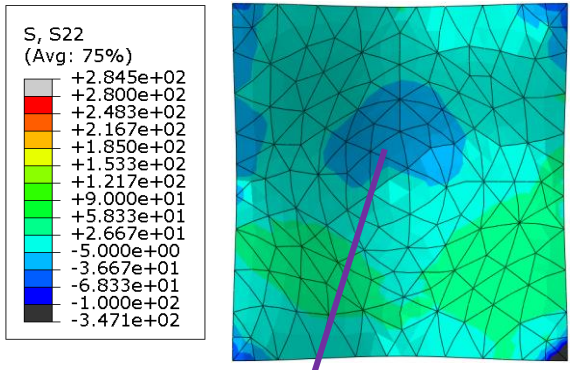

Element:1854

Element:5502

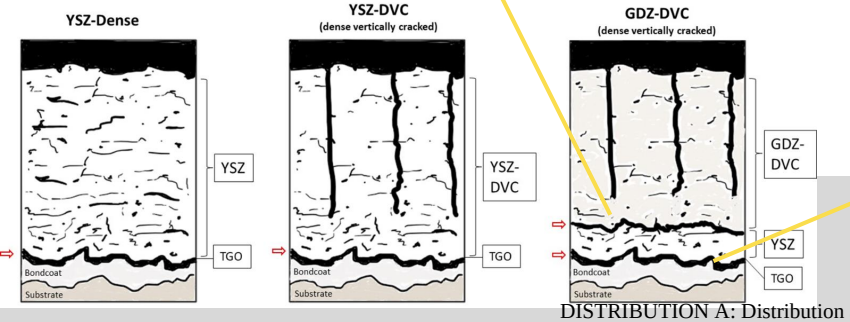

We find lower magnitude of stresses in the middle of the island and even lower in the YSZ-GDZ interface. Away from the middle of the island the stresses are lower, which decreases the number of failure points

capturing the microstructure

Introducing Defects

Image Generation, Image Processing and 3D Modeling

Scanning Electron Microscopy (SEM)

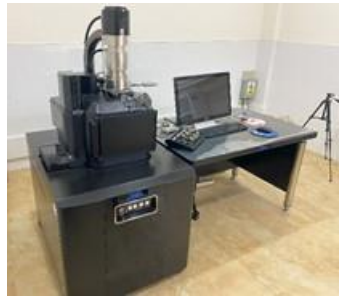

- The Vickers indentation is used to align the photos.
- The depth between photos is measured using the diameter of the indentation.

$$Depth = \frac{D_{avg}}{7}$$

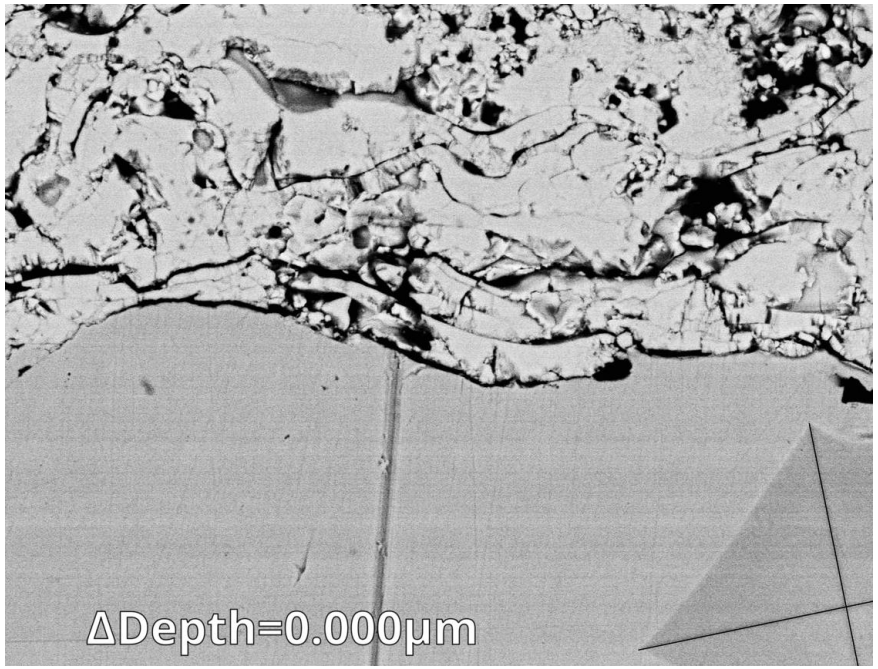

Image Processing

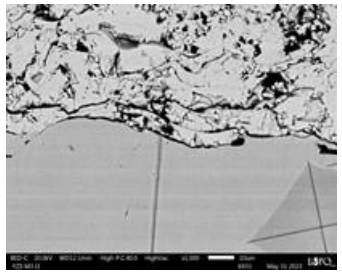

Images go through a thresholding process to highlight details, remove noise and make the edges of objects sharper.

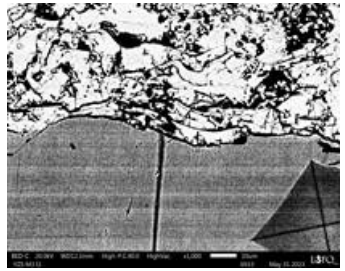

The defects we are interested in are isolated from the rest of the image and a reference point is placed to align them later.

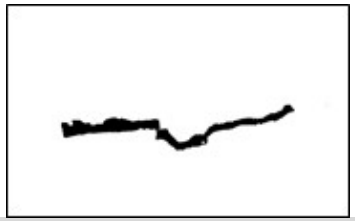

3D Modeling

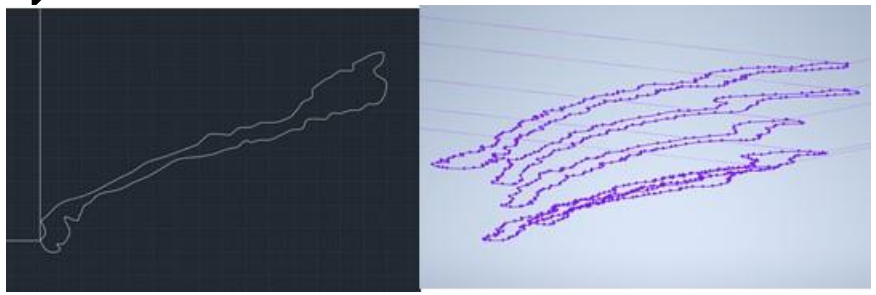

A 2D drawing of the defect outline is made as well as the reference to align the images. In Autodesk Inventor the drawings are placed at the measured depths and aligned, then finally, with the *Loft* tool, a solid of the defect is generated.

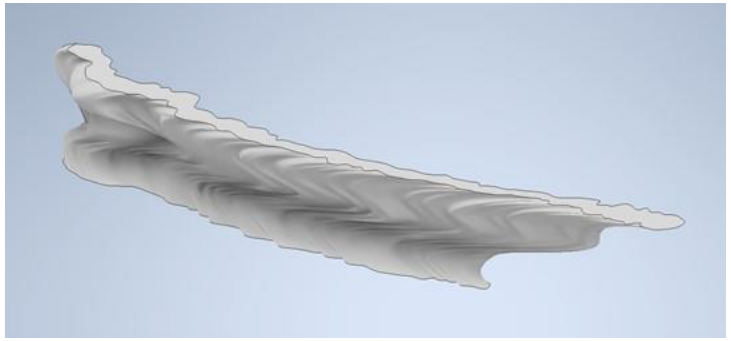

Crack recreated in 3d.

3D simulation of YSZ Dense, GDZ DVC: submodel

Defect - Crack Exploration

YSZ DENSE

YSZ

GEOMETRY MID CUT VIEW

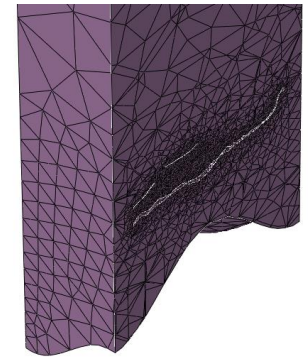

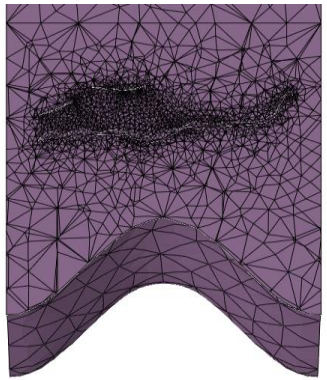

GDZ DVC

GDZ DVC

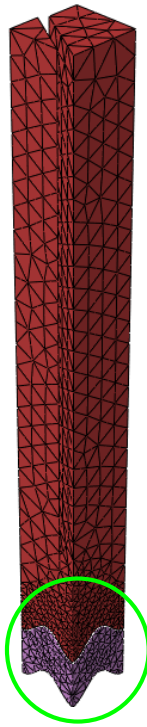

GEOMETRY MID CUT VIEW

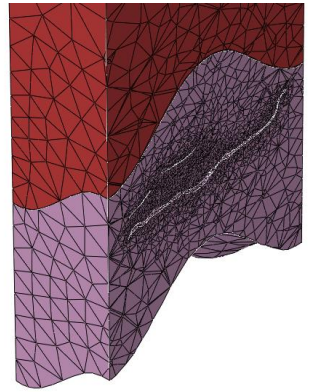

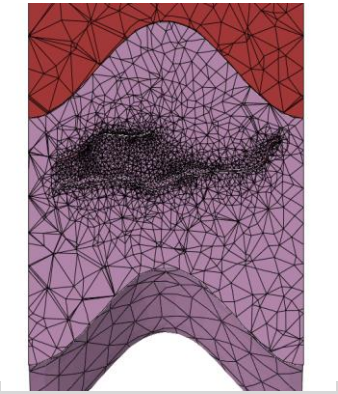

3D simulation of YSZ Dense, GDZ DVC: submodel

Defect - Crack Exploration

YSZ DENSE

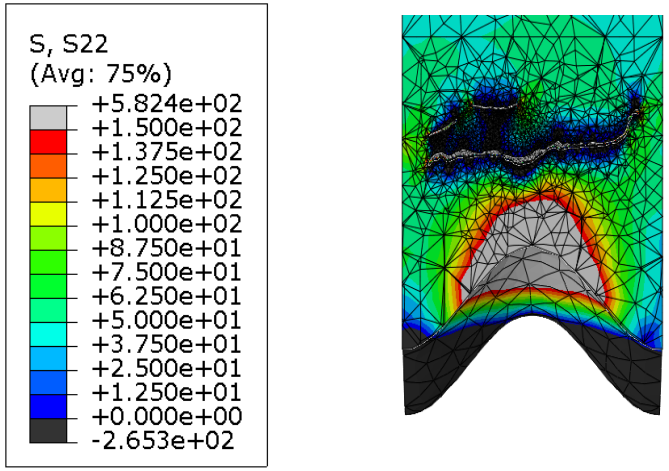

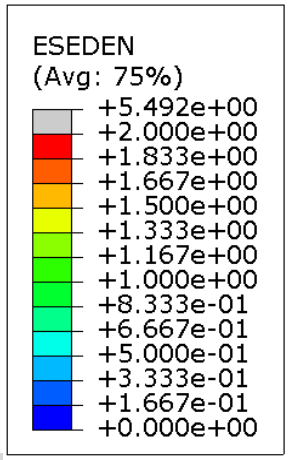

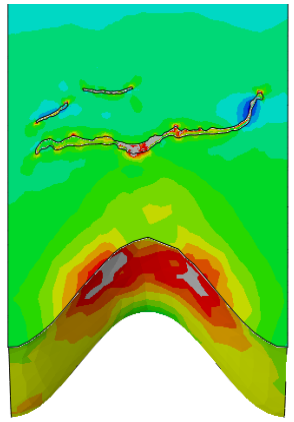

GDZ DVC

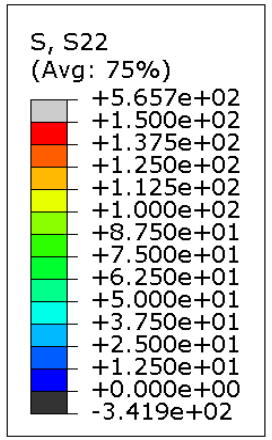

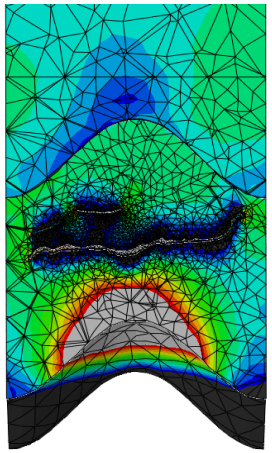

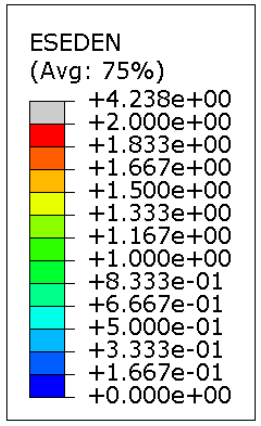

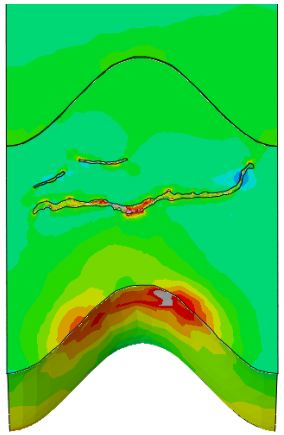

0,150,0,2

A defect graded microstructure can be optimum to reduce stresses and strain energy near the interfaces in the multilayered TBC. Some detriment on fracture toughness would be expected in such a region of defects

Conclusion

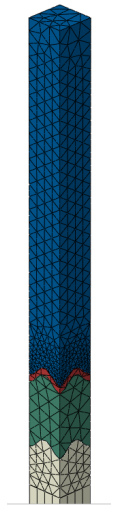

- A multi-scale model was successfully developed to understand thermal stresses and to suggest optimum TBC configurations in terms of layer thicknesses, compliance, roughness, and length of the vertical cracks.

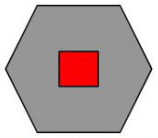

Middle of the island

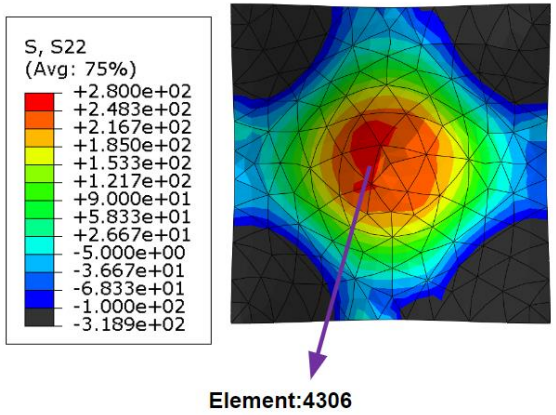

- Vertical cracks in the DVC-type of structure help to relieve stress in the TBC-TGO interface, although some high stress are also observed within the island of the mud-crack type surface morphology.

- Vertical cracks in the DVC-type of structure also create stress concentration in the bi-axial in-plane stresses.

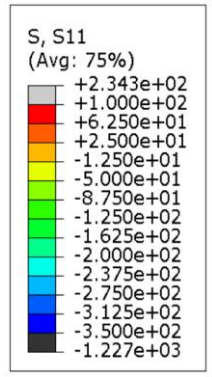

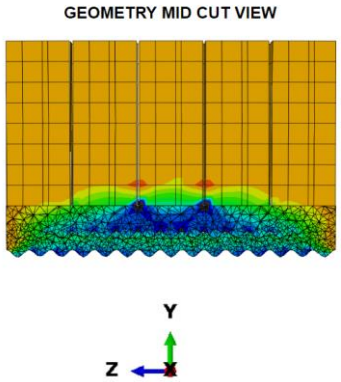

Conclusion

- The longer coating lifetime may respond to the low out-of-plane residual stress owing to the DVC-Dense vertically cracked structure.

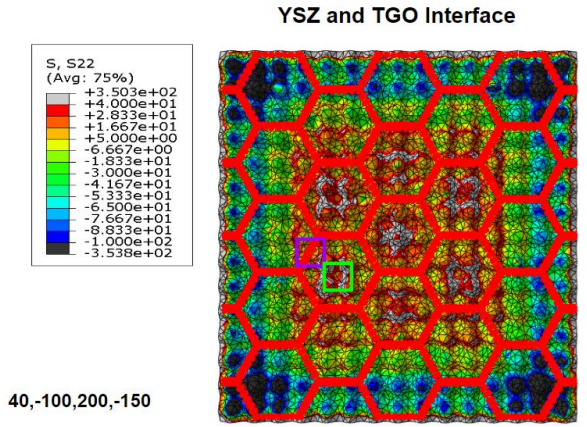

- Understanding the TBC interfaces (i.e. YSZ and GDZ) is important to minimize the strain energy and possible failure points.

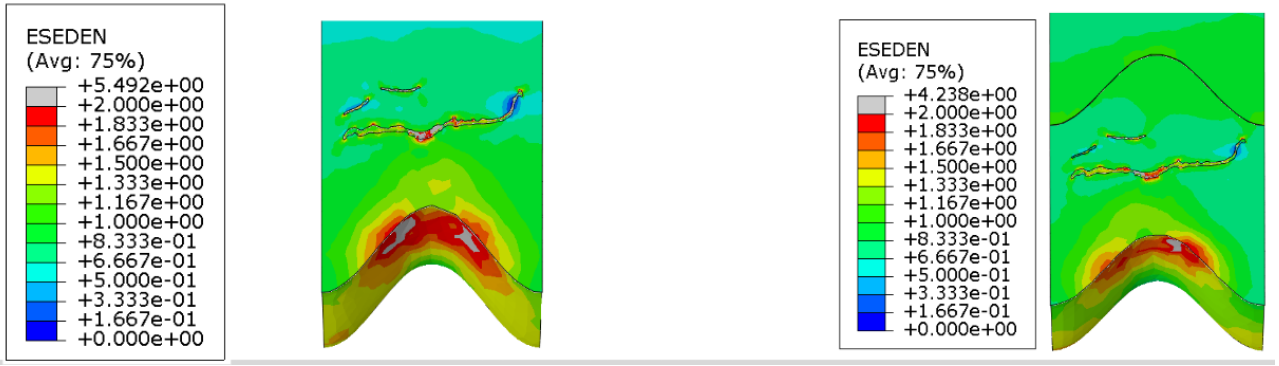

- The presence of graded structure (i.e pores, horizontal cracks) in the transition between the dense and DVC structure can help reduce even more the residual stress.

Universidad San Francisco de Quito

THANKS !!

avalarezo@usfq.edu.ec

Acknowledgment : SOARD – AFOSR

The Southern Office of Aerospace Research and Development (SOARD) is the branch of the Air Force Office of Scientific Research's International Office (AFOSR/IO)

Grant FA9550-20-1-0075